Engineering Defects and Disorder for Enhanced Pharmaceutical Properties

Al-Ani, Aneesa

Award date:
2022

Awarding institution:
University of Bath

Engineering Defects and Disorder for Enhanced Pharmaceutical Properties

submitted by

Aneesa Al-Ani

PhD thesis

University of Bath

Department of Chemistry

October 2021

Abstract

This thesis focuses on the research areas of crystallisation and solid-state chemistry and studies the relationship between crystallisation parameters and the resultant formation of a solid form (e.g. crystal nucleation, growth and morphology) and its associated attributes (e.g. disorder, solubility and stability), focusing on Active Pharmaceutical Ingredients (APIs). The work falls into the Healthcare theme of the Centre for Sustainable and Circular Technologies (CSCT) and focuses on approaches that have the potential to extract the maximum value out of pharmaceutical drugs by establishing methods to enhance a solid form under development.

In Chapter 1, an introduction into the research areas tackled in this work are discussed including context of research, background theory and the scope of research conducted. In Chapters 2 and 3, accounts of the experimental methods implemented in this work are reported and the theory behind the analytical methods utilised discussed.

Chapter 4 focuses on the development of a new crystallisation method, electrospraying, and investigates the influence of several crystallisation parameters on the electrosprayed product. This chapter focuses on gaining a higher level of control over the resulting solid form, including polymorphic control of paracetamol (PCM) via a templating approach and the formation of a novel multi-component complex of PCM and metacetamol (MCM). In addition, Chapter 4 explores the resultant physical properties and particle attributes of the electrosprayed product. The successful transfer of the material produced by electrospraying into a cooling crystallisation platform via crystal seeding is demonstrated, also showing that deploying electrosprayed seeds is to date the only established conventional route to access the PCM-MCM co-crystal.

Chapter 5 explores the co-crystallisation and characterisation of a series of molecular complexes of the API salbutamol (SA). Dicarboxylic acids of increasing chain length are used to facilitate the study of the effect of small changes in the molecular nature of the co-former on crystallographic disorder in the resulting co-crystal structure. Different crystallisation methods and conditions are studied and the presence of crystallographic disorder is identified in each multi-component complex of interest. A structural informatics assessment is conducted alongside a number of physical property studies that compare and contrast each form.

In Chapter 6, single crystals from a series of small scale crystallisations containing salbutamol sulfate (SAS) and the structurally similar salbutamol oxalate are analysed by X-ray crystallography to obtain a portfolio of crystallographic data. A systematic approach is used to characterise the presence of solid-state disorder in individual single crystals in a batch, quantifying variations in disorder between these single crystals. The crystallographic data collected is paired with a bulk analysis technique (solid-state NMR spectroscopy) to promote further understanding of the nature of disorder. The influence of different crystallisation and process parameters is investigated to study if the crystallisation conditions utilised can be used to control variations of disorder seen in a batch of crystals.

The research discussed in Chapter 7 looks to establish a simple empirical method of quantifying the extent of diffuse scattering in a material. A portfolio of crystallographic data is collected for a solid form known to show signs of stacking disorder, phloroglucinol dihydrate (PhG dihy-

drate), from single crystals prepared by evaporative, cooling and vapour diffusion methods. An investigation into the degree of disorder seen in a batch as a function of crystallisation method is presented alongside the establishment of a new empirical methodology for quantifying the amount of diffuse scattering seen in single crystals, the counting spots method.

The final chapter, Chapter 8, presents concluding remarks from the results presented in Chapters 4 to 7, pulling the findings together. The potential of future work in this area of research is discussed.

Acknowledgments

First and foremost, I would like to thank Professor Chick Wilson and Dr. Bernardo Castro-Dominguez for their endless support, guidance, expertise and enthusiasm during my PhD program; it has been a priceless experience and I have thoroughly enjoyed working in both research groups and all of the opportunities that have come from them. Thank you to all of my CSCT colleagues, I have had an enjoyable four years working with the Centre. A special thank you to Francesca Guiso Gallisai and cohort 17 for your continual support throughout my PhD program, my time with the CSCT would not have been the same without you.

I would like to thank my industrial partner, the Right Particle Team at AstraZeneca, especially Dr. Helen Wheatcroft and Dr. Amy Robertson, for all of the help and advice you have given me during my PhD program. Working with the team has been an amazing opportunity and has made a big difference to this work. Thank you to Helen, Chick and Bernardo for all of the MS teams calls during lockdown and for keeping me on track during such an uncertain time. Thank you to everyone at AstraZeneca who hosted my remote placement. I have learnt an incredible amount in such a short space of time. A special thank you to Dr. Helen Blade for all of your knowledge, help, and support during my time on placement; you really do make science fun!

Thank you to all of the members in the Wilson and Castro-Dominguez groups over the years. You have been a fun bunch of people to work with and I have had the pleasure of making some life-long friends. A special thank you goes to Dr. Pollyanna Payne for keeping me company and baking lots of sweet treats and the most delicious birthday cake! I thoroughly enjoyed our lockdown walks, if only we had the time to do more. Thank you to my office buddy Matthew Wilkinson for making my last few months in the office so much fun. Finally, thank you to Dr. Lauren Hatcher, for taking the time to teach me the practical side of crystallographic data collection and refinement, and for continuing to help me after your time in the Wilson group had ended. Thank you to Dr. Daniel Fonseca Segura for helping me troubleshoot problems with the electrospray. I have had the pleasure of supervising two fantastic project students, Cameron Wilson and Posy Sugden. Thank you for all of your hard work and your contribution to two great research projects.

Finally, a big thank you to Sam Wardell for all of your support and encouragement during my studies. Thank you for listening to my endless stories about crystals and for putting up with my grumpy moments. Thank you to my mum, Stephen, Harry, grandparents and my in-laws for your love and support and for trying to understand crystallisation science and crystallography.

This thesis is dedicated to my wonderful grandparents, Gerry and Joyce Prior, who inspire me everyday.

Contents

List of Figures

List of Tables

Glossary

^{1}H NMR spectroscopy proton nuclear magnetic resonance spectroscopy.

%RH relative humidity percentage.

$\boldsymbol{E}_{ex}$ external electric field.

$\boldsymbol{E}_{in}$ electric field inside droplet.

Ace acetone.

AD adipic acid.

APIs Active Pharmaceutical Ingredients.

BCS The Biopharmaceutics Classification System.

BET Brunauer–Emmett–Teller.

CD spectroscopy circular dichroism spectroscopy.

CQAs critical quality attributes.

CSCT Centre for Sustainable and Circular Technologies.

CSD Cambridge Structural Database.

DSC Differential Scanning Calorimetry.

E-field electric field.

ee enantiomeric excess.

EtOAc ethyl acetate.

EtOH ethanol.

FDA Food and Drug Administration.

GL glutaric acid.

HSM hot-stage microscopy.

hx hexane.

IPA iso-propanol.

LAG liquid assisted grinding.

MA malonic acid.

MCM metacetamol.

MCM-I metacetamol form I.

MCM-II metacetamol form II.

MeOH methanol.

MSZW metastable zone width.

OX oxalic acid.

PCM paracetamol.

PCM-I paracetamol form I.

PCM-II paracetamol form II.

PhG dihydrate phloroglucinol dihydrate.

PSD particle size distribution.

PXRD powder X-ray diffraction.

QbD quality by design.

SA salbutamol.

SA-AD salbutamol and adipic acid.

SA-GL salbutamol and glutaric acid.

SA-OX salbutamol and oxalic acid.

SA-SU salbutamol and succinic acid.

SA-SU-EtOH salbutamol succinate ethanol solvate.

SA-SU-MeOH salbutamol succinate methanol solvate.

SAS salbutamol sulfate.

SCXRD single crystal X-ray diffraction.

SEM Scanning Electron Microscopy.

SMPT solution mediated phase transformation.

SS-NMR spectroscopy solid-state nuclear magnetic resonance spectroscopy.

STR stirred tank reactor.

SU succinic acid.

$\mathbf{T}_g$ glass transition temperature.

TGA thermogravimetric analysis.

Chapter 1

Background

1.1 Context of research

The understanding and control of solid state behaviour in pharmaceutical materials is of importance; it is especially important within the crystallisation process, a vital step in the manufacture of pharmaceuticals and fine chemicals.[1–3] Gaining control over the crystallisation process is vital to obtain the desired solid form (molecular level solid-state structure, usually crystalline) and particle attributes of a compound, since different solid forms have different chemical and physical properties.[2,4–6] Because of this, there has been a vast amount of research into the prediction, characterisation and control of the solid form of Active Pharmaceutical Ingredients (APIs) to enhance their properties; experimental investigations of the solid form of API compounds include extensive and systematic screening for new polymorphic forms[7–9] in addition to salt[10,11] and co-crystal formation[5,12,13]. These processes are routinely investigated during drug development and are currently under strict regulation by licensing authorities such as the Food and Drug Administration (FDA) in the USA. In contrast, the understanding and control of disorder and defects in the solid-state structure of pharmaceutical materials has not been researched to a large extent, is not routinely investigated during drug development and is not required or monitored by the FDA.[14] This is a surprisingly overlooked area of research given that it is commonly recognised that disorder and defects in crystals have an influence on the solid state properties of materials, including pharmaceuticals and excipients.[15] This is not simply an oversight but is a result of a lack of analytical tools for the complete identification and characterisation of crystallographic disorder in pharmaceutical materials.

The work presented in this thesis was carried out as part of the EPSRC Centre for Doctoral Training in Sustainable Chemical Technologies (CSCT). The training and research programme of CSCT is interdisciplinary, bringing together science and engineering to carry out research in collaboration with industry. Research outputs from related work carried out during this doctoral programme are available in section 1 of the Appendix (Chapter 9) including publications, work presented at conferences, research collaborations and crystal structures deposited by the author into the Cambridge Structural Database (CSD).

1.2 The crystallisation process

Crystallisation is one of the most important steps in the manufacture of pharmaceuticals. It is the method used both for the purification and separation of APIs from a reaction mixture and for the production of primary crystalline products suitable to be used directly in downstream formulation. The methodology used in a crystallisation process is key to gaining control over the crystal structure, including the production of crystals with desired properties and macroscopic characteristics of the crystalline particle.[1,16] Crystallisation processes can yield both crystalline and amorphous solid forms. A crystalline solid exhibits long range order with a regular repeating structure that forms an infinite three-dimensional array, whereas an amorphous solid is a system that exhibits short range order in which molecules arrange with no particular regularity on longer length scales.[17] The length scale of the order in a crystal (short range or long range) is of high importance for crystallisation, as it is the arrangement of molecules within the solid state that is responsible for the building block interactions and stability of a solid form.[16] Various different crystallisation methods exist; the work conducted in this project focuses on crystallisation from solution, the primary production method of crystalline solids in the fine chemical and pharmaceutical industry. A solution-mediated crystallisation process can be characterised by three stages: supersaturation, nucleation and crystal growth. A crystallisation process is designed through the understanding of these three stages. A successful crystallisation process is determined by the thermodynamics of the system and the kinetics behind nucleation and growth of the solid form.[17]

1.2.1 Supersaturation

Supersaturation is the driving force behind crystal nucleation and therefore crystal growth. The range over which crystallisation can occur is dependent on the solubility of the API. The solubility of a material is defined as the maximum amount of solute that can dissolve in a given solvent at a given temperature.[18] When the solubility of a material is measured at different temperatures a solubility curve can be created for that solid form. A solubility curve, shown in figure 1-1, is thermodynamically driven and is not dependent on the crystallisation environment. The curve shows the equilibrium points, where at any given temperature the solution of a compound is saturated. A solution is supersaturated when it lies above the solubility curve and undersaturated when it lies below the solubility curve. A supersaturated solution contains a larger amount of dissolved solute than the solution at equilibrium.

Just above the solubility curve lies a kinetically controlled metastable region (the dotted line in figure 1-1). This region corresponds to a solution that is supersaturated, however no spontaneous (primary) nucleation can occur, only crystal growth. The metastable zone width (MSZW) describes two boundaries between the solubility line and the line which indicates when spontaneous nucleation can occur, above which the supersaturated solution is labile.[18]

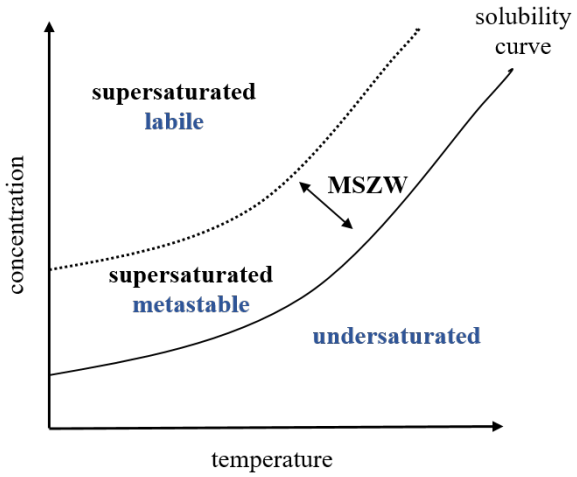

Figure 1-1: A schematic solubility curve, showing the solubility of a compound as a function of temperature and the metastable region.

The supersaturation of a solution can be calculated in multiple ways when the concentration of the solution (c) and the concentration of the solution at equilibrium saturation (c*) are known. Equation 1.1 calculates the difference between c and c* and is used to determine the supersaturation of a solution (Δc) when both values are at the same temperature. The greater the value of Δc the stronger the driving force for crystallisation. Equation 1.2 calculates the supersaturation ratio (S) of the c and c* values, where a value of 1 describes a supersaturated system. Finally, equation 1.3 calculates the relative supersaturation (σ), a dimensionless value. Supersaturation may also be described thermodynamically by calculating the difference in the chemical potential (μ) of a molecule in an equilibrium (μ_{eq}) and supersaturated (μ_{ss}) state (equation 1.4).[18–20]

$$\Delta c = c - c^* \tag{1.1}$$

$$S = \frac{c}{c^*} \tag{1.2}$$

$$\sigma = \frac{\Delta c}{c^*} = S - 1 \tag{1.3}$$

$$\Delta \mu = \mu_{ss} - \mu_{eq} \tag{1.4}$$

1.2.2 Nucleation

Nucleation is the first step in crystallisation. It describes the process that initiates the creation of a new solid phase from a supersaturated solution, starting from a crystal nucleus. Once formed, the crystal nuclei can grow during the crystallisation process. There are two types of nucleation, primary[16,17] and secondary[16], in addition to two different ways in which nucleation can be induced, homogeneously and heterogeneously. Figure 1-2 shows a schematic representation of the pathways for each type of nucleation; each pathway is discussed in detail below.

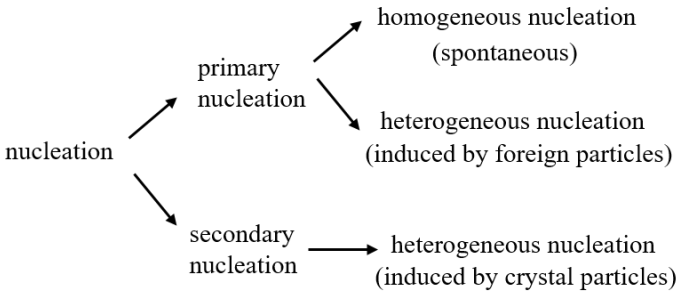

Figure 1-2: Pathways for the types of nucleation in a crystallisation process.

1.2.2.1 Primary nucleation

Primary nucleation is a spontaneous process that can be homogeneous or heterogeneous. Heterogeneous nucleation occurs in the presence of a solid foreign interface[16] (such as dust or a surface such as the vessel walls), whilst homogeneous nucleation is a result of supersaturation alone.[17] There are two mechanisms used to describe the kinetics behind primary nucleation from a saturated solution, classical nucleation theory and two step nucleation (also known as non-classical nucleation theory)[21], illustrated in figure 1-3.

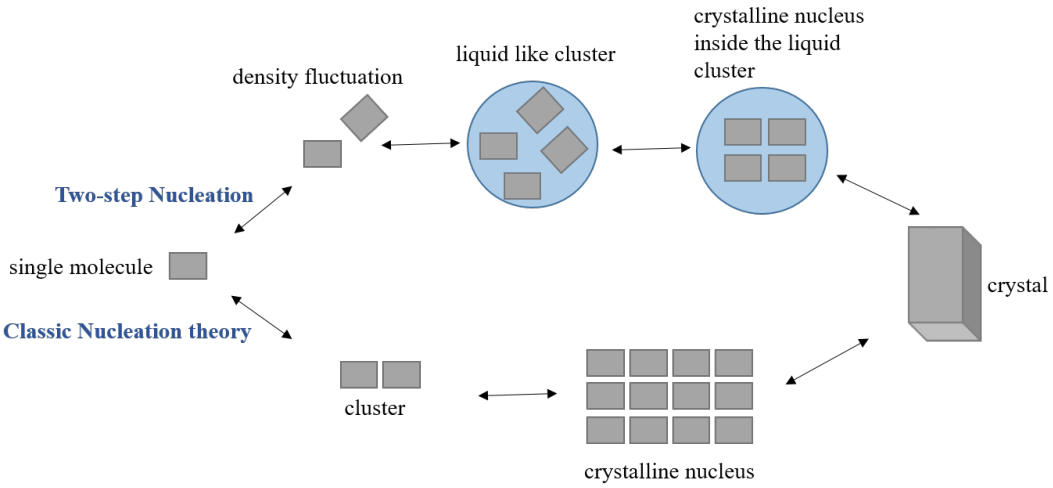

Figure 1-3: An illustration of two pathways that describe the mechanism behind nucleation; classical nucleation theory (bottom) and two-step nucleation theory (top).

Both classical nucleation theory and two step nucleation rely on cluster formation and are dependent on the Gibbs free energy (ΔG). Nucleation is dependent on a ratio between the interface free energy (surface area) and the bulk free energy (volume); figure 1-4 shows the relationship between these factors in contributing towards the value of ΔG. The formation of a nucleus is dependent on overcoming the system's free energy barrier. Initially, the interface free energy is dominant, however once the critical nuclei radius is reached the bulk free energy is dominant and results in a negative, thermodynamically favourable, ΔG. Clusters are formed in a stochastic process from molecule collisions in solution; as the size of the cluster increases the surface area to volume ratio decreases until a critical size is reached (known as the critical nuclei radius, r*). The critical nuclei can sustain crystal growth as dissolution becomes less

favourable in free energy terms than the addition of new molecules and the tendency for the nuclei to dissolve back into solution is overcome. Beyond this point (the maximum of the ΔG curve in figure 1-4), crystal growth becomes favoured and the intermolecular forces within the nuclei counteract the forces from the surrounding particles. The total free energy of nucleation in a homogeneous solution as a function of radius is shown in figure 1-4 (blue line).[17,21,22]

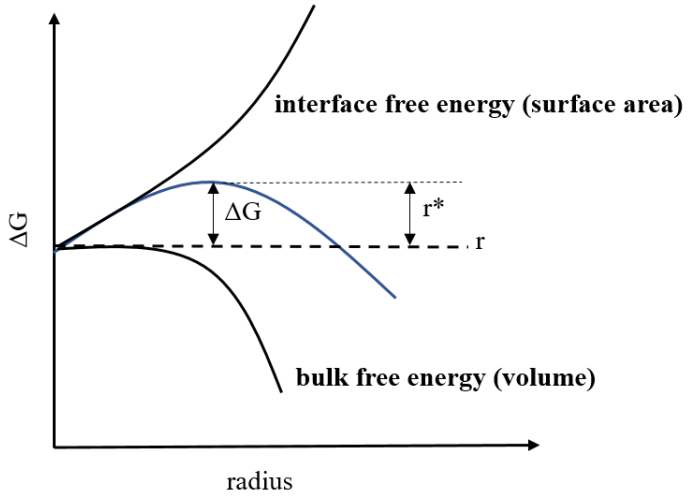

Figure 1-4: The free energy diagram of a droplet for nucleation, as a function of radius.

Classical nucleation theory assumes that nucleation occurs in a droplet-like system, where r is the droplet radius.[16] In this case, the bulk term refers to the droplet volume and is always negative and the interface term refers to the surface area of a droplet and is always positive. The height of the free energy barrier depends on the supersaturation of the system, a lower supersaturation increases the free energy barrier and decreases the rate of nucleation.[16,22,23]

Two step nucleation is an alternative theory that involves a two-step mechanism. It builds on a limitation to classical nucleation theory that assumes individual molecules add to a cluster one at a time. In the two-step model, clusters are described as rearranging as they are being assembled. Two step nucleation theory suggests the formation of a highly disordered liquid-like cluster in areas of the solution with a high concentration of solute. This disordered cluster reorganizes to form an ordered crystal nucleus that is larger than the critical size for crystal growth that hence will subsequently grow.[17,21,22]

1.2.2.2 Secondary nucleation

Secondary nucleation describes nucleation of crystals induced from the surface of deliberately introduced foreign particles (such as dust or additives) or solute crystals (known as seeding). Nucleation on a surface (in this case of one of the introduced particles) is energetically favoured and has a lower energy barrier than homogeneous nucleation due to a smaller interface energy, since the material can absorb onto a surface. Heterogeneous nucleation can therefore occur at a lower level of supersaturation (in the metastable zone)[16] than homogeneous (primary) nucleation which requires a higher level of supersaturation, in the labile region. The width of the metastable zone is kinetically driven and is dependent on experimental conditions, such as:

size and type of crystallisation vessel, rate of cooling, concentration of additive and agitation (e.g. stirring). There are three main mechanisms by which secondary nucleation can occur: 1) originating from the crystal, in which crystalline dust shed from the addition of a crystal seed can act as a secondary nucleus; 2) shear nucleation, which is caused by shear forces in the system that produce secondary nuclei from the seed surface; and 3) contact nucleation, the most common mechanism, in which secondary nuclei are created from collisions, for example, crystal-crystal, crystal-wall and crystal-stirrer bar collisions.[17,22,24]

1.2.3 Crystal growth

After the formation of stable nuclei from nucleation, crystal growth can begin and will lead to visible crystals in the crystallising solution. Crystal growth is dependent on two main parameters. The first parameter relates to the exposure of the crystal nucleus surface to a supersaturated environment and the second to the number of growth units (atoms, ions, molecules) reaching the surface, which must outweigh the number leaving.[25] The ability of a nucleus to grow by capturing growth units is dependent upon the number and strength of interactions between the nucleus surface and growth unit. Hartman and Perdok proposed that a growth unit can form a maximum of three bonds with a crystal surface. The formation of three bonds in this way is described as kinked (K), while the situation with two bonds formed is termed stepped (S) and that with one bond flat (F) crystal growth;[16,26] these are illustrated in figure 1-5.

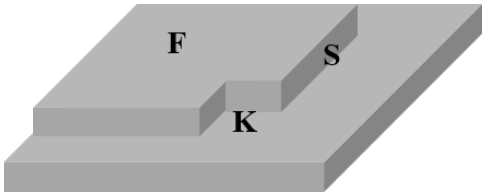

Figure 1-5: A three-dimensional crystal, showing the three types of crystal growth mechanisms, flat (F), surface (S) and kinked (K).

Crystal growth theory suggests that crystal growth is not solely led by flat growth units, as the strength of intermolecular interactions would be too low in comparison to covalent bonds. For a flat face to grow at a reasonable rate, a high interaction energy site must be created, for example through the removal of a surface growth unit to create a K or S site to start a new layer; the initial step involves an unfavourable positive Gibbs energy change. Crystal growth at a kinked face is the most energetically favoured (under a linear growth rate). In this case, three interactions contribute to an existing step and do not form a new step.[26] The term α (equation 1.5) describes the ease for a crystal surface to promote crystal growth by the creation of steps and kinks. The lower the value of α, the faster the formation of steps and kinks on the surface will be and in turn crystal growth rates will be faster.

$$\alpha = \Delta E \,/\, kT \tag{1.5}$$

The extent to which a crystal can grow depends on several parameters: 1) the number of nuclei

formed; 2) where the system lies in relation to the solubility curve (in the supersaturated zone or in the metastable zone); and 3) the width of the metastable zone.[27] Figure 1-6 displays an example of how these parameters can affect crystal growth. Upon initial nucleation (A), the concentration of solution will decrease due to formation of stable nuclei, at constant temperature. Crystal growth will then start and continue until the equilibrium concentration of solution is reached (B). The relative growth rate of each crystal face directly determines the resultant crystal's morphology.

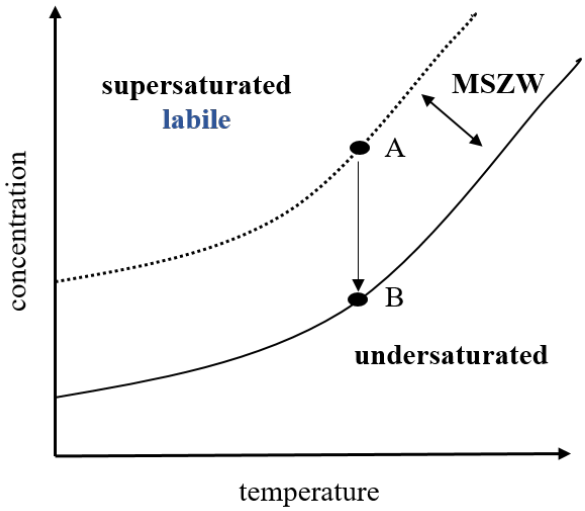

Figure 1-6: Schematic of key steps in crystal growth. A) initial nucleation. B) crystal growth will occur until equilibrium concentration is reached.

Crystal growth mechanisms consider the possible pathways that can lead to crystal growth, from which a molecule in solution becomes integrated into a particular lattice position on a crystal growth face. Figure 1-7 shows the free energy barriers that are overcome during the process of crystal growth, where growth units are transformed from the liquid state to the solid state. The Gibbs-Volmer theory describes crystal growth as a process that occurs layer by layer. Three Gibbs free energy barriers are overcome in this process including desolvation (ΔG_{desolv}), diffusion (ΔG_{diff}) and further desolvation to a kinked site position (ΔG_k). The first energy barrier, ΔG_{desolv}, is overcome when solute molecules are able to adsorb onto the crystal surface once some of its solvent molecules are lost. At this point the growth unit is left partially desolvated and can enter the absorption layer (position 1 in figure 1-7). The second energy barrier, ΔG_{diff} is overcome when the growth unit can diffuse across the surface to a step position (position 2 in figure 1-7). Further desolvation must occur to overcome the final energy barrier, ΔG_k, and a growth unit can absorb onto a kinked site (most favourable) or step site (less favourable).[26]

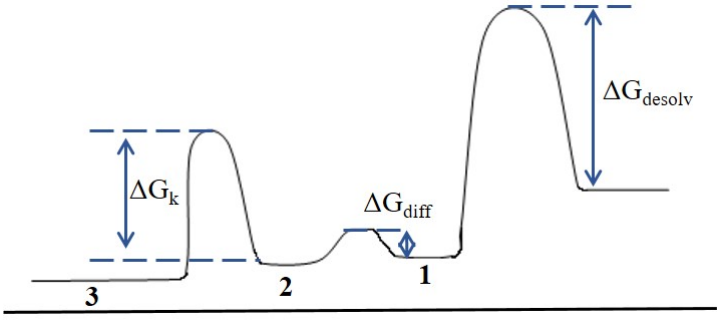

Figure 1-7: The free energy barriers that are overcome during crystal growth: desolvation (ΔG_{desolv}), diffusion (ΔG_{diff}) and further desolvation to a kinked site position.
*This figure was modified from Davey et al[26]

1.2.3.1 Crystal growth mechanisms

There are a number of possible pathways that lead to crystal growth: continuous growth, surface nucleation and spiral growth. In each case, the crystal growth mechanism is dependent on the value of α from equation 1.5.

A low value of α (less than three) corresponds to a low ΔE value. At this point the crystal surface will contain many step and kink sites and every growth unit that approaches the surface can attach to a growth site. In this case the crystal growth mechanism is known as continuous growth since the growth rate is linearly proportional to the supersaturation.[26]

At an α value between three and five, not all growth units that approach the surface can find a growth site to absorb onto. These growth units can return to the liquid phase or can form stable clusters or nuclei on a flat surface; once the clusters have reached the critical size for crystal growth an additional surface layer is formed. A new surface layer can become an additional source for growth sites.[25,26] This crystal growth mechanism is known as two-dimensional surface nucleation. An example of this crystal growth method is illustrated in figure 1-8a.

At an α value above five, the crystal surface is flat due to the enhancement of intermolecular interactions. Crystal growth may now only occur from the creation of a step from an "energetically cheap process".[26] This route can take place in the presence of lattice defects such as screw dislocations (a self-generated step). A perfect crystal lattice does not exist for real crystals and an array of defects will be observed.[16] Therefore, to obtain a perfectly flat crystal face that would require two-dimensional surface nucleation to grow is highly unlikely. A dislocation can form on a surface as a result of stresses from crystal growth. Once a surface has a dislocation, the crystal face will grow in a spiral, shown in figure 1-8b.[25,26]

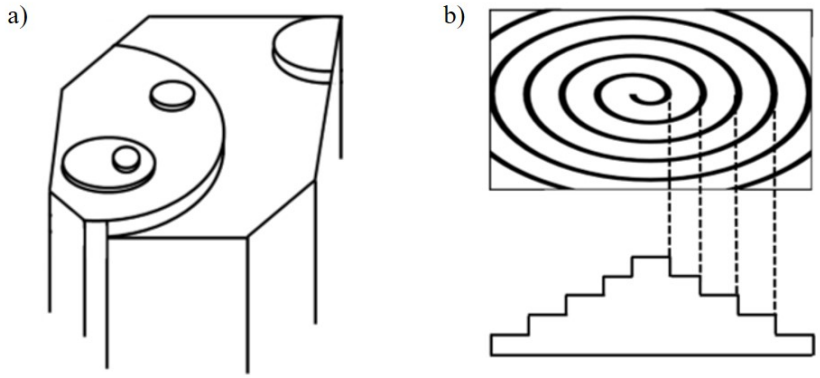

Figure 1-8: Illustrations of crystal growth mechanisms: a) two-dimensional surface nucleation and b) spiral growth.
*This figure was taken from Davey et al[26]

1.2.4 Crystal morphology

Crystal morphology, often referred to as habit, describes the external shape of a crystal. The morphology of a crystal depends on two factors. First, the symmetry of the internal crystal structure which governs the type and strength of intermolecular interactions present. Secondly, the relative growth rates of crystal faces, which are bound by the slowest growing face. Crystal growth and therefore growth rates are dominated by intermolecular interactions. A crystal face with the formation of strong interactions, for example hydrogen bonds, will have a faster growth rate than a face with weaker interactions, for example van der Waals forces.[28] This dependent nature means that the morphology of a crystal can be influenced by external factors, such as the temperature, nature of solvent, pH and the level of supersaturation used in a crystallisation method. In addition, the presence of impurities (or additives) and crystallographic defects can influence the morphology of a crystal, the effect being dependent on the nature, number and distribution of defects present.[25,28]

Crystal morphology is an important property in the fine chemicals and pharmaceutical industry. The shape and size of a crystal has a large influence on the ease of product processing and formulation; it can directly affect the flowability and compressibility of a system and downstream processes, for example filtration and drying. Figure 1-9 illustrates a common problem with filtration in the chemical industry. Crystals with a needle-like, plate-like or fibrous-like habit are undesirable since they have a tendency to pack and create an impervious layer (known as cake formation) that limits filtration and washing. In contrast, crystals of a cuboid-like habit are desirable and do not limit the flow of filtration and washing. The solution flow during filtration is represented in the image by arrows.[29,30]

The particle size of a crystal is another important property in the fine chemicals and pharmaceutical industry; it can influence many physical and chemical properties that can affect a material's behaviour. These properties include solubility, dissolution, bioavailability, bulk density and the segregation of powder mixtures. Typically, pharmaceutical materials in powder form have a variety of particle sizes; the range of sizes present in a material is described as the particle size distribution (PSD). The PSD may be a symmetrical bell curve with a maximum

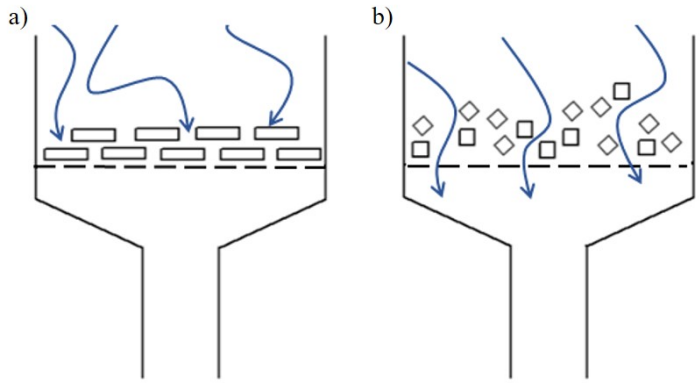

Figure 1-9: Comparison of the ease of filtration with (a) a plate-like morphology and (b) a cuboid-like morphology. An impervious layer is created in (a) that limits the flowability in comparison to (b).

frequency value, or an asymmetrical curve that suggests an increased amount of smaller or larger particles that result in a skewed distribution.[25] A small uniform particle size with a narrow distribution is highly desired. It allows for uniform dissolution rates of particles and an increased ease of compaction for tablet formation. Manufacturing processes such as milling, micronisation and spray-drying are extra steps that are commonly used to gain a desired particle size with a uniform distribution in cases where these desired properties are not achieved by the primary crystallisation method.[31,32]

1.3 Crystallisation methods

For crystal nucleation and growth to occur from solution, a crystallisation method must be designed for a system to reach supersaturation. As previously discussed in section 1.2.1, the solubility of a material must be fully characterised in a chosen solvent before an efficient crystallisation process can be designed. Once the solubility of a material is determined, the type of crystallisation method can be chosen.[7] Five solution mediated crystallisation techniques and one mechanical crystallisation technique are discussed below and are used in this work. These are evaporative, cooling, solution-mediated (slurry), vapour diffusion, electrospraying crystallisation and mechanical grinding. The translation of a target solid form into a different crystallisation platform is routinely investigated, as presented in chapters 4, 5 and 6.

1.3.1 Evaporative crystallisation

Evaporative crystallisation is typically used as a screening method in solid-state materials discovery; many small scale crystallisations are set up with differing values of a range of variables that are known to affect crystal growth, such as the temperature, saturation and solvent system. In evaporative crystallisation, supersaturation is reached through solvent evaporation at a fixed temperature. As the solvent evaporates an undersaturated system will become more saturated and pass through the MSZW into the labile supersaturated zone, where spontaneous nucleation will start to occur, illustrated by path A in figure 1-10.

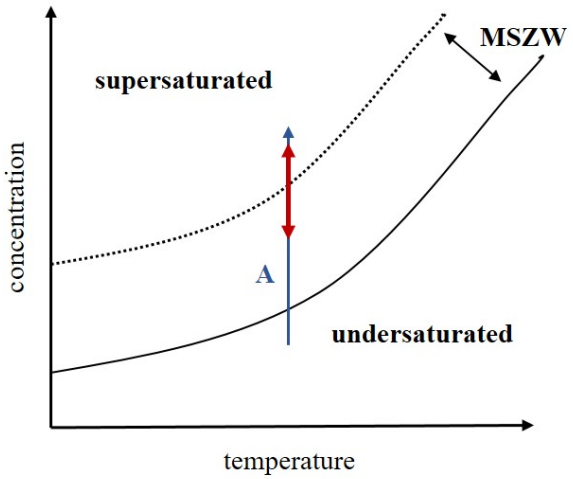

Figure 1-10: The generation of a supersaturated environment by evaporative crystallisation (arrow A).

Continual evaporation ensures that the system remains in the supersaturated region upon nucleation and crystal growth, where the system's concentration will decrease, illustrated by the red arrow in figure 1-10. Slow evaporation at low temperatures provides good conditions for single crystal growth.[33] Evaporative crystallisation is used in this work as a screening method for the production of new multi-component complexes and as a method of growing strongly diffracting large single crystals in chapters 5, 6 and 7.

1.3.2 Cooling crystallisation

Cooling is typically the preferred crystallisation method in the pharmaceutical industry for both batch and continuous platforms. It is favoured due to a relatively high level of control over the final product and the ease of scale up.[25] However, a material must be significantly soluble in the chosen solvent in order to achieve a satisfactory product yield. A cooling profile is designed and optimised to gain control over the crystallisation process; this uses the solubility curve of the material. In a typical cooling profile, supersaturation is reached by decreasing the temperature of crystallisation at a fixed rate. A decrease in temperature causes a decrease in solubility of the solute and pushes the system into a supersaturated state, where spontaneous nucleation and crystal growth can occur, illustrated by path B in figure 1-11.

1.3.2.1 Seeded cooling crystallisation

If the system's MSZW is known, a seeded cooling crystallisation can be designed. This strategy is often introduced to gain a higher level of control over the crystallised solid form including selectivity and reproducibility and to improve the PSD of the resultant material. A seed of the desired crystal form (crystal seeding) is introduced when the system is held in the MSZW. This ensures the occurrence of secondary nucleation alone, which promotes crystal growth of the seed, and the suppression of spontaneous nucleation.[34] For a successful process with a high level of control, a cooling profile is usually designed such that the concentration of the solution remains in the MSZW after initial nucleation has taken place. An important factor

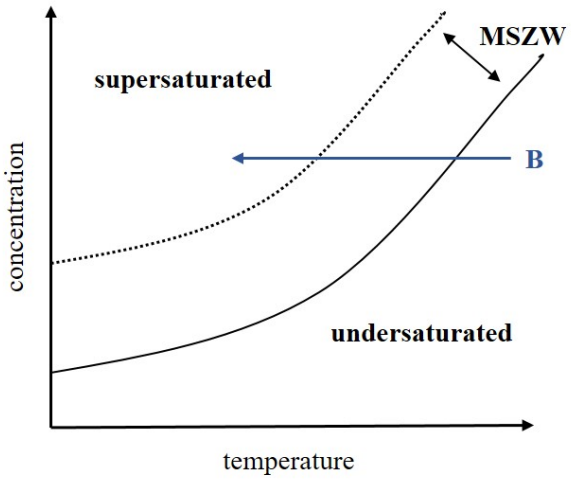

Figure 1-11: The generation of a supersaturated environment by cooling crystallisation (arrow B).

in the design of a cooling profile is the temperature at which the seeds are added. Figure 1-12 shows four different temperatures (A, B, C and D) at which crystal seeds may be added to a crystalliser.

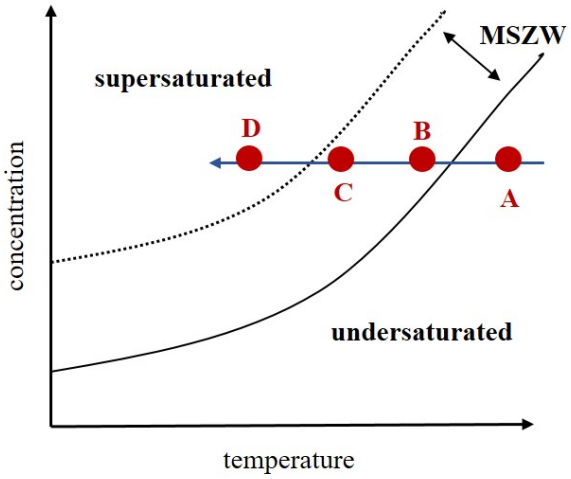

Figure 1-12: The addition of seeds at different temperatures: in the undersaturated temperature zone (A); in the MSZW, close to the solubility curve (B), or close to the metastable limit curve (C); in the supersaturated labile zone (D).

The addition of seeds at point A, an unsaturated solution, will lead to dissolution of the seeds and no crystal growth. In-contrast, seed addition at point B and C, in the metastable zone, leads to crystal growth. Seed addition at point B is most favoured since the supersaturation is low at this point, therefore, secondary nucleation is minimal. This leads to slow crystal growth conditions and the formation of larger crystals. Seed addition at point C occurs close to the metastable zone limit. At this point there is a higher level of supersaturation in the solution and secondary nucleation may occur. This leads to the generation of numerous small crystals and rapid crystal growth rates. Crystal seeding at point D, in the labile supersaturated zone, will lead to the occurrence of secondary and primary nucleation. This may introduce an

undesired solid form and can cause a broad particle size distribution. Crystal seeding is used in this work for the controlled crystallisation of elusive solid forms in chapter 4.

1.3.3 Solution-mediated crystallisation (slurrying)

Solution-mediated crystallisation, also known as slurrying, is a technique that is based upon solution-mediated phase transformations that can occur due to the thermodynamic relationship between different solid forms in solution, such as polymorphs and multi-component complexes. Slurrying is an efficient method for identifying new polymorphic forms, salts and co-crystals (and determining their relative thermodynamic stabilities). Figure 1-13 shows the solubility curves of two components, A (black) and B (red). In a slurrying crystallisation an excess of A and B is added to a chosen solvent until the solution is saturated with respect to both components. In this case, a co-crystal of A and B, termed AB (blue), is more stable in solution than the components as single entities and is therefore less soluble. At this point the system is saturated with components A and B and supersaturated with respect to the co-crystal (AB). Spontaneous nucleation of the co-crystal can thus occur (assuming the system is in the labile supersaturated region). Upon co-crystal nucleation, the concentration of components A and B will start to deplete from solution. This will result in a continuous cycle of A and B further dissolving in solution, leading to further nucleation of the co-crystal (AB), until all of the starting material is converted into the least soluble form, in this case AB.[35] Slurrying is used in this work for the co-crystallisation of multi-component complexes in chapters 4 and 5.

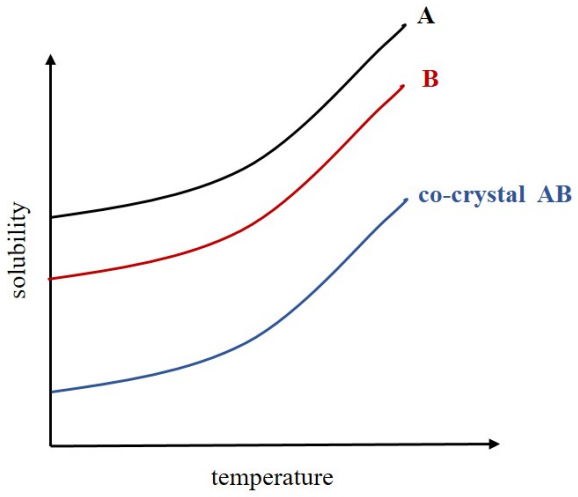

Figure 1-13: Solubility curves of starting components A (black), B (red) and a co-crystal AB (blue).

1.3.4 Vapour diffusion

Vapour diffusion uses a binary solvent system, with two solvents that are miscible. The solute to be crystallised must be soluble in the solvent with the higher boiling point and insoluble in the solvent with the lowest boiling point (anti-solvent). The solvent containing the solute is contained in a smaller open beaker that is placed inside a larger closed beaker that contains the anti-solvent. The more volatile anti-solvent will diffuse into the second solvent that contains the

solute. This decreases the solubility of the solute and pushes the system into a supersaturated state, illustrated by A in figure 1-10, hence inducing crystallisation. The diffusion speed can be controlled by the crystallisation temperature.

1.3.5 Electrospraying

Electrospraying is an electrohydrodynamic atomisation technique that has been extensively studied for pharmaceutical applications. It has been acknowledged to be a promising approach due to a high level of flexibility with the ability to tailor the particle size and change the morphology of an API.[36] The use of electrospraying is emerging in a wide range of industries for advanced pharmaceutical and biomedical applications, particularly drug encapsulation.[37,38] A similar technique, electrospinning, utilises the same working principle as electrospraying and is extensively used in a wide range of industries such as the textiles[39] and food.[40] Electrospinning is different from electrospraying: during electrospinning the charged liquid does not break up into droplets (discussed below) but is elongated by the applied electrical potential to afford ultra-fine micro to nano scale fibers upon solvent evaporation. This outcome is usually due to the dissolution of high molecular weight polymers in the liquid.[41]

Electrospraying may currently be lagging behind this counterpart technology, but it promises to become more prominent with the growth of nanotechnology as an emerging tool within the pharmaceutical industry. Nanotechnology, in terms of crystallisation, can be defined as the manipulation of materials at the nanometer scale, to gain control of how individual molecules and atoms arrange.[42] Electrospraying is a technique that can achieve a micro to nano scale crystallisation environment through liquid droplets and is therefore of interest. The capabilities of electrospraying for polymorphic control and co-crystallisation are investigated in chapter 4. The theory of electrospraying involves phenomena known as the Taylor cone and Rayleigh disintegration, discussed below.

1.3.5.1 The Taylor cone-jet

A standard electrospray set up consists of a pump, a metal emitter that is connected to a voltage supply and a grounded collector plate. The set up is usually contained within a closed environment that can control temperature. In the course of electrospraying, a liquid is slowly pumped through a metal emitter where electrical potential is applied.[41] Upon contact, a liquid parent droplet formed at the emitter becomes statically charged with an even distribution over the surface. At this point, there is an accumulation of charge which distorts the droplet into a conical shape[43] known as the Taylor cone (figure 1-14). A critical electrical potential is reached once repulsive electrostatic forces overcome the attractive surface tension forces of the distorted parent droplet and the liquid breaks up into smaller primary droplets at the tip of the Taylor cone; this is known as the Taylor limit.[41,44,45] These primary droplets are electrically charged, evaporating and unstable and therefore undergo Rayleigh disintegration.

1.3.5.2 Rayleigh disintegration

Rayleigh disintegration (or Coulomb fission) describes the journey of the primary droplets to the collector plate (figure 1-14). The primary droplets undergo solvent evaporation and shrink, this leads to an increase in their charge concentration. The primary droplets continue to rupture into smaller droplets until they reach a micro or nano droplet size. Complete solvent evaporation occurs effectively instantaneously at these sizes, yielding micro or nano particulates within the liquid droplet that accumulate on the collector plate.[41,46]

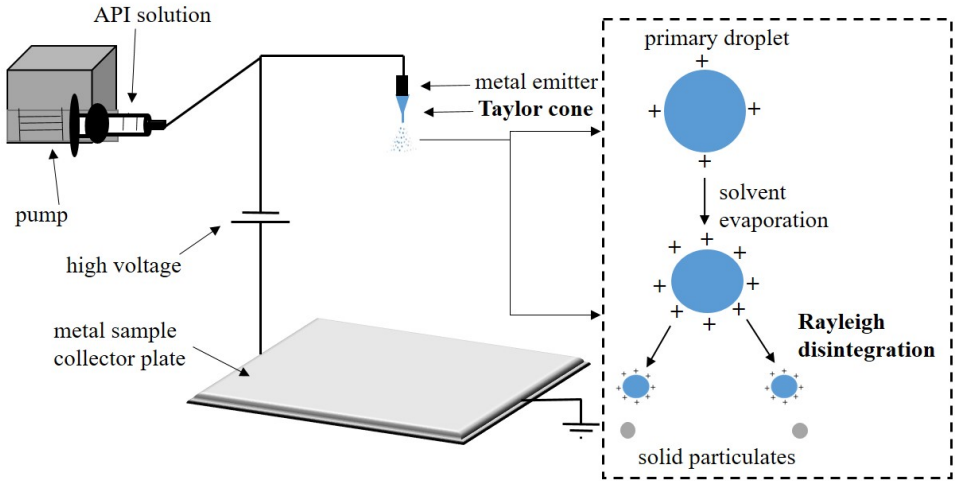

Figure 1-14: The formation of a Taylor cone and the resultant Rayleigh disintegration from an electrospraying set up.

1.3.5.3 The importance of a stable Taylor cone-jet

Electrospraying as a crystallisation technique can offer desired properties for drug performance and processability including small sized particles with a narrow PSD range,[41] and control over morphology,[47,48] polymorphism[47] and solid form.[49] However, a high level of control over these properties may only be achieved with the formation of a stable Taylor cone-jet. This is arguably one of the biggest limitations of electrospraying, which usually offers a narrow window for obtaining a stable cone-jet. The achievement of a stable cone-jet is highly dependent on the crystallisation media (for example solvent properties such as conductivity, viscosity, surface tension) and system parameters such as the applied voltage and flow rate. Usually, high voltages and low flow rates are more likely to produce a stable Taylor-cone jet. Trial and error is often used to unravel the parameters required to reach the narrow window.[41]

1.3.6 Mechanical grinding

Mechanical grinding is a crystallisation technique that uses mechanical energy (e.g. compression, shear and friction) to achieve chemical transformations. It is often used in the co-crystallisation of multi-component complexes where target components are ground together in defined stoichiometric amounts. Mechanochemical grinding is often conducted as a solvent-free method, which is of particular significance in the context of sustainable chemistry,[50] or with small amounts of solvent, known as liquid assisted grinding (LAG). In the case of LAG

the solvent is used as a lubricant to assist the occurrence of phase transitions.[50,51] In this work mechanical grinding is conducted both manually, with a pestle and mortar, and through automation with a ball mill to investigate possible transformations between a target API and co-former in chapters 4 and 5.

1.4 Types of solid state materials

Crystalline solid state materials can exist in a number of different forms; each of these forms are defined by a different repeating array of molecules that can significantly alter the physical properties of a material. If a given crystalline solid can form different arrangements in the solid state, it is defined as polymorphic. A crystalline solid that can incorporate a solvent is known as a solvate or hydrate. The incorporation of another molecule to form a multi-component complex is known as a co-crystal or salt.[52,53] Figure 1-15 illustrates the possible crystalline forms in the solid state that are described above.

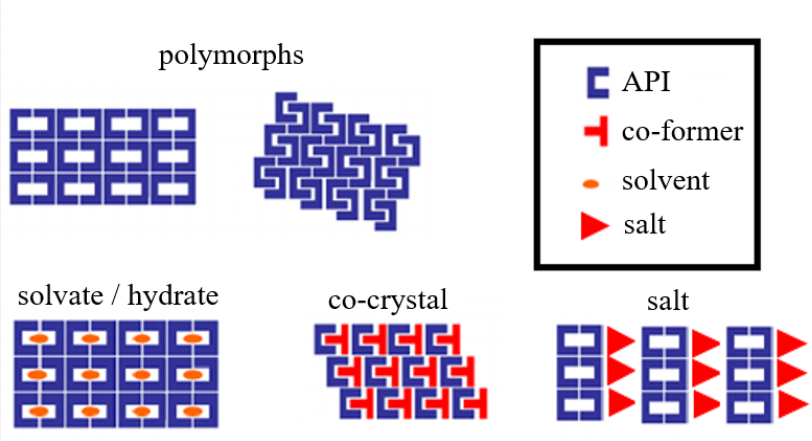

Figure 1-15: An illustration of possible crystalline forms in the solid-state.

1.4.1 Polymorphism

Approximately 90% of small organic molecules are known to be polymorphic.[16,54] This means that the molecular building blocks that form the crystal structure pack together differently.[53] The different packing arrangements can lead to physical property differences, such as solubility,[55] since each polymorphic form has a different free energy. The physical property differences that polymorphic forms often possess can have substantial benefits in the production of APIs. However, an in-depth knowledge of the polymorphic landscape of a solid must be known and control of the desired polymorphic form is essential for drug development. This is because the thermodynamic stability of different polymorphic forms varies; it is thus vital to know the thermodynamics behind polymorphic forms to avoid unexpected transformations. The case of Ritonavir,[56,57] an anti-HIV drug, is a prime example that highlights the importance of gaining a full understanding of the thermodynamic stability of polymorphs and gaining control over polymorphism. Only one polymorphic form (form-I) of Ritonavir was initially discovered, the drug was produced and marketed as Norvir. A new polymorphic form (form-II) was later discovered after two years. The new form had an increased thermodynamic stability and a

reduced solubility in comparison to form-I. The enhanced stability of the more thermodynamically stable form-II caused problems in reproducing the desired, more soluble, form-I. As a consequence Norvir was withdrawn from the market and much time and effort was expended to reformulate and re-design the manufacturing process of this important drug.

1.4.1.1 Thermodynamics of polymorphism

The stability of a polymorphic form is determined by its free energy, G, which is dependent on the thermodynamic functions enthalpy (H), entropy (S) and temperature (T), as shown in equation 1.6.

$$\Delta G = \Delta H - T\Delta S \tag{1.6}$$

Polymorphic forms have different non-covalent interactions and therefore also have different molar heat capacities (C_m). The enthalpy and entropy of a polymorph can be calculated from the integration of the C_m with respect to temperature at a constant pressure, shown in equations 1.7 and 1.8. The differences in enthalpy and entropy can be calculated between two polymorphs, in this case at absolute zero polymorph I is more stable than polymorph II, shown in equations 1.9 and 1.10.[58,59] The Gibbs free energy difference can be calculated between two polymorphs with these equations, however a monotropic relationship is assumed; additional terms are required to calculate the change in enthalpy and entropy for a enantiotropic relationship (in which a solid-solid transformation between the polymorphs is possible, see below).

$$H^{T1} = \int_0^{T1} C_{m.p}\, dT + H^0 \tag{1.7}$$

$$S^{T1} = \int_0^{T1} \frac{C_{m.p}}{T}\, dT + S^0 \tag{1.8}$$

$$\Delta H^{T1}_{II-I} = \int_0^{T1} \Delta C_{m.p}(II - I)\, dT + \Delta H^0_{II-I} \tag{1.9}$$

$$\Delta S^{T1}_{II-I} = \int_0^{T1} \frac{\Delta C_{m.p}(II - I)}{T}\, dT + \Delta S^0_{II-I} \tag{1.10}$$

At a given temperature, the polymorphic form with the lowest free energy is termed the thermodynamically most stable form and other polymorphic forms with higher free energies are termed metastable.[16] Metastable forms can have enhanced physical properties such as solubility[54] and can therefore be desirable solid forms for drug development. Solubility is an important property to enhance since approximately 90% of molecules in the discovery pipeline are poorly water-soluble.[60] However, the formulation of a metastable form is complicated and the requirement for stabilisation of a metastable form adds an additional risk. Polymorphic systems are thermodynamically driven to transform into a more stable form and reduce their free energy, obeying Ostwald's Law of Stages.[61] In a polymorphic system, this Law states that the least stable form will nucleate first. This initial form may be a metastable (unstable)

crystalline form, amorphous solid or oil. The unstable form is thermodynamically driven to transform into a more stable form through a solution mediated phase transformation (SMPT) and Ostwald's Law further states that the system will pass through the successively more stable forms *en route* to reaching the thermodynamic form (figure 1-16).[16,53,61]

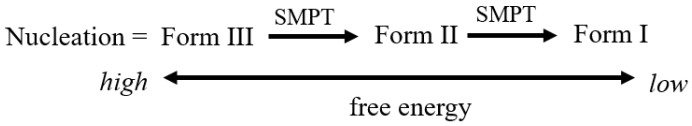

Figure 1-16: A summary of Ostwald's Law of Stages, where form III is the most unstable and form I the most stable polymorphic form.

In order to crystallise the relevant polymorph, the thermodynamic relationship between the forms must be known, to minimise unwanted polymorphic transitions. Polymorphic systems tend to fall into two categories that explain their thermodynamic behaviour: monotropic or enantiotropic.[59] Plotting an energy-temperature diagram indicates which category describes the polymorphic system, illustrated in figure 1-17.

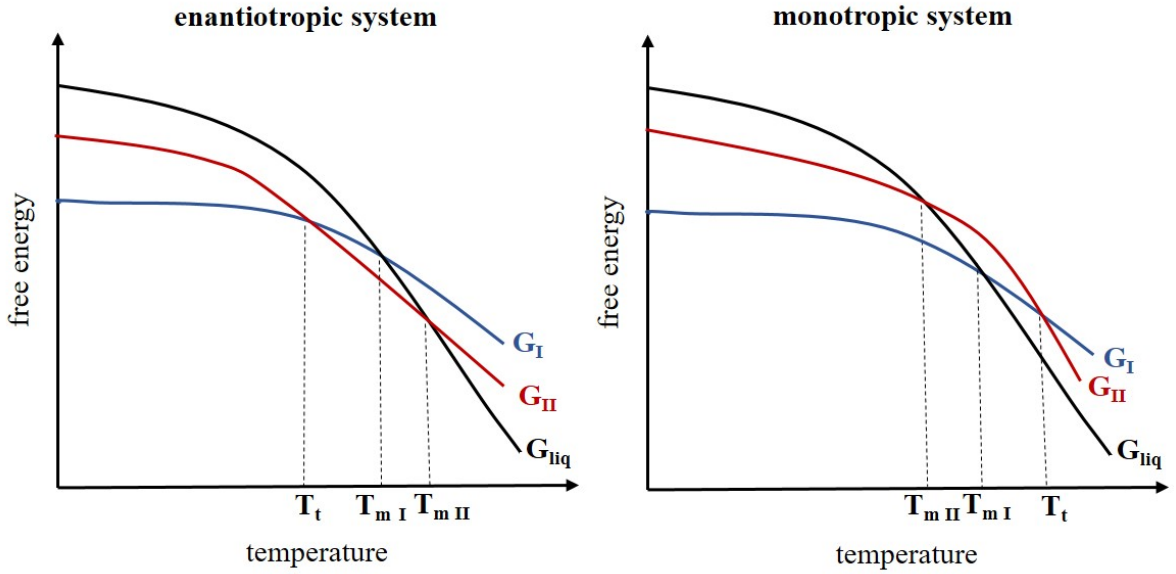

Figure 1-17: An example energy-temperature plot for an enantiotropic (left) and monotropic (right) polymorphic related system. G is the free energy, T is the temperature, I and II refer to the polymorphs, liq refers to the liquid phase, Tm refers to the melting point and Tt refers to the transition point.

The relationship between two polymorphs is described as enantiotropic if the point at which one polymorphic form transforms into another polymorphic forms occurs in the solid state i.e. below the melting point of both polymorphs. In contrast, the relationship between two polymorphs is considered to be monotropic if the point at which one polymorphic form transforms into another is after the melting temperature of the forms; in this case the forms will melt before a polymorphic transition can occur. It is important to determine if a polymorphic system exhibits enantiotropic or monotropic behaviour before the design of a crystallisation method to eliminate unwanted polymorphic transitions.[58,59] In addition to an energy-temperature plot,

the thermodynamic relationship between polymorphic forms can be identified from their solubility curves. In a monotropic system, the solubility curves of the forms do not cross and their relative values are independent of temperature. In an enantiotropic system, the solubility curves of the forms intersect and their relative values are thus dependent on temperature; at the transition temperature the relative stability of the polymorphic forms will switch and reversible transformations can occur, as shown in figure 1-18.[53,62]

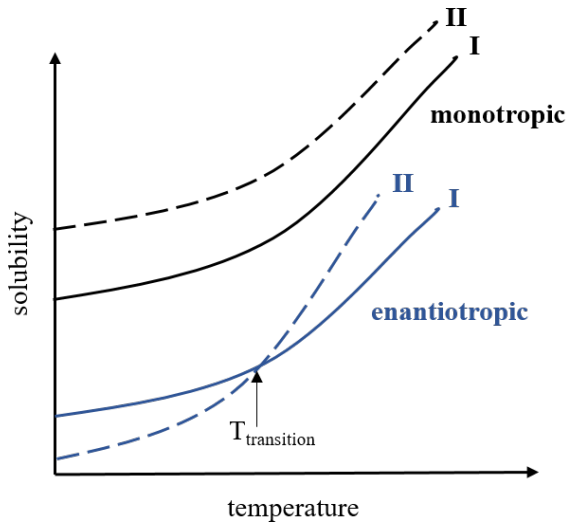

Figure 1-18: The solubility curves of monotropic and enantiotropic polymorphic systems.

In the pharmaceutical industry the ultimate goal is to develop a drug with optimal qualities for the proposed use. The most stable polymorphic form (thermodynamic) is usually chosen as the active ingredient, since it does not convert to a different form over time. However, a compromise between thermodynamic stability versus desired properties such as solubility and compressiblity is often a consideration. A metastable form may be considered if the thermodynamically stable form suffers from poor properties that are improved in the metastable form.[9] The optimal polymorphic form is found by a polymorph screen, to identify all solid forms of the drug.[7] Screening for potential solid form candidates based on the polymorphic landscape of an API determines the amount of potential solid-state variations available for a given substance; other systems such as multi-component, solvates and hydrates offer a larger range of solid forms to explore.

1.4.2 Multi-component systems

Multi-component crystalline complexes offer the potential to manipulate a drug's solid form to fine-tune its properties, such as solubility, dissolution rate, chemical stability, melting point and hygroscopicity.[52] Different types of multi-component systems are used in the pharmaceutical industry, which are dependent on the properties of an API. These multi-component systems can form as salts, co-crystals and solvates.

1.4.2.1 Salt formation

If the API possesses ionisable functional groups, salt formation can be considered. A salt describes a crystalline solid that contains more than one type of ion, with one of the ionic components on the free API. Most APIs contain an acidic or basic group[11] which is required for salt formation. The formation of a salt relies upon proton transfer between the free API and the other component. Equation 1.11 shows an example of proton transfer for a weak base (B) in water. pKa describes acid dissociation and is used to indicate the strength of an acid. The pKa value is the negative base-10 logarithm of the acid dissociation constant (Ka) of a solution (equation 1.12).[63] The pKa values of the acidic and basic groups that belong to both components can be used as a rough guide to estimate the likely success of salt formation, where $\Delta pKa = pKa_{base} - pKa_{acid}$. A value above zero suggests that the components have an increased potential to form an ionic bond and therefore a salt. A value below or equal to zero suggests that proton transfer is unlikely and co-crystallisation may be considered more favourable. Values within the range of zero and three are categorised as a salt-co-crystal continuum; the formation of a salt or neutral complex is difficult to predict within this range. The majority of approved drug molecules are salts[3] as they possess the superior properties discussed above in-comparison to the free API. For example, the active ingredient in the Nurofen Rapid brand is ibuprofen and the amino acid lysine in a salt formulation. Nurofen Rapid has an enhanced water solubility because of the salt formation in comparison to free ibuprofen and therefore an increased bioavailability. The main limitation of salt formation is the requirement of an API to be ionisable and the addition of a synthesis step.[52]

$$B + H_2O \rightleftharpoons BH^+ + OH^- \tag{1.11}$$

$$pKa = -log_{10}K_a \tag{1.12}$$

1.4.2.2 Co-crystallisation

A co-crystal describes a crystalline multi-component complex that contains two or more distinct molecular components that are uncharged. For pharmaceutical co-crystals, one component must be an API, the other components may be another API or a co-former.[52,64] Unlike salts, co-crystals do not need the API to be ionisable since the formation of a co-crystal solely relies on intermolecular interactions, usually hydrogen bonding. Target drug molecules usually contain several functional groups containing hydrogen bond donors and acceptors and are therefore likely to favor co-crystallisation with a compatible second component, such as a co-former. The driving force for co-crystallisation is reliant upon the formation of intermolecular interactions that are stronger between the two distinct molecular components than those in the single component.[25,64]

In some cases, co-crystallisation is more desirable than salt formation especially in the development of APIs with non-ionisable functional groups. Co-crystallisation opens a vast new range of potential API-co-former or API-API combinations and has led to a recent rise in

the number of known pharmaceutical co-crystals that have a higher solubility than the free API.[64–66] The method of co-crystallisation can therefore be used to increase the bio-availability of a drug, a common limitation in many pharmaceutical compounds. The enhancement of an API's physical properties by the method of co-crystallisation is desirable since it is achieved without compromising the structural integrity of the free API.[52,64]

1.4.2.3 Solvates and hydrates

A solvate describes a crystalline multi-component complex that incorporates one or more solvent molecules into the crystal structure; a free API, salt or co-crystal can incorporate these solvent molecules and become solvated. A hydrate is the most common form of solvate and describes the incorporation of water molecules into the crystal structure. Solvents may be incorporated into a crystal structure during crystallisation due to their small size and natural tendency to form hydrogen bonds. The incorporation of a solvent changes the crystal structure which leads to a new solid form with different physicochemical properties in comparison to the free API, including melting point, solubility, processability, stability and dissolution.[62] The main limitation of solvate formation is the lack of stability of the solvent in the crystal structure. Solvent loss can occur over time which can cause degradation or a change of solid form. In some cases, solvate formation is unavoidable and if not the intended outcome, solvates can be desolvated through drying. However, desolvation may have a destructive effect on the solid form, including loss of crystallinity or destruction of the unit cell.[67]

Multi-component systems, including salts, co-crystals, solvates and hydrates all possess the ability to be polymorphic, which can lead to further physicochemical changes in the system.[52,62] Similar to free APIs, all polymorphic forms of these systems must be investigated, before a drug can be added to the commercial market. All the different types of solid-state materials discussed have enabled a vast increase in the amount of emerging pharmaceutical compounds. The principles of crystal engineering have been in many case key to achieving this, coupled with a quality by design (QbD) approach, with clear impacts observed on the production and marketing of APIs.[68]

1.5 Crystal Engineering

> Crystal engineering: *the understanding of intermolecular interactions in the context of crystal packing and in the utilisation of such understanding in the design of new solids with desired physical and chemical properties*- Desiraju[69]

Crystal engineering is a term that describes the controlled design of organic solids. In contrast to synthetic chemistry which exploits the making and breaking of covalent bonds, crystal engineering considers the non-covalent (intermolecular) interactions that hold molecules together in the solid state. This controls crystal packing and describes the arrangement of molecular components that are held in position by intermolecular interactions. The intermolecular interactions within a crystal structure are responsible for a solid-state system's free energy and physical properties. The manipulation of these interactions can lead to the possibility

of controlling the physical properties of a solid form. This is the fundamental basis of crystal engineering, which can deliver an optimised material from the prediction of possible new bonding motifs, from the knowledge of intermolecular interactions and the use of computational methods.[52,70]

1.5.1 Supramolecular synthons

The process of crystal engineering looks at the self assembly of molecular synthons (intermolecular interactions between molecular fragments) to predict possible crystalline systems that may lead to desired properties. Synthons are described as building blocks in a crystal lattice that regularly repeat and define the crystal structure.[70,71] Supramolecular synthons can be described as either homosynthons, which are composed of two identical functional groups or heterosynthons, which are composed of two different functional groups. Figure 1-19 displays examples of homosynthons (a and b) and heterosynthons (c and d) between carboxylic acid, amide, amine and alcohol dimers.[72]

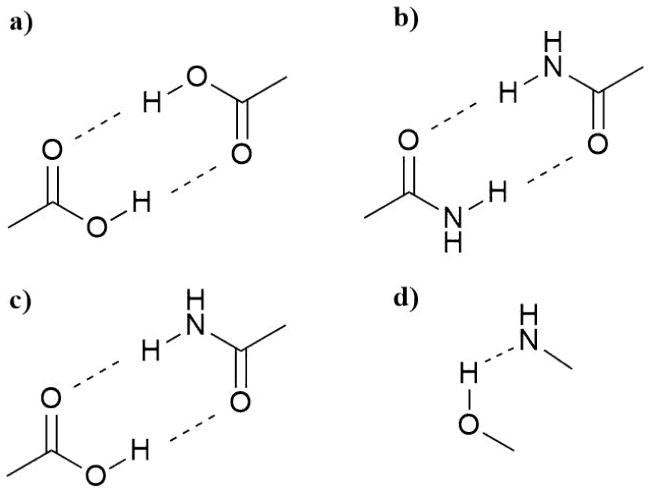

Figure 1-19: Supramolecular synthons. a) homosynthon of a carboxylic acid dimer, b) homosynthon of an amide dimer, c) heterosynthon of an amide-carboxylic acid dimer and d) heterosynthon of an amine-alcohol dimer.

Etter et al developed a method called graph set notation that can be used to describe the characteristics of complex hydrogen bonded networks present in such synthons and hence in crystal packing arrangements. The graph set notation approach simplifies these networks with four simple designators: chains (C), rings (R), intramolecular hydrogen bonded patterns (S), and other finite patterns (D). A general graph set descriptor can be seen from equation 1.13, where G is one of the designators, a is the number of hydrogen bond acceptors, d is the number of hydrogen bond donors, and n is the number of atoms in the motif.[73,74] For example the homosynthon in figure 1-19a has graph set notation R_2^2 (8).

$$G_d^a(n) \tag{1.13}$$

Hydrogen bonds are arguably the most important interactions within such synthons for crystal

engineering of solid-state pharmaceuticals. Nonetheless, weaker forces such as $\pi - \pi$ and van der Waals interactions are also of importance in crystal engineering.

1.5.2 Intermolecular interactions

1.5.2.1 Hydrogen bonding

A hydrogen bond (X-H···Y) is defined as an electrostatic force of attraction involving a hydrogen atom (H) that is covalently bonded to a molecule or fragment (X-H); X must be an electronegative atom, such as O, N or F and can belong to the same or a different molecule. The electronegativity of X induces a partial positive charge in the H atom ($H^{\delta+}$). Once the H atom has a partial positive charge it can form an attraction to an atom (Y) that has a partial negative charge, or an electron lone pair.[75] The X atom is termed the hydrogen bond donor since it is bonded to the H atom, while the Y atom is termed the hydrogen bond acceptor. Hydrogen bonds can be classified as strong, moderate or weak interactions. The strength of a hydrogen bond can conveniently be classified by the bond lengths and angles of X-H···Y; table 1.1 summarises the properties of each bond strength class. The position of the hydrogen atom within the bond can affect the strength; the H atom in a strong bond often has equal attraction to X and Y, whilst the H atom in moderate and weak bonds is situated closer to the X atom. The formation of strong hydrogen bonds occurs when the Y atom is electron rich and the X atom is electron deficient,[76] as a result the interaction strength of X-H and H···Y becomes almost equal (with the hydrogen atom tending to become centred in the hydrogen bond) and the overall distance between X···Y is shortened.[77]

Table 1.1: The properties of strong, moderate and weak hydrogen bonds.

Property	**Strong**	**Moderate**	**Weak**
interaction affect (X-H···Y)	primarily covalent	primarily electrostatic	electrostatic
bond length	X-H $\approx$ H···Y	X-H < H···Y	X-H << H···Y
bond angles (^{o})	175-180	130-180	90-150
X···Y (Å)	$\approx 2.2 - 2.5$	$\approx 2.5 - 3.2$	$\approx 3.2 - 4.0$
H···Y (Å)	$\approx 1.2 - 1.5$	$\approx 1.5 - 2.2$	$\approx 2.2 - 3.2$
bond energy ($kJmol^{-1}$)	62-167	16-62	4-16

* This table was modified from the book: An Introduction to Hydrogen Bonding[76]

1.5.2.2 $\pi - \pi$ interactions

$\pi - \pi$, or $\pi - \pi$ stacking, interactions are an attractive force prominently found in aromatic systems and can be a dominant supramolecular interaction for crystal engineering.[78] $\pi - \pi$ interactions are weaker than hydrogen bonds but can be a powerful force through the cumula-

tive effect of multiple interactions: for example the $\pi - \pi$ interactions in aromatic amino acids play a significant role in the binding of RNA.[79] Sanders and Hunter proposed a model that explains the interaction between two π systems; each system contains two partial negatively charged clouds of electron density with a partial positively charged σ-framework in between, displayed in figure 1-20. Sanders and Hunter stated that two π systems within proximity will form one of four geometries; the preferred geometries are edge-to-face (T-shaped) and parallel displaced, over a stacked geometry or a reversal of polarisation. A reversal of polarisation will only occur if the aromatic ring is attached to a strong electron withdrawing group, such as in hexafluorobenzene. In this case the system contains two partial positively charged clouds of electrostatic potential with a partial negatively charged cloud of electrostatic potential in between. An electron-deficient aromatic ring may form an electrostatic attraction to an aromatic ring that has undergone reversal of polarisation, in which case the system forms a stacked geometry.[78,80]

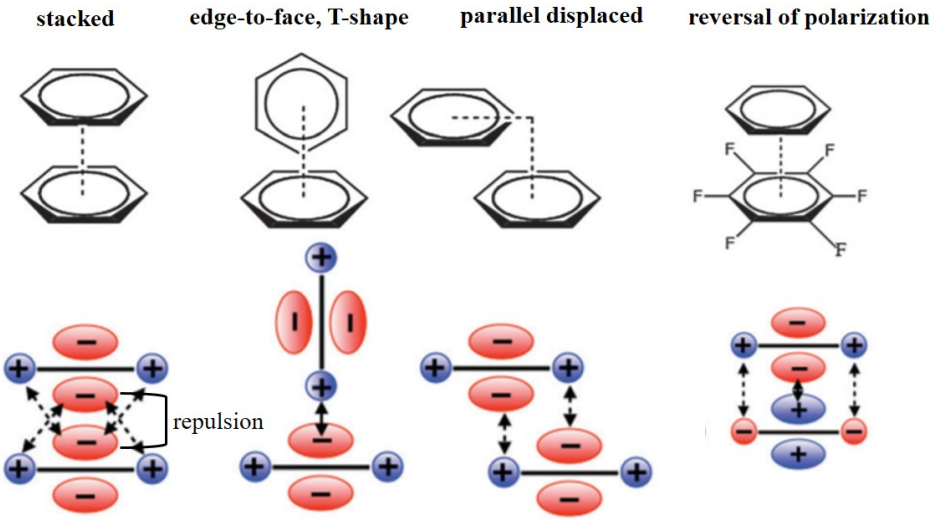

Figure 1-20: The different types of geometries and electrostatic interactions between two aromatic systems. The arrows in the image point to forces of attraction.
*This image was modified from Matthews et al[80]

1.5.2.3 Weak interactions

Weak electrostatic forces are commonly termed van der Waals interactions and can be categorized into three groups: Keesom forces, Debye forces, and London (dispersion) forces, summarised in figure 1-21. Keesom forces describes a system with two polarised molecules that interact due to difference in their charge distribution. Debye forces describes a system with a molecule that holds a permanent dipole and can induce charge redistribution to neighboring molecules that do not have dipole moments. London forces arise between molecules that do not have permanent dipoles.[81]

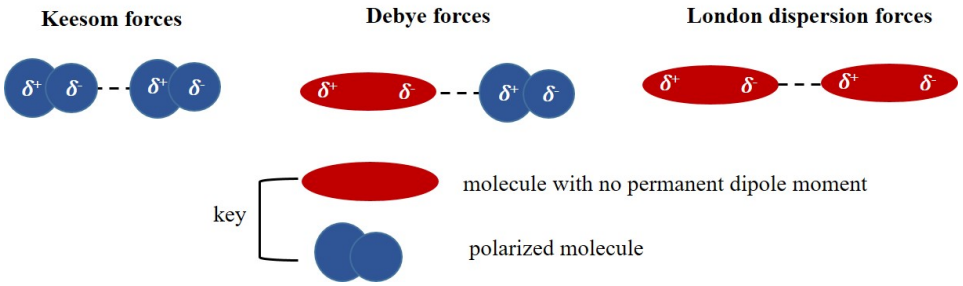

Figure 1-21: The different types of van der Waals interactions: Keesom forces, Debye forces, and London (dispersion) forces.
*This image was modified from Hadjittofis et al[81]

Halogen atoms are generally considered to be sites of higher electron density due to their electronegativity. The electron density in halogen atoms is anisotropically distributed when covalently bound to another atom.[82] Figure 1-22 shows the electron distribution around a halogen (Hal) when covalently bound to an atom (X) with a region of higher electron density (and a negative electrostatic potential) and a region of lower electron density (a σ-hole) with a positive electrostatic potential. A σ-hole is a positive charge (δ^+) that can form interactions with lone pairs on adjacent Halogen atoms and is typically opposite to the X atom along a X-Hal bond.

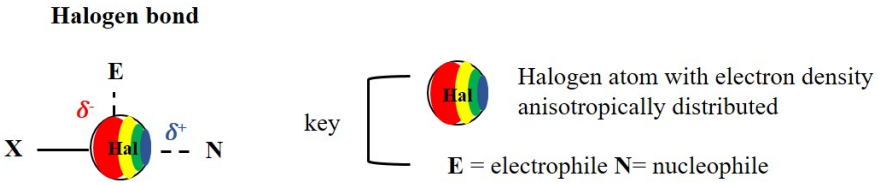

Figure 1-22: The electron distribution around a halogen when covalently bound to another atom (X)

In addition to utilising crystal engineering to gain a higher level of control in a crystallisation process, the type of crystallisation process used is also key for gaining control.

1.6 Industrial crystallisation. Batch versus Continuous

Traditionally, in the majority of industries including the pharmaceutical, batch processes are used for production and manufacturing. However, recently there has been a significant amount of interest in industry and academia towards moving from a batch into a continuous crystallisation platform. Continuous crystallisation provides significant advantages and disadvantages compared to batch processes. By design (and because of their modes of operation), continuous platforms are usually smaller and have lower operating expenses. These advantages can lead to a significant reduction in production cost (approximately 20%[20] when compared to batch platforms) and a decrease in the carbon footprint. The design of continuous crystallisers also eases the scale-up from laboratory to industry. Continuous platforms tend to have a higher level of control and can therefore offer enhanced reproducibility of API products and their physical properties.[22] Table 1.2 summarises the advantages and disadvantages of continuous crystallisation compared to batch crystallisation.[20,22,83]

Table 1.2: Batch versus continuous crystallisation, advantages and disadvantages.

Advantages	**Disadvantages**
Reduction in equipment size and cost and improved mass heat transfer	Higher initial start-up cost for plants with existing batch equipment
More sustainable platform from solvent and energy reduction	Batch processes are well understood and trusted, while continuous platforms are currently difficulty to design and develop
Reduction in batch to batch variation	Fouling and encrustation issues exist for many continuous methods
Higher continuous yields which are feasible with a recycling strategy	Generally a batch process produces a higher product yield in terms of a once through system
Increased level of control over particle attributes such as crystal size distribution and polymorphic form	The procedure and equipment used is dependent on each individual system, no 'one size fits all' platform exists
Increased level of control over physical properties	

The main batch reactor currently used for crystallisation in the pharmaceutical and fine chemical industry is a stirred tank reactor (STR), which consists of a jacketed vessel that can hold large volumes, in which a motor facilitates mixing with an impeller. Although STRs are well established and have many benefits, challenges currently exist in obtaining homogeneous conditions at large scales. In an STR, as the scale increases, the amount of of issues that can lead to significant batch to batch variability also increase, such as mass and heat transfer. Overall, this decreases the level of control and increases reaction times.[84,85] The large size of a STR requires significant amounts of plant space as well as substantial time for cleaning the vessel between batches. This has a direct impact on the amount of downtime and solvent that is required to maintain the process.[22]

1.7 The importance of controlling the properties of a solid form

Oral pharmaceuticals are the most common route of administration, such as tablets or capsules.[6] The properties of these drugs are highly influenced by the chosen solid form of the active ingredient. The physical nature of a solid form can determine many properties that are important for solid state pharmaceuticals, especially in the stages of preclinical drug development and the manufacturing process.[86] Solubility, morphology and stability (physical and thermal) are the properties investigated in the new solid forms discovered in this work. These properties are of importance and can have a large influence on a drug's performance and processability.

1.7.1 Solubility

Approximately 90% of molecules in the discovery pipeline have poor water-solubility,[60] with 40% of these insoluble in water.[6] Drugs that are poorly water soluble absorb slowly into the body, this leads to an undesired bioavailability in aqueous gastrointestinal fluids that is inadequate and in some cases can lead to gastrointestinal toxicity (including nausea and abdominal pain).[6] The Biopharmaceutics Classification System (BCS) classifies drugs into four groups based on their solubility and permeability: a class I drug has a high permeability and a high solubility, a class II drug has a high permeability and low solubility, a class III drug has a low permeability and high solubility and a class IV drug has a low permeability and low solubility.[87] Overcoming poor bioavailability of an API is one of the largest challenges for formulation scientists in drug development. Solubility, permeation and dissolution are properties that affect the bioavailability of a drug. In this work, the solubility of new solid forms is investigated and compared to the free, thermodynamically stable, API.

1.7.2 Morphology and particle size

Morphology and particle size are properties that can affect a number of important physical properties of a drug in addition to manufacturing processability and quality attributes. The morphology of a solid form can significantly influence the filterability, dissolution and compressibility of a drug. If a drug has poor filterability during solid -liquid separations in downstream processes, cake formation can occur upon filtration which can cause blockages. If the solid form is prone to agglomeration, the efficiency of the washing process can decrease; the mother liquor is unable to reach and wash inside the agglomerate. An irregular shape can affect how a material packs and therefore ease of compressibility.[29,88] The particle size and shape can have influences on the manufacturability of a solid form. A small particle size with a narrow distribution range is desired as it affords a material with a larger surface area to volume ratio and increases the dissolution rate and drying rate of a material. In addition, it increases the efficiency of flowability and packing properties which affect downstream process such as mixing, filtration and compression into tablets.[4] In this work, the morphology of new solid forms is investigated.

1.7.3 Stability

Knowledge of stability of a solid form is important for the manufacture and processing of a drug and for the prediction of shelf life and storage conditions.[89] The stability of a solid form is generally evaluated under conditions that cover the requirements for storage, shipment and subsequent use. Stability studies usually test the thermal stability, thermodynamic stability and sensitivity to moisture or solvent loss (in the case of a solvated solid form). Hygroscopicity describes the absorption or adsorption of water, the water is taken from the atmospheric air present in the surrounding environment.[90] The amount of water an API adsorbs or desorbs is an important factor: in some cases the water molecules may bond with the solid form and transform into a hydrate, while in contrast, a hydrate formulation may desolvate; a physical change in the solid form may occur such as an increase in volume, boiling point and viscosity.[29,88,90] This work investigates the thermal and physical stability of new solid forms. The thermal behaviour of a solid form is investigated to identify exothermic and endothermic transitions. A low thermal stability (e.g. 60^{o}C) is undesired, due to an enhanced risk of melting during downstream processes, shipping or storage. The thermodynamic stability of a solid form is investigated to identify any polymorphic transitions of metastable forms and / or the stability of new multi-component complexes of target APIs over a period of time.

1.8 Disordered pharmaceutical materials

The majority of pharmaceutical drugs are formulated in the solid state as crystalline or amorphous solid forms; these are susceptible to the presence of disorder, which can be particularly evident in crystalline solids. The nature of disorder that exists in organic solids can be placed into two categories: long and short range translational order, shown in figure 1-23. Crystalline compounds possess long range translational order and therefore adopt a particular external shape. Despite possessing this long range order, crystalline compounds can suffer from varying degrees of disorder; this includes apparently ordered crystals which have a degree of intrinsic disorder from the thermal motion of atoms and molecules.[14] Amorphous compounds do not have long range translational order and have no particular external shape. An amorphous material can be either a solid or liquid; a solid amorphous material is commonly called glassy. An amorphous solid lacks the three symmetry operators that give rise to long range order (conformational, orientational and translational or positional order) but contains local short range order.[91] The degree of molecular mobility over time in a solid form changes with the range of order present; amorphous solids are known to have a large degree of molecular mobility whereas crystalline solids have a very low degree of molecular mobility.[14]

1.8.0.1 The implications of disordered pharmaceutical materials in drug development

Disordered materials can have similar implications for product performance within the drug development process as polymorphism, and as such the presence of disorder is a product quality that must be strictly controlled. Disordered materials generally vary in their degree of disorder and can therefore display different batch to batch bulk sample properties.[92] The case

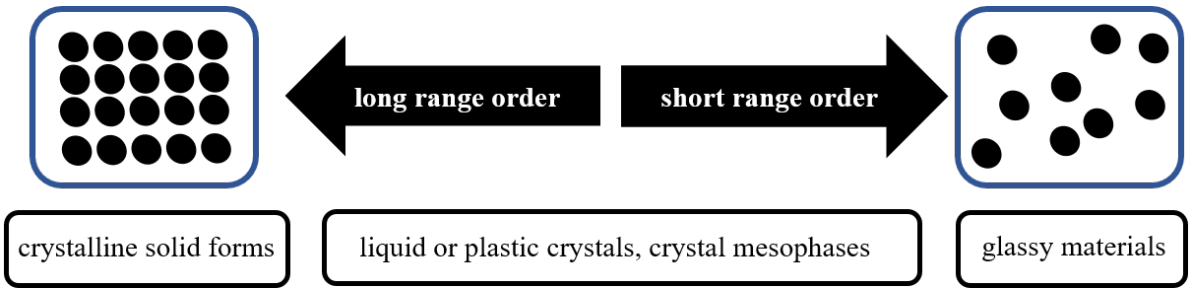

Figure 1-23: Examples of materials that possess long to short range order.

of Eniluracil[93], a potential anticancer agent under development by GlaxoSmithKline in the 1990s, is a classic example that highlighted the implications disordered materials have in drug development. In this case, problems in the development of a successful production process was arguably due to a lack of understanding of the structural disorder in the material. At the time of development, differences between samples were interpreted as polymorphism, however later studies from systematic single crystal X-ray diffraction (SCXRD) data revealed that the degree of disorder was uncontrollable and varied under different crystallisation conditions. It is clear that the identification of disorder is important, however in order to relate structures to their bulk properties, disordered materials must be fully characterised and understood. Unfortunately, the link between disordered organic materials and their physical properties is limited in the literature.

This work focuses on disorder, or instabilities, in crystalline solids, an aspect that can arise from the level of crystallographic disorder within a solid form. Varying levels of crystallographic disorder can change the thermodynamic (free energy) and kinetic (molecular mobility) properties of a solid form and result in physical and chemical property instabilities.[14,91] Such instabilities can lead to a decrease in bioavailability and dissolution rates and to chemical degradation.[91]

1.9 Different types of disorder in crystalline materials

In this section different types of disorder that are relevant to this work are categorised and discussed, including structural disorder (static and dynamic) and crystalline defects.

1.9.1 Structural disorder

Structural disorder describes a system where an atom or functional group appears to occupy more than one position in a unit cell based on an average representation of a model determined from crystallographic data.[94] The occurrence of structural disorder can arise from mobility (dynamic disorder) or from the freedom to access multiple configurations or conformations (static disorder). Rotational disorder and whole molecule disorder are examples of structural disorder. Rotational disorder is the term used when a group with a high level of rotational freedom, for example a tert-butyl group, exists in different rotated conformations. In whole molecule disorder, the molecule is typically disordered around a symmetry element; it is often found in co-crystallised solvent systems. Figure 1-24 contains an illustrated example of whole

molecule disorder. The disordered molecule allows the average symmetry of the crystal to be kept; even though the single molecule does not contain the same symmetry itself. As a note of caution, whole molecule disorder can often be a misrepresentation of other effects such as the selection of an incorrect space group or twinning.[94]

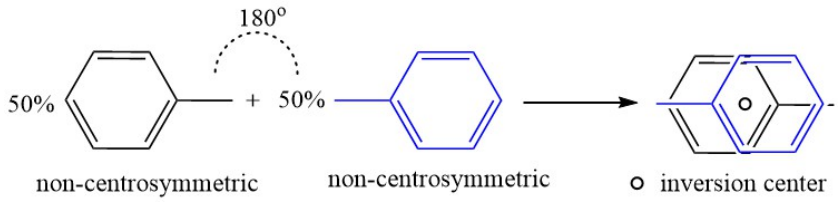

Figure 1-24: An illustrated example of whole molecule disorder.

1.9.1.1 Static and dynamic disorder

Structural disorder can be divided into two categories termed static and dynamic. Static disorder describes a system where the deviation from a uniform arrangement exists between unit cells. The disordered site is variant amongst each unit cell in the crystal lattice.[95] Static disorder is created during the crystallisation process. During crystal growth, the growth units that join the system find a position with the lowest energy. If there are multiple sites with comparable low energy for a growth unit to attach, a combination of these will exist throughout the crystal, leading to functional groups with partial chemical occupancy between unit cells. An absence of intermolecular interactions to hold the functional group in place is responsible for the random freedom in orientation.[96]

Dynamic disorder describes a system with atoms in a molecule that are not fixed but gain potential mobility through their vibrations within the lattice. The atoms are able to move and change their positions in the lattice through enhanced harmonic oscillations that increase with temperature and are effectively able apparently to access multiple sites in a single unit cell.[97] In this case, the disorder deviation is the same in every unit cell.[96]

The final diffraction pattern of a disordered API differs due to the freedom of movement around multiple positions. Since this movement cannot be resolved, the refined structure represents an average of all the possible positions (figure 1-25 a). In the case of static disorder, further refinement that allows partial occupancy of atomic sites is required and offers an improved crystal structure model. Partial occupancy allows parts of a molecule to have several orientations (corresponding to partial occupancy of multiple atomic sites) that may have different interactions and hence physical parameters. The sum of each partial occupancy position will equal one and contribute to description of a single atom in the disordered region (figure 1-25 b). Static disorder is often independent of changes in the conditions under which the crystal is studied, the disordered parts will remain in position. For example, a decrease in temperature would not necessarily affect the disordered regions; in some cases only the displacement parameters may be affected. However, static disorder can be dependent on external conditions (e.g. temperature); temperature-dependent static disorder is sometimes loosely termed dynamic disorder, but should be distinguished from true dynamic disorder as defined above.

Temperature dependent static disorder is sensitive to ambient condition changes, an decrease in temperature will affect the level of site disorder refined during structure determination.

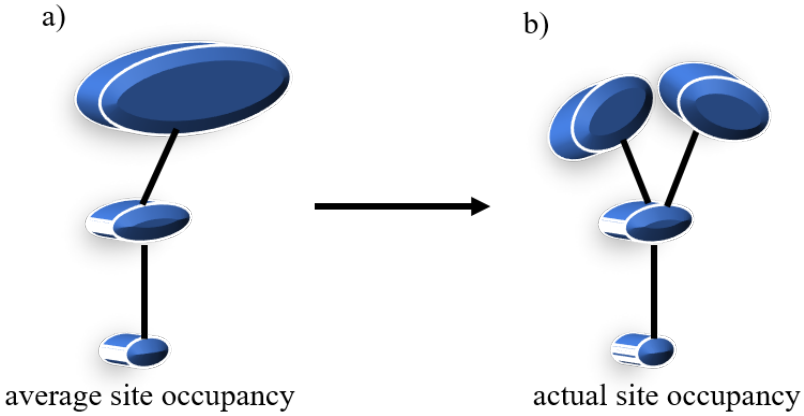

Figure 1-25: A disordered ethyl group. a) model with a single site representing the average of all possible positions. b) model allowing for partial site occupancy of each position.

1.9.2 Crystal defects

Crystal defects can arise both during crystallisation and from downstream processing steps. It is widely recognised that crystal defects exist in pharmaceutical materials; however, the nature behind defects in a crystal is not yet fully understood, particularly in molecular materials.[15] Crystalline defects generally fall into three categories based on their geometry: point defects, line or linear (dislocations) and planar defects (stacking disorder).

1.9.2.1 Point defects

A point defected lattice can describe several imperfections of a crystal lattice, illustrated in figure 1-26: 1) a vacancy, in this case either an atom or whole molecule is missing; 2) an interstitial, where a molecule may occupy a non-lattice site; and 3) an impurity, which replaces an atom or whole molecule.[15]

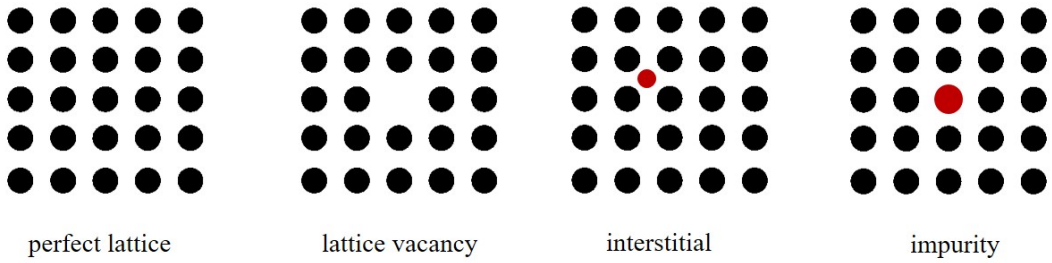

Figure 1-26: An illustration of a variety of point defects in a crystal lattice including a perfect lattice, a lattice vacancy, an interstitial and a lattice impurity.

1.9.2.2 Line defects

Line defects, also known as dislocations, are caused by the displacement of atoms from a lattice position at equilibrium. Line defects are usually generated by the application of shear

stress, this creates motion and allows the lattice planes to slip.[15] Figure 1-27a displays an edge dislocation, where an extra half-plane of atoms is present in the lattice above the dislocation core (red dashed line). In this case, it is only the atoms towards the edge of the core that become displaced, any atoms away from the dislocation core remain ordered. The Burgers vector 'b' indicates the direction and magnitude of the shear distortion and always lies perpendicular to the dislocation core. Figure 1-27b displays a screw dislocation, in this case the Burgers vector lies parallel to the dislocation core. The movements of a screw dislocation are not constrained by a single slip plane.[15]

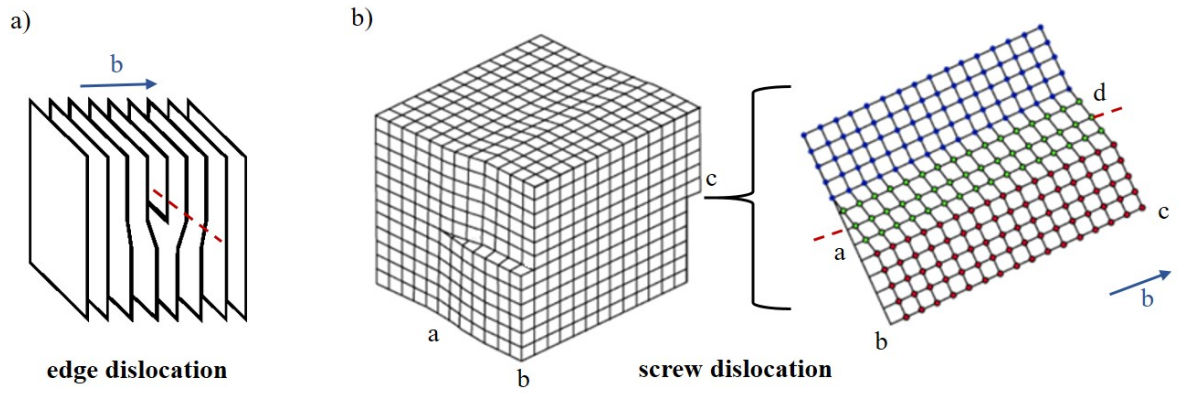

Figure 1-27: An illustration of an edge dislocation (a) and a screw dislocation (b). The blue arrow represents the Burgers vector which runs either perpendicular (edge) or parallel (screw) to the dislocation core (red dashed line).

*This image was taken and modified from Jones et al and Nondestructive Testing resource.[15,98]

1.9.2.3 Planar defect

Stacking disorder describes a crystal system that consists of defined layers in its structure. A stacking fault within these layers causes the layers to stack in a disordered manner. A stacking fault commonly occurs in layered materials that have strong chemical bonding within their layers and weak interactions between their layers.[99] However, stacking disorder can exist in chemical systems where the bonding is very similar within and between their layers, for example in ice.[100] Stacking disorder is known to influence the physical properties of materials. For example, stacking disorder in ice has been reported to affect the material's morphology.[101] Figure 1-28 shows an example of stacking disorder in ice;[100] the image displays sequences of the hexagonal structure of ice disordered with cubic sequences.[101]

Aspirin is an example of a pharmaceutical compound that exhibits stacking disorder. In this case, two known polymorphic arrangements of aspirin, form I and form II, have very closely related structures. The two polymorphs have identical hydrogen-bonded arrangements that form layers; the arrangement of these layers differs between the two forms. As a result, the two polymorphic forms are able to crystallise as inter-growth structures that contain domains of both form I and form II, illustrated in figure 1-29. The distribution ratio of domains is reported to vary between samples.[102]

Although it is out of scope of this project, it is important to note a second example of a planar

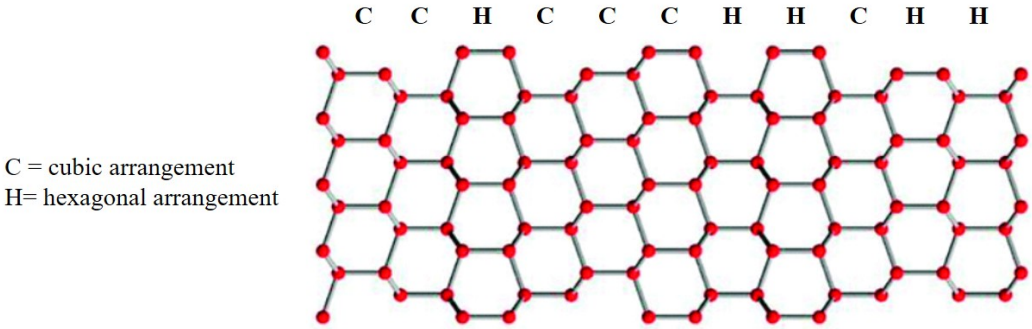

Figure 1-28: An illustration of stacking disorder in ice. The connection of oxygen atoms by hydrogen bonds illustrates either the cubic (C) or hexagonal (H) stacking of layers.
*This image was modified from Bond et al.[102]

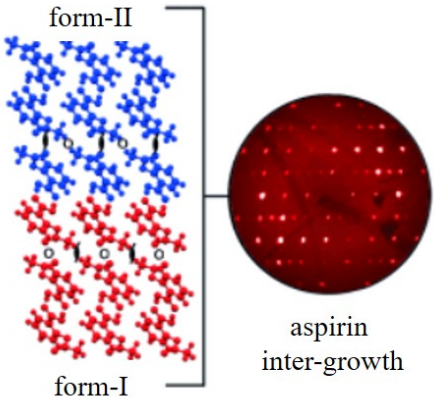

Figure 1-29: An illustration of stacking disorder in aspirin where two inter-growth arrangements within a crystal are illustrated. The resulting diffuse scattering in the diffraction patterns is also shown.
*This image was modified from Malkin et al.[100]

defect - a grain boundary. This type of defect is similar to a stacking fault but can occur in solid crystallites instead of single crystals as discussed for stacking disorder. A grain boundary describes the border at which one crystal domain stops and another starts. The orientation of a crystal domain can differ with respect to a neighboring one.[15]

1.9.3 Current bulk analysis techniques used to characterise disordered organic materials

The majority of tools used to characterise a disordered material look at the surface or particulate level of a material and are limited in the characterisation of disorder at the molecular level. These include: isothermal micro-calorimetry,[103,104] to study the adsorption behaviour of partially amorphous materials; dynamic vapour sorption,[104,105] to characterise the crystallinity of a bulk material; atomic force microscopy,[106–108] to visualise signs of disorder on a surface of a crystalline material; and transmission electron microscopy,[108] to characterise defects within the bulk of crystals. Such methods are limited to the identification of small degrees of amorphous content in a crystalline material or the observation of variations on the surface of a crystalline material. In-addition to the characterisation of disorder at the surface

and particulate level, molecular level disorder is of importance. Its presence can influence the overall Gibbs free energy of a material and create an environment with instabilities; this can cause weaker molecular packing and an increase in molecular motion.[91] Molecular disorder at the bulk level can be characterised by: powder X-ray diffraction (PXRD),[109,110] to estimate lattice strain through X-ray line broadening and characterise the crystallinity of a bulk material; solid-state nuclear magnetic resonance spectroscopy (SS-NMR spectroscopy),[93,111,112] to provide information on the nature of disorder (e.g. static or dynamic) and estimate intramolecular motions of functional groups; and Raman spectroscopy,[113] to analyse internal and external molecular motions between molecules and their neighbors. Disorder can cause an increase in molecular flexibility which, in this case, can reduce the gap between internal and external vibrational modes.

Alternatively, single crystal X-ray diffraction (SCXRD) is a crystallographic method that is routinely used to gain detailed information with respect to the internal lattice of a crystalline material and to distinguish the nature of disorder (e.g. static or dynamic). However, SCXRD can only produce long range structural data from selected single crystals and is not a bulk analysis technique.[114] The ability of SCXRD to distinguish subtle changes of molecular level disorder remains a challenge since standard structure refinement using the technique is limited to an average value from one single crystal with no clear picture of molecular disorder across a bulk material. It is clear that there is a large knowledge gap in the understanding of molecular disorder in single crystals and their influence on the bulk. This work studies a combination of characterisation methods including SCXRD (to gain long range structural data in individual crystals) and bulk analysis techniques to help build a methodology that can provide a comprehensive picture of molecular disorder in a material and expand the perspective we have of molecular disorder; including the identification of parameters that influence and define disorder in both single crystal and bulk material.

1.10 Research scope

The research presented in this thesis falls into the Healthcare theme of the Centre for Sustainable and Circular Technologies (CSCT) and focuses on extracting the maximum value from pharmaceutical drugs by optimising the manufacturing process to improve product attributes and efficacy and in turn increasing profit, energy efficiency and the development of more environmentally friendly approaches. The alteration of solid forms of the same parent molecule, is investigated in a number of systems through the modification of a range of parameters. Figure 1-30 outlines a workflow that is used in this work to influence and control the properties of a solid form through the alteration of various input properties and process parameters during the crystallisation process. The relationship between these crystallisation parameters and the resultant transformation of the solid form (e.g. crystal nucleation, growth and morphology) and attributes (i.e. disorder, solubility and stability) is investigated. Gaining an understanding of the crystallisation process is of importance since it directly affects the performance of a solid form drug (e.g. solubility, dissolution rate, stability and melting point) and processability (e.g. morphology, filterability and drying efficiency).

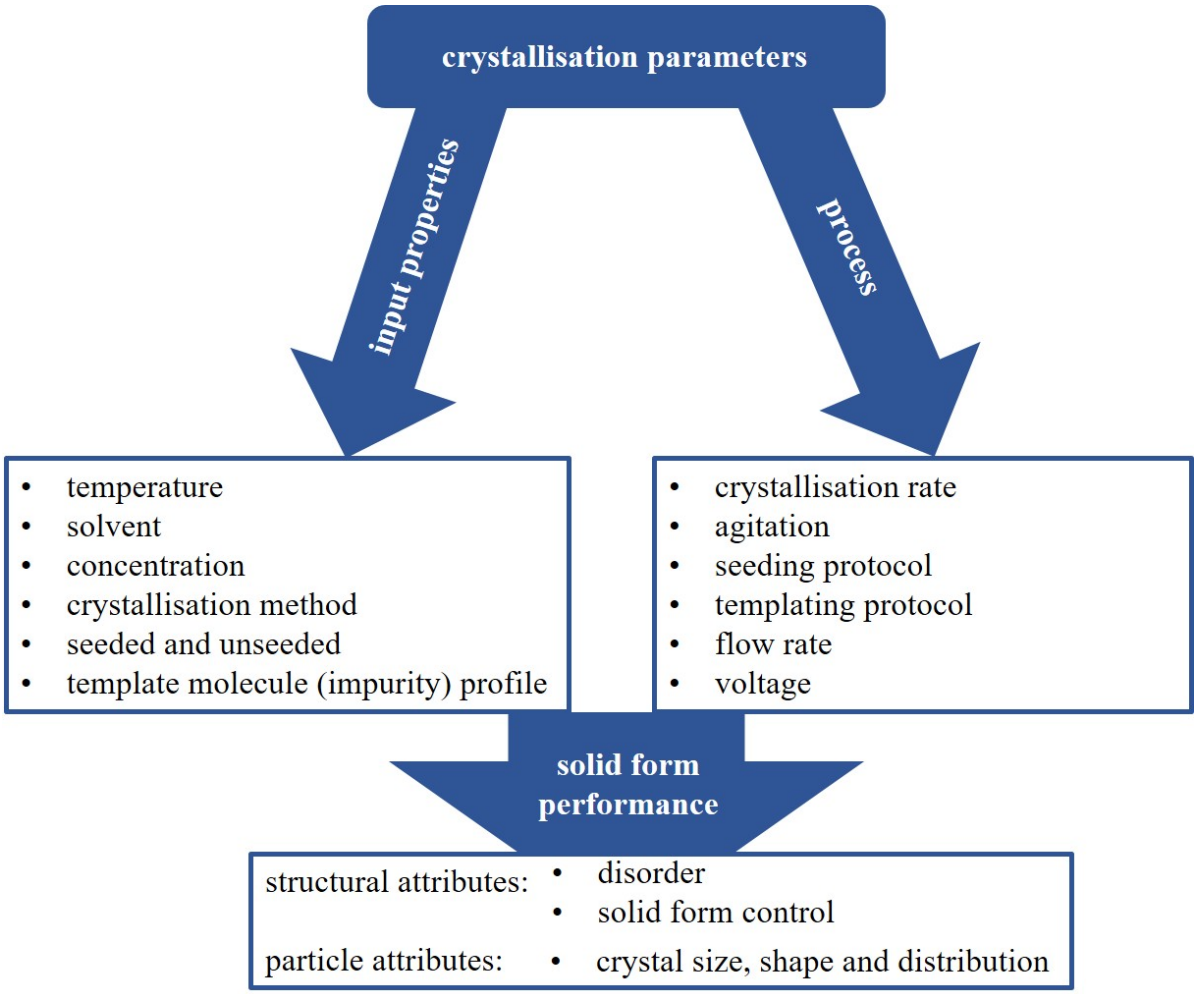

Figure 1-30: The crystallisation parameters investigated in this thesis and their influence on solid form performance.

Chapter 2

Theory of analytical methods

2.1 X-ray crystallography

X-ray crystallography is currently the most favoured scientific method used for the analysis of crystal structures. It can determine the arrangement of atoms of a crystalline solid-state material in three dimensional space. When a crystal is exposed to an X-ray beam, the atoms and their regular arrangement cause the X-rays to diffract into specific directions, unique to the material. The angles and intensities of the diffracted beam are related to the symmetry of the crystal and to the electron density of its contents through Fourier transformation. The average position and thermal motion of each atom in a material can be determined from the electron density determined by structure solution methods in crystallography, in addition to chemical bonding behaviour and disorder.[115,116] Two X-ray crystallography techniques are used for analysis within this thesis: SCXRD and PXRD.

In a crystalline solid, constituents such as atoms, molecules, or ions are arranged in a highly regular repeating three-dimensional pattern, that extends in all directions. Each structural unit in the repeating pattern can be represented by a single point, the lattice point, and the regular array of equivalent points forms the crystal lattice. The full three-dimensional crystal is produced when neighbouring lattice points are linked in three-dimensional space, creating a volume which is repeated by translation; this volume is defined as the unit cell.[115,117]

2.1.1 The unit cell

The unit cell is the building block of a crystal; it contains the smallest repeating unit and highest symmetry within a crystal structure. The unit cell is a parallelepiped, which is constructed by joining adjacent lattice points together. There are many different possible ways to link the lattice points, which would afford different lattice types for the unit cell; the unit cell that offers the highest internal symmetry is chosen. Unit cell parameters, consisting of three lengths (a,b,c) and three angles (α, β, γ), describe the unit cell,[115,116,118] displayed in figure 2-1.

Four different crystal lattice types exist. The simplest type is a primitive (P) lattice, which

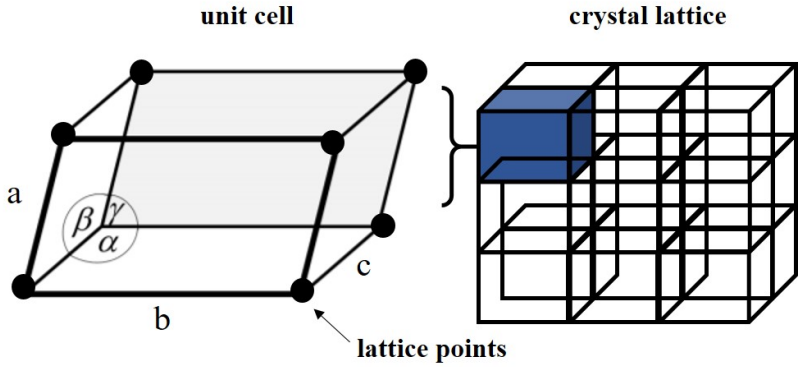

Figure 2-1: An illustration of a unit cell, showing lengths (a,b,c) and angles (α, β, γ) and a crystal lattice.

has one lattice point and only the unit cell holds translational symmetry. In contrast, other lattice types have additional lattice points at the faces or within the unit cell. This means each lattice type holds a different number of lattice points and additional translational symmetry. These lattice types are known as centred (C), face centred (F) and body centred (I) and are illustrated in figure 2-2.[116–118]

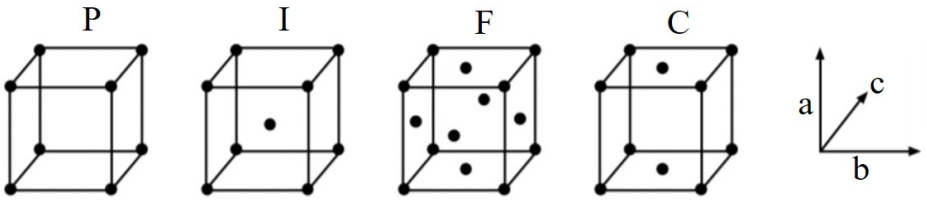

Figure 2-2: An illustration of the four lattice types and the positions of lattice points.

The relations between unit cell lengths and angles vary depending on the lattice symmetry, and each unit cell can be assigned to one of seven crystal systems, summarised in table 2.1. A combination of the four lattice types and seven crystal systems gives rise to 14 Bravais lattices, to which all crystal structures belong.[116–118]

2.1.1.1 Unit cell symmetry

The minimum building block within the unit cell from which the whole crystal can be generated by symmetry is defined as the asymmetric unit. The asymmetric unit relates to the unit cell by the internal unit cell symmetry present and can contain one or several whole molecules or molecule fragments. A unit cell can be generated from the asymmetric unit via symmetry operations which can be categorised into two groups, known as non-translational and translational symmetry elements (a symmetry element is a reference point for which a symmetry operation can take place). Non-translational symmetry elements include rotation around an axis (n-fold, n= 2, 3, 4 and 6), reflection across a mirror plane, inversion through a specific point and roto-inversion: rotation followed by inversion. Translational symmetry elements include translation of the asymmetric unit within the unit cell, combined with other internal

Table 2.1: The unit cell parameters for each crystal system and the distribution of lattice types.

crystal system	**unit cell parameters**	**Bravais lattice**
triclinic	$a \neq b \neq c \quad \alpha \neq \beta \neq \gamma \neq 90^o$	P
monoclinic	$a \neq b \neq c \quad \alpha = \gamma = 90^o \quad \beta \neq 90^o$	P, C
orthorhombic	$a \neq b \neq c \quad \alpha = \beta = \gamma = 90^o$	P, C, I, F
tetragonal	$a = b \neq c \quad \alpha = \beta = \gamma = 90^o$	P, I
trigonal	$a = b \neq c \quad \alpha = \beta = 90^o \quad \gamma = 120^o$	P
hexagonal	$a = b \neq c \quad \alpha = \beta = 90^o \quad \gamma = 120^o$	P
cubic	$a = b = c \quad \alpha = \beta = \gamma = 90^o$	P, I, F

symmetries. There are two types of translational symmetry elements which combine both non-translational and translation symmetry elements, known as screw axes and glide planes. A screw axis describes the translation of an object followed by a rotation, whereas a glide plane describes the translation of an object followed by a reflection.[118,119] Illustrations of each type of symmetry element are displayed in figure 2-3a. Overall there are six symmetry elements which can co-exist to yield a crystal structure with a more complex symmetry; there are 32 possible combinations defined as crystallographic point groups. Furthermore, a combination of the 32 point groups and 14 Bravais lattices types previously discussed affords a space group, with 230 combinations possible. Every crystal structure possesses the symmetry of only one space group and an entire crystal structure can be built with the knowledge obtained from the asymmetric unit and appointed space group,[116,118] summarised in figure 2-3b.

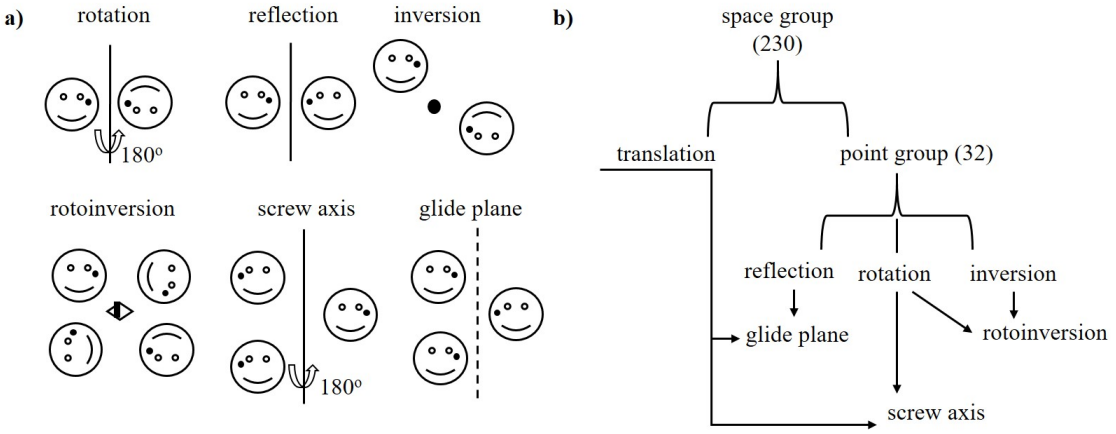

Figure 2-3: A summary of each symmetry element (a) and the combination of translational symmetry of a unit cell and the point group symmetry operations (b).

2.1.1.2 Lattice planes (direct space)

Lattice points connected in three-dimensions afford a unit cell and lattice planes are afforded when lattice points are connected in two-dimensions. A lattice plane can be defined in a crystal by connecting lattice points to produce two-dimensional planes in a large number of orientations, with a corresponding range of interplanar separations. The orientation of a plane defines where it intercepts the three cell axes (a, b, c), known as Weiss indices (x, y, z). However, the more common indices used in crystallography are Miller indices (h, k, l), which are integers calculated from the reciprocal of the Weiss indices (a/h, b/k and c/l).[116] Miller indices describe a set of parallel planes that are separated by the same spacing, d-spacing (d_{hkl}) within a crystal lattice,[120] in comparison to Weiss indices which only describe individual planes. Figure 2-4 illustrates an example of Miller planes within a unit cell.

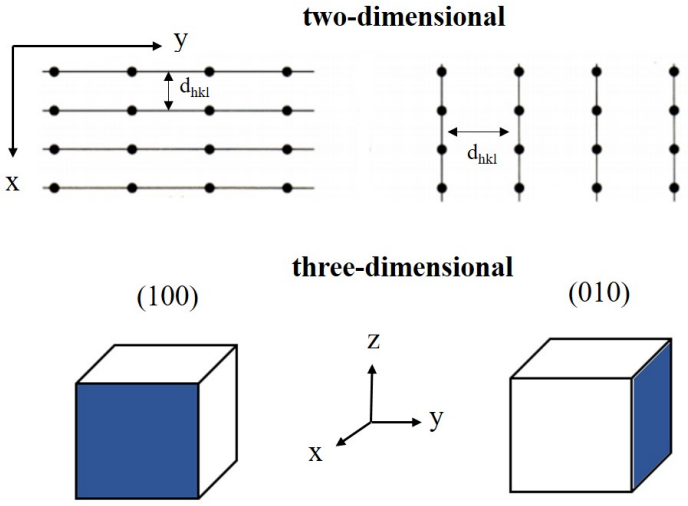

Figure 2-4: An example of two different Miller planes (100) and (010), separated by different d-spacings (d_{hkl}) in two and three dimensions.

2.1.1.3 The reciprocal lattice

The reciprocal lattice is a mathematical space constructed from direct space with vectors relating to the orientation and separations of the real space Miller planes, as shown in figure 2-5. The construction is related to Bragg's Law (see below), which states that $\sin\theta$ (which is proportional to the distance of each diffraction spot) is directly proportional to 1/d. In this case, the vectors have a length (d*) that is the inverse of d_{hkl} ($1/d_{hkl}$) and a direction that is normal to the planes in direct space. As a result, the reciprocal lattice is defined as a*, b* and c* in contrast to a, b and c in direct space.[120] A family of Miller planes can be represented by a reciprocal lattice point, labelled 'O' in figure 2-5. For example, the vector for a reciprocal point with indices (210) would be located perpendicular to the (210) plane and its distance to the origin (O) will be $1/d_{210}$.[120,121]

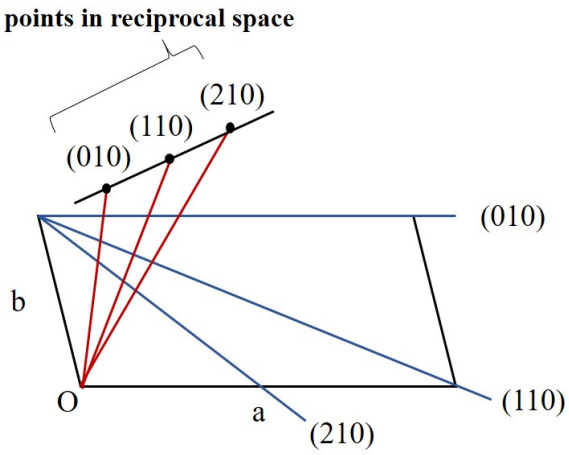

Figure 2-5: The construction of reciprocal space from direct space.

2.1.2 X-ray diffraction

Crystalline materials that possess long range order produce regular and unique patterns under X-ray diffraction, that contain structural information. X-rays are used since they have a wavelength that is comparable to interatomic bond distances in molecules (0.8 - 3.0 Å). Laboratory diffractometers generally use Cu or Mo as the X-ray source since they provide characteristic X-rays with wavelengths of 1.5418 Å (Cu-Kα) and 0.71073 Å (Mo-Kα) respectively. During a diffraction experiment, the crystal under investigation is irradiated with X-rays. An interaction between the electrons in each atom of the crystal and the X-ray beam causes X-ray scattering, leading to the observed diffraction. The amount of X-ray scattering is dependent on the number of electrons in each atom. Naturally, hydrogen atoms have weak scattering and it is therefore difficult to determine their position within a crystal structure.[115,122] The X-ray diffraction data are usually collected by a charge coupled device (CCD) detector, which affords distinctive diffraction spots that are unique to the crystal. The positions of the spots depend on the unit cell dimensions and symmetry while the intensities of diffraction spots can be used to solve and refine a crystal structure as they are related to the electron density through Fourier transformation.[115,117,123]

2.1.2.1 Bragg's law

For X-ray diffraction to take place Bragg's law must be satisfied, equation 2.1. W. L. Bragg (1912) studied the conditions for diffraction and determined that the diffraction of X-rays in a crystal could be analysed by comparison with the reflection of light in a mirror. It was determined that the diffraction of X-rays by electrons can be considered as a reflection from sets of planes (Miller planes) within a crystal. Upon diffraction, X-rays interact with sets of Miller planes, which are described by Miller indices h, k and l (discussed in section 2.1.1.2). The separation of each set of Miller planes is given by the characteristic distance (d_{hkl}). Bragg's law concludes that for a reflection to be observed as a high intensity peak in the diffraction pattern, the path difference between the incident and diffracted beam ($2dsin\theta$) must be equal to an integer number of wavelengths ($n\lambda$) in order that the reflected waves for successive parallel

planes remain in phase to yield constructive interference. Figure 2-6 illustrates Bragg's law. When Bragg's law is not satisfied, the emergent beams are out of phase and cancel each other out, in this case no reflection is observed.[117,124,125]

$$n\lambda = 2dsin\theta \tag{2.1}$$

Bragg's law is applied in diffraction geometry by noting that the angle through which the X-ray beam is scattered is 2θ, that the wavelength is usually constant for each experiment and the value of n can be taken as 1. The Ewald construction, discussed in the next section, is used to determine when the conditions are met for Bragg's law.[117,120]

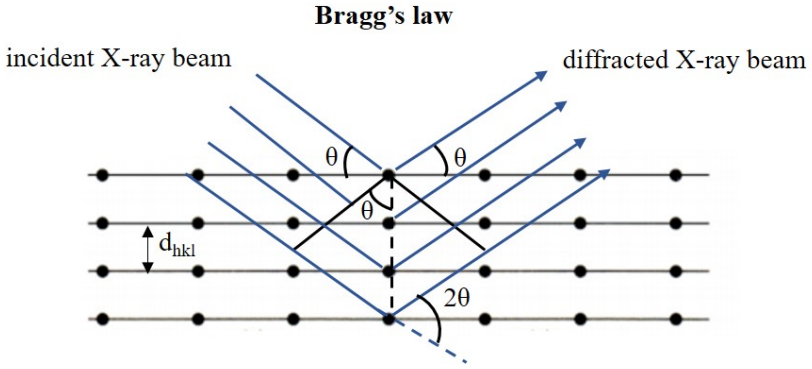

Figure 2-6: The conditions for X-ray diffraction from a set of Miller planes, as described by Bragg's law.

2.1.2.2 The Ewald sphere

The Ewald sphere is a geometric construction used in X-ray crystallography to understand the appearance of diffraction spots when Bragg's law is satisfied for a set of hkl lattice planes, figure 2-7. The sphere is constructed with a radius of $1/\lambda$, where λ is equal to the wavelength of the incident X-ray beam. The crystal is located at the centre of the sphere and the origin (O) of the reciprocal lattice is located at the edge of the sphere at the point of the transmitted beam. The Ewald construction can determine when Bragg's law is satisfied for a set of hkl lattice planes by the rotation of the reciprocal lattice around the origin. Diffraction will only occur when a reciprocal lattice point lies exactly on the edge of the sphere, labelled x in figure 2-7. The direction of diffraction is shown by a line starting at the centre to the set of planes at point x. Although the reciprocal lattice is rotated during a diffraction experiment to maximise the amount of lattice points intersecting the sphere, not all reflections are able to be observed. This is determined by the limiting sphere of radius $2/\lambda$, shown in the figure 2-7.[117,120]

Each diffraction spot is representative of a specific Miller plane, hkl. The intensities of the diffracted beam are measured for each hkl value during an X-ray diffraction experiment.[117] Once these data are collected crystal structure solution can be used to determine the crystal structure from the obtained X-ray diffraction pattern.

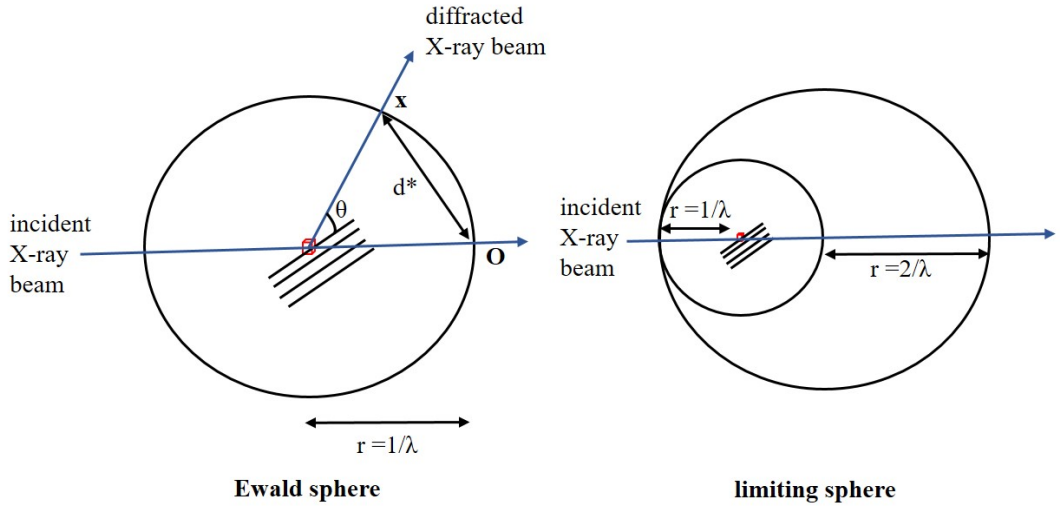

Figure 2-7: The Ewald sphere, a construction for satisfying the Bragg equation and the limiting sphere for observable reflections.

2.1.3 Crystal structure solution

Crystals contain atoms which scatter X-rays from their electrons, discussed in section 2.1.2. Information on the type of atoms and their arrangement in the unit cell (i.e. the molecular structure in the crystal) can be gained from the intensity of scattered X-rays, I_{hkl}, via a term called the structure factor. The structure factor describes the contributions to a particular reflection intensity from all atoms in the unit cell (n) and is the sum of all waves that are scattered in the hkl direction. It is dependent on the position of each atom in the unit cell (x_j, y_j, z_j) and the atomic scattering factor of each (f_j).[126]

2.1.3.1 The atomic scattering factor

The atomic scattering factor (f_j) represents the amount of scattering from each atom; it relates to the number of electrons in the atom and varies with the scattering angle (figure 2-8). A scattering angle of zero yields scattered X-rays that are all in phase; as the scattering angle increases the scattered X-rays become increasingly out of phase as the scattering from different parts of the extended electron cloud becomes less constructive. The atomic scattering factor is also directly dependent on the number of electrons (see equation 2.2). Hydrogen, for example, has one electron and therefore has a low scattering intensity (even at low scattering angles). This means that it is harder to locate a hydrogen atom position from an electron density map gained with an X-ray diffraction source.[125] It should be noted that the measured atomic scattering also falls off due to thermal motion of the atom, and indeed the diffraction intensities are used to quantity these thermal motions.

$$f_j = \frac{\text{amplitude scattered by the atom}}{\text{amplitude scattered by a single electron}} \tag{2.2}$$

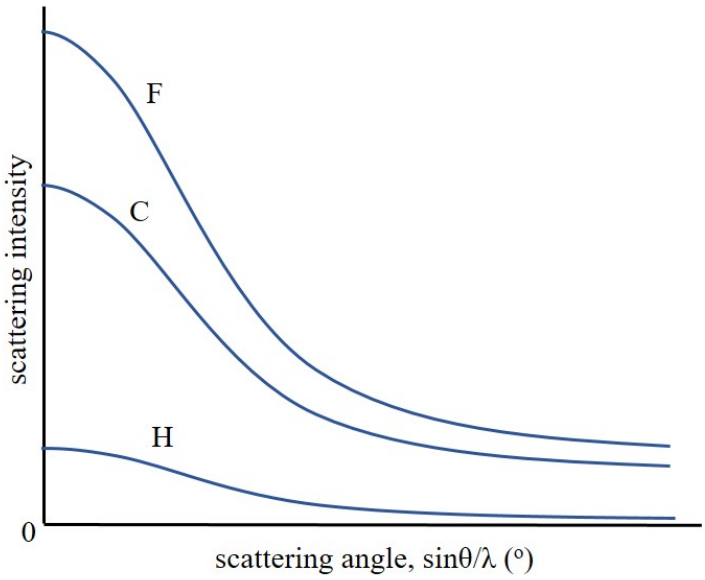

Figure 2-8: The relative atomic scattering factors of fluorine, carbon and hydrogen atoms.

2.1.3.2 The structure factor and electron density map

The structure factor, F_{hkl} (equation 2.3) is used in crystal structure determination to establish the distribution of electron density within the unit cell. The F_{hkl} can be calculated from the observed intensities I_{hkl} (equation 2.4), however this only provides a magnitude of the structure factor and not its phase. The addition of phase information is required to access a three dimensional image of the crystal structure. This is known as the phase problem and is discussed further below. If the phases are known, the F_{hkl} can be recombined via Fourier transformation to obtain the electron density at position x,y,z in the unit cell, ρ_{xyz} (equation 2.5) expressed with units e $\mathring{A}^{-3}$. The summation considers the contribution of all the reflections in a diffraction pattern and yields an electron density map of the whole crystal structure.[123,125,127]

$$F_{hkl} = \sum_{j=1}^{N} f_i exp[2\pi i(hx_j + ky_j + lz_j)] \tag{2.3}$$

$$I_{hkl} = (F_{hkl})^2 \tag{2.4}$$

$$\rho_{xyz} = \frac{1}{V} \sum_{hkl} F_{hkl}.e^{-2\pi i[hx+ky+lz-\phi(hkl)]} \tag{2.5}$$

When ρ_{xyz} is evaluated, areas of high electron density concentrations in the unit cell are revealed which relate to the location of atoms. In order to evaluate equation 2.5, the phases for at least some F_{hkl} reflections must be known.[123,127] This well known problem in crystallography is termed the phase problem. Several methods have been devised to overcome this problem including: Patterson methods, direct methods and duel space methods.[123] Direct methods are used to solve crystal structures in this work, as it is ideally suited for light organic molecules.

2.1.3.3 Direct methods

Direct methods are commonly used to solve organic small molecules with no heavy atoms. It is a trial and error based approach that exploits the relationship between the phase values of different reflections and their intensities, which are based on statistical relations between the reflections. The method works in reciprocal space to solve the phase problem, working with normalised structure factor values (E_h). Two assumptions regarding the electron density are made in direct methods: 1) the electron density must be positive and can never equal zero; and 2) concentrated electron density areas relate to atomic positions. The simplest statistical relationship employed in direct methods is the triplet relationship between between triples of reciprocal lattice vectors of the type E_h, E_k and E_{h-k}, which allows for the phases of strong reflections to be estimated[126] from the Sayre Equation[128] (equation 2.6). There are other such sets of reflections that can also be utilised to generate phase relationships. The strongest E_h reflections with the largest number of phase relationships are used in an automated direct methods calculation to determine a set of potential phases. These initial phases are then used to derive new phases using statistical relationships such as the tangent formula (equation 2.7). The tangent formula utilises a vast number of triplet relationships for each phase set; the phase sets generated are ranked by a figure of merit and the highest values are used to calculate possible electron density maps by a Fourier transformation calculation similar to that in equation 2.5.[126] Examination of these maps can reveal potential atomic positions based on recognisable molecular fragments, such as an aromatic ring. Once a structure has been solved the refinement process begins, to generate the best structural model.[126,129]

$$\phi_h \approx \phi_{h-k} + \phi_k \tag{2.6}$$

$$tan\phi_h \approx \frac{\sum_k |E_k E_{h-k}| sin(\phi_k + \phi_{h-k})}{\sum_k |E_k E_{h-k}| cos(\phi_k + \phi_{h-k})} \tag{2.7}$$

2.1.4 Crystal structure refinement

Structural solution through direct methods yields an initial, possibly incomplete model of the crystal structure; the model will contain inaccuracies from errors in the data collected and the fact that not all atoms may initially be identified. These errors are minimised through crystal structure refinement to improve the model to obtain best agreement with the observed data. The most common method used is the least squares method, where structural parameters such as atom types, positions and displacement parameters are optimised. Structure factors calculated from the structure solution model (Fc) are compared to the structure factor values observed in the experiment (Fo); the phases for each of Fo and Fc can be calculated from the structural model and used in evaluating observed and calculated density maps and, importantly, the difference map which may reveal further atomic positions or features. The least squares refinement method aims to minimise the difference between Fc and Fo (equation 2.8) by adjusting various parameters, including the positions and thermal motions of the atoms in the model, to improve the fit and further optimizes the refinement by assigning a weight to

each reflection (w). The weight represents the accuracy of each measured intensity which has a inversely proportional relationship to the amplitude of F, and estimated variance (equation 2.9).[123,130,131]

$$\sum w(|F_o|^2 - |F_c|^2)^2 \tag{2.8}$$

$$w = \frac{1}{\sigma^2({F_o}^2)} \tag{2.9}$$

The agreement between the structural model obtained from solution and least squares refinement methods and the data set obtained from an X-ray diffraction experiment is quantified by the R-factors. A weighted R-factor (wR_2, equation 2.10) with a value less than 0.2, an R-factor (R, equation 2.11) with a value range of 0.02-0.05 and a goodness of fit (GooF, equation 2.12) value of close to 1 are highly desired and conclude a good structural model fit to the data set.[123,130,131]

$$wR_2 = \left[\frac{\sum w|{F_o}^2 - Fc^2|^2}{\sum w|{F_o}^2|^2}\right]^{1/2} \tag{2.10}$$

$$R = \frac{\sum ||F_o| - |F_c||}{\sum |F_o|} \tag{2.11}$$

$$GooF = \left[\frac{\sum w({F_o}^2 - {F_c}^2)^2}{N - P}\right]^{1/2} \tag{2.12}$$

Where N is equal to the number of data and P is equal to the number of refined parameters.

2.1.5 Powder X-ray diffraction (PXRD)

Not all crystallisation experiments yield single crystals, more often a polycrystalline powder is crystallised. PXRD is a method used to analyse polycrystalline material and the patterns obtained from PXRD analysis are commonly used as a tool to determine the composition of a sample. A polycrystalline powder contains a large number of small crystallites in random orientations; each individual crystallite in the powder will produce a diffraction pattern. When a powder sample is exposed to an X-ray beam, diffraction will occur in all directions. As a result, a cone of diffraction that represents each Bragg reflection at an angle corresponding to its d-spacing is produced, governed by Bragg's Law (figure 2-9). A detector is used to measures the intensity of each diffraction cone at different 2θ values. The result is a ring of intensity, which is plotted against the angle (2θ) to afford a one-dimensional PXRD pattern.[117,132,133] Valuable information can be gathered from the peak positions in a PXRD pattern; these will be unique to the unit cell dimensions of the material or materials present (there may be more than one material present in a multi-phase sample). In this work the peak positions are used to identify different solid forms, using the pattern as a fingerprinting tool. PXRD patterns can be used for quantitative assessment of a sample and can measure the degree of

crystallinity, phase composition, unit cell parameters and can sometimes be used to solve and refine the crystal structure. High quality data is required to refine a crystal structure through Rietveld refinement; this method was not used in this work. There are limitations with PXRD analysis. One example is preferred orientation, which can occur when each Miller plane is not fairly represented in the randomised orientations of the crystallites and lead to variation of the diffraction peak intensities; the sample is rotated during data collection to minimise this. [117,133]

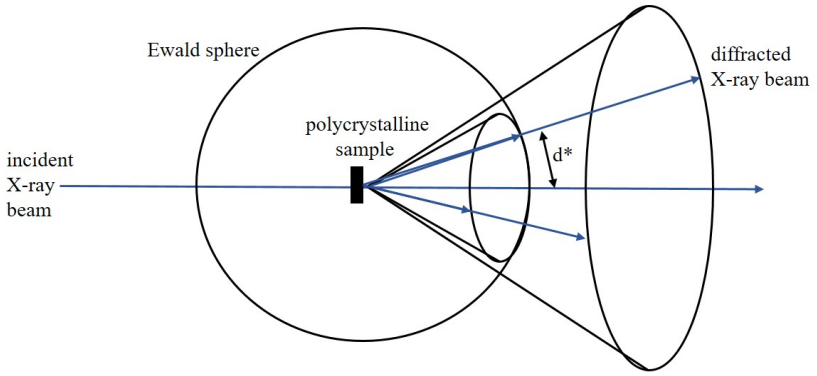

Figure 2-9: An illustration of X-ray diffraction of a polycrystalline powder, PXRD.

2.2 Thermal analysis

Thermal techniques were used to analyse the thermal behaviour of materials and to identify different solid forms. The qualitative technique hot-stage microscopy (HSM) and the quantitative technique Differential Scanning Calorimetry (DSC) were used in this work.

2.2.1 Differential Scanning Calorimetry (DSC)

DSC measures the difference in heat flow between two aluminium pans, an empty reference pan and a pan with 1-5 mg of sample enclosed. The two pans are heated or cooled at a set rate. The technique measures the heat flow required to keep both pans at the same temperature, to identify the occurrence of thermal events. In the case of an exothermic event, heat is released and less heat is required to increase the temperature of the sample pan compared to a reference pan; the opposite is the case for endothermic events. [134]. This allows for the temperature (and the enthalpy changes) of exothermic events (e.g. crystallisation) and endothermic events (e.g. melting) to be measured. Figure 2-10 shows an example DSC trace with a number of different thermal events that can be observed in a material including: glass transition (a), recrystallisation (b), phase transition or desolvation (c), melting (d) and decomposition (e).

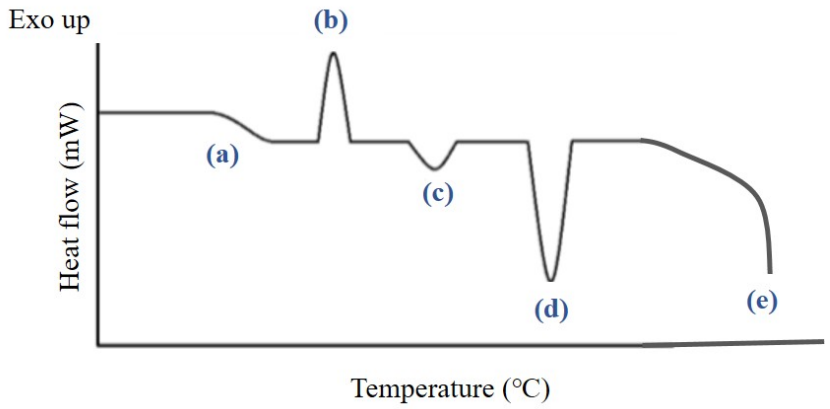

Figure 2-10: An example DSC trace that includes the follow thermal properties: glass transitions (a), recrystallisation (b), phase transitions or desolvation (c), melting (d) and decomposition (e).

2.2.2 Hot-stage microscopy (HSM)

HSM is a method used to visualise (live and recorded) the effect of temperature on a material. It is a thermal analysis tool that provides a visual aid for the interpretation of thermal events, such as melting and phase transitions and is often paired with DSC.[134]

2.3 Microscopy

2.3.1 Optical microscopy

Optical microscopy was used as a tool to examine the product gained from crystallisation experiments. An optical microscope uses visible light and magnifying lenses. Polarised lenses are used to determine if a sample is crystalline through optical extinction; a rotation of 90^o yields extinction of light for a single crystal sample. Optical microscopy can be used to examine crystal morphology, size and colour. A change in one of these properties may indicate the formation of a different solid form. In this work an integrated camera is used to capture an image of the magnified sample.[30]

2.3.2 Scanning Electron Microscopy (SEM)

SEM is used for the production of highly detailed images that capture the topography of a sample. It uses an electron beam to illuminate the sample in the place of visible light. Upon impact, the sample ejects secondary electrons or X-rays which are detected. The detector converts this into a signal that is converted into an image and allows the morphology and surface of a material to be visualised. It is important that samples submitted for SEM analysis do not contain water since the system is operated under a vacuum. All non-metallic samples are pre-coated with a thin layer of gold to increase the resolution and to prevent the accumulation of charge when the sample is illuminated by an electron beam.[135]

2.4 Spectroscopy

2.4.1 Circular dichroism spectroscopy (CD)

The technique of CD spectroscopy is used in this work as a method to study chiral molecules in solution and to establish the enantiomeric excess of the product yielded from various crystallisation methods. CD spectroscopy uses wavelengths of light, typically from the ultraviolet and visible regions (190-750 nm), that are manipulated to travel in a circular pattern with simultaneous clockwise and anti-clockwise light waves.[30] Figure 2-11 displays these polarised light waves which are represented by the combination of two spiralling waves. Chiral chromophores are capable of optical rotation (optically active) and will only absorb one direction of the circularly polarised light. CD spectroscopy can measure and quantify the difference in absorption (ΔA) of the left and right-handed circularly polarised light from equation 2.13.[136] A chromophore describes a molecule that can absorb particular wavelengths of ultraviolet and visible light due to the possession of conjugated π bonds which interact with the radiation.[137]

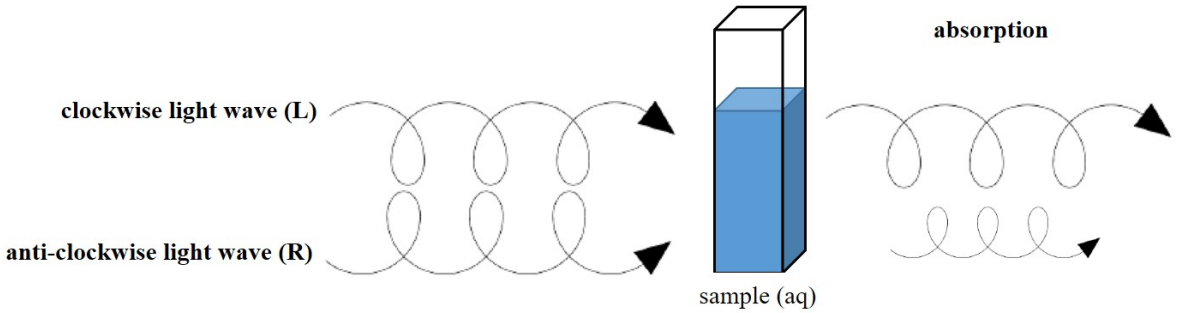

Figure 2-11: An illustration of the clockwise (left handed, L) and anti-clockwise (right handed, R) waves of circular polarised light.

ΔA can be converted into ellipticity, θ, a value that describes the extent of rotation of polarised light after interaction with a chiral sample, through equation 2.14. Equation 2.15 calculates the molar ellipticity, $[\theta]$, a value independent from the concentration of solution and an extension of the Beer-Lambert Law (equation 2.16).[138] Figure 2-12 displays an example of the measurement $[\theta]$ as a function of wavelength. The method in this example is used to distinguish the proportion of enantiomers present in solution including racemic mixtures, from which the absorption of both enantiomers are cancelled out (black trace). The blue trace in figure 2-12 represents a solution that contains a higher proportion of S(+)enantiomers and the red trace a higher proportion of R(-) enantiomers of salbutamol sulfate.

$$\Delta A = A_L - A_R \tag{2.13}$$

$$\theta = \Delta A.(32.98) \tag{2.14}$$

$$[\theta] = \Delta\epsilon.(3298) \tag{2.15}$$

$$c = \frac{\Delta A}{\Delta\epsilon.l} \tag{2.16}$$

where A_L and A_R are the difference in absorption of the left and right-handed circularly

polarised light, θ is the ellipticity in in millidegrees, ϵ is the extinction coefficient for absorbance spectroscopy in mol^{-1} cm^{-1} dm^3, [θ] is the molar ellipticity in deg cm^2/dmol, 32.98 is a scale factor, c is the concentration in mol dm^{-3} of solution and l is the path length in cm.

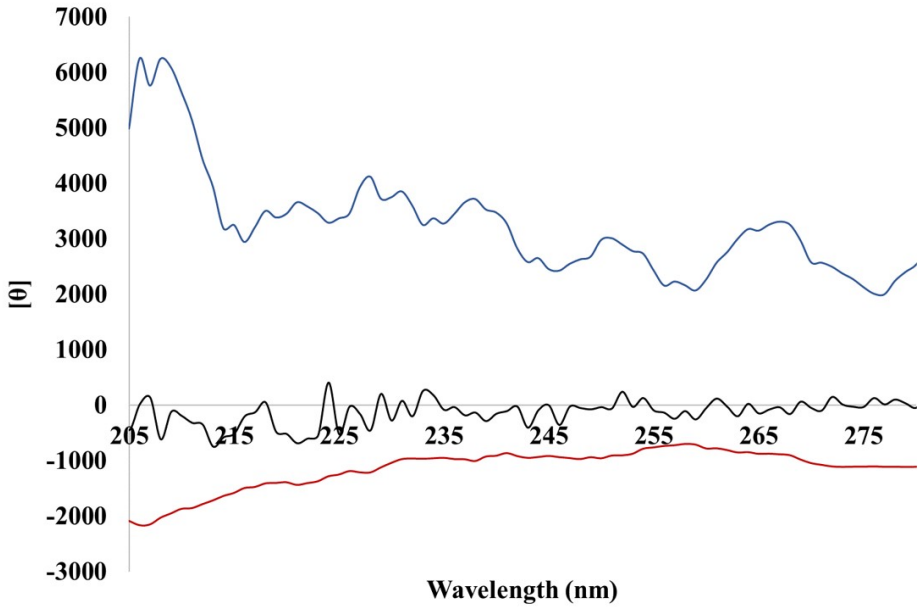

Figure 2-12: A molar ellipticity verses wavelength plot with three traces that represent: 1) a racemic solution (black); 2) a solution with a higher proportion of R enantiomers (red); and 3) a solution with a higher proportion of S enantiomers (blue) of salbutamol sulfate.

2.4.2 Proton nuclear magnetic resonance (^{1}H-NMR spectroscopy)

^{1}H NMR spectroscopy is an analytical method used in this work to analyse quantitatively the composition of components in a material by peak identification and integration. The technique is based on the principle that proton nuclei contain a magnetic moment which can lead to a splitting of nuclear energy levels when an external magnetic field is applied. Under these conditions, the nuclei can undergo an energy transfer from a low to a higher energy level when an external field is applied (which is at radio wave frequencies). When the nuclei return to a low energy state, energy is emitted at the relevant radio wave frequency. Peaks are observed at different positions for protons in different molecular environments, as the local electron density variations in a molecule mean that the localized magnetic field experienced by protons in different environments are slightly altered, leading to the phenomenon of chemical shift. The emitted frequencies are processed to yield a ^{1}H NMR spectroscopy spectrum from which the chemical shifts and peak intensities allow the proton-containing groups to be characterised and hence allow for molecular identification.[139]

Chapter 3

Techniques and instrumentation

This chapter contains a description of the routine techniques and instrumentation used to prepare and characterise the materials that are studied during this research project. A general overview is presented in this chapter and more specific details for each experiment can be found in the experimental section of each results chapter. The theory behind the various crystallisation methods employed is explained in section 1.3.

3.1 Crystallisation methods used for material preparation

A large portion of the research conducted in this project was reliant upon SCXRD for material characterisation. As a result, the preparation of target materials in chapters 5 and 6 focused on growing single crystals with the required characteristics; consistent sets of well diffracting crystals with a size of 100 to 200 μm required for in-house laboratory source diffractometers. The use of micro crystalline powders was sufficient for other material characterisation techniques used in this project such as PXRD, DSC, SEM, ^{1}H NMR spectroscopy and CD spectroscopy. A number of crystallisation methods were employed in this research project including slow evaporation of solvent (referred to as evaporative crystallisation), slow cooling, solution-mediated (referred to as slurrying), mechanical grinding, vapour diffusion and electrospraying crystallisation.

3.1.1 Evaporative crystallisation

The samples for evaporative crystallisation were prepared and placed into 7 mL glass vials. Milligram quantities of the sample was added to the appropriate solvent. Sonication in a temperature-controlled water bath (set at the temperature of evaporation) was used to aid dissolution. After dissolution, the vial lids were pierced with ten small holes (unless stated otherwise) to ensure slow evaporation of solvent. The vials were left in hotplates at a controlled set temperature to crystallise or a refrigerator for experiments at 4^{o}C (figure 3-1a). To access different conditions for crystal nucleation and growth, several input properties and crystallisation parameters were altered including the concentration, solvent system, temperature and speed of crystallisation. The speed of crystallisation was varied by altering the surface area

allowing evaporation and pressure of crystallisation at a set temperature (figure 3-1b). The surface area was altered with the use of vial lids which were pierced with either 1 hole, 10 holes or with no lid. An increase in pressure of crystallisation to slightly higher than ambient was afforded by the use of a fan.

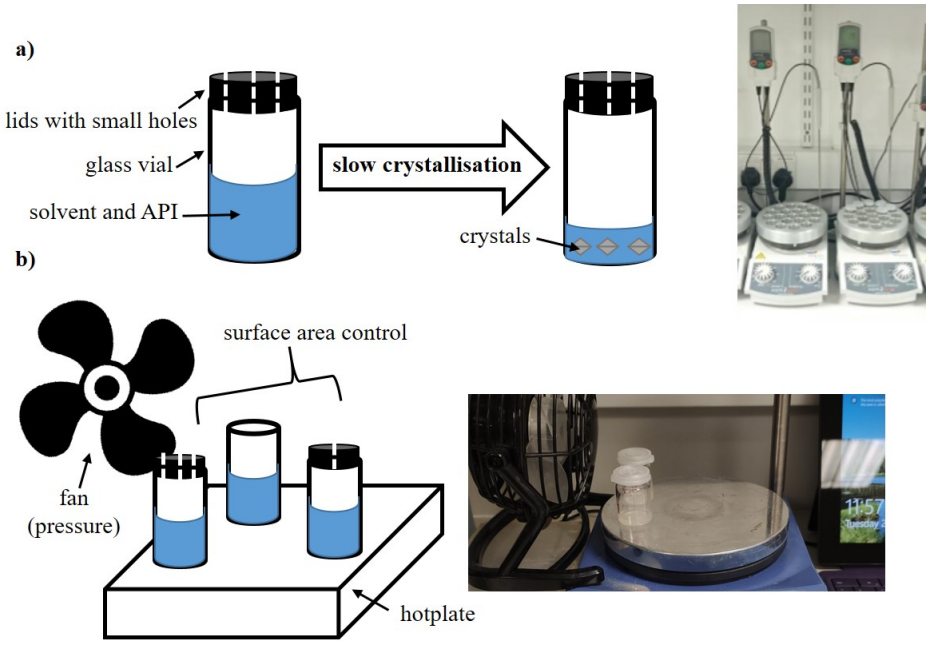

Figure 3-1: The set up and equipment used under (a) general evaporative crystallisation methods and (b) evaporative crystallisation with control over the speed of crystallisation at a set temperature.

3.1.2 Cooling crystallisation

A Cambridge Reactor Design Polar Bear Plus heating and cooling platform (figure 3-2b) was used to implement batch cooling crystallisations at different scales (figure 3-2c). The crystalliser enforced a high level of control over a programmable heating and cooling profile in addition to magnetic bottom stirring rates. Various crystallisation scales were accessed through changeable vial holders; scales of 1.5 mL, 7 mL and 20 mL were used in this work. Cooling experiments were carried out at various cooling temperature ranges, ramping speeds, concentrations and solvent systems. The product gained from crystallisation was filtered and left to dry at room temperature.

Seeded crystallisation experiments were used as a method to reduce the solution mediated phase transformation kinetics of the crystallisation process. The aim of adding a crystal seed to a cooling crystallisation process is to encourage the formation and stabilisation of elusive solid forms. The cooling profile and protocol for each experiment is available in the experimental section of the relevant results chapter.

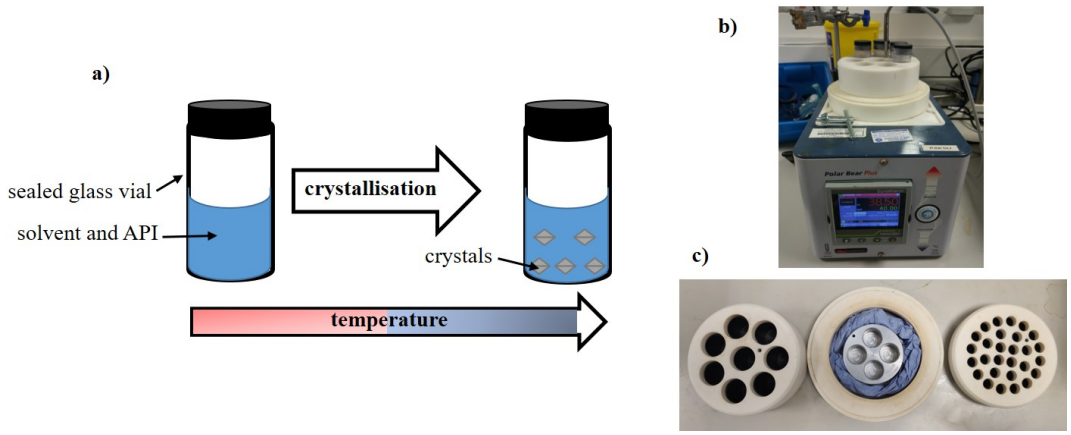

Figure 3-2: The set up used for cooling crystallisation methods (a), an image of the Cambridge Reactor Design Polar Bear Plus platform (b) and an image of the adaptors used (c).

3.1.3 Solution-mediated crystallisation (slurrying)

Solution-mediated crystallisation (slurrying) experiments were prepared in 7 or 20 mL glass vial. An excess amount of sample that contained the desired molar ratios of the target multi-component materials were added to 3-5 mL of the chosen solvent system. It was ensured that enough sample was added to create a suspension that remained in solution. The vials were left in hotplates at a controlled set temperature and agitated with a magnetic bottom stirrer at 700 rpm. The vials were left undisturbed for a set amount of time before product gained from crystallisation was filtered and left to dry at room temperature.

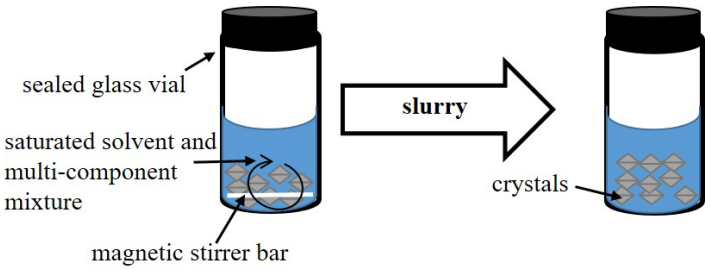

Figure 3-3: The set up used for solution-mediated crystallisation methods (slurrying).

3.1.4 Mechanical grinding

Grinding crystallisation experiments were conducted manually with the use of a pestle and mortar and mechanically with a Retsch cryomill (figure 3-4). An appropriate amount of material (2-5 mg) that contained the desired molar ratios of the target multi-component materials was placed into a pestle and mortar or cryomill. Experiments conducted with a pestle and mortar were ground by hand for 15 minutes and experiments that were conducted with a cryomill were paired with a metal ball of 5 mm and ran at a frequency of 30 s^{-1} for 15 minutes. All grinding crystallisations were conducted neat (neat grinding) or with a few droplets of solvent (LAG).

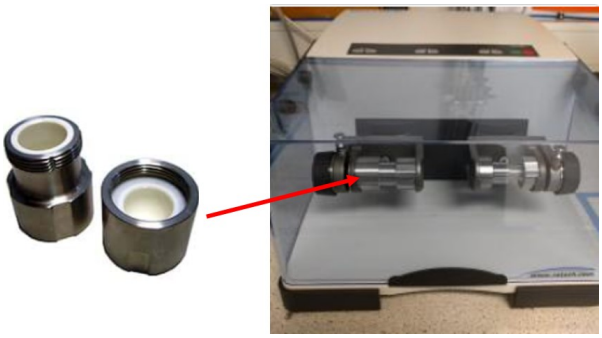

Figure 3-4: The Retsch cryomill used for grinding crystallisation experiments.

3.1.5 Vapour diffusion crystallisation

Vapour diffusion crystallisation experiments consisted of a solution that contained a saturated amount of sample in a highly soluble solvent. This solution was placed into a 1 mL glass vial. Sonication in a temperature controlled water bath (set at the temperature of crystallisation) was used to aid dissolution. The 1 mL glass vial was left unsealed and placed inside a larger sealed glass vial. The larger glass vial contained enough anti-solvent to ensure that the solvent level was raised above the level of the solvent in the 1 mL vial but did not enter it. Figure 3-5 contains an illustration of the vapour diffusion set up used in this work. The larger vials were left in hotplates at a controlled set temperature to crystallise or a refrigerator for experiments at 4^{o}C. Upon crystallisation the product was filtered and left to dry at room temperature.

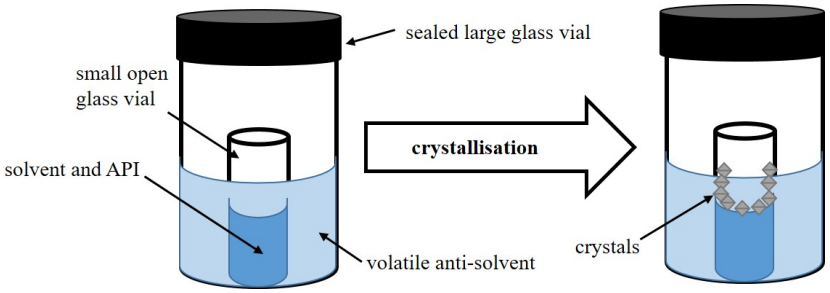

Figure 3-5: The set up used for vapour diffusion crystallisation methods.

3.1.6 Electrospraying crystallisation

The electrospray unit was purchased from SPRAYBASE; figure 3-6 displays an image of the unit used and a schematic depiction of the crystalliser. The set up consists of a syringe pump, which was programmed to a set flow rate (0.1-0.5 mL h^{-1}) and transported the solution to a metallic emitter. A high voltage (12-16 kV) was supplied to the emitter which atomised the solution, generating an electrostatic repulsion within highly charged micro-nano sized droplets. The atomised solution then entered a drying chamber, set at 40^{o}C and atmospheric pressure, where crystallisation occurred. An E-field ensured that resulting product crystals deposited on to a cathodic collector plate that is covered in a single layer of aluminium foil. A set distance of 12 cm between the emitter and collector plate was used for each experiment, which allowed the E-field generated to be dependent on the voltage supplied, calculated from equation 3.1.

$$\textit{E-field (kV cm}^{-1}\textit{) =voltage (kV) / distance (cm)} \tag{3.1}$$

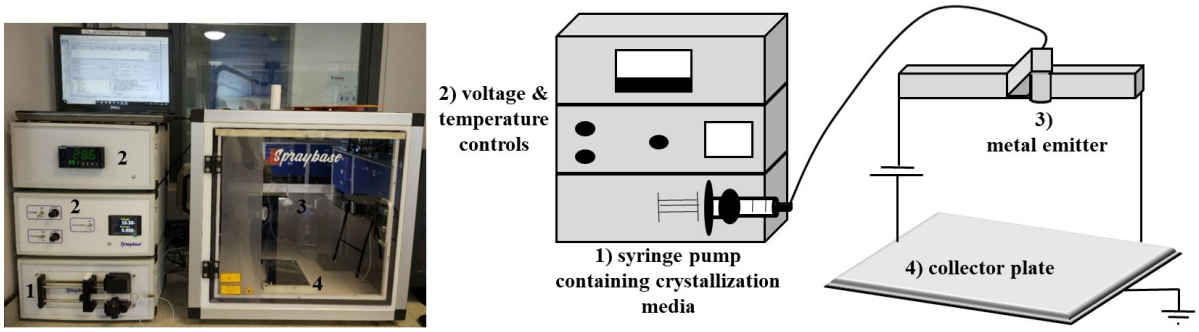

Figure 3-6: The SPRAYBASE unit used for electrospraying and a schematic of the electrospray set up.

The electrospray set up is a method capable of inducing electrical confinement within the crystallisation media from the influence of electric fields, that are created from the addition of voltage to the system. The voltage applied charges the crystallisation solution and generates an electrostatic repulsion which counteracts the surface tension of the liquid meniscus produced at the tip of the metal emitter.[47] As a result of the electrostatic repulsion, nano-droplets are formed that confine the crystallisation solution.[140] These resultant nano-confined droplets affect the surface and volume free energies of crystal formation.[141]

3.2 Solubility and metastable zone width measurements

Information on a material's solubility is a vital parameter required for any solution based crystallisation method. In this work, the solubility curves and in some cases MSZW for all model systems were taken from the literature or determined by gravimetric or observational methods using a Cambridge Reactor Design Polar Bear Plus crystallisation platform.

3.2.1 Determination of sample solubility

3.2.1.1 Gravimetric methods

Gravimetric analysis was used to calculate a material's solubility at a fixed temperature. All measurements were prepared in a 20 mL glass vial that contained 10 mL of the chosen solvent. An excess amount of sample was added to the vial until the solution was vastly over saturated and a suspension was created. The glass vial was sealed and put into the Polar Bear Plus at a set temperature and the system was agitated with a magnetic bottom stirrer for over 12 hours at 700 rpm. After 12 hours, the stirring was turned off and the remaining solid suspended in solution was left to settle at the bottom of the vial, leaving a clear solution at the top. 1 mL aliquots of the clear solution were taken. The aliquots were placed into previously weighed empty vials by a syringe fitted with a filter that ensured no solid was present. The vials containing the solution aliquots were left to evaporate at 40^{o}C on a hot plate. Upon complete evaporation the vials were weighed and the concentration of sample dissolved in the

1 mL aliquots was calculated at the set temperature. Solubility measurements were taken at three or more temperatures between 4-60^{o}C to yield a solubility curve plot; the temperature range depended on the solvent boiling point. At least three repeats were taken for each sample at each temperature to calculate an average solubility value and estimated error bar for the solubility curve plots.

3.2.1.2 Observational methods

Observational solubility methods were used to calculate a material's solubility from the addition of material increments of known mass. All measurements were prepared in a 20 mL glass vial that contained 3 mL of the chosen solvent. The sealed glass vial was placed in the Polar Bear Plus platform and left to equilibrate at 4^{o}C for 1 hour at a set magnetic bottom stirring rate of 700 rpm. Upon solvent equilibrium, small increments of the sample were added to the glass vial. The solution was subjected to a slow heating profile of 0.2^{o}C min^{-1} at a stirring rate of 700 rpm. The temperature was noted once all of the sample had dissolved from the first increment addition; this value represented the first solubility point on the solubility curve. Further fixed sample increments were added to the solution; the temperature at which all the sample had fully dissolved was recorded before the addition of the next sample increment. This method was repeated until the desired end temperature was reached, usually 50 or 60^{o}C. The solubility curves were calculated from the sum of the known masses added from each increment of sample in the solution at the recorded temperature.

3.2.2 Determination of metastable zone width

MSZW measurements were used as a guide in the preparation of cooling crystallisation experiments utilising crystal seeding. All measurements were prepared in the same crystalliser as the subsequent seeded experiments and the same conditions were used (e.g. type and rate of agitation). This ensures that the MSZW afforded reflects the same crystallisation kinetics as the seeded crystallisation experiments. Saturated concentrations of the sample were added to the chosen solvent, based on data taken from a solubility curve. The solution was cooled at a controlled rate of $1^oC\,min^{-1}$ until the first instance of spontaneous nucleation was observed. The temperature of nucleation was recorded for the known concentration of sample. Various saturation temperatures were explored in a range of 4-60^{o}C. At least three temperatures were investigated in order to obtain a MSZW plot. 2-3 repeats were taken for each sample at each temperature to calculate an average value.

3.3 X-ray diffractometers

3.3.1 Single crystal X-ray diffraction (SCXRD)

Three in-house laboratory diffractometers were used in this work for the collection of crystallographic data: a Rigaku Oxford Diffraction SuperNova, Xcalibur and Gemini A Ultra. All diffractometers are equipped with a four-circle kappa goniometer and a graphite monochromator. The SuperNova and Gemini A Ultra have dual sources Mo-Kα (λ = 0.71073 Å) and Cu-Kα (λ = 1.54045 Å) of X-rays. The Xcalibur has a sealed tube Mo-Kα X-ray source. Both

the SuperNova and Xcalibur are equipped with an Eos S2 detector and the Gemini A Ultra diffractometer is equipped with an Atlas CCD detector.

The four-circle kappa goniometer enables a complete data set to be collected through movement of the crystal via diffractometer positions $(\kappa, \omega, \psi, 2\theta)$. Data were collected at 150 K or 298 K; the temperature was controlled with a Oxford Diffraction Cryostream 700 series or an Oxford Instruments CryoJetXL. All data collected were processed with the CrysAlisPro[142] software package. All structures were solved by direct methods using SHELXS-2013[143] and refined using SHELXL-2015[144] with the software package Olex2.[145] Crystal structures were visualised using Mercury 4.3.[146]

3.3.2 Powder X-ray diffraction (PXRD)

PXRD data were collected with a STOE STADI P diffractometer equipped with monochromatic Cu-Kα1 radiation (λ = 1.54045 Å). Sample preparation involved placing a polycrystalline sample (2-5 mg) into a sample holder. The sample was secured into the holder by a non-diffracting transparent thin film material. The sample was placed between two of the thin films and secured into place with a metal plate that was screwed into the sample holder. Samples were carefully ground with a pestle and mortar before analysis to achieve a homogeneous powder mixture and to minimize the preferred orientation of crystallites, which can affect diffraction peak intensities. All samples were analysed at 298 K by transmission PXRD, with a range of $2\theta = 2 - 60^o$. The identity of the polycrystalline sample was evaluated by visually comparing the resultant pattern to known patterns in the CSD. The reference and resultant pattern were stacked or overlapped in the software package diffractWD for the comparison of peak positions. All samples characterised by PXRD in this work were submitted to the materials and chemicals characterisation service (MC^2) for PXRD pattern measurement. The analysis and interpretation of results were conducted by the author.

3.4 Thermal analysis

3.4.1 Differential Scanning Calorimetry (DSC)

A Thermal Advantage Q20 Instrument was used with a Thermal Advantage Cooling System 90. It was operated with a dry nitrogen purge gas that had a flow rate of 18 cm^3 min^{-1}. 2-10 mg of sample were placed into a sealed Tzero aluminium pan. The pans (sample and reference) were heated at a controlled temperature program with a rate of 5^oC min^{-1} within a temperature range that varied between -20 and 300^{o}C; the maximum temperature was dependent on the melting point of the material being studied. Data were collected with the software package Advantage for Qseries and analysed with the TA Universal Analysis program.

3.5 Microscopy

3.5.1 Optical microscopy

An Infinity 2 microscopy camera fitted to a Leica DM1000 microscope with a polarising lens was used to assess the crystallinity of a material and observe the morphology and size of a solid form crystals. Optical extinction was used to find a crystalline single crystal suitable for SCXRD experiments. Extinction is a term that describes the effect polarised light has on a material. Anisotropic materials (crystalline) demonstrate clear extinction of light for every 90^o rotation. Isotropic materials (amorphous) show no light variation on rotation due to constant extinction.[147]

3.5.2 Scanning Electron Microscopy (SEM)

All images were taken on a JEOL JSM-6480LV instrument and samples were prepared with an Edwards 150B sputter coater. The sample surface or an area of the sample is scanned with a focused beam of electrons. Atoms in the sample interact with the electrons and produce various signals including X-rays, backscattered electrons and secondary electrons. These signals are used to construct an image that shows the sample surface topography.[148] All samples characterised by SEM in this work were submitted to the MC^2 service for measurement; the interpretation of results was conducted by the author.

3.6 Spectroscopy

3.6.1 Circular dichroism spectroscopy (CD)

A Chirascan Circular Dichroism Spectrometer was used, coupled with a nitrogen-cooled 150 watt Xenon arc lamp with a dual polarising and dual dispersing monochromator and a photomultiplier detector. All samples were diluted with water and placed into a Quartz cuvette of either 1 cm or 0.1 cm path length. All experiments were conducted at 20 ^{o}C with a scan range of 205 to 300 nm; a step size of 1 nm and a bandwidth of 2 nm were used. CD spectroscopy and UV-visible absorption spectra were collected for each sample which provided the relevant information required to calculate the concentration and molar ellipticity (enantiomeric composition) of the solution.

3.6.2 Proton nuclear magnetic resonance (^{1}H-NMR spectroscopy)

An Agilent Technologies 300 MHz ^{1}H-NMR spectroscopy instrument was used for all proton ^{1}H NMR spectroscopy studies. 2-5 mg of sample were dissolved in an appropriate deuterated solvent before analysis. The data were analysed with the software package MestReNova.

3.7 Stability studies

3.7.1 Humidity studies

Two closed glass chambers were set at a relative humidity of 80 and 10% with saturated salt solutions of KCl and NaOH respectively. The relative humidity percentage (%RH) in each chamber was tested by a humidity sensor made in house, shown in figure 3-7. 0.01 g of sample were placed inside a 1 mL glass vial without a lid, and removed and monitored by PXRD measurements at intervals over a 6 week time period.

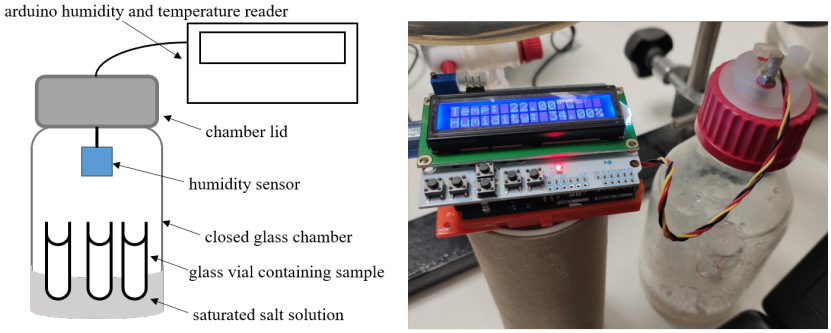

Figure 3-7: The relative humidity chamber in house set up used to measure the stability of samples.

3.7.2 Temperature studies

0.01 g of sample were placed inside a 7 mL open glass vial and placed onto a hotplate set at 70^oC. The sample was removed and monitored by PXRD measurements at intervals over a 6 week time period.

Chapter 4

Exploring the capabilities of electrospraying, a novel crystallisation method.

Parts of this chapter have been published as journal articles in Crystal Growth and Design:

A. J. Al-Ani, P. Sugden, C. C Wilson, and B. Castro-Dominguez, Elusive Seed Formation via Electrical Confinement: Control of a Novel Cocrystal in Cooling Crystallization, *Cryst. Growth Des.*, 2021, 6, 3310–3315.

A. J. Al-Ani, C. Herdes, C. C. Wilson, and B. Castro-Dominguez, Engineering a New Access Route to Metastable Polymorphs with Electrical Confinement, *Cryst. Growth Des.*, 2020, 20, 1451-1457.

4.1 Introduction

One of the hardest challenges to overcome in crystallisation science is to gain a high level of control over the crystallisation process and modify the critical quality attributes (CQAs) of a drug product. The work presented in this chapter investigates the influence of an E-field and confinement on the crystallisation process, using an electrospray set-up, and focuses on the formation and stabilisation of elusive solid forms. Through process development, a new crystallisation technique, known as electrospraying, is investigated as a method with the capability to control and tune the formation of different solid forms, including polymorphic and multi-component complexes, through parametric optimisation. This promises to provide a tool and capability that directly relates to the control of physical properties in the solid state.

The basis of electrospraying is the application of an E-field to a solution which causes atomisation. The atomised solution is charged and produces an electrostatic repulsion that generates a confined solution of nanodroplets.[140] As a result, the surface and volume crystal formation free energies decrease.[141] Modifications to the surface-to-volume ratios in the crystallisation milieu, due to electrical confinement, seems to show favorability towards the formation of higher energy solid forms, for example metastable polymorphs[47,49] and co-crystals.[149,150] An in-depth discussion on the theory of electrospraying is available in the background chapter of this thesis, section 1.3.5.

4.1.1 Project aim

Aim: To design, develop and optimise a novel crystallisation technique, electrospraying, and to study the effect of an electrical confined environment on the crystallisation process.

The research in this chapter focuses on method development and investigates the influence of a number of crystallisation parameters on the product of electrospray crystallisation, including polymorphic control of metastable forms and the formation of elusive solid forms. The investigation aims at decoupling the roles of an E-field and confinement within electrospraying on formation of new electrosprayed solid forms and evaluating if the solid form is accessible through other crystallisation methods. A new solid form discovered by electrospraying is fully characterised and translated into a cooling crystallisation platform with crystal seeding. Table 4.1 displays the crystallisation parameters investigated in this chapter and the resultant product qualities studied.

Table 4.1: Crystallisation parameters investigated in this chapter under electrospray crystallisation and other crystallisation methods and the product qualities studied.

input properties	**process parameters**	**product qualities**
temperature	electric field	solid form
multi-component composition	flow rate	purity
solvent	agitation	morphology
seeded vs unseeded	seeding protocol	particle attributes
	dwell time and temperature	physical properties

4.1.2 Model API systems investigated

Two model API systems are used in this work to investigate the effect of electrical confinement on the crystallisation process. Acetaminophen, the API in paracetamol (PCM), used to treat moderate pain relief and metacetamol (MCM), a non-toxic regioisomer of PCM with analgesic properties that has not yet been marketed as a drug. Figure 4-1 displays the chemical structure of the model systems.

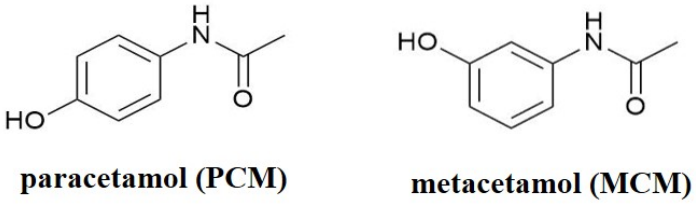

Figure 4-1: The chemical structures of PCM and MCM.

4.1.2.1 Paracetamol (PCM)

There are three experimentally known polymorphic forms of PCM. In 1973, the structure of the thermodynamically stable form I (PCM-I) was discovered,[151] closely followed by the metastable form II (PCM-II) in 1974[152] and a second metastable form III, proven to be difficult to isolate,[153] characterised in 2002.[154] The isolation of PCM-II via electrospraying is the focus of this work due to its elusive nature and enhanced physical properties in comparison to the thermodynamically stable form I.

The layered packing arrangement in PCM-II (figure 4-2b) is responsible for the increased solubility and compressibility over those of the herringbone arrangement observed in PCM-I (figure 4-2a). PCM-II is a potentially more attractive polymorph for formulation as these properties aid a drug's bioavailability and processability into a tablet, which increases the efficiency of energy usage and waste production for the manufacturing process.[6,155]

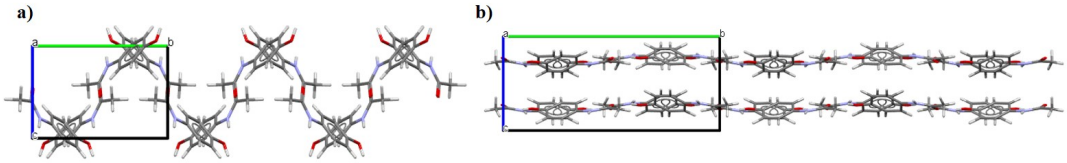

Figure 4-2: The packing of paracetamol forms I and II. a) PCM-I, a herringbone arrangement, viewed along the a axis (CSD code: HXACAN01). b) PCM-II a layered arrangement, viewed along the a axis (CSD code: HXACAN).

4.1.2.2 Metacetamol (MCM)

There are two experimentally known polymorphic forms of MCM. The thermodynamically stable form I was discovered in 2006[156] and has a zig-zag-like packing arrangement, followed by the metastable form II, discovered in 2015[157] with a layered s-shape-like packing arrangement (figure 4-3).

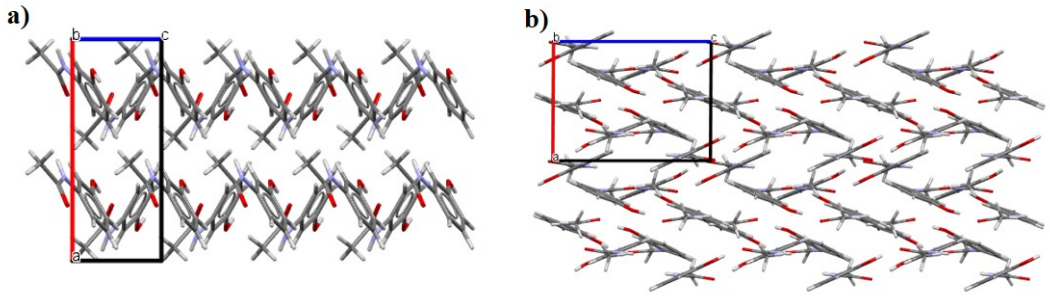

Figure 4-3: The packing of metacetamol. a) metacetamol form I, a zig-zag-like arrangement, viewed along the b axis (CSD code: MENSEE). b) metacetamol form II, a layered arrangement, viewed along the b axis (CSD code: MENSEE04).

4.1.3 The influence of a second component, MCM, in the crystallisation of PCM

The mechanistic behaviour between PCM and MCM during crystallisation has been extensively studied in the literature. The influence of MCM on PCM has been described as a templating approach,[55,158,159] and as a blocking approach termed surface docking.[160]

4.1.3.1 A templating approach

A template can be defined as a structurally similar molecule that influences the structure of another molecule without being present in the final product. Template molecules are thought to aid the formation of metastable polymorphs by decreasing their free energy barrier of nucleation. The kinetics are enhanced which delivers a more favourable, higher, rate constant for production of the metastable form. The literature shows that template molecules with a lattice match to APIs have been reported to lower the energy barrier to nucleation due to favourable interactions between, in this case MCM and PCM-II's pre-nucleation aggregate.[161]

Thomas et al (2011)[158] first proposed a templating mechanism between PCM and 4-halobenzoic acids as a multi-component system. It was suggested that the template molecule altered the solution environment. Agnew et al in 2016-17[55,159] developed the templating approach with the structurally-similar MCM molecule, further suggesting that the template molecule affected the solution-mediated phase transition that would occur in a single component cooling crystallisation with PCM. However, it was noted that "the mechanism of this templating process is unknown".[55]

Previously, MCM was studied in relation to its effect on the morphology of PCM by Hendriksen et al, (1998)[162] Thompson et al (2004)[163] and Saleemi et al (2013).[164] All three authors reported that small amounts of MCM (1-4wt%) acted as an inhibitor when added to PCM crystallisations. The structurally similar additive, MCM, influenced the nucleation and crystal growth process of PCM.[162–164] Moreover, an increased mole percentage of MCM reduced the nucleation time of PCM-I.[164]

4.1.3.2 A blocking approach

A recent study by Liu et al (2020)[160] described the impact of MCM as an additive molecule that inhibits crystallisation of the stable PCM-I phase. The evidence reported from adsorption simulations suggested that MCM is able to stabilise the formation of PCM-II by adsorbing onto the (011) face of PCM-I in the wrong orientation (displayed in figure 4-4). Thus, PCM-I growth units start to attach in the wrong orientation and growth along the 011 direction is blocked, influencing the overall crystal growth volumes. Increased amounts of MCM selectively inhibit the formation of PCM-I and allow the growth of PCM-II to dominate.

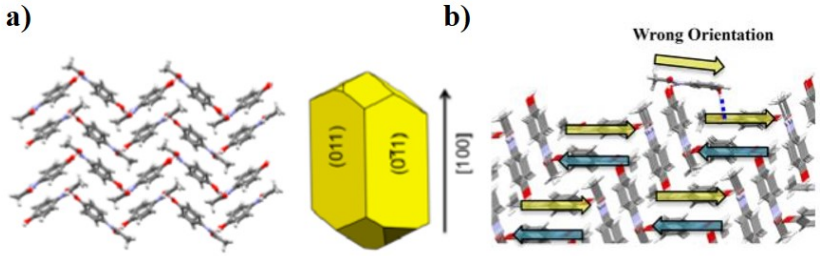

Figure 4-4: a) The 011 face of PCM form I. b) An example of MCM adsorbing onto the 011 face of PCM form I in the wrong orientation.
All images in this figure were taken from Liu et al.[160]

The findings of Liu et al[160] are relevant and in agreement with this work. It is reported that 5wt% of MCM slows down the formation of PCM-I, this inhibiting effect increases with the addition of MCM until an additive concentration of >25wt%, at which point the formation of PCM-II is found to be dominant and PCM-I was unable to grow and possibly nucleate. In a single component system without MCM, the growth rate of PCM-I was faster than PCM-II and therefore polymorphic form I dominated, as calculated from experimental growth volumes. The nature of this kinetic effect explains why PCM-II has been previously described as elusive (difficult to crystallise)[160,165] as a single component system.

Overall two mechanisms are discussed: 1) inhibition of nucleation, in which the emerging nucleus was disrupted;[162] and 2) blocking, adsorption of the solute PCM-I molecules is blocked.[160] Both of these mechanisms are in agreement and suggest that low concentrations of MCM have an impact on PCM's growth kinetics and high concentrations of MCM (>25wt%) impact the nucleation kinetics of PCM.

4.1.4 Polymorphic control of PCM with MCM

Previous studies have successfully isolated PCM-II through an additive approach in a batch[55] and continuous[159] cooling crystallisation platform. In both cases, a second component, MCM, was added to the crystallisation media and used as a template (or inhibitor) molecule; the purpose of a templating molecule is to isolate a desired solid form. Crystal engineering methods can be used as a method to choose a template molecule that is structurally similar (e.g. similarity in size and intermolecular interactions) to the first component. This templating approach offers a simple route to isolate PCM-II and overcomes the limitations of other isolation methods. Previous single component crystallisation techniques investigated for PCM-II

production, such as reaction coupling,[166] crash cooling crystallisation[167] and heterogeneous nucleation,[161] suffered from poor control and a lack of scalability. To emphasise the potential of these approaches, other multi-component systems have been successful in the isolation of PCM-II, including benzoic acid derivatives[55,165] and polymer additives.[168] In this work polymorphic control of PCM was investigated both through a multiple-component templating approach with MCM and with PCM as a single entity.

4.1.5 PCM MCM co-crystallisation

As noted above, the multi-component system of PCM and MCM has previously been extensively studied, and the second component MCM described as interacting with PCM as a template,[55,159] an additive[163] and an inhibitor.[160] While it is clear from these studies that PCM and MCM interact when in solution, there have been no reports of co-crystal formation between the two components; a potential PCM-MCM co-crystal is yet to be discovered and can be regarded as an elusive solid form.

4.2 Experimental information

PCM was obtained from Sigma Aldrich, MCM from Tokyo Chemical Industry and iso-propanol (IPA) from VWR.

4.2.1 Gaining polymorphic control of paracetamol (PCM)

4.2.1.1 Electrospraying experiments

The effect of electrical confinement as a method of gaining the elusive PCM-II as product was investigated with PCM as a single component (experiments 01-03, table 4.2) and in multi-component co-crystallisations with MCM (experiments 04-14, table 4.2). A range of molar compositions of PCM and MCM, with a total weight of 0.75 g, were dissolved in 13 mL of IPA and water (4:6). The influence of crystallisation parameters, E-field, flow rate, stoichiometric ratios of components, solvent and concentration were explored. The polymorphic form obtained for each experiment was characterised by PXRD; the traces are available in the Appendix (figure 9-1 displays PCM-II patterns and figure 9-2 displays PCM-I patterns).

Table 4.2: An investigation into how electrical confinement and second component MCM influences polymorphism in PCM.

experiment	**PCM MCM ratio**	**flow rate** (mL h^{-1})	**E-field** (kV cm^{-1})	**polymorphic form**
01[a b c]	100 : 0	0.5	1.0	PCM-I
02[b]	100 : 0	0.5	1.10	PCM-I
03[b]	100 : 0	0.25	1.30	PCM-I
04[b]	75 : 25	0.5	1.00	PCM-I
05[b]	75 : 25	0.15	1.00	PCM-I
06[b]	75 : 25	0.5	1.30	PCM-I
07[b]	75 : 25	0.15	1.30	PCM-II
08[b]	75 : 25	0.25	1.30	PCM-II
09[b]	75 : 25	0.25	1.29	PCM-II
10[b]	75 : 25	0.25	1.25	PCM-I
11[b]	90 : 10	0.25	1.30	PCM-I
12[b]	85 : 15	0.25	1.30	PCM-I
13[b d e]	50 : 50	0.15	1.30	PCM-II
14[b]	50 : 50	0.25	1.30	PCM-II

a) solvent system = water b) binary solvent system = IPA and water (4:6) c) solvent system = IPA d) saturated solution e) undersaturated solution.

4.2.1.2 Confinement crystallisation

Confinement crystallisation was used to gain an insight into the individual role of confinement within electrospraying, eliminating the effect of an E-field that is present in the full electrospraying method. Ideally, the method of spray drying would have been used to achieve a confined crystallisation environment in absence of an E-field. Unfortunately, suitable equipment was not available for use and an in-house set up was created as an alternative. A 50 μm stainless-steel sieve from Endecotts (certified to align to the ISO3310-1 specification) was fixed inside the electrospray environmental chamber (figure 4-5). The chamber was set to the same temperature (40^{o}C) and humidity (30 %RH) as when used in electrospraying experiments. Confinement crystallisation experiments were conducted under the same electrosprayed conditions as experiment 08 (table 4.2), but without the supply of voltage being applied.

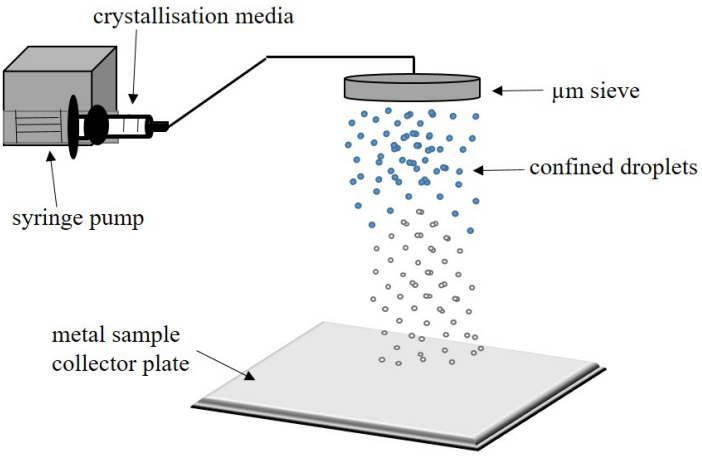

Figure 4-5: The confinement crystallisation set up.

4.2.1.3 Evaporative crystallisation

A crystallisation solution was prepared which consisted of 0.31 g of PCM and MCM (25 w/w%, MCM) dissolved in 3.5 mL of a 4:6 binary IPA:water solvent mixture. The solution was placed into 7 mL glass vials with ten small holes pierced into the vial lids, to ensure slow evaporation of the solvent. The vials were placed into hotplates set at 40^{o}C and left to crystallise.

4.2.1.4 Mechanical grinding

PCM and MCM (0.31 g, 25 w/w%, MCM) were placed into a cryomill for 30 minutes with a 5 mm metal ball at a frequency of 30 s^{-1}.

4.2.2 Co-crystallisation of PCM and MCM

4.2.2.1 Solubility measurements

The solubility curve was measured for a 1:1 mixture of starting materials (PCM and MCM, in the binary IPA and water (4:6) system) by gravimetric methods, as described in the general experimental section 3.2.1.1. The resultant solubility curve is available in the Appendix (figure 9-5) and was used in the design of electrospraying, evaporative, vapour diffusion and slurrying experiments.

In addition, the solubility curve of the PCM-MCM co-crystal, discovered in this work (see below), was measured in IPA and water (4:6). The solubility curve of PCM and MCM, as single entities, were measured in IPA and water (4:6) to allow for the solubilities of each system to be compared. Observational methods, as described in the general experimental section 3.2.1.2, were used to determine the solubility of each form. The solubility curve of the PCM-MCM co-crystal is shown in figure 4-6 (black) and was used in the design of seeded cooling crystallisation experiments, alongside the MSZW.

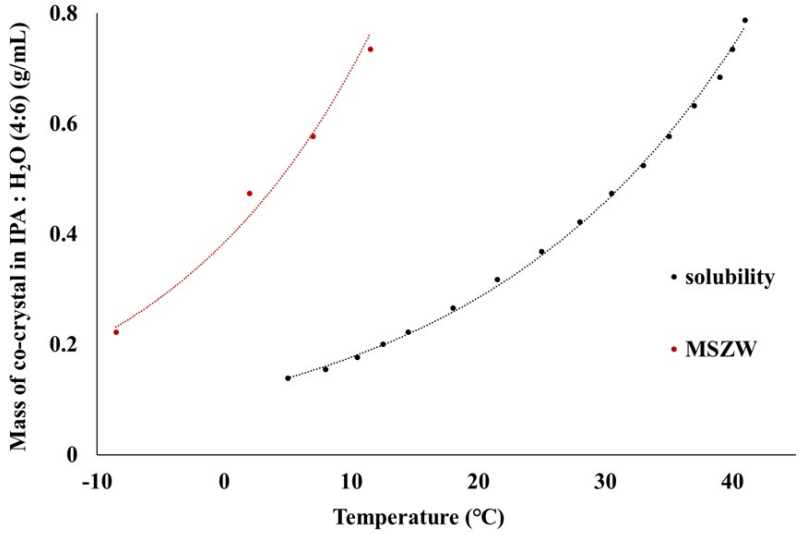

Figure 4-6: The measured solubility curve (black) and MSZW (red) for the PCM-MCM co-crystal in IPA and water.

4.2.2.2 Metastable zone width (MSZW) measurements

The MSZW of the crystallisation solution, used to crystallise the PCM-MCM co-crystal through crystal seeding, was determined with a working volume of 5 mL, in IPA and water (4:6), in a 7 mL sealed glass vial. The mass of the starting components (PCM-MCM, 1:1) was based on the measured solubility curve of the co-crystal. Four different saturation temperatures were studied (15, 30, 35 and 40^{o}C) to gain a curve that resembled the MSZW limit for this system. The starting components were added to the solvent system at the same time and the system was heated to 10^{o}C above the saturation temperature. The system was held for 10 minutes under a magnetic bottom stirring rate of 700 rpm to ensure full dissolution. The stirring was turned off and the solution was cooled at a controlled rate of 1^{o}C min^{-1} until the first instance of spontaneous nucleation was observed. At the point of observed nucleation, the

crystallisation was stopped and the resultant product was filtered, dried and characterised by PXRD to identify the solid forms present (figure 9-6 in the Appendix). A mixture of PCM-I, PCM-II, MCM-I and MCM mono-hydrate was observed in the isolated products. The temperature of nucleation was recorded for the known concentration of sample and two repeats were conducted for each sample at each temperature to calculate an average value. Figure 4-6 shows the measured MSZW of the co-crystal in red.

4.2.2.3 Electrospraying experiments

The effect of electrical confinement on samples comprising different compositions of PCM and MCM (100:0, 90:10, 75:25, 50:50, 25:75, 10:90, 0:100 % of each component) were investigated. All process parameters were kept constant; a flow rate of 0.5 mL h^{-1} and an E-field of 1.30 kV cm^{-1} were used for each experiment at a set temperature of 40^oC. The crystallisation media of each experiment contained a total solid weight of 0.75 g dissolved in 13 mL of IPA and water (4:6).

4.2.2.4 Evaporative crystallisation

A saturated solution of 3.5 mL (at 40^oC) of PCM and MCM (1:1) in a binary solvent system of IPA and water (4:6) was placed into 7 mL glass vials with ten small holes pierced into the vial lids, to ensure slow evaporation of the solvent. The vials were placed into hotplates set at 40^oC and left to crystallise.

4.2.2.5 Cooling crystallisation

A solution of 5 mL, containing PCM and MCM (1:1) in a binary solvent system of IPA and water (4:6) was placed into a sealed 7 mL glass vial. The concentration of solution was saturated at 40^oC and was based on the measured solubility curve of the PCM-MCM co-crystal. The solution was heated to 10^oC above the temperature of saturation and held for 10 minutes, stirred at 700 rpm. The stirring was turned off and the solution was cooled at 1^oC min^{-1} in accordance to the stepped cooling profile in figure 4-7. The crystallisation solution was left to dwell for 72 h after reaching a temperature of 4^oC.

4.2.2.6 Seeded cooling crystallisation

A solution of 5 mL, containing PCM and MCM (1:1) in a binary solvent system of IPA and water (4:6) was placed into a sealed glass 7 mL glass vial. The concentration of solution was saturated at 40^oC based on a measured solubility curve of the PCM-MCM co-crystal. The solution was heated to 50^oC at a rate of 1^oC min^{-1} and held for 10 minutes under a magnetic bottom stirring rate of 700 rpm. Upon complete dissolution the stirring was switched off and the solution was cooled to 40^oC at a rate of 1^oC min^{-1} and held for 1 h. The solution was then cooled to 30^oC at a rate of 1^oC min^{-1} and held for 2 h. Crystal seeds were added to the solution after 1 h. A crystal seeding temperature of 30^oC was chosen based on the measured MSZW of the co-crystal. At this point, the supersaturation level is low, secondary nucleation is minimal, and crystal growth is favored. These conditions favor the growth of larger single

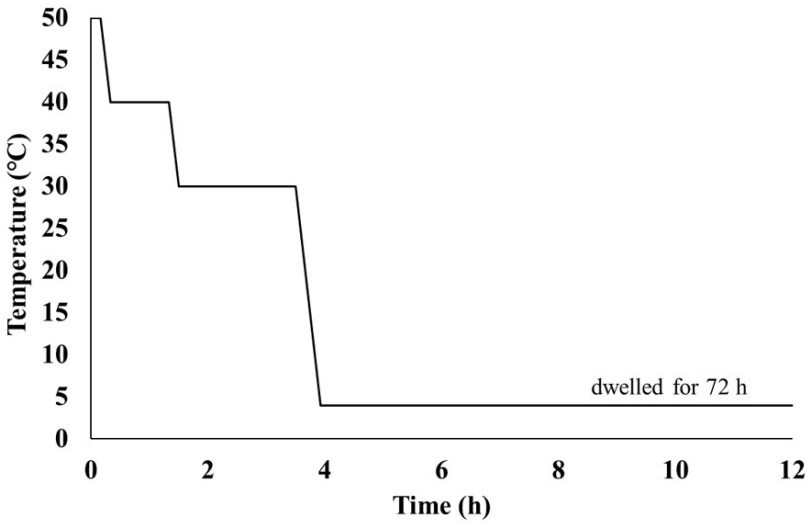

Figure 4-7: The cooling profile used in cooling crystallisation experiments.

crystals, suitable for characterisation by SCXRD. After seed addition the solution was cooled to a temperature of either 15^{o}C or 4^{o}C at a rate of 1^{o}C min^{-1} and left to dwell for up to 144 h. Figure 4-7 shows the seeded cooling profile utilised. A stainless-steel sieve from Endecotts, certified to align to the ISO3310-1 specification, was used to prepare crystal seeds from the electrosprayed co-crystal. A variety of crystal seed sizes were tested (25-150 μm) alongside different seed loadings (0.5-5%).

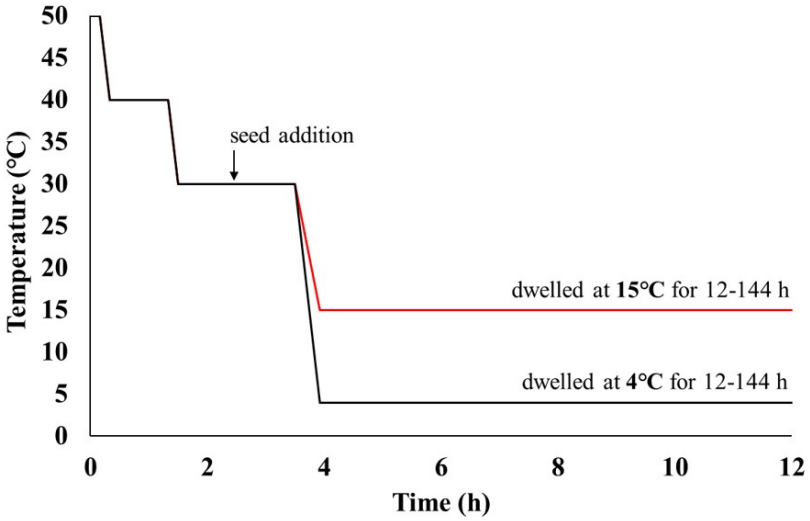

Figure 4-8: The cooling profile used in crystal seeding experiments.

4.2.2.7 Vapour diffusion

A 0.7 mL solution, saturated at 40^{o}C, containing PCM and MCM (1:1), dissolved in IPA and water (4:6), was placed into a 1 mL glass vial. Sonication in a temperature-controlled water bath set at 40^{o}C was used to aid dissolution. The 1 mL glass vial was left unsealed and placed inside a larger sealed glass vial. The larger glass vial contained hexane (anti-solvent); the level of hexane was raised above the level of the solvent in the 1 mL vial but did not enter it. The

large glass vial was sealed and was left to crystallise in a hotplate set at 40^{o}C.

4.2.2.8 Solution-mediated crystallisation (slurrying)

A solution containing an excess amount of PCM and MCM (1:1) in a binary solvent system of IPA and water (4:6) was stirred at 700 rpm and left at 40^{o}C for 2 weeks. A sample of the solution was taken after 1 day, 3 days, 7 days and 14 days to monitor the crystallisation media.

4.2.2.9 Mechanical grinding

A 1:1 mixture of PCM and MCM was used for grinding experiments. Neat grinding experiments were carried out manually with a pestle and mortar, LAG experiments followed the same procedure with the addition of two drops of solvent.

4.2.3 Single crystal structure determination of the new PCM-MCM multi-component complex

Single crystals of the new multi-component molecular complex, the PCM-MCM co-crystal, were formed under seeded cooling crystallisation. The crystal structure was characterised by SCXRD; the structure was solved with direct methods using SHELXS-2013[143] and refined with SHELXL-2015[144] with the software package Olex2.[145] Table 4.3 displays the crystallographic data for the complex.

Table 4.3: The unit cell and refinement parameters of the PCM-MCM co-crystal.

complex code	**PCM-MCM co-crystal**
formula	$C_{16}H_{18}N_2O_4$
g mol^{-1}	302.32
T (K)	150 (2)
radiation	Mo Kα($\lambda = 0.71073$)
2θ range (^{o})	5.81 - 58.73
crystal system	orthorhombic
space group	Pbca
a (Å)	13.3570(4)
b (Å)	13.7805(5)
c (Å)	16.4780(5)
$\alpha(^o)$	90
$\beta(^o)$	90
$\gamma(^o)$	90
volume (Å^3)	3033.04(17)
Z	8
density (g cm^3)	1.324
$\mu(mm^{-1})$	0.096
completeness (%)	99.9
reflections collected	25754
independent reflections	3813
data/restraints/parameters	3813/0/226
R int	0.0433
GooF	1.070
R_1 (obs)	0.0532
R_1 (all)	0.0765
wR_2 (all)	0.1132
$\rho_{max,min}$ (e Å^{-3})	0.28, -0.24

4.3 Gaining polymorphic control of paracetamol

This section identifies the key factors that were found to have an influence on the selective formation of the metastable form of PCM (PCM-II). The influence of crystallisation parameters, a confined environment and an E-field during electrospraying, on the formation of PCM-II is discussed in section 4.3.1. In addition, reference crystallisation methods (evaporative crystallisation and neat mechanical grinding) were investigated under similar conditions to ensure that the formation of PCM-II was solely induced by electrical confinement, discussed in section 4.3.2. The bulk material of PCM-II gained from electrospraying is analysed and the stability and reproducibility of the metastable form is discussed in section 4.3.3.

4.3.1 An investigation into the key factors that influence the formation of PCM-II during electrospraying

4.3.1.1 The influence of crystallisation parameters

Polymorphic control in PCM was successfully achieved with the electrospray set-up using a multi-component templating approach with MCM. It was found that a template molecule was needed to stabilise the formation of PCM-II. The formation of PCM-I was observed for all experiments that utilised PCM as a single component (experiments 01-03 in table 4.2). This study successfully identifies the parameters that influence the formation of PCM-II during electrospraying. A methodology was developed that could predict the selective formation of either PCM-II or PCM-I under a range of conditions; this allows for polymorphic control of PCM with a templating approach. Table 4.4 contains a summary of the parameter ranges found to isolate PCM-II, the formation of PCM-I results when one or more of the parameter ranges are not met.

Table 4.4: The experimental parameter ranges required for the isolation of PCM-II.

experimental parameter	**parameter range**
flow rate	$\leq$ 0.25 mL h^{-1}
weight % metacetamol	$\geq$ 25%
E-field	$\geq$ 1.29* - 1.30 kV cm^{-1}
saturation of solution	no effect

* trace amounts of PCM-I were observed alongside PCM-II under an E-field of 1.29 kV cm^{-1}. This data was obtained from experiments 01-14 in table 4.2.

Slower flow rates with a maximum of 0.25 mL h^{-1} and a large E-field of at least 1.30 kV cm^{-1} stabilised and isolated PCM-II. A system with reduced flow rates and a higher E-field affords a higher level of confinement in a droplet produced and a more concentrated charge surrounding the droplet's surface. The quantity of MCM required to stabilise PCM-II, of at least 25%, is in strong agreement with the findings of Liu et al.[160] The presence of smaller weight % quantities of MCM merely slows down the formation of PCM-I; larger concentrations of at least 25% are needed to inhibit the formation of PCM-I.

It can be postulated that the kinetics and thermodynamics of formation of metastable PCM-II are favored under the electrical confined conditions outlined in table 4.4 due to a combination of

the parameters: 1) a larger surface-to-volume ratio of the crystallisation media (nano-droplets); 2) the formation of droplets with a high surface charge; and 3) a stabilising effect gained from the second component (MCM) during nucleation.

4.3.1.2 The influence of confinement

In order to study the influence of the confinement component within electrical confinement, pure confinement crystallisation experiments in the absence of electric field were conducted to detach any effects that are influenced by the E-field alone. It was found that confinement crystallisation successfully afforded PCM-II. However, trace amounts of PCM-I were also observed in the PXRD pattern alongside MCM. It is well known that in the presence of PCM-I, PCM-II is unstable and transforms into the thermodynamically stable form. As expected, PCM-II obtained from confinement crystallisation alone was not stable due to the presence of the thermodynamic polymorphic form in the product material. The bulk material was monitored by PXRD and clear Bragg reflections for PCM-I were observed after eleven days. Figure 4-9 shows the PXRD patterns of the material after zero and eleven days; the blue boxes show Bragg reflections for PCM-II, the green boxes MCM-I and the red boxes PCM-I. After zero days, trace amounts of PCM-I were observed close to the background of the pattern, however they are not visible in the figure. After eleven days, visible Bragg reflections for PCM-I are observed. It is clear that PCM-II is not stable in the product mixture from the confinement-only experiment and slowly converts into the more thermodynamically stable form, PCM-I.

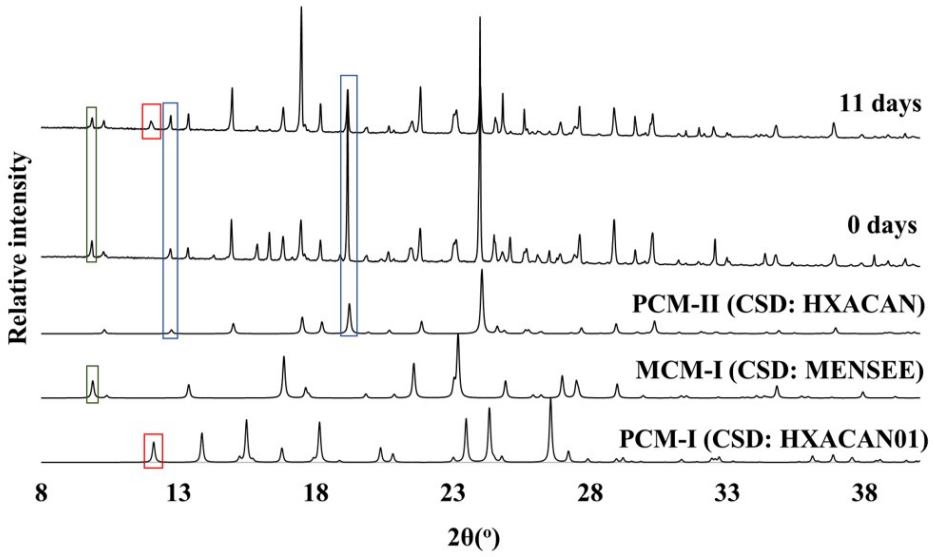

Figure 4-9: The PXRD patterns of the bulk material from confinement crystallisation monitored after zero days and eleven days. The blue boxes show Bragg reflections for PCM-II, the green boxes MCM-I and the red boxes PCM-I.

This study provides evidence that confinement plays an important role in polymorphic control of PCM under electrospraying. However, confinement crystallisation alone was unable to achieve polymorphic control of PCM. Pure PCM-II was not isolated without the presence of PCM-I as an impurity. This is particularly problematic as the results confirm previous findings that trace amounts (seeds) of the thermodynamic polymorph can induce a solid mediated

polymorphic transition from PCM-II to PCM-I. Confinement crystallisation may have yielded PCM-II, however the product was unstable. As will be seen below, the extra energy available in the additional presence of electrical confinement ensures there is no PCM-I present in the material to catalyse the PCM-II to PCM-I conversion; electrosprayed PCM-II was found to be stable for at least one year, see section 4.3.4.

It can be argued that a confined environment of ≈50 μm gained under confinement crystallisation is not a direct comparison to the nano-scale confined environment achieved with electrospraying. Nevertheless, studies in the literature suggest that a nano-confined crystallisation environment under mild temperatures and atmospheric pressure cannot in itself stabilise PCM-II. Rengarajan et al[169] were successful in the formation of PCM-II from melt crystallisation methods in nanoporous glasses (approximately 43 nm pore diameter). However, to obtain PCM-II under nano-confinement harsh conditions were required; five thermal cycles between 90 and 120^{o}C were required for the selective formation of PCM-II. The addition of extra energy (in the form of heat) was thus an additional factor required to obtain PCM-II, alongside a nano-confined environment. In electrospraying as described below, the additional energy comes from the presence of an electric field at mild temperatures.

4.3.1.3 The influence of an electric field

Two electric fields are formed in the electrospray set-up, illustrated in figure 4-10. The first is an external E-field (E_{ex}), formed between the metal emitter and sample collector plate. At the start of electrospraying, neutral droplets elongate along the field's axis and form a spheroidal shape. When the critical E_{ex} is reached (corresponding to the Taylor limit) a confined jet consisting of nano-droplets is formed.[43,44] The second is an internal E-field inside each droplet (E_{in}). The E_{in} produced is dependent on the droplet's diameter and therefore E_{ex}. At a constant voltage, an increased droplet diameter will afford a decreased E_{in}. The crystallisation solution's geometry is altered by an E-field and directly influences the surface energy of the confined system.

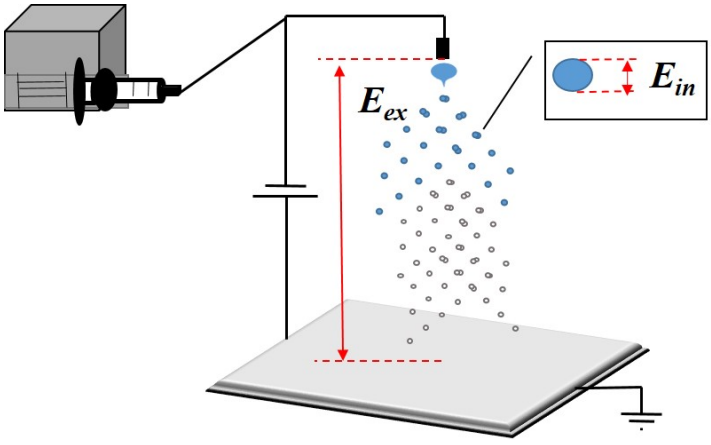

Figure 4-10: An illustration of the two electric fields formed under electrical confinement with the electrospray set-up.

Each nano-droplet contains an E_{in} that is able to influence a material's orientation and mo-

bility inside a droplet at the molecular level. Both PCM and MCM contain positive and negative dipolar constituents; the positively charged dipoles are thought to align towards the droplet's core whilst the negatively charged dipoles migrate towards the positively charged droplet surface. This would lead to a change in the droplet's surface free energy, since charged groups would reside at the surface of the liquid. This hypothesis is supported by a molecular dynamics simulation study conducted by Dr Carmelo Herdes from the University of Bath. The simulations conducted by Dr Herdes were designed to mimic the experimental parameters from experiments that afforded PCM-II in this chapter. Dr Herdes found that under an electrical confined crystallisation environment the molecular mobility is significantly altered. Confinement was found to play a key role within electrical confinement; when an E-field was applied to an unconfined environment no change in molecular mobility or the orientation of PCM and MCM was observed. The results from the study conducted by Dr Herdes have been published.[47]

4.3.2 Benchmark crystallisation methods

To confirm further that the electrical confinement combination utilised in the electrospray experiment was critical in enabling the formation of PCM-II (in pure form) in these experiments, reference crystallisation methods (evaporative crystallisation and neat mechanical grinding) were investigated under similar crystallisation conditions (see experimental section 4.2.1) and the polymorphic form of PCM identified; the polymorphic form for each method was characterised by PXRD. Figure 4-11 shows the patterns obtained from samples produced from each method. The blue box highlights the presence or absence of Bragg reflections for MCM-I, the green box PCM-II and the red box PCM-I.

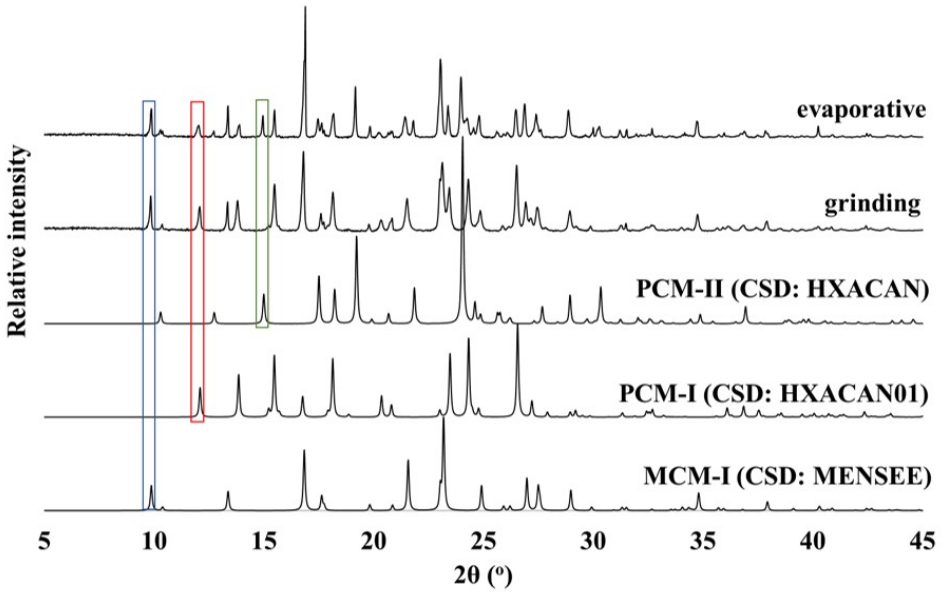

Figure 4-11: The PXRD patterns from reference crystallisation methods, evaporative crystallisation and neat mechanical grinding.

A concomitant mixture of PCM-I, PCM-II and MCM was found under evaporative crystallisation. Previous studies in the literature have shown that PCM-I is formed at the bulk of an

aqueous solution, while PCM-II is formed around the edge of the reactor or the meniscus.[170] The edge provides higher concentrations of PCM due to an increased evaporation rate, caused by a concave meniscus, providing a possible explanation to why PCM-II nucleated around the edge. Similarly, electrical confined droplets produce a convex configuration (according to the Taylor limit)[43,44] which could drive the nucleation of PCM-II at the droplet surface, while MCM plays a role in inhibiting the formation of PCM-I. Only PCM-I and MCM were found under neat mechanical grinding, therefore, a structural rearrangement from the starting material was not induced.

4.3.3 Analysis of the bulk material

The bulk material of PCM-II formed under electrospraying (the product from experiment 08 in table 4.2) was characterised by PXRD, DSC, ^{1}H NMR spectroscopy and SEM. The selective formation of PCM-II was confirmed by PXRD; Bragg reflections were solely observed for the metastable form II, highlighted with red boxes in figure 4-12.

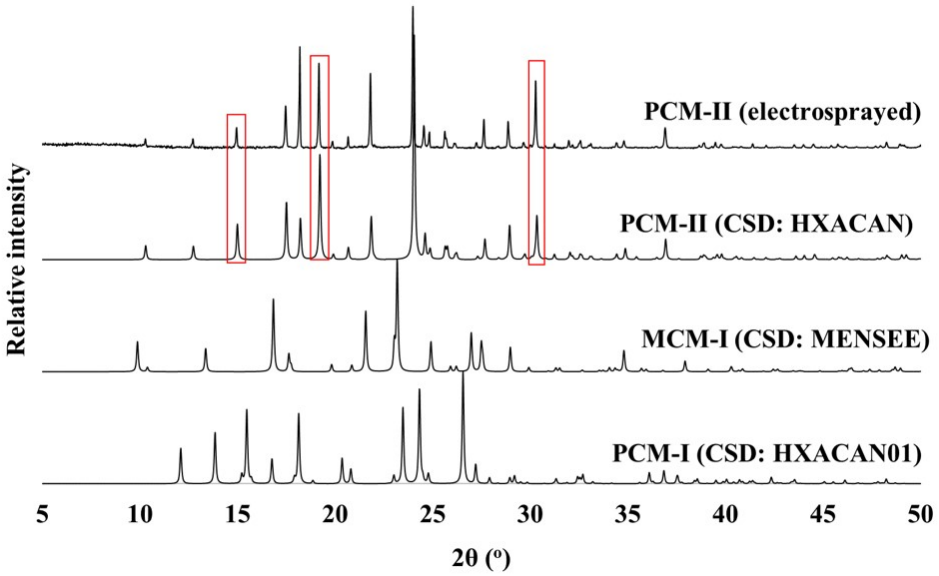

Figure 4-12: The PXRD pattern of electrosprayed PCM-II.

A single endotherm was observed in the DSC trace and the melting point of the material was found to be close to 150^{o}C (onset). This confirmed the formation of PCM-II which is reported to have melting endotherm onset of 140-150^{o}C with a 'small shoulder peak observed'.[171] The DSC traces of PCM-II and PCM-I (onset= 169^{o}C)[171,172] are displayed in figure 4-13.

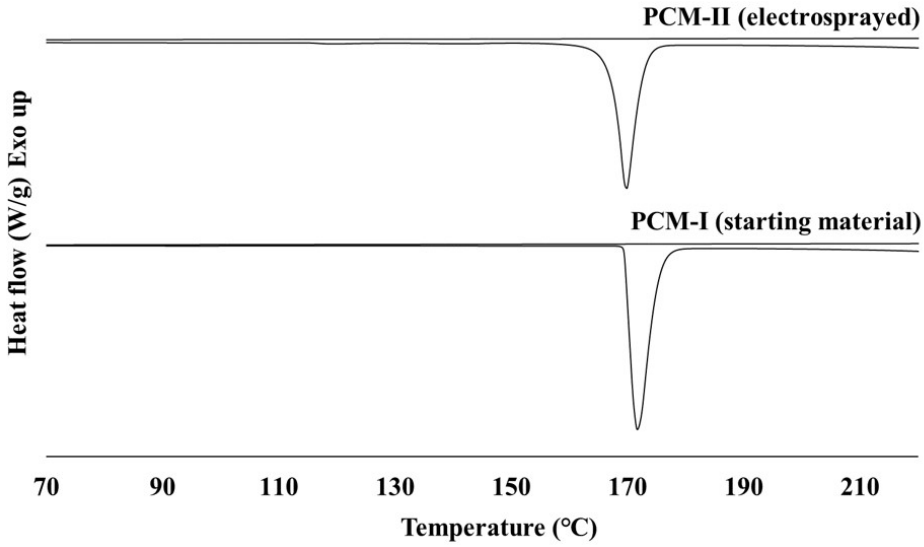

Figure 4-13: The DSC trace of electrosprayed PCM-II (onset= 155^{o}C) and the starting material used corresponding to PCM-I (onset= 169^{o}C).

MCM was not observed in the PXRD pattern. However, it was detected via ^{1}H NMR spectroscopy (figure 4-14). A 3:1 multi-component ratio of PCM and MCM was found in the product by peak integration (figure 9-3 in the Appendix) and it was concluded that MCM may have turned amorphous under electrical confinement, as a consequence not being evident in the PXRD.

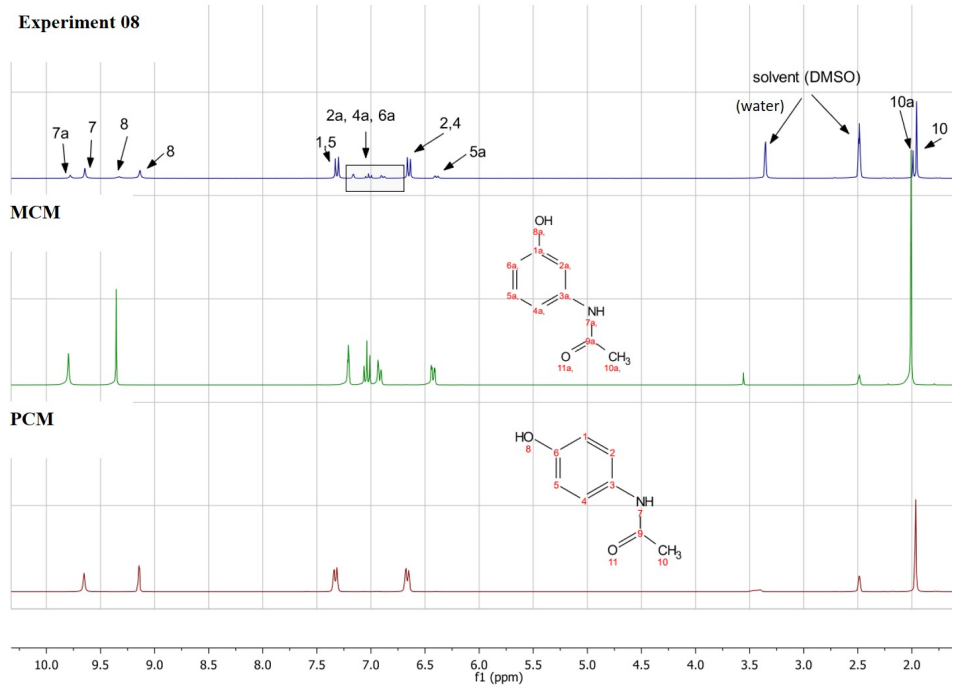

Figure 4-14: The ^{1}H NMR spectrum of electrosprayed PCM-II compared to the spectrum of PCM and MCM gained from starting material in DMSO (d6).

The bulk material of electrosprayed PCM-II was further characterised by SEM (figure 4-15). The electrosprayed material showed an irregular plate-like precipitate with particles that were prone to agglomeration. The topography appeared to be rough and porous, with visible voids, an "imperfection" that may reside from an inter-phase boundary of crystallising solid particles separated by regions of solvent pockets that migrate through diffusion, resulting in a vacancy within the solid material. The electrosprayed PCM-II material was thus found to be significantly different to the starting material (PCM-I), for which a tabular morphology was found with a smooth surface.

Interestingly, the literature reports a different morphology for PCM-II. When the product was crystallised as a single component, a needle shaped habit is observed.[168,173] Moreover, when PCM-II was formed under cooling crystallisation with MCM a rhombic habit was reported.[159] The habit observed here demonstrates that electrospraying is a technology capable of influencing the morphology and hence an important CQA of a material, a factor that is important in crystal engineering for desirable downstream processing properties.

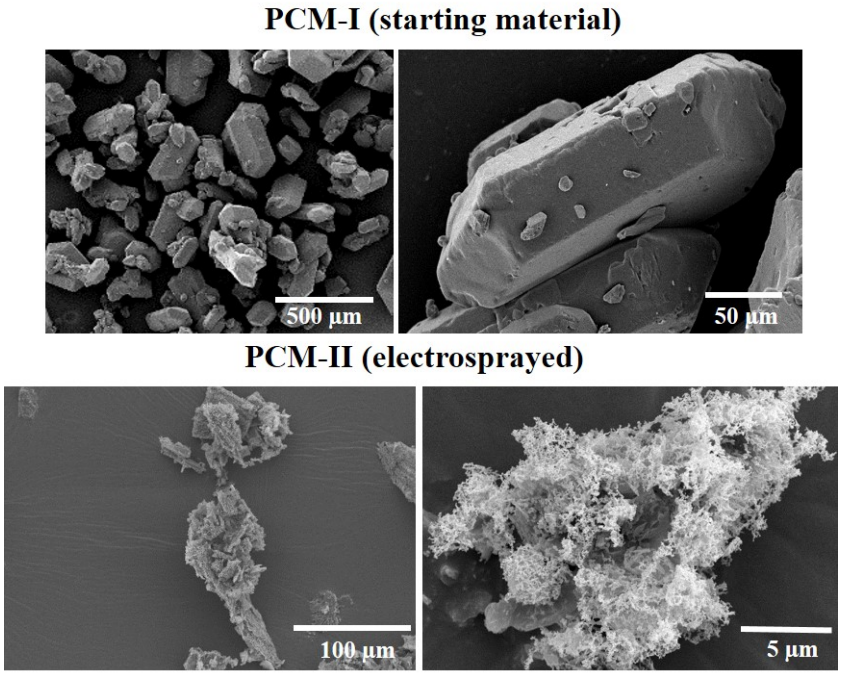

Figure 4-15: Images from SEM analysis of electrosprayed PCM-II and starting material.

4.3.4 Stability and reproducibility studies

The metastable form, PCM-II, was successfully reproduced three times under identical experimental conditions with electrospraying (figure 9-4 in the Appendix). Electrosprayed PCM-II was found to be stable at room temperature and atmospheric pressure for at least one year (figure 4-16). No signs of polymorphic transformations into the thermodynamically stable form were observed by PXRD during the time-frame of 0 to 12 months. The stability of electrosprayed PCM-II suggests the formation of only PCM-II in the bulk material, and specifically the absence of PCM-I to avoid a polymorphic transformation into the thermodynamically stable form.

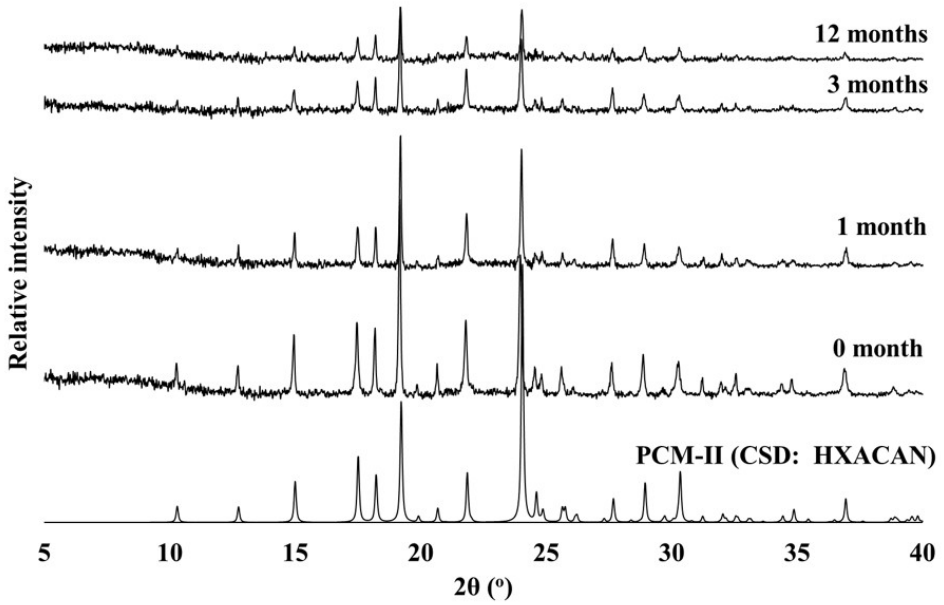

Figure 4-16: The PXRD patterns of electrosprayed PCM-II shown to be stable for up to 12 months.

4.4 Electrospraying vs other crystallisation methods for the co-crystallisation of PCM and MCM

4.4.1 Co-crystallisation by electrospraying

The effect of electrical confinement on crystallisation media containing different stoichiometric ratios of the two components, PCM and MCM, was investigated. The solid form crystallised and the crystalline quality of the material was studied. Table 4.5 contains a summary of the results. The bulk material from each experiment was characterised by PXRD (figure 4-17). It was discovered that electrospraying facilitated the amorphisation (the process of making a material structurally amorphous) of either PCM or MCM, a factor which was found to be dependent on the stoichiometric ratio of components present. In addition, a novel, crystalline form was discovered in these experiments. The new form was identified as a multi-component co-crystalline complex that contained PCM and MCM; the full characterisation of the complex is discussed in section 4.5.

Table 4.5: An investigation into how electrical confinement and different stoichiometric ratios of PCM and MCM influence the solid form and crystalline quality of product material.

experiment	MCM (%)	PCM (%)	solid form observed via PXRD
15	100	0	MCM-I
16	90	10	MCM-I
17	75	25	MCM-I, co-crystal
18	50	50	co-crystal
19	25	75	PCM-I
20	10	90	PCM-I
21	0	100	PCM-I

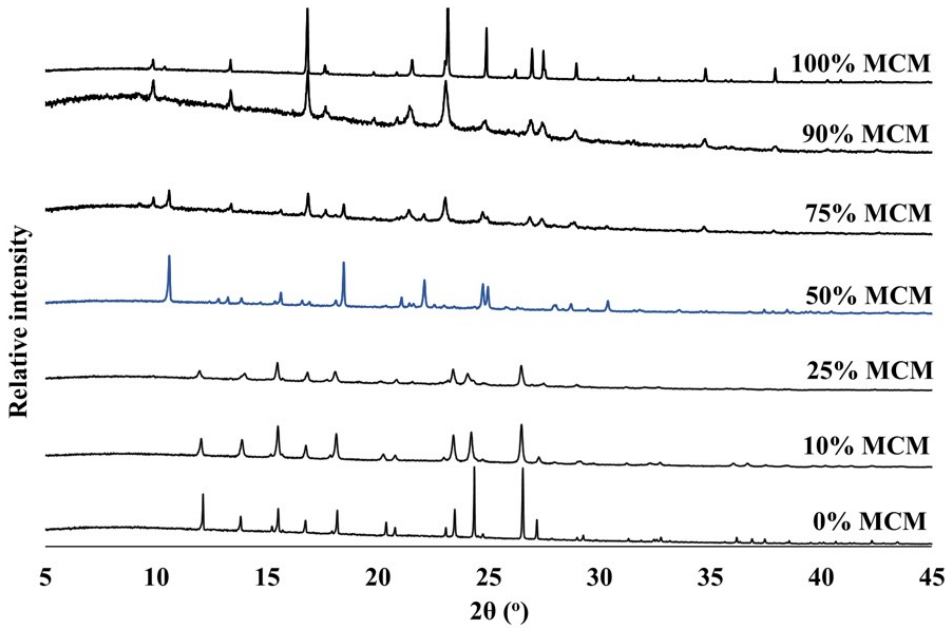

Figure 4-17: The PXRD patterns of electrospraying of experiments 15-21 in table 4.5. The pattern of a new solid form is highlighted in blue.

The selective isolation of this newly discovered solid form was successfully achieved from a 50:50 multi-component ratio of PCM and MCM (experiment 18). The new solid form was also observed in experiment 17, from a multi-component ratio of 75:25, however, the material was found to be impure and contained starting material. An interesting phenomenon was observed in experiments 16, 19 and 20. Bragg reflections for PCM-I were solely observed for experiments 19 and 20 that used low loadings of MCM (10-25%). In-contrast, Bragg reflections for MCM-I were solely observed for experiment 16 with a higher loading of MCM (90%). Further analysis by ^{1}H NMR spectroscopy confirmed that both PCM and MCM were present in the material for each experiment in table 4.5 (figure 9-10, 9-11 and 9-12 in the Appendix). From this finding, it seemed that a higher loading of MCM stabilised the amorphisation of PCM and vice versa.

The material from each experiment was characterised by DSC to investigate the thermal behaviour of the seemingly amorphous material. There are no reports of a glass transition temperature (T_g) for MCM in the literature, however, PCM is reported to have a T_g of 23^{o}C.[174] No T_g endotherm was observed in the DSC traces that would correspond to amorphous PCM (around 23^{o}C) or amorphous MCM, in the studied temperature range between -15 and 200^{o}C. The DSC traces for each experiment are available in the Appendix (figure 9-13). Interestingly, although no sign of co-crystal formation was observed in the PXRD trace of experiment 19, evidence of the presence of the co-crystal form was suggested by DSC. Figure 4-18 shows the DSC trace of experiment 19 (25% MCM) compared to the trace of experiment 18 (50% MCM) and experiment 21 (100% PCM). A small endotherm at 104^{o}C is observed (highlighted in red) for experiment 19. This suggests that trace amounts of co-crystal may be present in the crystalline state or as a poorly crystalline form. Re-crystallisation (highlighted in blue) is then observed in the trace of experiment 19, followed by the melting of PCM-I. The material was further analysed by HSM (figure 9-14 in the Appendix); trace amounts of material were observed to melt between 110 and 140^{o}C, followed by visible melting of the bulk material at 160^{o}C. In this case, re-crystallisation was not visible by HSM.

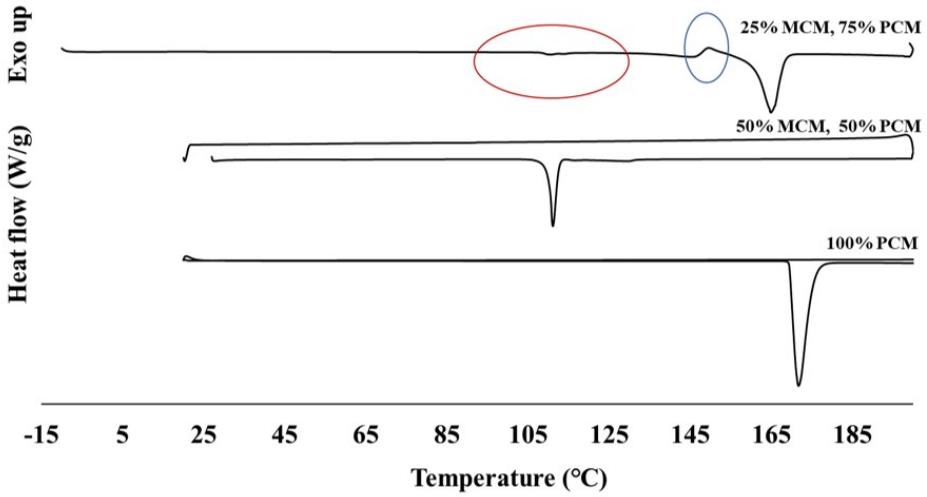

Figure 4-18: The DSC trace of experiment 19, showing a endotherm for the co-crystal (red) followed by re-crystallisation (blue) and the melting of PCM-I. The DSC trace of experiment 18 (50% MCM) and 21 (100% PCM) is shown for comparison.

4.4.2 Co-crystallisation by other crystallisation methods

The translation of co-crystal production was explored using several different crystallisation methods including cooling and evaporative crystallisation, slurrying, LAG, neat grinding and vapour diffusion. Table 4.6 contains a summary of the results. The material gained from each method was characterised by PXRD, apart from vapour diffusion, in which case no crystallisation occurred. No sign of co-crystal formation was observed for any of the crystallisation methods tested. Figure 4-19 displays the PXRD traces from each method; the absence of Bragg reflections characteristic of the co-crystal is highlighted in red.

Table 4.6: An investigation into different types of crystallisation methods, screened for the formation of the PCM-MCM co-crystal.

crystallisation method	solvent	solid forms observed
evaporative	IPA : water	PCM-I, MCM-I
cooling	IPA : water	PCM-I, PCM-II, MCM-I
vapour diffusion	IPA : water	-
slurrying	IPA : water	PCM-I, MCM-I
grinding	-	PCM-I, MCM-I
LAG	IPA	PCM-I, MCM-I
LAG	IPA : water	PCM-I, MCM-I

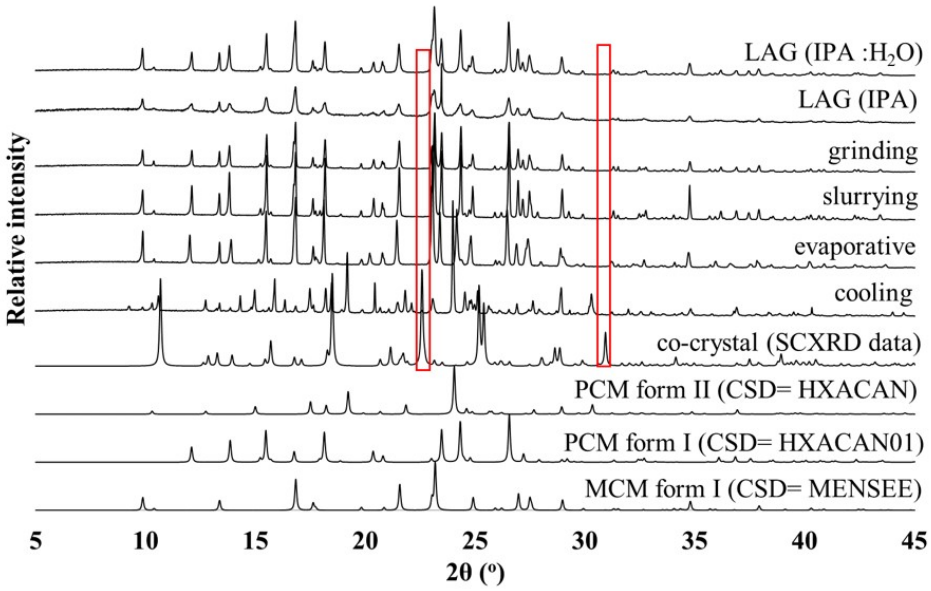

Figure 4-19: The PXRD traces from products of several different crystallisation methods targeting the formation of PCM:MCM co-crystal. The red box highlights the absence of characteristic co-crystal Bragg reflections in each material.

This study demonstrates that electrospraying is a technology capable of generating elusive solid forms that seem unobtainable by other crystallisation methods. However, it is important to be able to translate the formation of elusive solid forms into conventional crystallisation methods, such as a cooling crystallisation platform, for their large scale manufacturing. Crystal seeds from the elusive co-crystal gained under electrospraying were therefore used to investigate if co-crystal production is accessible in a seeded cooling crystallisation platform.

4.4.3 Translation of the electrosprayed co-crystal into a cooling crystallisation platform with crystal seeding.

Crystallisation trials were prepared with two objectives: 1) a method development study to identify the crystallisation parameters required for successful co-crystal formation; and 2) a seeding protocol to produce a single crystal of the co-crystal suitable for crystal structure determination by SCXRD methods.

Five crystallisation parameters were investigated to determine the optimal seeding protocol including seed size, seed loading, dwell time, dwell temperature and solvent; it should be noted that, importantly, these initial seeded experiments used seeds produced from the electrospray experiments. The material from each experiment was characterised by optical microscopy, to assess the crystallinity and crystal size for objective 2 (figure 9-7 in the Appendix) and PXRD, to identify the solid form(s) of a material for objective 1. All PXRD traces are available in the Appendix, including traces from experiments that show the influence of seed loading (figure 9-8) and seed size (figure 9-9). Table 4.7 summarises the results. The influence of each crystallisation parameter on the success or failure of co-crystallisation is discussed below.

Table 4.7: Cooling crystallisation experiments with the electrosprayed PCM-MCM co-crystal as crystal seeds.

seed size (μm)	**seed load** (%)	**solvent system**	**stir rate** (rpm)	**dwell time** (h)	**solid form(s) observed**	**single crystals**
influence of dwell time (held at 4^{o}C)						
150	2	IPA : water	x	12	MCM, PCM	-
150	2		x	24	co-crystal, MCM, PCM	✓
150	2		x	72	co-crystal	✓
influence of dwell temperature (held at 15^{o}C)						
150	2	IPA : water	x	48	co-crystal, MCM, PCM	✓
150	2		x	24	co-crystal, MCM, PCM	✓
150	2		x	144	MCM, PCM	-
influence of seed loading						
150	0	IPA : water	x	72	MCM, PCM, MCM-hy*	-
150	0.5		x	72	co-crystal	✓
150	1		x	72	co-crystal	✓
influence of solvent						
150	2	IPA	x	24	no product	-
150	2		700	24	co-crystal	x
influence of seed size						
100	2	IPA : water	x	72	co-crystal	✓
75	2		x	72	co-crystal, MCM, PCM	✓
50	2		x	72	co-crystal, MCM, PCM	✓
25	2		x	72	co-crystal, MCM, PCM	✓

*MCM-hy = MCM hydrate, CSD code KOTDUV.

4.4.3.1 The influence of dwell time and temperature on co-crystallisation.

Dwell time and temperature were found to have a significant influence on the formation and stabilisation of the co-crystal. The products from two co-crystallisation experiments were characterised by PXRD, one held at 4^{o}C and another held at 15^{o}C under the cooling profile shown in figure 4-8 in section 4.2.2.6. A seed size of 150 μm and a seed loading of 2% were used in a solvent system of IPA and water (4:6).

When the system is held at a dwell temperature of 4^{o}C, PCM and MCM initially crystallise as single phases and are observed after 12 h (Bragg reflections for PCM are highlighted in green and MCM in blue in figure 4-20). Co-crystal formation is then observed by PXRD after 24 h alongside starting material. Co-crystal formation continues over time and pure co-crystal is observed within 48 h at which point the co-crystal is stable in solution for at least 120 h (Bragg reflections for the co-crystal are highlighted in red in figure 4-20).

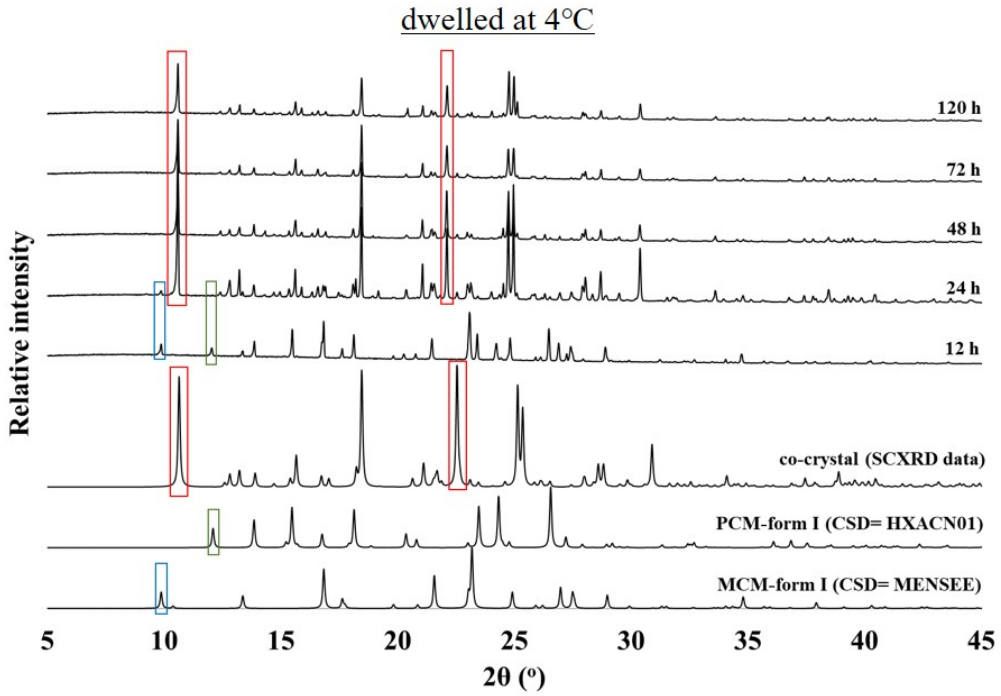

Figure 4-20: The PXRD traces of a monitored co-crystallisation experiment held at a dwell temperature of 4^{o}C. Bragg reflections for the co-crystal are highlighted in red, PCM in green and MCM in blue.

When the system is held at a dwell temperature of 15^{o}C, co-crystallisation occurs after 48 h; however, the co-crystal is unstable, recrystallising back into the starting material after 144 h, as shown in figure 4-21. In this figure, Bragg reflections for the co-crystal are highlighted in red, PCM in green and MCM in blue.

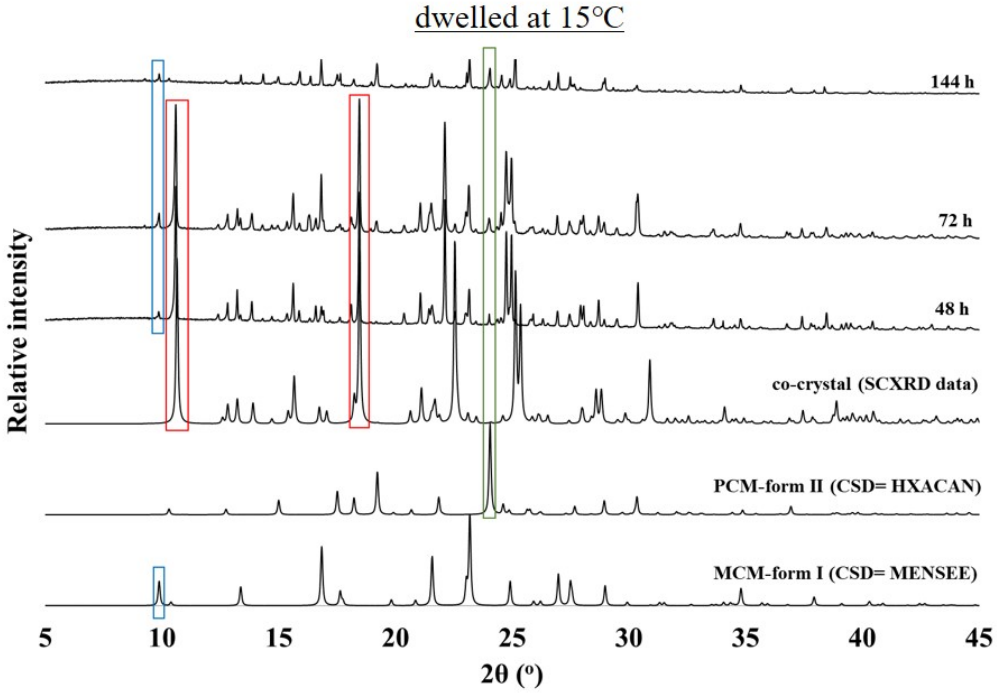

Figure 4-21: The PXRD traces of a monitored co-crystallisation experiment held at a dwell temperature of 15^{o}C. Bragg reflections for the co-crystal are highlighted in red, PCM in green and MCM in blue.

These results suggest that temperature plays a large role in stabilising co-crystal production. The results suggest that at 4^{o}C the energy barrier for co-crystallisation is decreased relative to that at 15^{o}C where both the kinetics and extent of co-crystallisation are limited. The temperature dependency for co-crystal formation implies that the thermodynamic and kinetic stabilities cross over with a temperature change. It is important to note that in each of the experiments mentioned above, the samples were in open air and not purged under nitrogen.

4.4.3.2 The influence of seed size and seed loading on co-crystallisation.

A crystal seed size of 100-150 μm, with a seed loading of 0.5-2%, was required to obtain a single crystal of the co-crystal without any impurities, in a solvent system of IPA and water (4:6) with a dwell time of 72 h. This suggests larger seed sizes that have a decreased surface-area-to-volume ratio are favored during co-crystallisation. Usually crystal seeds with a larger surface-area-to-volume ratio are desired to ensure the formation of small particles with a narrow distribution range. However, small particles can agglomerate and decrease the effect of surface area. Furthermore, a crystal seed's surface can easily become poisoned, from exposure to ambient air.[175] A poisoned surface would halt crystal growth at low supersaturation and could induce spontaneous nucleation of an unwanted form, in this case the additional formation of PCM and MCM as single entities, as observed here with a seed size range between 25 and 75 μm. Seed loading was not found to have a significant effect on the success or failure of co-crystallisation, in the explored range of 0.5-2%. Real-time microscopy would offer a better understanding of seeding events in this crystallisation system, however, such equipment was not available during this work.

4.4.3.3 Analysis of the co-crystal material obtained from seeded cooling crystallisation and electrospraying

Optical microscopy was initially used to characterise the co-crystal material obtained from seeded cooling crystallisation and electrospraying. Figure 4-22 shows an image of the co-crystal formed under seeded cooling crystallisation, where large single crystals with a cube-like morphology were crystallised, and from electrospraying which afforded poly-crystallites. In the absence of co-crystal seeds (0% seed loading), crystals needle and plate-like morphologies were observed, identified as PCM and MCM. Single crystals suitable for crystal structure determination by SCXRD were successfully crystallised under seeded cooling crystallisation methods.

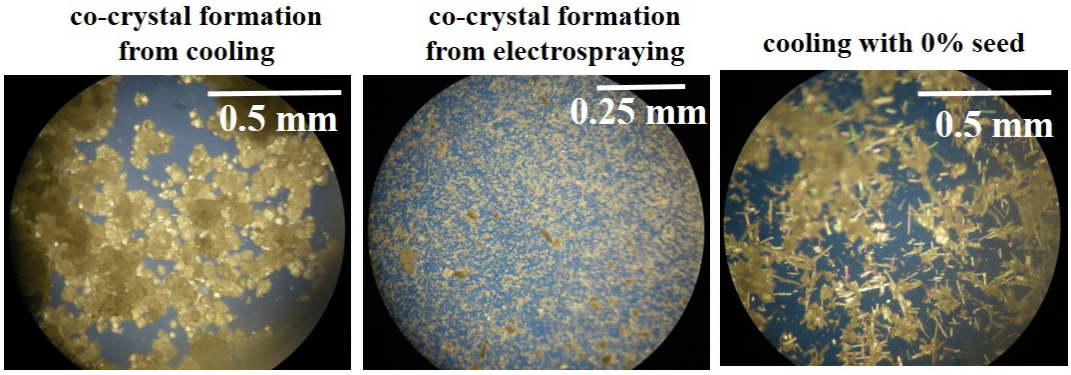

Figure 4-22: Microscopy images of the co-crystal formed under seeded cooling crystallisation (left) and electrospraying (centre), compared to an non-seed cooling crystallisation that formed PCM and MCM (right).

The co-crystal products obtained from seeded-cooling and electrospraying were further characterised by SEM (figure 4-23). Under electrospraying, the co-crystal particles have a sponge-like appearance. A porous, rough topography was observed that have a similar frame-work to that seen in electrosprayed PCM-II (discussed in section 4.3.3). In contrast, under the seeded cooling crystallisation environment the co-crystal particles have a smooth topography with visibly fewer crests on the surface. The electrosprayed co-crystal particles appear to have a larger surface area than the particles formed under seeded-cooling crystallisation; this is an important property that would likely enable faster dissolution rates of the APIs crystallised in this manner. The surface area of both materials was measured by Brunauer–Emmett–Teller (BET) sorption (the samples were submitted to the University of Bath materials characterisation service, MC^2, and the analysis and interpretation of results was conducted by Dr. Rémi Castaing). The electrosprayed material was found to have a surface area of 6.313 $m^2\ g^{-1}$, a value 2.5x larger than the surface area of the material formed under seeded-cooling crystallisation with an area of 2.446 $m^2\ g^{-1}$. A summary of the BET results is available in the Appendix (figure 9-15).

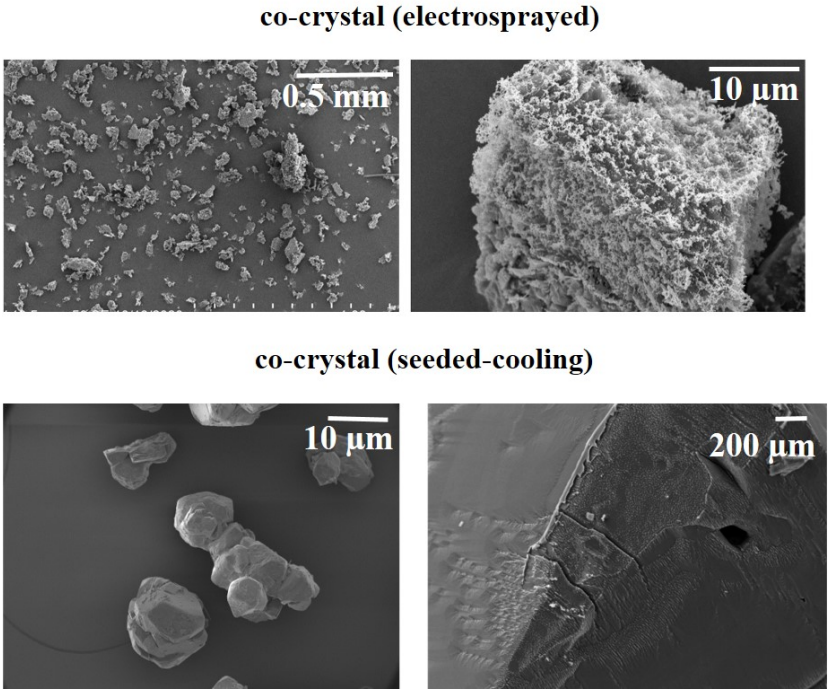

Figure 4-23: Images from SEM analysis of the PCM-MCM co-crystal formed under electrospraying and seeded-cooling crystallisation.

The next section of this chapter discusses if these observed particle differences between electrospray produced seeds and those from seeded cooling have an influence on the use of the materials as a crystal seed.

4.4.3.4 The influence of particle attributes on crystal seeding

Crystal seeds obtained from the cooling co-crystallisations were explored, with sizes ranging from 25-150 μm alongside seed loadings of 1-5%. Each experiment was conducted in a solvent system of IPA and water (4:6), and was held at a dwell temperature of 4^{o}C for 144 h. A sample was taken from each crystallisation after 12, 24, 48, 72 and 144 h and characterised by PXRD. Figure 4-24 displays the PXRD traces gained from each experiment after 144 h. In contrast to the findings for the seeds obtained from electrospray, all of these experiments were unsuccessful in co-crystal formation (table 4.8). A mixture of PCM-II, MCM-I and a hydrate of MCM were identified in the product material from each experiment that explored seed loading using these seeds (figure 4-24a). Similarly PCM-II and a hydrate of MCM was identified in the product material from each experiment that explored seed size (figure 4-24b).

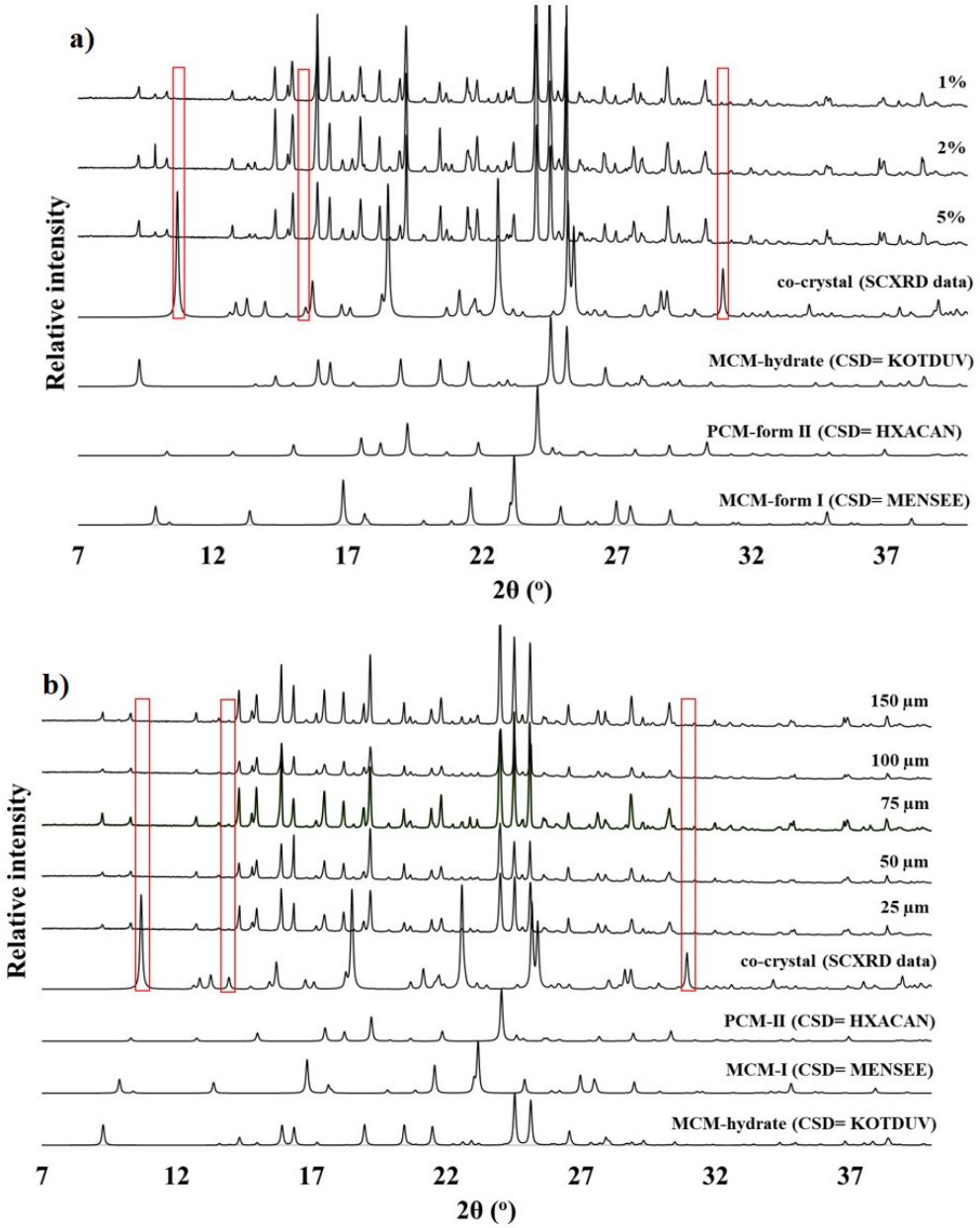

Figure 4-24: PXRD traces from experiments that used crystal seeds from the seeded-cooling co-crystal product. The influence of seed loading (a) and seed size (b) is studied. The absence of Bragg reflections for the co-crystal is highlighted in red.

The difference in topography observed between the two co-crystal products (from electrospraying and from seeded cooling using the electrospray products as seeds) may provide an explanation for these unsuccessful results. Upon crystal seeding, the ease of contact between a particle in the bulk material and the crystal seed can be strongly related to the roughness of the crystal seed's surface. A rough (or porous) surface can significantly impact the strength of contact and degree of adhesion during the crystallisation process. The study of dwell time revealed that PCM and MCM first crystallise as single entities and co-crystallise over a period of 72 h. When two particles collide in solution, the chance of particulate interactions is increased when a particle, in this case the electrosprayed seed, has a rough surface. The surface energy of the seeds is another possible difference between the two co-crystal products as it may cause

a charge difference; this could be electrospray-induced or due to the difference in surface area. The modification of a particle's surface energy can influence crystal growth.

Table 4.8: Cooling crystallisation experiments with the PCM-MCM co-crystal obtained from cooling crystallisation as crystal seeds.

seed size (μm)	**seed load** (%)	**solvent system**	**stir rate** (rpm)	**dwell time** (h)	**solid form(s) observed**
influence of seed loading					
150	1	IPA : water	x	72	MCM, PCM, MCM-hy*
150	2		x	144	MCM, PCM, MCM-hy*
150	5		x	144	MCM, PCM, MCM-hy*
influence of seed size					
150	2	IPA : water	x	72	PCM, MCM-hy*
100	2		x	144	PCM, MCM-hy*
75	2		x	144	PCM, MCM-hy*
50	2		x	144	PCM, MCM-hy*
25	2		x	144	PCM, MCM-hy*

*MCM-hy = MCM hydrate, CSD code KOTDUV.

4.5 Characterisation of the new PCM-MCM multi-component complex (co-crystal).

The structural nature of the PCM-MCM co-crystal was characterised with a range of analytical methods. X-ray crystallography (SCXRD and PXRD) and ^{1}H NMR spectroscopy were used to determine the structure of the new solid form and the purity of the bulk material.

4.5.1 Structural characterisation

The multi-component complex crystallises in the orthorhombic, centrosymmetric, space group Pbca. Figure 4-25a displays the asymmetric unit with one molecule of each component, PCM (blue) and MCM (green). The packing arrangement of the co-crystal, shown in figure 4-25c, shows molecules of PCM packed in a herringbone arrangement and sandwiched between molecules of MCM which are packed in a cross like arrangement. The herringbone packing of PCM in the co-crystal is similar to that observed in PCM-I. In contrast, MCM-I displays a zigzag-like packing arrangement as a single entity (figure 9-16 in the Appendix). There are no hydrogen bond interactions between the two components and the main interactions are Van der Waals forces (figure 4-25b), including a C-C contact of 3.275(2) Å and a H-C contact of 2.81(3) Å. It is not uncommon for two components in a co-crystal system to not interact by hydrogen bonding; the CSD contains many examples[176] which display $\pi-\pi$ stacking interactions between planar complexes. However, a rare case is presented for the PCM-MCM co-crystal studied here, where the two components are not linked by significant interactions between planar constituents.

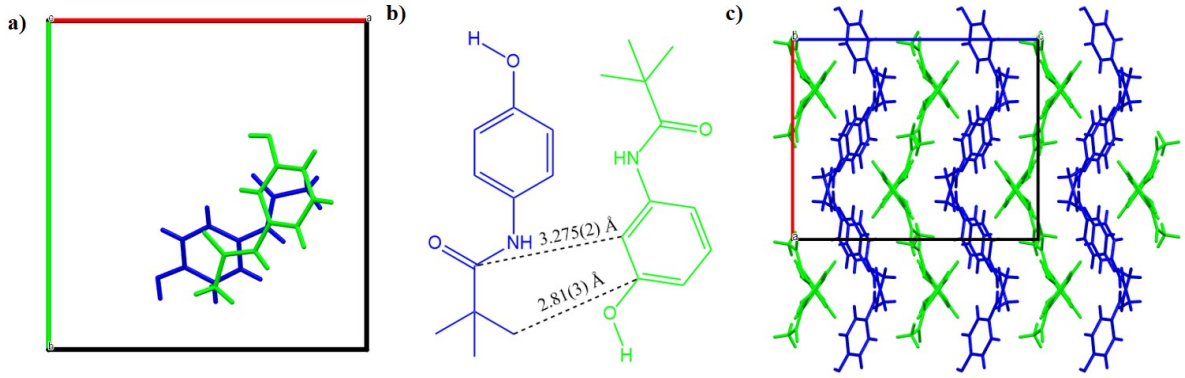

Figure 4-25: The unit cell and structure of PCM (blue)-MCM (green) co-crystal including a) the asymmetric unit viewed along the c axis, b) Van der Waals forces observed between the two components and c) the packing arrangement viewed along the b axis.

Within the identified "single component" segments of the co-crystal, hydrogen bonds are key interactions and are observed between PCM-PCM and MCM-MCM molecules. There are four unique hydrogen bonds, two link the molecules of PCM and two link the molecules of MCM. The first hydrogen bond for each molecule is between an amine group and a para/meta hydroxyl group, N-H...O-C (labelled 1 and 4 in figure 4-26), with a distance of 1.80(3) Å and 1.76(3) Åfor PCM and MCM respectively. The second bond for each molecule is between a para/meta hydroxyl group and a carbonyl group, O-H...O=C (labelled 2 and 3 in figure 4-26),

with a distance of 2.10(2) Å and 2.11(2) Å, respectively.

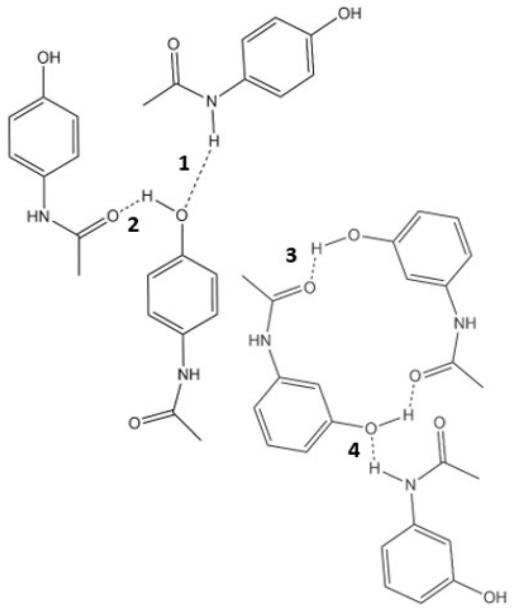

Hydrogen bond	Distance (Å)
1	1.80(3)
2	2.10(2)
3	2.11(2)
4	1.76(3)

Figure 4-26: The hydrogen bond framework within the single components, showing interacting molecules in the PCM-MCM co-crystal.

The hydrogen bond framework observed between the single component molecules in the co-crystal was found to mimic the frameworks seen in different polymorphic forms of PCM and MCM as single entities. Figure 4-27 displays the hydrogen bond frame work observed between PCM molecules in PCM-I (CSD code: HXACAN01), PCM-II (CSD code: HXACAN) and the co-crystal. In this case, all three solid forms show the same hydrogen bond arrangement between molecules of PCM.

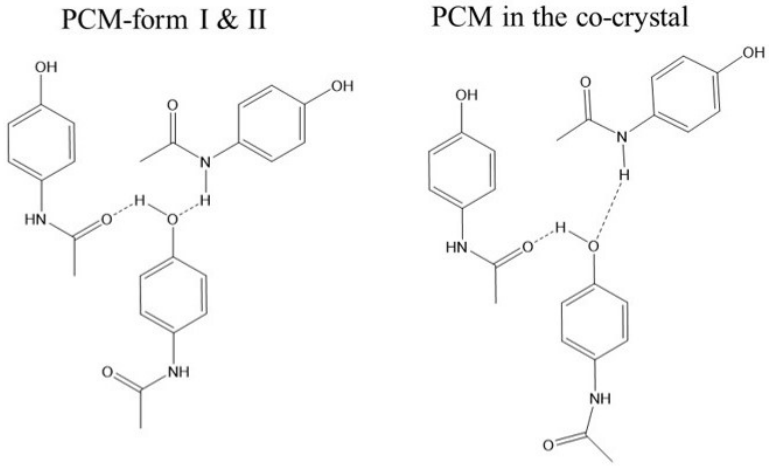

Figure 4-27: A comparison of the hydrogen bond framework between PCM molecules in PCM-I, PCM-II and the co-crystal.

Figure 4-28 shows a comparison of the hydrogen bond framework between the molecules of MCM in MCM-I (CSD code: MENSEE), MCM-II (CSD code: MENSEE04) and in the co-crystal. It is observed that the hydrogen bond framework in the co-crystal comprises a combination of both polymorphic forms of MCM. In this figure, elements of the hydrogen bond

framework that are observed in the co-crystal and polymorphic forms of MCM are highlighted in black.

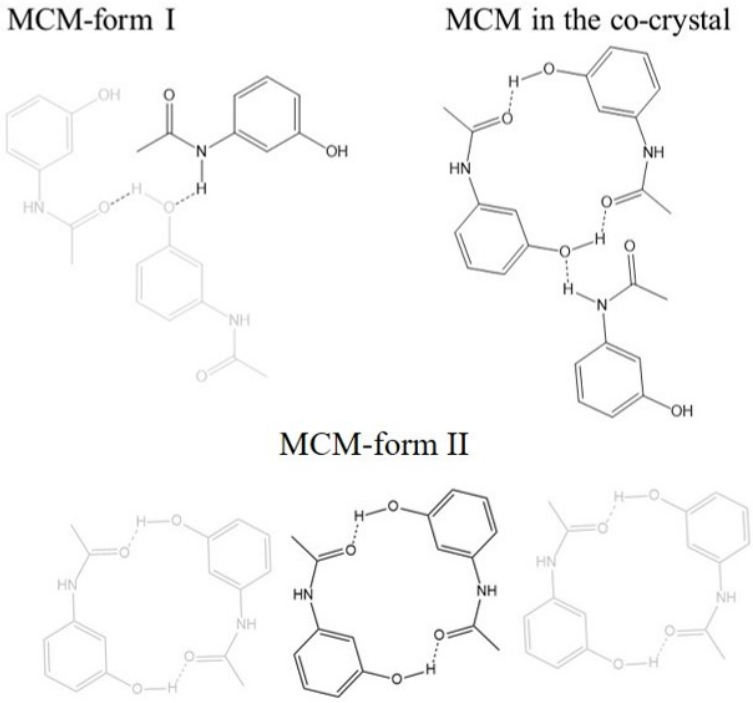

Figure 4-28: A comparison of the hydrogen bond framework between MCM molecules in MCM-I, MCM-II and the co-crystal.

The ^{1}H NMR spectroscopy spectrum of the co-crystal showed peaks that related to the hydrogen environments of both PCM and MCM. Integration of these peaks suggested a 1:1 multi-component ratio between the two molecules (figure 9-17 in the Appendix), consistent with the crystallographic structure determination and with no evidence of proton transfer. PCM and MCM have the same pK_a value of 9.5; this is consistent with the description of the multi-component complex as a co-crystal, with the two components having a difference in pK_a that is equal to zero (Δp$K_a = 0$).

4.5.2 Analysis of bulk material

The bulk material of the co-crystal, crystallised both under electrospraying and in seeded-cooling crystallisation using the electrospray-produced seeds, was characterised by PXRD. The formation of pure PCM-MCM co-crystal was observed for both methods, shown in figure 4-29. No reflections corresponding to starting material PCM or MCM were observed in the PXRD traces. The patterns show the bulk co-crystal samples to be pure co-crystal (top two traces) due to the good match with the PXRD predicted from the single crystal structure (allowing for peak shifts due to different data collection temperatures).

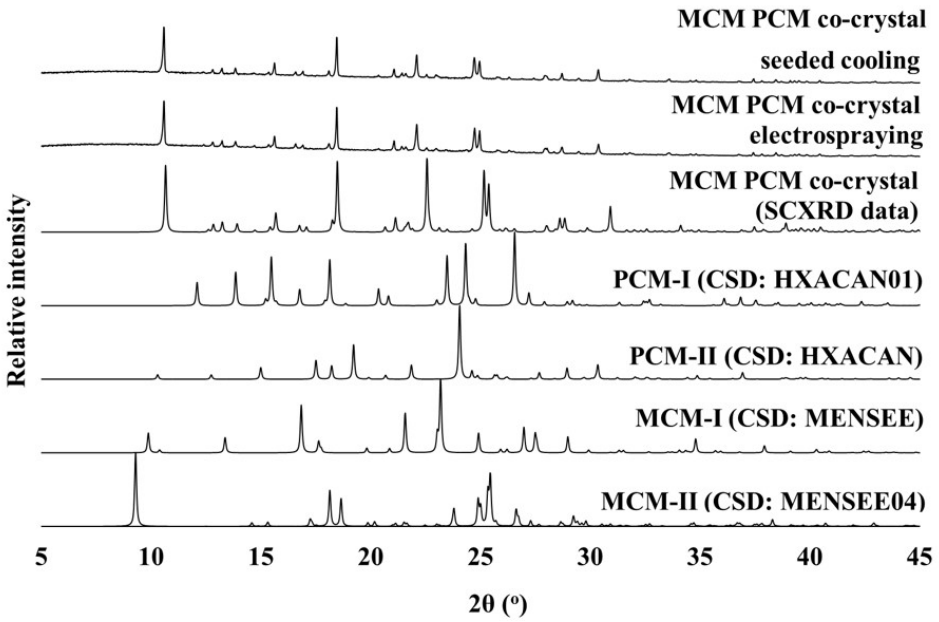

Figure 4-29: PXRD traces of the PCM-MCM co-crystal from electrospraying and seeded cooling crystallisation.

4.5.3 Physical property characterisation of the PCM-MCM co-crystal

4.5.3.1 Thermal behaviour

The thermal behaviour of the co-crystal was characterised by DSC, together with HSM. A significantly lower melting point of 104^{o}C was observed for both the electrosprayed co-crystal (figure 4-30a) and the cooling co-crystal (figure 4-30b), compared with those of the APIs as single entities (169^{o}C for PCM and 148^{o}C for MCM).

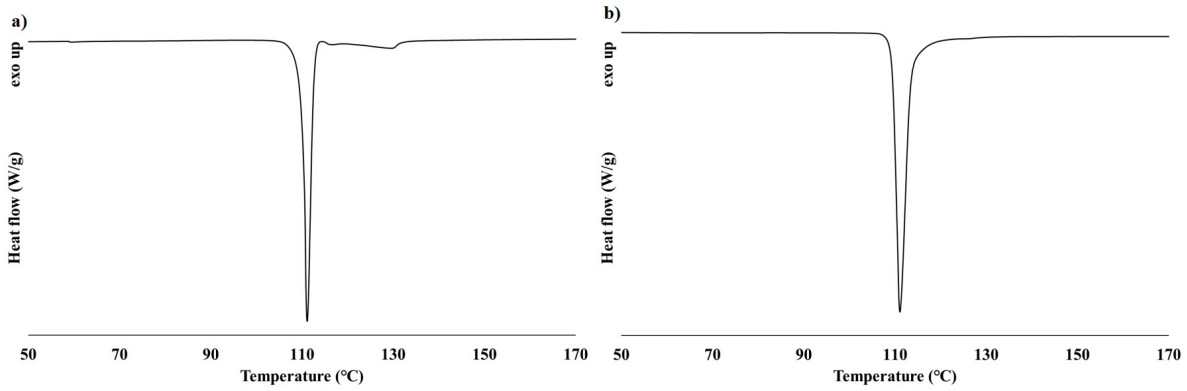

Figure 4-30: The DSC traces of the PCM-MCM co-crystal from a) electrospraying and b) seeded cooling crystallisation.

HSM was used to visualise the thermal activity observed in the DSC trace of the electrosprayed co-crystal. At 40^{o}C, the co-crystal is in the solid state and is seen to melt at 112^{o}C (figure 4-31). Further material melting is observed in the temperature range 112^{o}C to 140^{o}C, relating to trace amounts of material that do not resemble either starting material (PCM and MCM). This material could be an impurity, for which high-performance liquid chromatography paired with

mass spectrometry could be used to separate and identify the unknown material. However, detailed analysis of impurities is outside the scope of this investigation.

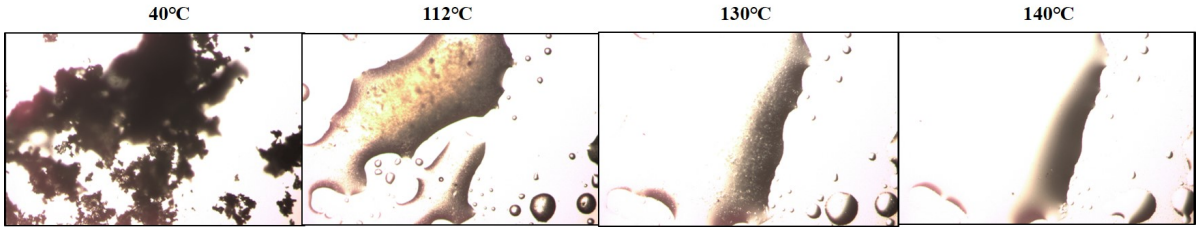

Figure 4-31: HSM images of the electrosprayed co-crystal monitored between 40-140^{o}C.

4.5.3.2 Solubility measurements

The solubility of the PCM-MCM co-crystal (formed under electrospraying) was determined in a solvent mixture of IPA and water (4:6) and compared to those of the APIs, PCM and MCM, as single entities in the same solvent system. The solubility curves were measured using observational methods (as described in section 3.2.1.2). The solubility measurements were taken twice and an average value plotted with a maximum error of +/- 1^{o}C for the co-crystal, +/- 2.5^{o}C for PCM and +/- 4^{o}C for MCM. The co-crystal (black plot) showed a significantly higher solubility compared to PCM (blue plot) and MCM (red plot) in figure 4-32.

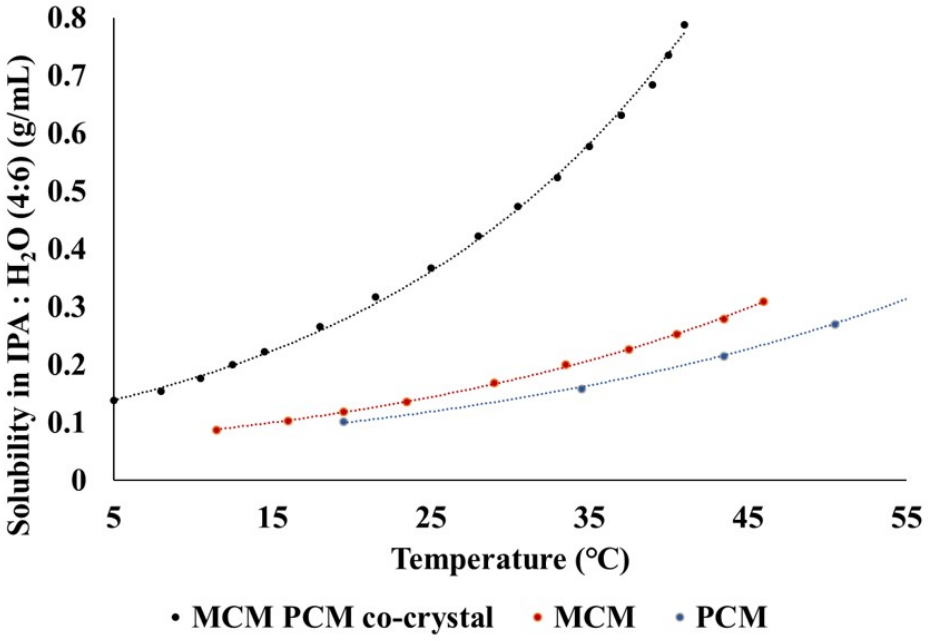

Figure 4-32: The solubility curves of the PCM-MCM crystal, PCM and MCM.

A four-fold solubility enhancement is observed at 37^{o}C. However, in terms of weight, a 2-fold solubility increase is observed, as the co-crystal contains half the number of PCM or MCM molecules weight for weight.

4.5.3.3 Basic stability studies

The stability of the new multi-component complex was characterised empirically over a period of six weeks at elevated temperatures (up to 70^{o}C) and at low (10%) and high (80%) relative humidity. The PCM-MCM co-crystal (formed under electrospraying) was found to be stable for six weeks when stored at 70^{o}C and in a humidity chamber at both 10% and 80% RH. Figure 4-33 displays the PXRD traces of the co-crystal after six weeks under these environmental conditions. No signs of transition, decomposition or amorphisation were observed.

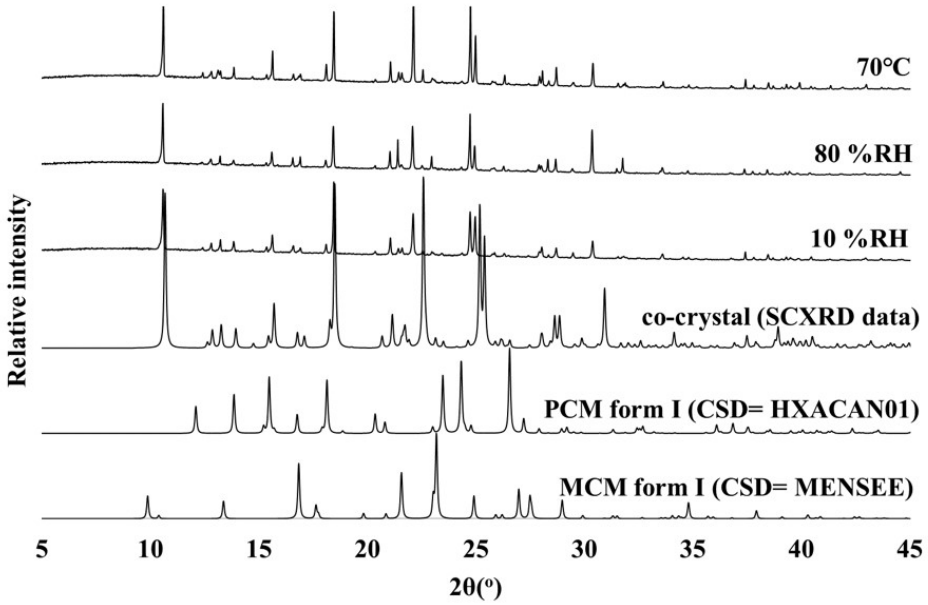

Figure 4-33: The stability of the PCM-MCM crystal after six weeks when stored at 70^{o}C and in a relative humidity chamber of 10% and 80%.

4.6 Conclusion

The work presented in this chapter investigated the influence of an E-field and confinement on the crystallisation process, with a novel crystallisation method known as electrospraying. The relationship between crystallisation parameters during electrospraying and the resulting solid form characteristics (e.g. type of solid form and particle attributes) compared to other crystallisation methods was a large focus. The capability of electrospraying for the optimisation of the manufacturing process in an industrial pharmaceutical setting was established, through determining that electrospray products can be used as seeds in bulk crystallisations.

Method development was used to investigate the influence of different crystallisation parameters on the solid form crystallised during electrospray crystallisation with a model multi-component API system of PCM and MCM. Three crystallisation parameters were found to play a vital role in solid form control during electrospraying: flow rate, applied voltage, and the ratio of the components PCM and MCM. The first two of these parameters are known to determine the size and charge of a droplet's surface during electrospraying. The latter is thought to have a significant effect on PCM molecules in the crystallisation solution. Polymorphic control of PCM was successfully achieved and a parameter range for the selective formation of either metastable PCM-II or stable PCM-I under electrospraying was identified. It was found that slower flow rates (with a maximum of 0.25 mL h^{-1}), a larger E-field (of at least 1.30 kV cm^{-1}), and a multi-component ratio containing at least 25% MCM, was required for the isolation of PCM-II. In addition to polymorphic control, successful co-crystallisation of the two components was achieved by electrospray techniques and afforded a novel solid form, the PCM-MCM co-crystal, forming this elusive solid form for the first time. It was found that under the same applied voltage of 1.30 kV cm^{-1} (for polymorphic control) a significantly faster flow rate of 0.50 mL h^{-1} was needed for successful co-crystallisation. In this case, the ratio of PCM and MCM was of importance, the selective crystallisation of pure co-crystal was solely achieved with a 1:1 ratio of the multi-components. Interestingly, these results show that under an E-field of 1.30 kV cm^{-1}, a multi-component ratio of 50% MCM and a solvent mixture of IPA and water (4:6), the electrospray is capable of selectively forming either PCM-II (alongside MCM) or co-crystallised PCM-MCM through the change of a single variable, flow rate. In this case, a flow rate between 0.15 and 0.25 mL h^{-1} will afford PCM-II while 0.50 mL h^{-1} will afford the co-crystal. A change in flow rate is known to directly change the droplet diameter under electrospraying. A change in droplet diameter can in turn be summarised as influencing the following key electrospray parameters:

Confinement, the bulk crystallisation medium is split into smaller volumes which increases the surface area-to-volume ratio. Smaller droplet diameters result in a crystallisation medium with higher surface energy interactions. This directly affects the nucleation kinetics of favourable solid form formation.

Molecular mobility, each droplet formed during electrospraying contains an E_{in} that influences the orientation and mobility of molecules inside a droplet at the molecular level. In this case, PCM and MCM contain positive and negative dipolar constituents. For a droplet with a positively charged surface, negatively charged dipoles are thought to migrate towards the

droplet's surface and positively charged dipoles migrate towards the droplet's core. This would lead to a change in the droplet's surface free energy, since charged groups would reside at the surface of the liquid.

The individual role of confinement within electrical confinement was studied for this system under a confined crystallisation environment in absence of an applied E-field. Confinement crystallisation was found to be capable of isolating PCM-II without any applied voltage. However, under all conditions trace amounts of PCM-I were observed alongside the final product. The PCM-II formed via confinement alone was found to be unstable in the presence of PCM-I, with the expected polymorphic transformation into the thermodynamically stable form observed by PXRD. In contrast, PCM-II formed via electrospraying was found to be stable for at least one year. It was concluded that confinement plays a key role in polymorphic control of PCM under electrospraying; however, confinement crystallisation alone was unable to achieve full polymorphic control of PCM without the additional application of voltage at mild temperatures.

The successful formation of electrosprayed PCM-II was characterised by a range of analytical tools. Pure PCM-II was solely observed by PXRD and DSC, however, the presence of MCM in the bulk material was indicated via ^{1}H NMR spectroscopy, in a 3:1 ratio of PCM to MCM. It was concluded that the MCM present in the product may have turned amorphous under electrospraying. The topography of the electrosprayed PCM-II particles was visualised by SEM. Irregular, plate-like agglomerated particles were observed, with visible voids. The formation of porous particles was concluded to be an "imperfection" that may result from an inter-phase boundary of crystallising solid particles separated by regions of solvent pockets that migrate through diffusion, resulting in a vacancy within the solid material.

Electrospraying seemed to facilitate the amorphisation of PCM or MCM, a factor which seemed to be dependent on the stoichiometric ratios of components. It was observed that under higher loadings of PCM, Bragg reflections for MCM were absent when the material was measured by PXRD and vice versa. However, a T_g was not observed by DSC; such an observation would support the presence of an amorphous material. The amorphisation of material is currently an active research area, as it has the potential to significantly improve the solubility and thus the bioavailability of solid forms. The possible amorphisation of MCM was an interesting discovery that was relevant to this research project's aim but its full characterisation was not possible within the current project.

The translation of co-crystal formation was attempted under several different crystallisation methods. The electrosprayed co-crystal was successfully translated into a cooling crystallisation platform with seeding, but only by using the electrospray-produced crystals as seeds. Other crystallisation methods investigated were unsuccessful in co-crystallisation. Five crystallisation parameters were investigated to discover an optimal seeding protocol that selectively afforded single crystals of the co-crystal. The crystal seeding protocol used was found to be a linear and not circular system; crystal seeds taken from the seeded-cooling co-crystal product were unsuccessful in seeding further co-crystal formation – only the electrosprayed co-crystals were able to act successfully as seeds. Interestingly, the co-crystals formed under electrospraying

and seeded-cooling crystallisation were found to have significantly different particle attributes. A rough, sponge-like topography, with a 2.5x larger measured surface area, was found for the electrosprayed co-crystal. In contrast, a smooth topography was observed for the co-crystal formed under seeded cooling. The evidence suggests that this may affect the ability of these crystals to act as seeds. The electrosprayed co-crystal was found to have a similar rough, porous type morphology to that observed in electrosprayed PCM-II. This demonstrates that electrospraying is a technology capable of influencing the CQAs of APIs by influencing the particle level characteristics as well as offering solid form control at the molecular level.

The structural nature and physical properties of the co-crystal were characterised. In the crystal structure, separate hydrogen bonded associations of PCM-PCM and MCM-MCM molecules are held together by van der Waals forces. A significantly lower melting point of 104^oC was measured for the co-crystal compared to those of 169^oC for PCM and 148^oC for MCM. A four-fold solubility enhancement was observed for the electrosprayed co-crystal (at 37^oC) compared to the measured solubility of PCM and MCM in the same solvent system, representing a two-fold w/w enhancement for each component individually. This suggests that the co-crystal would outperform PCM and MCM in a biological setting, however, this enhancement will require further validation. Basic stability studies were conducted; the electrosprayed co-crystal was found to be stable for at least six weeks at an elevated temperature of 70^oC and at humidities of 10 and 80% RH.

Overall, these investigations indicate that electrospraying is an exciting crystallisation technique that can offer a high level of control over polymorphism and access to elusive solid forms. This work highlights the capability of electrospraying and shows that it has the potential to be integrated into an industrial pharmaceutical setting as a seed manufacturing technology, for the discovery and production of elusive solid forms that are hard to crystallise by other methods. Conventional seeding methods can then be used for large-scale manufacturing, which could be implemented under conventional regulatory standards.

Chapter 5

Exploring multi-component complexes of salbutamol (SA) through co-crystallisation.

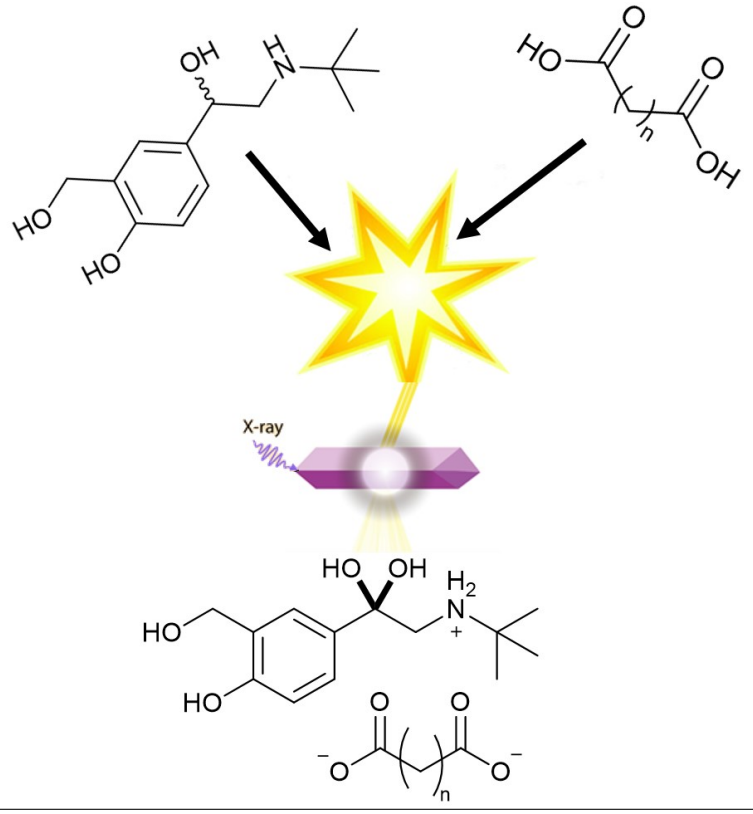

Crystallographic data collection made by the author and presented in this chapter were included in the following article submitted for publication:

A. J. Al-Ani, P.M.J Szell, Z. Rehman, H. Blade, H. P. Wheatcroft, L. P Hughes, S. P. Brown, C. C. Wilson, Combining X-ray and NMR Crystallography to Explore the Crystallographic Disorder in Salbutamol Oxalate, *Cryst. Growth Des.*, 2021

5.1 Introduction

One of the main challenges in crystallisation science is to gain control over the process and in turn the structural, chemical and physical attributes of the crystallised solid form. Crystal engineering has been used previously as a method of controlling these attributes through the formation of multi-component complexes including co-crystals[12,177] and solvates[12] and the production of metastable polymorphs.[55,159] The production of co-crystals is particularly attractive as a potential option for enhanced products in the pharmaceutical industry since they frequently demonstrate significantly different structural (including disorder), chemical and physical properties to those of the single components.

5.1.1 Project aim

Aim: to induce the co-crystallisation of salbutamol (SA) with dicarboxylic acids of various chain lengths and investigate SA disorder in the resulting complexes.

The research in this chapter focuses on gaining new multi-component complexes of SA through a co-crystallisation screen that utilises several different crystallisation methods. The structural and physical attributes including crystallographic data collection, thermal behaviour, solubility and basic stability, at elevated temperatures and different humidities, are investigated for the product of each successful co-crystallisation. The results in this chapter are used to find a suitable new multi-component complex of SA that exhibits crystallographic disorder, one of the aims of the co-crystallisation screen. The understanding and control of disorder in this new complex is subsequently discussed further in chapter 6 and compared to the disorder in a commercial form of SA.

5.1.2 Model API system investigated

SA (figure 5-1) is an API used in the treatment of respiratory diseases and is listed as an essential drug product by the World Health Organization. SA, as a single entity, shows no signs of crystallographic disorder.[178] However, this API system is of interest as some of the multi-component complexes of SA reported in the CSD are disordered. These multi-component complexes are salbutamol sulfate (SAS),[179] a mono hydrated form of SAS,[180] salbutamol benzoate,[181] and salbutamol adipic acid and adipate.[182] The type of disorder reported in these systems is structural, with multiple site occupancies observed around the chiral centre of SA (*C-OH in figure 5-1). Other multi-component complexes of SA in the CSD feature a number of different molecules including the pharmaceutically relevant oxaprozin,[183] prop-2-enoate,[184] hydrochloride,[185] and succinate methanol solvate.[182]

5.1.3 Structural targets

This work aims to produce new multi-component complexes of SA that exhibit structural disorder, the presence of which can offer difficulties in obtaining full structural characterisation but can also potentially offer benefits in terms of favourable physical properties of the solid form. Aliphatic, dicarboxylic acid co-formers were chosen to be used in a multi-component crystallisation study with this target in mind since co-crystallisation with these types of molecules

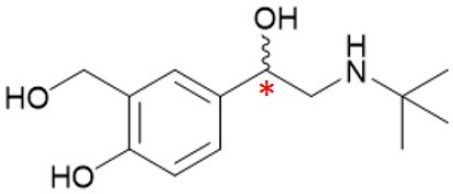

salbutamol (SA)

Figure 5-1: The molecular structure of the target API. The typically disordered chiral center in multi-component complexes is highlighted (*C-OH).

seems to be favourable from previous structures reported in the CSD and have been reported to show signs of disorder.[182] A dicarboxylic acid describes a molecule with two carboxyl groups (R-COOH). Each of these carboxyl groups can independently ionise and have two dissociation constants, termed K_{a1} and K_{a2} (equations 5.1 and 5.2). The first carboxyl group (K_{a1}) is generally regarded as more acidic than the second group (K_{a2}) since it has a lower pKa value and therefore dissociates more easily, an effect which increases as the proximity between the two carboxyl groups decreases.[186]

$$K_{a1} = \frac{[HA^-][H^+]}{[H_2A]} \tag{5.1}$$

$$K_{a2} = \frac{[A^{2-}][H^+]}{[HA^-]} \tag{5.2}$$

Aliphatic dicarboxylic acids are solely used as co-formers in this work to facilitate the study of small changes in the molecular nature of the co-former (chain length) on the resulting solid form obtained, with a focus on attempts to generate disorder in the resulting co-crystals. Figure 5-2 displays the molecular structures of the target co-formers used in this study: oxalic acid (OX), malonic acid (MA), succinic acid (SU), glutaric acid (GL) and adipic acid (AD).

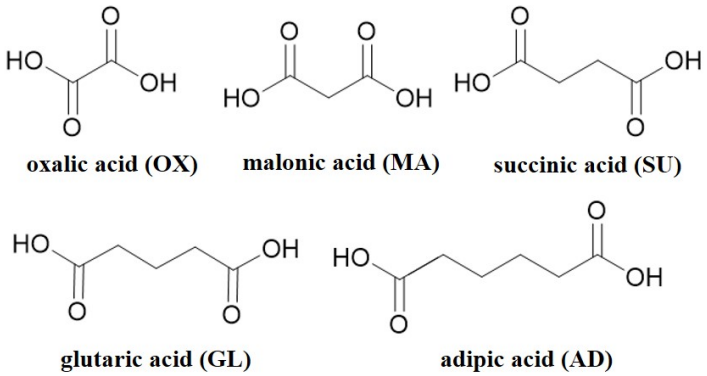

oxalic acid (OX) **malonic acid (MA)** **succinic acid (SU)**

glutaric acid (GL) **adipic acid (AD)**

Figure 5-2: The molecular structures of the dicarboxylic acid co-formers used in the SA co-crystallisations.

5.2 Material preparation and experimental information

All dicarboxylic acids were obtained from Sigma-Aldrich and Fluka. SAS was obtained from Tokyo Chemical Industry. SA was initially obtained from Sigma-Aldrich and then isolated from SAS and ethanol (EtOH) was obtained from VWR.

5.2.1 Isolation of SA from SAS

The active ingredient used in the co-crystallisation experiments conducted in this chapter, SA, was isolated from affordable materials; it was not cost effective to purchase SA at approximately £1490.00 per gram from Sigma-Aldrich. Figure 5-3 displays a schematic of the process that was thus used to isolate SA from SAS; the production of SA was calculated to cost approximately £10.00 per gram via this method. The base in SAS was liberated from a saturated aqueous solution of sodium carbonate. Once free, the base remained in solution and SA precipitated out of solution over a period of time. The resultant product, SA, was filtered and left to dry at room temperature before being characterised by DSC (figure 9-19 in the Appendix) and PXRD (figure 9-18 in the Appendix) and NMR spectroscopy (see below).

$C_{13}H_{21}NO_3$: ^{1}H NMR spectroscopy (DMSO-d6, 300 MHz): δ 0.97 (9H), 3.33 (2H), 4.24 (2H), 6.67 (1H), 6.96 (1H), 7.25 (1H). ^{13}C NMR spectroscopy (D_2O-d2, 300 MHz): δ 25.92 (3C), 47.94 (1C), 55.12 (1C), 60.69 (1C), 71.04 (1C), 118.48 (1C), 121.68 (1C), 126.86 (1C), 127.35 (1C), 128.72 (1C), 162. 44 (1C).

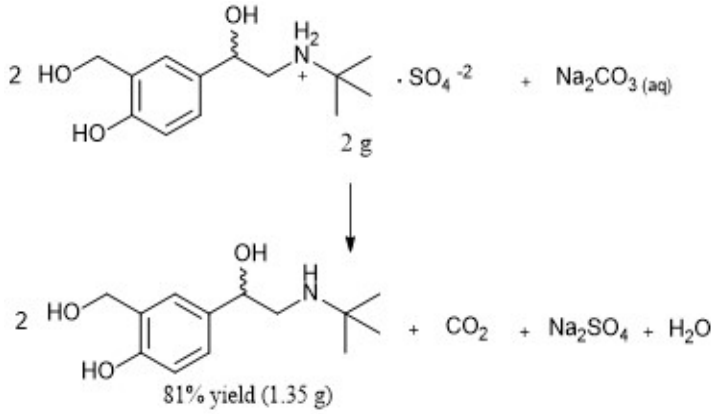

Figure 5-3: A schematic of the steps used in the isolation of SA from SAS.

5.2.2 Evaporative crystallisation

Evaporative crystallisation was used as an initial method to screen and identify promising dicarboxylic acid candidates for co-crystallisation with SA. Aliphatic dicarboxylic acids with carbon chain lengths that varied from two to six (as illustrated in figure 5-2) were investigated, with API:co-former stoichiometric ratios of 1:1 and 2:1, in both water and EtOH.

All screening experiments were initially conducted at a 1 mL scale. Experiments that suggested the formation of a new solid form were investigated further with other crystallisation methods, including the scale up of evaporative crystallisations under a working volume of 3 mL.

1 mL scale: SA, 0.01 g, was dissolved in 1 mL of the chosen solvent alongside the corresponding weight of co-former. The resultant solvent system was left to evaporate at room temperature in a 1.5 mL open glass vial.

3 mL scale: SA, 0.03 g, was dissolved in 3 mL of the chosen solvent alongside the corresponding weight of co-former. The resultant solvent system was left to evaporate at 40^{o}C in a 7 mL glass vial with 10 holes pieced into the lid to ensure slow evaporation.

5.2.3 Cooling crystallisation

5 mL of a solution, saturated at 40^{o}C, containing SA and the corresponding weight of co-former was placed into a sealed 20 mL glass vial. The saturation of solution was calculated from a solubility curve (if known) or was formed by taking 5 mL of clear solution from a slurry of the target components left for at least one hour at 40^{o}C. The solution was heated to 10^{o}C above the temperature of saturation and was held for 10 minutes with magnetic bottom stirring set at 700 rpm. The stirring was turned off and the solution was cooled at 1^{o}C min^{-1} until it reached a temperature of 4^{o}C. The solution was then held at 4^{o}C and left to crystallise overnight.

5.2.4 Solution mediated crystallisation (slurrying)

A solution that contained an excess amount of SA and the corresponding weight of co-former was placed into a 20 mL sealed glass vial. The solution was stirred at 700 rpm with magnetic bottom stirring, in the chosen solvent, and left at room temperature for 2 weeks.

5.2.5 Mechanical grinding

SA, 0.01 g, and the corresponding weight of co-former were ground manually with a pestle and mortar for 30 minutes.

5.2.6 Solubility measurements

The solubilities of multi-component complexes were determined in water, in addition to the solubility of SA; this allowed for the solubility of each system to be compared. Observational methods, described in section 3.2.1.2 and gravimetric methods, described in section 3.2.1.1, were used to determine the solubility of each form.

5.2.7 Single crystal structures

Crystal structures were determined for each multi-component complex of interest. A Rigaku Oxford Diffraction SuperNova diffractometer was used for data collection of all crystals in this chapter, with a Cu-Kα (λ = 1.54045 Å) X-ray source at 150 K. All crystal structures were solved by direct methods using SHELXS-2013[143] and refined using SHELXL-2015[144] with the software package Olex2[145]. Isotropic displacement parameters were used for the refinement of atoms with multiple site occupancies. Following this, refinement under anisotropic displacement parameters (ADPs) were conducted with free site occupancy factors. All hydrogen atoms were refined freely where possible; if the position of a hydrogen atom was unclear, constraints were used to fixed hydrogen atoms in an idealised position based on a riding model.

Table 5.1 displays the crystallographic data for each complex. SA-OX and SA-SU are novel solid forms discovered in this work. The crystal structures of SA (CSD code= BHHPHE) and SA-AD (CSD code= ORUWUU) are already known and reported in the CSD. The crystal structures of SA and SA-AD are re-characterised in this work to confirm the refinement of disorder in the published structure and to allow for direct comparison of the new co-crystals found.

5.2.7.1 Single crystal preparation methods and structural information

1. **salbutamol with oxalic acid (SA-OX)**

   A single crystal was isolated from a batch crystallised under evaporative methods. A 1:1 stoichiometric ratio of SA (0.01 g) and OX (0.0018 g) was dissolved in 1 mL of water. The solution was placed into a 1.5 mL open glass vial and left to evaporate at room temperature.

2. **salbutamol with succinic acid (SA-SU)**

   A single crystal was isolated from a batch prepared under cooling crystallisation. A 2:1 stoichiometric ratio of SA and SU was dissolved in 5 mL of EtOH. The solution was placed into a 7 mL glass vial, with 10 holes pieced into the lid, and left to evaporate at 40^{o}C.

3. **salbutamol with adipic acid (SA-AD)**

   A single crystal was isolated from a batch crystallised under evaporative methods. A 1:1 stoichiometric ratio of SA (0.01 g) and AD (0.0061 g) was dissolved in 1 mL of water. The solution was placed into a 1.5 mL open glass vial and left to evaporate at room temperature.

4. **salbutamol (SA)**

   A single crystal was isolated from a batch crystallised under evaporative methods. SA, 0.05 g, was dissolved in 5 mL of EtOH. The solution was placed into a 7 mL glass vial, with 10 holes pieced into the lid, and left to evaporate at 40^{o}C.

Table 5.1: The unit cell and refinement parameters of crystal structures determined in this chapter.

complex code	**(1) SA-OX**	**(2) SA-SU***	**(3) SA-AD**	**(4) SA**
formula	$C_{14}H_{22}N_1O_5$	$C_{32}H_{55}N_2O_{11}$	$C_{19}H_{32}N_1O_7$	$C_{13}H_{21}N_1O_3$
g mol^{-1}	284.32	643.84	386.45	239.31
T (K)	150 (10)	150 (10)	150 (10)	150 (10)
radiation	Cu Kα($\lambda = 1.54184$)	Cu Kα($\lambda = 1.54184$)	Cu Kα($\lambda = 1.54184$)	Cu Kα($\lambda = 1.54184$)
2θ range (^{o})	10.702 to 147.202	7.96 - 147.3	8.832 - 146.478	8.274 to 146.194
crystal system	monoclinic	triclinic	triclinic	orthorhombic
space group	$P2_1/n$	$P\bar{1}$	$P\bar{1}$	Pbca
a (Å)	8.3996(2)	8.3654(9)	9.7545(10)	8.7871(3)
b (Å)	6.20369(16)	11.6365(12)	10.7272(10)	14.4645(5)
c (Å)	27.6549(6)	19.116(3)	10.9823(7)	21.3744(7)
$\alpha(^o)$	90	105.935(10)	66.257(8)	90
$\beta(^o)$	97.214(2)	100.848(10)	85.732(7)	90
$\gamma(^o)$	90	93.647(9)	67.917(9)	90
volume (Å^3)	1429.65(6)	1744.2(4)	970.72(17)	2716.72(16)
Z	4	2	2	8
density (g cm^3)	1.321	1.226	1.322	1.170
$\mu(mm^{-1})$	0.830	0.757	0.830	0.668
completeness (%)	99.8	99.8	98.6	99.8
reflections collected	7185	18998	8479	6797
independent reflections	2881	6909	3842	2674
data/restraints/parameters	2881/2/216	6909/2/449	3842/1/277	2674/0/170
R int	0.0231	0.0997	0.0333	0.0385
GooF	1.076	1.640	1.036	1.123
R_1 (obs)	0.0406	0.1729	0.0568	0.1088
R_1 (all)	0.0448	0.2125	0.0678	0.1235
wR_2 (all)	0.0991	0.5002	0.1601	0.3300
$\rho_{max,min}$ (e Å^{-3})	0.34, -0.28	0.6, -0.67	0.60, -0.32	0.78/-0.68
atomic occupancy (*C-OH)	0.148(4) : 0.852(4)	0.129(18) : 0.871(18)	0.316(5) : 0.684(5)	-

*The crystallographic data collected is of poor quality due to poorly diffracting crystals. The experiment was run to gain a complete over view on the influence of chain length. A synchrotron source may be required to gain a more accurate structural model.

5.3 Preliminary co-crystallisation results under evaporative crystallisation

An evaporative co-crystallisation screen identified the formation of three new solid forms, henceforth referred to as SA-OX, SA-SU and SA-GL. The reproduced formation of salbutamol-adipate - adipic acid (CSD code= ORUWUU) was also observed, henceforth referred to as SA-AD. The formation of SA-AD is still of interest to this this work, as examination of its structure will aid the study of the effect of systematic changes in the molecular nature of the co-former (chain length) on the resulting solid form obtained. The co-crystallisation of all four solid forms discovered in these screening experiments was further investigated by other crystallisation methods and the products fully characterised. Other experiments from the screening afforded hard to characterise materials of poor crystalline quality, or an oil. Table 5.2 contains a summary of the screening results. The products from all experiments, apart from those which oiled out, were characterised by PXRD. The traces are available in the Appendix: SA and OX experiments in figure 9-20; SA and MA in figure 9-21; SA and SU in figure 9-22; SA and GL in figure 9-23; and SA and AD in figure 9-24.

Table 5.2: A summary of the evaporative screening crystallisations of SA (pKa= 10.3) with various dicarboxilic acids.

co-former	**pK_{a1}, pK_{a2}**	**molar ratio**	**solvent**	**solid forms/ material observed**
oxalic acid	1.36, 4.1	1:1	water	new solid form (SA-OX)
		2:1	water	new solid form (SA-OX), SA
		1:1	EtOH	poorly crystalline solid
		2:1	EtOH	oil
malonic acid	2.85, 5.7	1:1	water	poorly crystalline solid
		2:1	water	oil
		1:1	EtOH	poorly crystalline solid
		2:1	EtOH	SA*
succinic acid	4.21, 5.64	1:1	water	oil
		2:1	water	oil
		1:1	EtOH	new solid form (SA-SU), SA, SU
		2:1	EtOH	new solid form (SA-SU), SA, SU
glutaric acid	4.34, 5.22	1:1	water	poorly crystalline solid
		2:1	water	oil
		1:1	EtOH	oil
		2:1	EtOH	new solid form (SA-GL)*
adipic acid	4.43, 5.41	1:1	water	SA-AD (CSD code= ORUWUU)
		2:1	water	poorly crystalline solid
		1:1	EtOH	SA-AD* (CSD code= ORUWUU)
		2:1	EtOH	poorly crystalline solid

*The solid form was identified by PXRD but the material was of poor crystalline quality.

5.4 Translation of co-crystallisation experiments under other crystallisation methods

Other crystallisation methods were explored for the formation of the multi-component complexes of SA crystallised under evaporative screening, namely SA-OX, SA-SU, SA-GL and SA-AD. Different crystallisation methods investigated included evaporative (on a larger scale), cooling, slurrying and neat mechanical grinding. The phase purity of the material from each successful co-crystallisation was characterised by PXRD and DSC and in some cases TGA.

5.4.1 Salbutamol and oxalic acid

The formation of the new solid form SA-OX was further investigated by crystallisation from solution that contained stoichiometric SA:OX ratios of 1:1 and 2:1 in water. Table 5.3 shows a summary of the crystallisation conditions explored and the solid forms identified from characterisation of the material with PXRD and DSC.

Table 5.3: The material obtained from various crystallisation methods with oxalic acid.

crystallisation method	**volume (mL)**	**material obtained**
salbutamol + oxalic acid (2:1) in water		
evaporative	3	SA-OX, SA
cooling	5	SA-OX
slurry	5	SA-OX
grinding	-	SA-OX, SA
salbutamol + oxalic acid (1:1) in water		
evaporative	3	SA-OX
cooling	5	SA-OX, SA
slurry	5	SA-OX
grinding	-	SA

The formation of SA-OX was successful under all of the experiments investigated apart from neat grinding with a stoichiometric ratio of 1:1. Selective isolation of SA-OX was found to be successful under cooling crystallisation and slurrying with a stoichiometric ratio of 2:1 and evaporative crystallisation and slurrying with a stoichiometric ratio of 1:1. Characteristic strong Bragg reflections for the new solid form, SA-OX, are highlighted in red and those of SA in blue in figure 5-4 and figure 5-5.

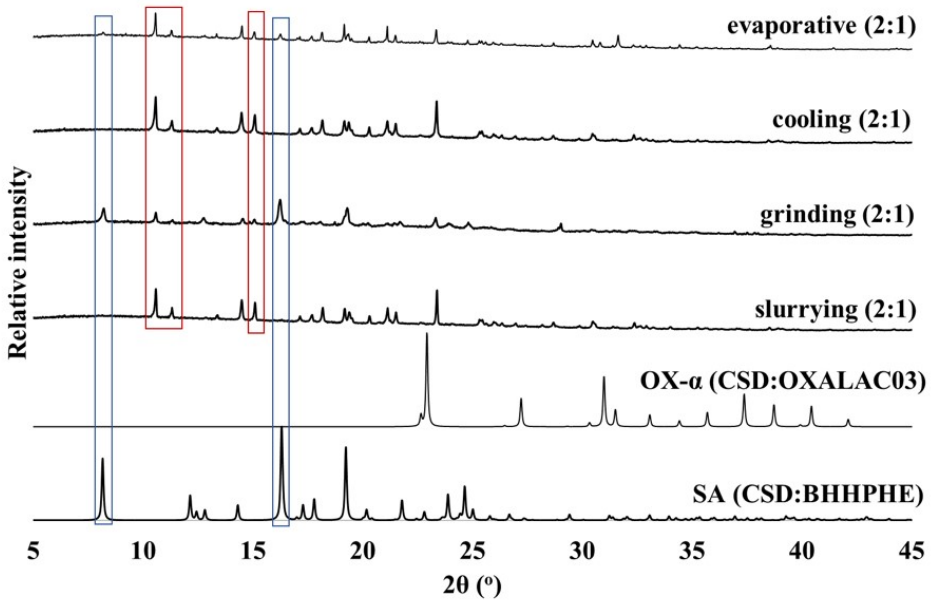

Figure 5-4: The PXRD traces for 2:1 SA and OX co-crystallisation experiments under different crystallisation methods. Characteristic Bragg reflections for a new solid form are highlighted in red and those for SA are in blue.

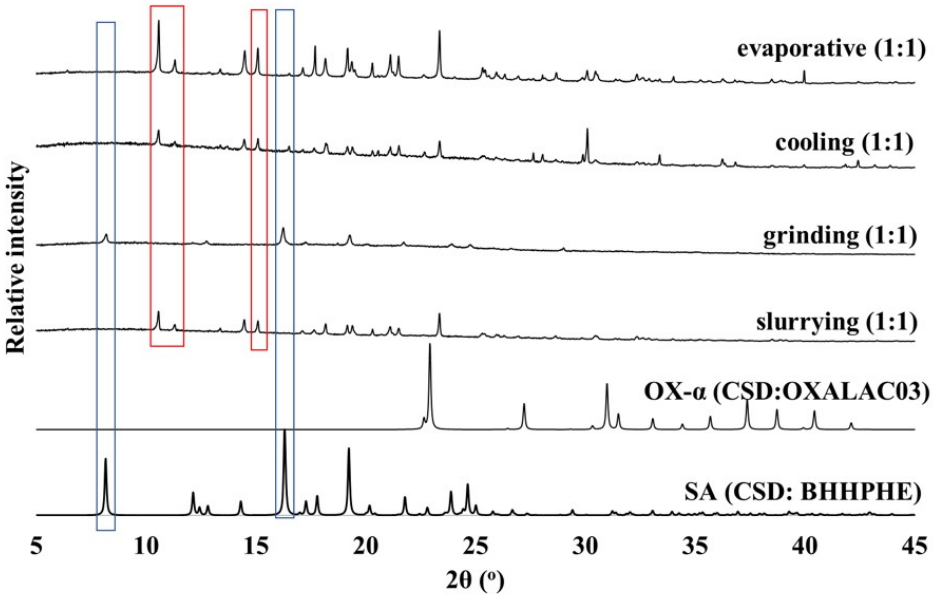

Figure 5-5: The PXRD traces for 1:1 SA and OX co-crystallisation experiments under different crystallisation methods. Characteristic Bragg reflections for a new solid form are highlighted in red and those for SA are in blue.

Further analysis by DSC confirmed the successful isolation of SA-OX and identified the melting point of SA-OX to be 195^{o}C. Figure 5-6 shows the DSC traces of products from co-crystallisation experiments under slurrying (2:1), cooling crystallisation (2:1) and evaporative crystallisation (1:1).

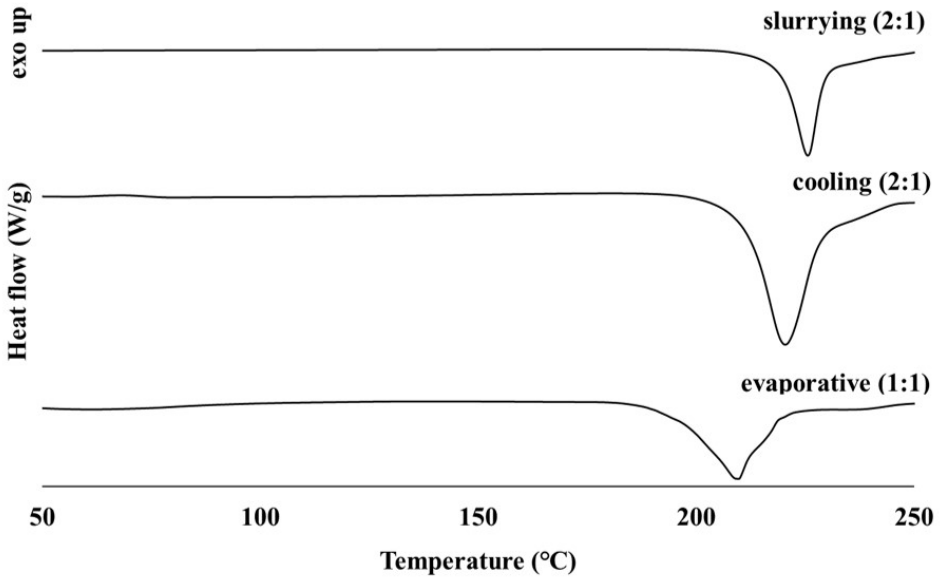

Figure 5-6: The DSC traces of SA and OX co-crystallisation experiments under slurrying (2:1), cooling crystallisation (2:1) and evaporative crystallisation (1:1).

5.4.2 Salbutamol and succinic acid

The formation of the new solid form SA-SU was further investigated with a stoichiometric ratio of 2:1 in EtOH. Table 5.4 shows a summary of the crystallisation conditions explored and the solid forms identified from the characterisation of material with PXRD and DSC. Figure 5-7 displays the PXRD traces for each experiment.

Table 5.4: The material obtained from various crystallisation methods with succinic acid.

crystallisation method	**volume (mL)**	**material obtained**
salbutamol + succinic acid (2:1) in EtOH		
evaporative	3	SA-SU, SA
cooling	5	SA-SU, SA
slurry	5	SA-SU, SA
grinding	-	SA, SU

The formation of SA-SU was successful under slurrying, evaporative and cooling crystallisation with a stoichiometric ratio of 2:1 in EtOH. Characterisation by PXRD suggested the formation of pure SA-SU under slurrying and cooling crystallisation; no Bragg reflections for starting materials SA or SU were observed. Characteristic Bragg reflections for the new solid form, SA-SU, are highlighted in red and those for SA in blue in figure 5-7.

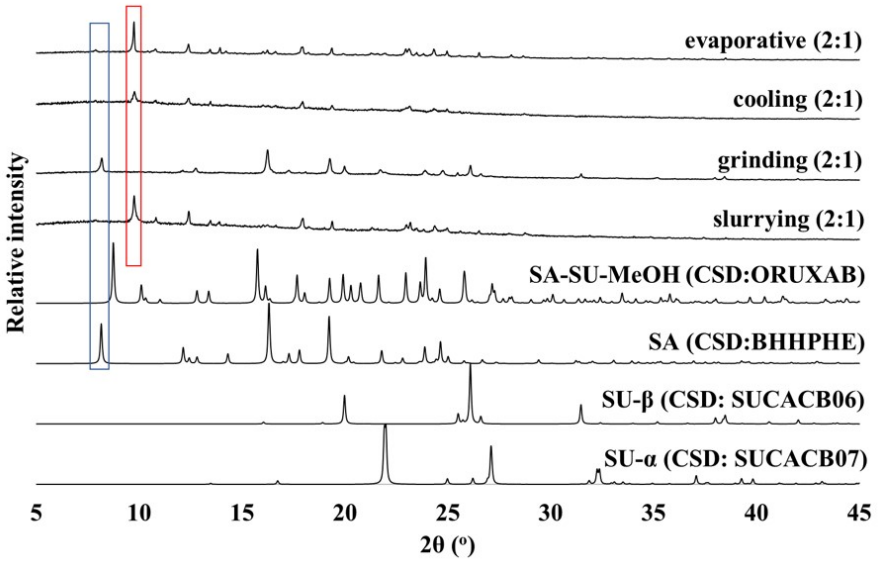

Figure 5-7: The PXRD traces for 2:1 SA and SU co-crystallisation experiments under different crystallisation methods. Characteristic Bragg reflections for a new solid form are highlighted in red and those for SA are highlighted in blue.

Material characterisation by DSC identified impurities in the bulk material; SA was observed alongside SA-SU in the product from slurrying and cooling co-crystallisation experiments. SA melting was observed at 158^{o}C[187] in the DSC traces alongside that of SA-SU at 110^{o}C (figure 5-8). A endotherm was observed at *ca.* 70^{o}C in the DSC trace under slurrying, which could be due to EtOH desolvation and suggest presence of a solvate. A melting endotherm for the co-former SU as a single entity (at 188^{o}C)[188] was not observed in the DSC traces.

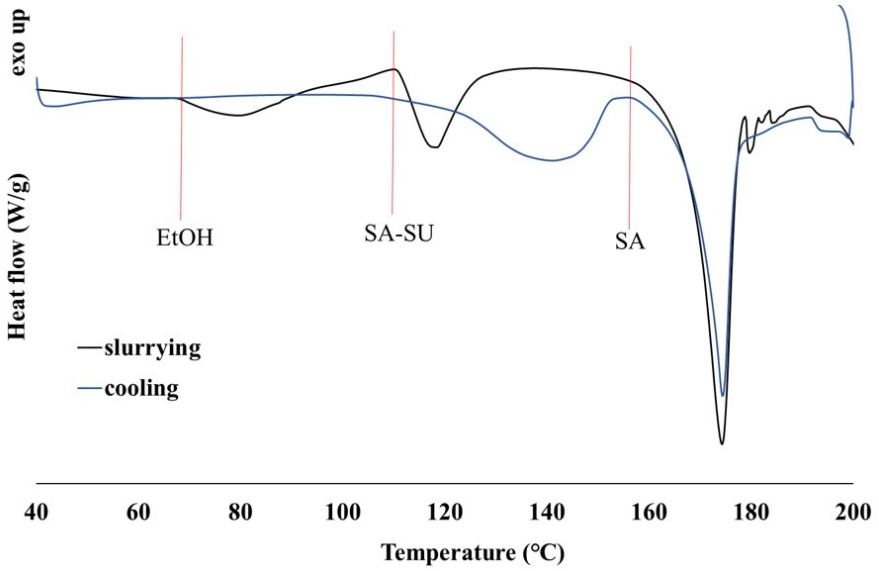

Figure 5-8: The DSC traces for 2:1 SA and SU co-crystallisation experiments under slurrying (black) and cooling crystallisation (blue).

5.4.3 Salbutamol and glutaric acid

The formation of the new solid form SA-GL was further investigated with a stoichiometric ratio of 2:1 in EtOH. Table 5.5 shows a summary of the crystallisation conditions explored and the solid forms identified from the characterisation of material with PXRD and DSC. Figure 5-9 displays the PXRD traces for each experiment.

Table 5.5: The material obtained from various crystallisation methods with glutaric acid.

crystallisation method	**volume (mL)**	**material obtained**
salbutamol + glutaric acid (2:1) in EtOH		
evaporative	3	SA-GL
cooling	5	SA-GL
slurry	5	SA-GL, GL
grinding	-	SA

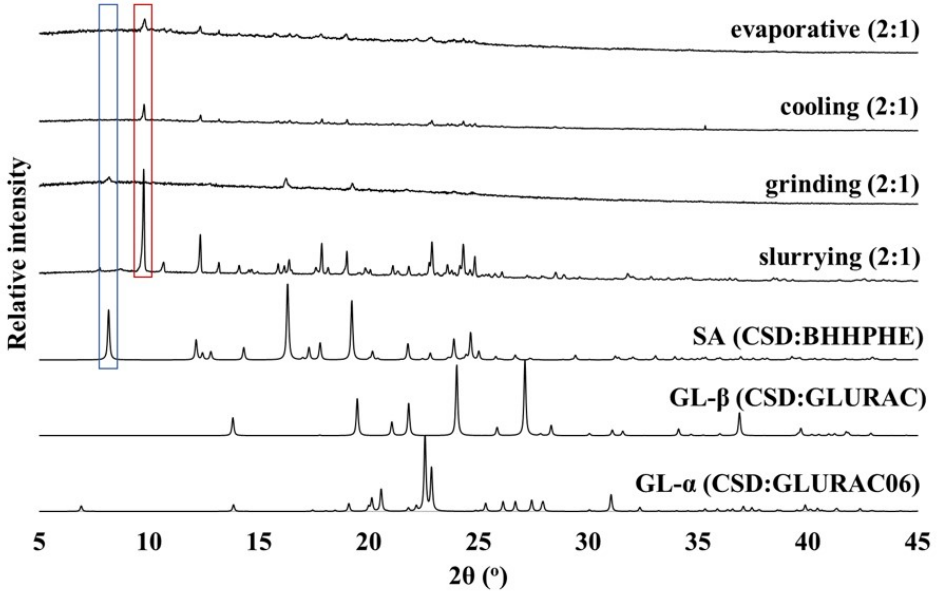

Figure 5-9: The PXRD traces for 2:1 SA and GL co-crystallisation experiments under different crystallisation methods. Characteristic Bragg reflections for a new solid form are highlighted in red and for SA are highlighted in blue.

The formation of SA-GL was successful under slurrying, evaporative and cooling crystallisation with a stoichiometric ratio of 2:1 in EtOH. Weak intensity Bragg reflections were observed in the PXRD traces (from the evaporative, cooling and grinding experiments) which made it difficult to identify the presence of residual starting material. Characteristic Bragg reflections for a new solid form are highlighted in red and SA in blue in figure 5-9. The material obtained under slurrying was selected for further characterisation by DSC and TGA (figure 5-10) since it appeared the most crystalline compared to the material afforded from other methods. Two potential melting points for the product of these SA-GL experiments were identified. The first endotherm, labelled SA-GL-X, was seen at 144^{o}C and the second endotherm, labelled SA-GL-Y, at 180^{o}C after a re-crystallisation (circled in blue). It is believed that SA-GL-Y

is a thermodynamically stable form and SA-GL-X is a metastable form of SA-GL. A weak endotherm around 60°C was observed in the DSC trace, potentially indicating desolvation, but no mass loss was observed in the TGA trace (green) to confirm the presence of solvent.

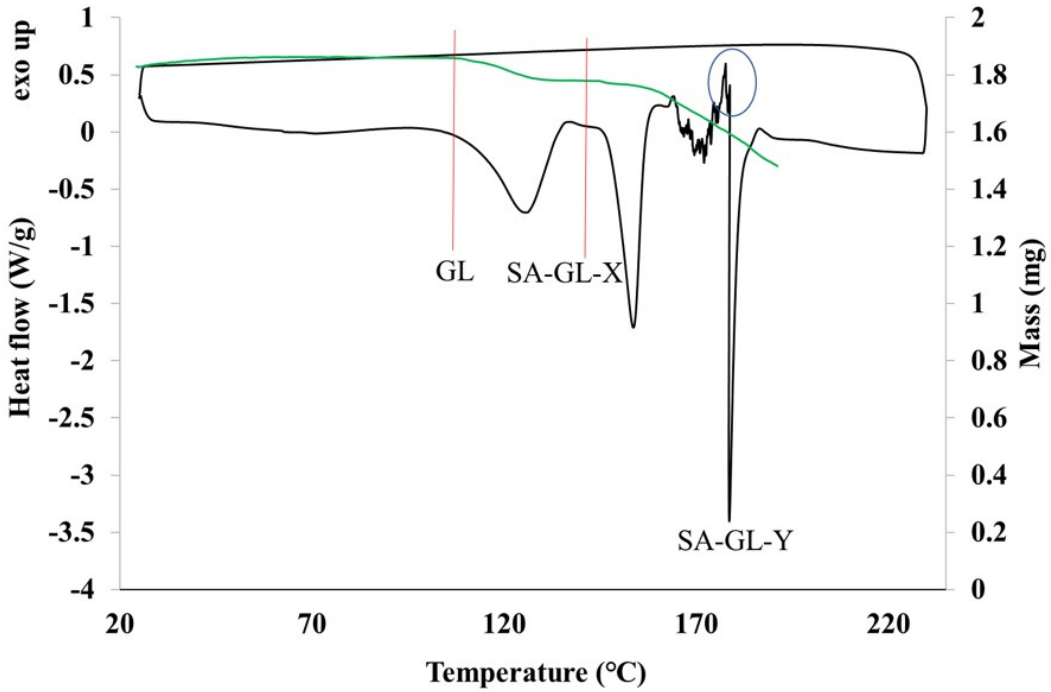

Figure 5-10: The DSC (black) and TGA (green) traces for the co-crystallisation of 2:1 SA and GL under slurrying.

5.4.4 Salbutamol and adipic acid

The formation of SA-AD was further investigated by crystallisation from a solution that contained stoichiometric ratios of 1:1 and 2:1 SA:AD in water. Table 5.6 shows a summary of the crystallisation conditions explored and the solid forms identified from the characterisation of material by PXRD, DSC and ^{1}H NMR spectroscopy. Figure 5-11 and figure 5-12 display the PXRD traces for each experiment.

Table 5.6: The material obtained from various crystallisation methods with adipic acid.

crystallisation method	volume (mL)	material obtained
salbutamol + adipic acid (1:1) in water		
evaporative	3	SA-AD
cooling	5	SA-AD
slurry	5	SA-AD
grinding	-	SA-AD
salbutamol + adipic acid (2:1) in water		
evaporative	3	amorphous material
cooling	5	AD, solid form-X
slurry	5	SA-AD, solid form-X
grinding	-	SA-AD, SA, AD, solid form-X

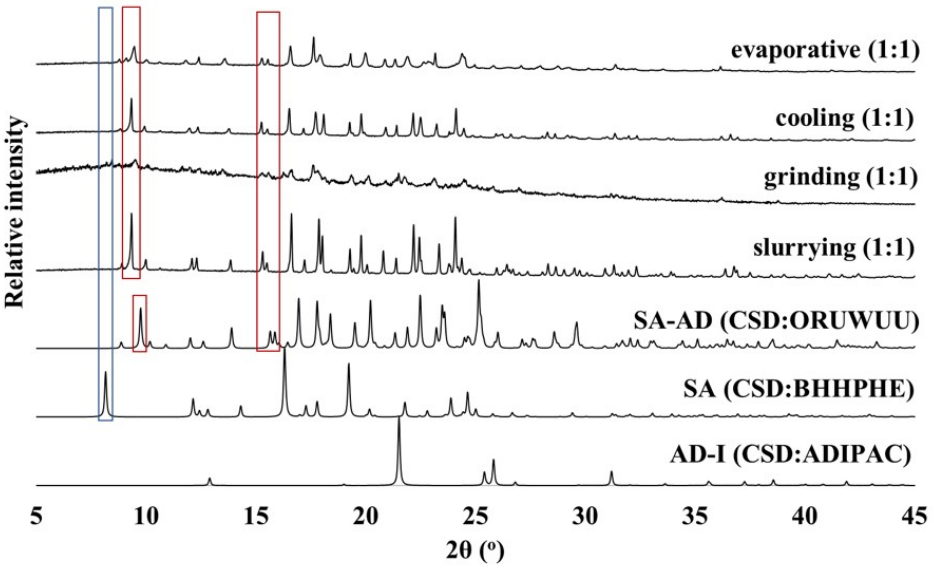

Figure 5-11: The PXRD traces for 1:1 SA and AD co-crystallisation experiments under different crystallisation methods. Characteristic Bragg reflections for SA-AD are highlighted in red and those for SA are highlighted in blue.

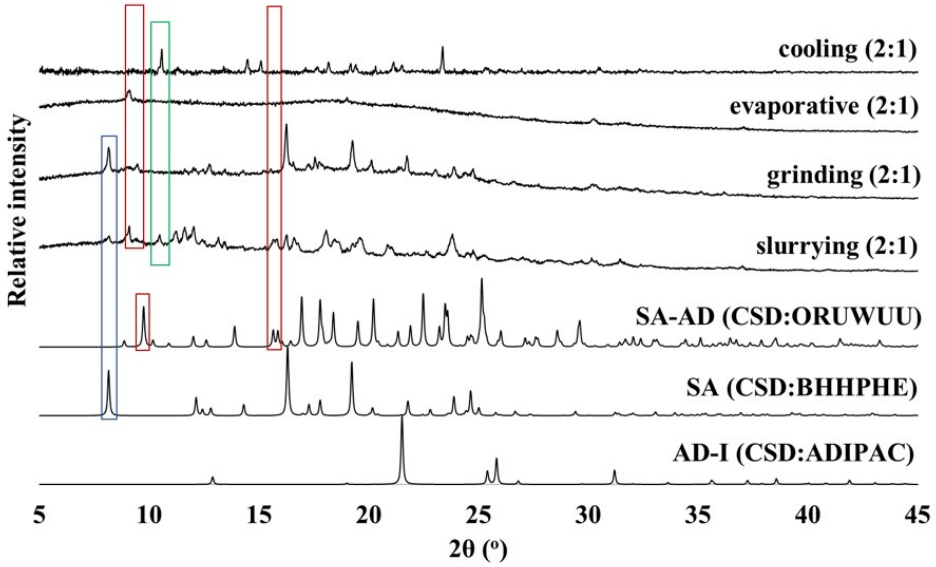

Figure 5-12: The PXRD traces for 2:1 SA and AD co-crystallisation experiments under different crystallisation methods. Characteristic Bragg reflections for SA-AD are highlighted in red, those for SA in blue and those for form-X in green.

The selective isolation of SA-AD was found to be successful under all of the experiments investigated with a stoichiometric ratios of 1:1. Mechanical grinding was found to afford a product material of poor crystallinity. Experiments with a stoichiometric ratio of 2:1 afforded a new solid form, henceforth referred to as form-X, under cooling crystallisation and slurrying. Bragg reflections for form-X are highlighted in green, SA in red and SA-AD in blue in figure 5-11 and figure 5-12. Bragg reflections for form-X were not observed in the PXRD trace from the product obtained under grinding but a melting endotherm corresponding to this phase was observed by DSC.

The bulk material from 2:1 experiments was further characterised by DSC (figure 5-13). A melting point at 175-180^{o}C was observed for form-X in the DSC trace from the product obtained under grinding and slurrying. A very broad melting endotherm corresponding to this phase was found in the product obtained under cooling crystallisation. Re-crystallisation of SA-AD to form-X is observed in the traces for grinding and slurrying experiments but form-X is not seen to precede SA-AD in the product obtained under cooling crystallisation. The re-crystallisation of SA-AD to form-X could be a polymorphic transition, which would suggest that form-X is another polymorphic form of SA-AD. Additional endotherms were observed including a broad melting endotherm for AD at 140-150^{o}C (a melt point of 151^{o}C is reported by Sigma-Aldrich), in the product obtained under cooling and grinding experiments, and a melting endotherm for SA at 160^{o}C,[187] in the product obtained under grinding experiments. Single crystals of form-X were crystallised under cooling, however, attempts by in-house data collection to determine a crystal structure were unsuccessful.

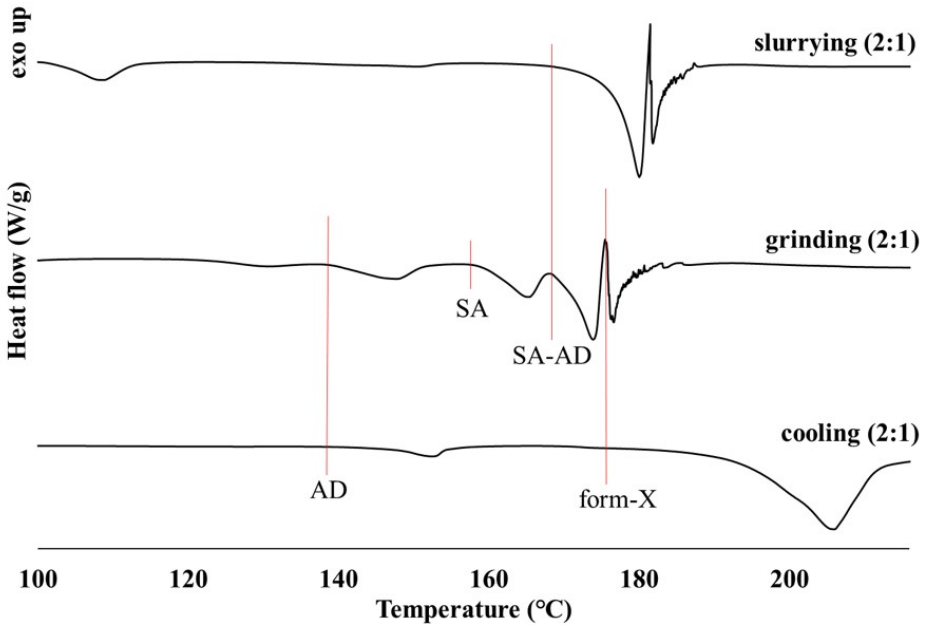

Figure 5-13: The DSC traces for the co-crystallisation of 2:1 SA and AD under slurrying, grinding and cooling crystallisation.

The stoichiometric ratio of components used under evaporative crystallisation experiments was found to have a large influence on the crystallinity of the resultant material. A stoichiometric ratio of 2:1 afforded an amorphous material with a visually orange colour, as seen in figure 5-14. In contrast, a 1:1 stoichiometric ratio afforded a crystalline white material identified as SA-AD, also shown in figure 5-14.

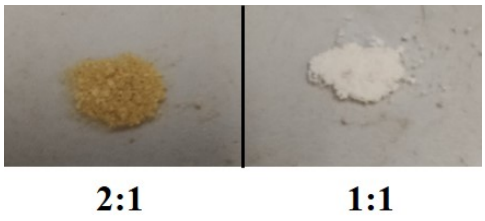

Figure 5-14: Images of the material afforded under evaporative crystallisation with stoichiometric ratios of 2:1 and 1:1 SA and AD.

The crystallinity of both materials was compared by PXRD (figure 5-15). A broad hump and a lack of sharp Bragg reflections suggested the presence of an amorphous material alongside small amounts of crystalline material under a 2:1 stoichiometric ratio. In comparison, a crystalline material was observed under a 1:1 stoichiometric ratio with sharp Bragg reflections seen in the PXRD pattern.

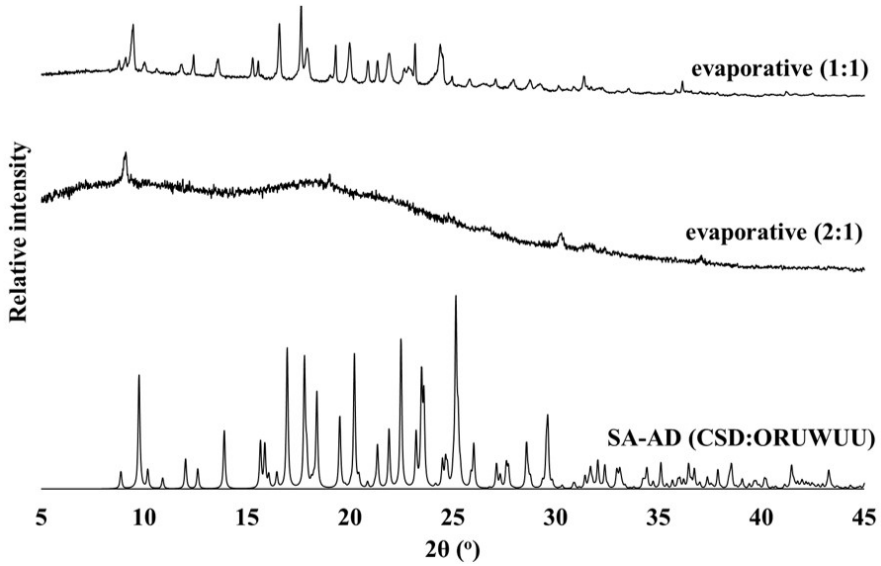

Figure 5-15: The crystallinity difference between the co-crystallisation product of SA and AD, 1:1 and 2:1, under evaporative crystallisation.

The DSC traces (figure 5-16) confirmed these results, a T_g at 35^{o}C (highlighted in red) was observed in the DSC trace of the amorphous 2:1 material while a melting endotherm at 160^{o}C was observed in the crystalline 1:1 material. Further characterisation of the amorphous material by ^{1}H NMR spectroscopy confirmed the presence of SA and AD (figure 9-25 in the Appendix). From these results it was concluded that the amorphous material is likely to be SA-AD or form-X.

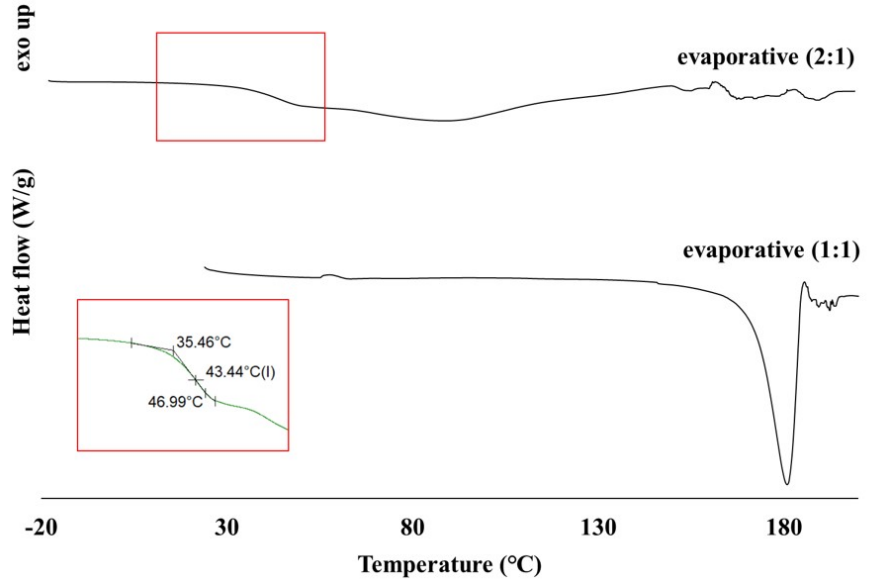

Figure 5-16: The DSC traces for the co-crystallisation of SA and AD, 1:1 and 2:1, under evaporative crystallisation. The red box highlights and provides a larger image of the glass transition event observed in the upper 2:1 trace.

5.5 Stability studies at elevated temperatures and humidities

Stability testing of new materials is important, as it can provide evidence of how the quality of an API may vary over time, when under the influence of environmental factors such as temperature and humidity. The purpose of stability testing is to identify the environmental limits of a drug material for storage and transportation. The stability of SA-OX, SA-SU, SA-GL and SA-AD (crystalline and amorphous material) were characterised empirically for up to six weeks at elevated temperatures of 70^{o}C and at low (10%) and high (80%) relative humidity.

5.5.1 Stability testing results for SA-OX

SA-OX was found to be stable for six weeks when stored at 70^{o}C and in a relative humidity chamber at 10% and 80% RH. Figure 5-17 displays the PXRD traces of the multi-component complex when under the influence of the environmental factors discussed. No signs of transition, decomposition or amorphisation were observed.

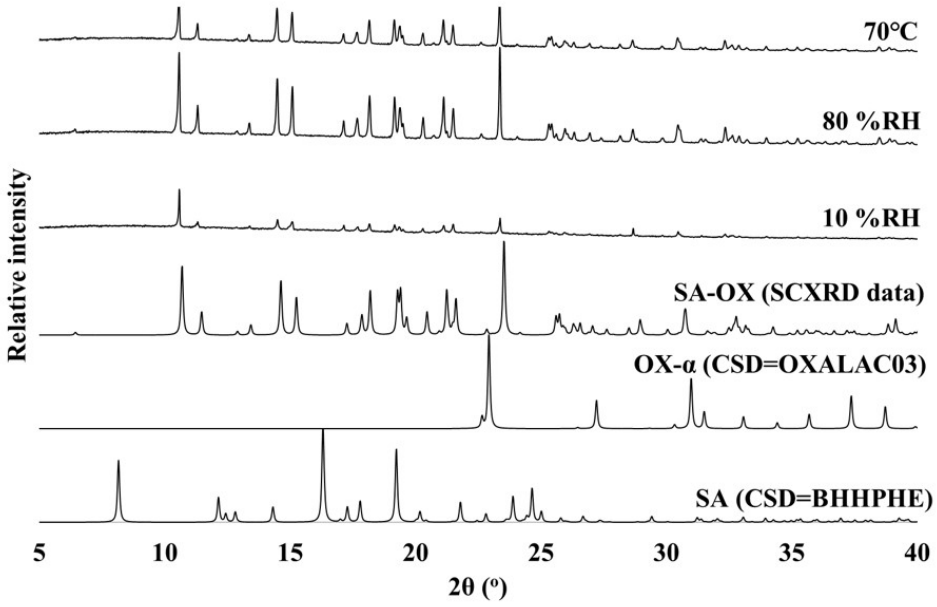

Figure 5-17: The stability of SA-OX, characterised by PXRD, after six weeks when stored at 70^{o}C and at relative humidities of 10% and 80%.

5.5.2 Stability testing results for SA-SU

The bulk material from slurrying methods, found to contain SA-SU, was used for stability tests. The material was characterised by PXRD (figure 5-18) and DSC (figure 5-19) and was found to be unstable after one week of storage. Desolvation occurred when held at 70^{o}C and a relative humidity of 10%. EtOH desolvation was no longer seen in the DSC traces and a melting point was seen at 172^{o}C (compared to the solvated form at 110^{o}C). Bragg reflections for the desolvated form were seen to become more prominent by PXRD (highlighted in green). Isolation of desolvated-SA-SU was obtained when stored at 70^{o}C. In contrast, reflections for SA-SU (highlighted in red) were seen alongside desolvated-SA-SU when held at a relative

humidity of 10%. Interestingly, a melting point for SA-SU was not seen in the DSC trace but another endotherm (circled in blue in figure 5-19) was seen at 160^{o}C. This could be SA (melting point = 157^{o}C)[187] or an additional new solid form. The PXRD pattern supports the formation of a new solid form; unidentified Bragg reflections are highlighted in yellow.

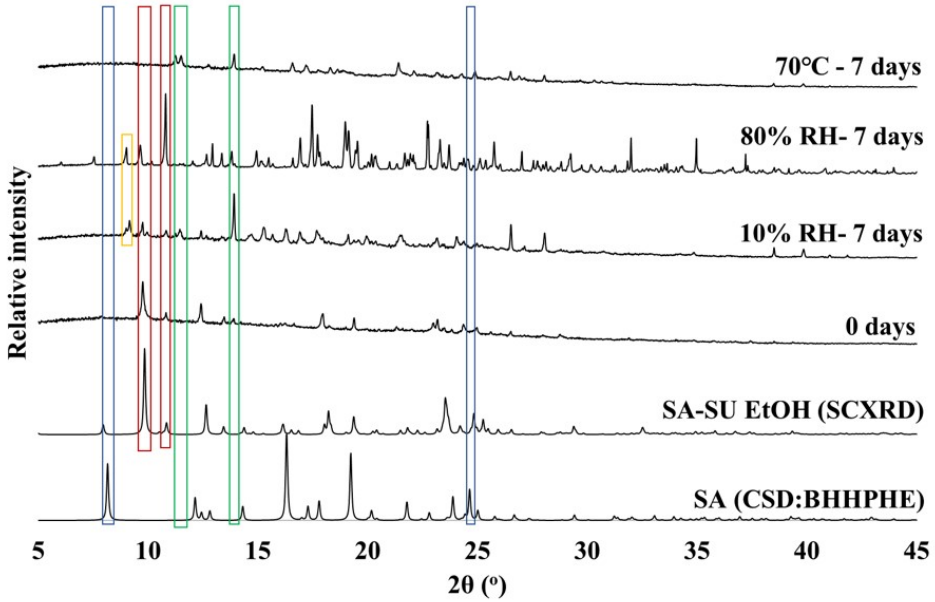

Figure 5-18: The stability of SA-SU, characterised by PXRD, after one week when stored at 70^{o}C and at relative humidities of 10% and 80%.

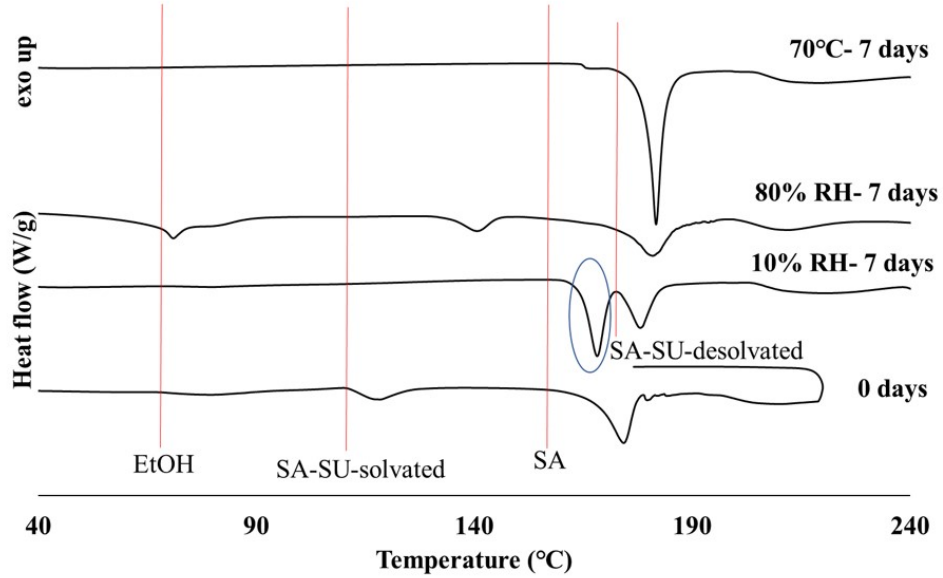

Figure 5-19: The stability of SA-SU, characterised by DSC, after one week when stored at 70^{o}C and at relative humidities of 10% and 80%.

When held in a relative humidity chamber at 80% RH, the material was found to be stable and desolvation did not occur. SA-SU was observed by PXRD (highlighted in red) and DSC. Signs of a transition into an additional, unidentified, solid form were again seen in the PXRD pattern

(also highlighted in yellow in figure 5-18). Broad endotherms made it difficult to identify this form, a sign of an impure material. A broad endotherm for SA appeared to be present in the DSC trace, however, Bragg reflections for SA are not seen by PXRD (absent reflections are highlighted in blue).

5.5.3 Stability testing results for SA-GL

The bulk material from slurrying methods, showing good crystallinity and found to contain two polymorphic forms, SA-GL-X and SA-GL-Y, was used for stability tests. The material was characterised by PXRD (figure 5-20) and DSC (figure 5-21) after one week of storage at an elevated temperature of 70^{o}C and in a relative humidity chamber at 10% and 80% RH. A new set of Bragg reflections was seen by PXRD under each of the conditions tested suggesting a new solid form, with a melting endotherm at 150^{o}C (similar to the melting endotherm for SA-GL-X).

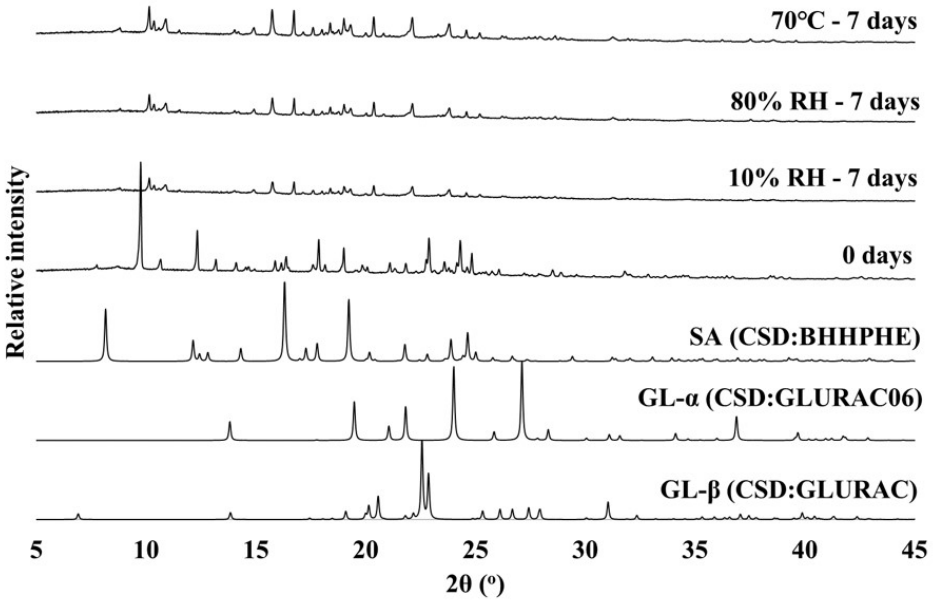

Figure 5-20: The stability of SA-GL, characterised by PXRD, after one week when stored at 70^{o}C and at relative humidities of 10% and 80%.

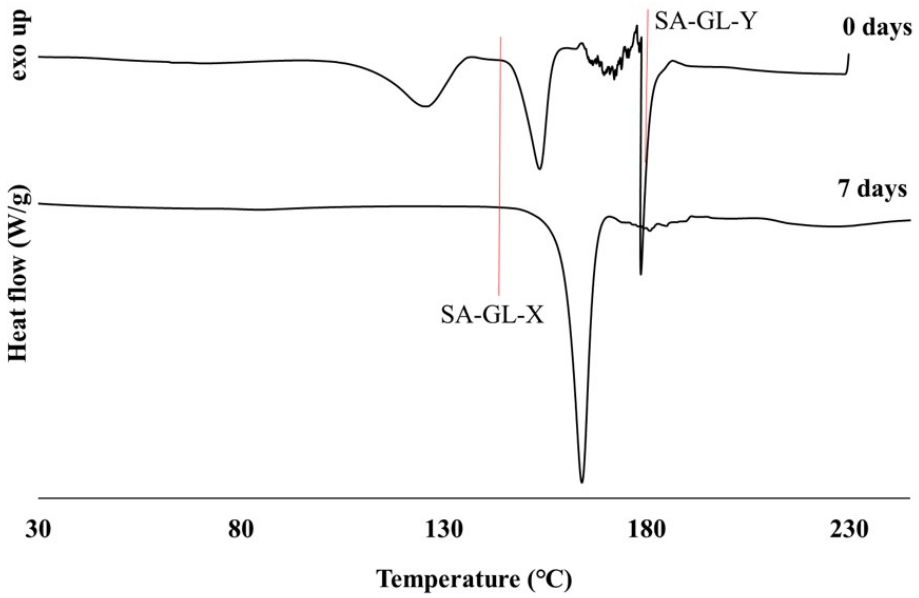

Figure 5-21: The stability of SA-GL, characterised by DSC, after one week when stored at 70^{o}C and at relative humidities of 10% and 80%.

5.5.4 Stability testing results for SA-AD

The stability of crystalline and amorphous SA-AD were tested. Crystalline SA-AD was found to be stable for six weeks when stored in a relative humidity chamber at 10% and 80% RH (figure 5-22). No signs of transition, decomposition or amorphisation were observed. The crystalline material was not stable when held at 70^{o}C. At this temperature, no Bragg reflections were seen in the pattern, a sign of amorphisation.

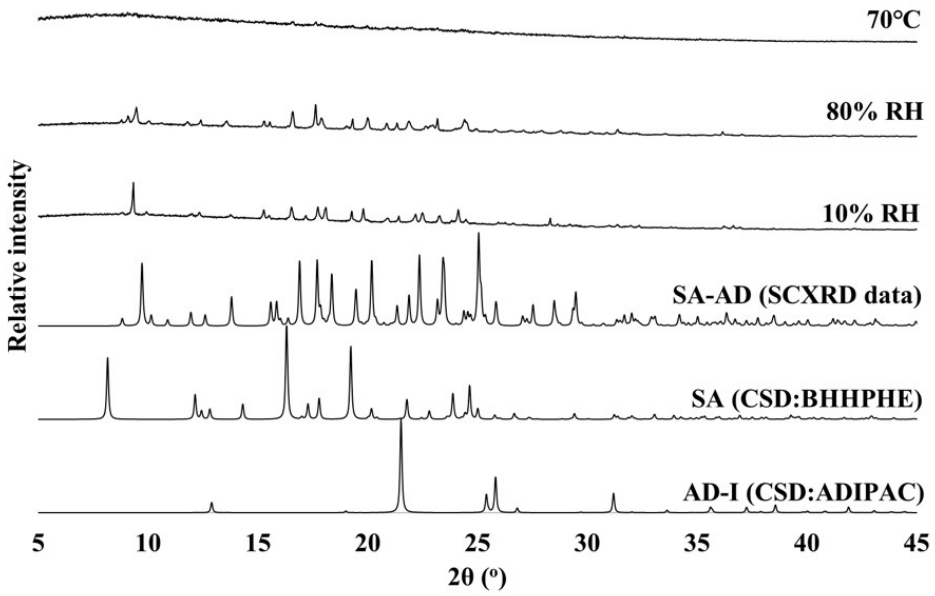

Figure 5-22: The stability of crystalline SA-AD, characterised by PXRD, after six weeks when stored at 70^{o}C and at relative humidities of 10% and 80%.

Amorphous SA-AD was stable in an amorphous state when held for six weeks at an elevated temperature of 70^{o}C and at a relative humidity of 10% and 80%. The amorphous material remained in a solid state after stability testing at 70^{o}C and a relative humidity of 10% and characterisation by PXRD was conducted (figure 5-23). The material held in a relative humidity of 80% turned into an oil shortly after being placed into the chamber and was not characterised by PXRD. The material remained in this state for six weeks.

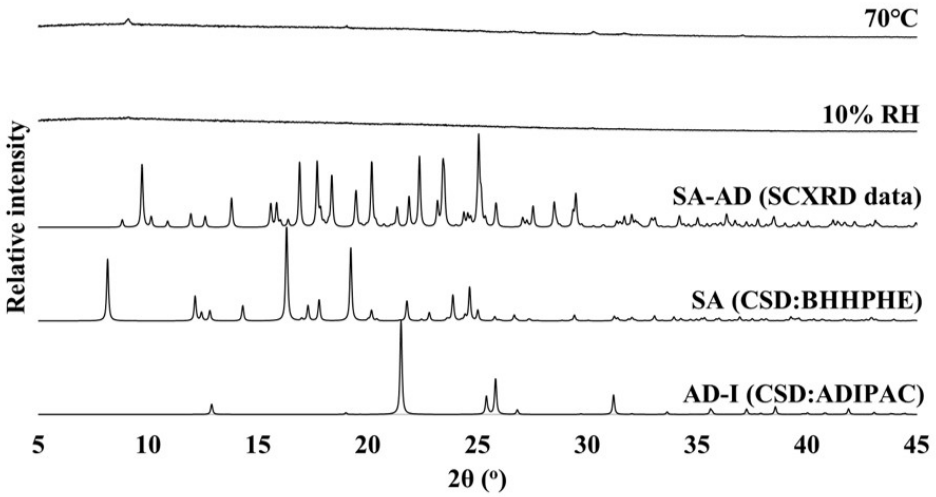

Figure 5-23: The stability of amorphous SA-AD, characterised by PXRD, after six weeks when stored at 70^{o}C and at relative humidities of 10% and 80%.

5.6 Solubility measurements

The solubility of multi-component complexes SA-OX and SA-AD was determined in water and compared to the active ingredient, SA, in water. The solubility curve of SA-OX was measured using observational methods (as described in section 3.2.1.2). The solubility measurements were taken twice and an average value was plotted with an error of +/- 1^{o}C. The solubility curves of SA-AD and SA were measured using gravimetric methods (as described in section 3.2.1.1). The solubility measurements were taken twice and an average value plotted with an error of +/-0.004 g for SA-AD and +/-0.003 g for SA. The solubilities of SA-SU and SA-GL were not measured in this work since the pure material of each form was not isolated.

SA-OX and SA-AD have a limited solubility in water and have a slightly lower solubility than SA in water (figure 5-24). The solubility of SA-OX is slightly increased by temperature, whilst that of SA-AD is essentially unchanged by temperature. According to the US. Pharmacopoeia, a solid form that has an aqueous solubility of 10-33 mg mL^{-1}, such as SA-OX and SA-AD, is characterised as sparingly soluble.[6]

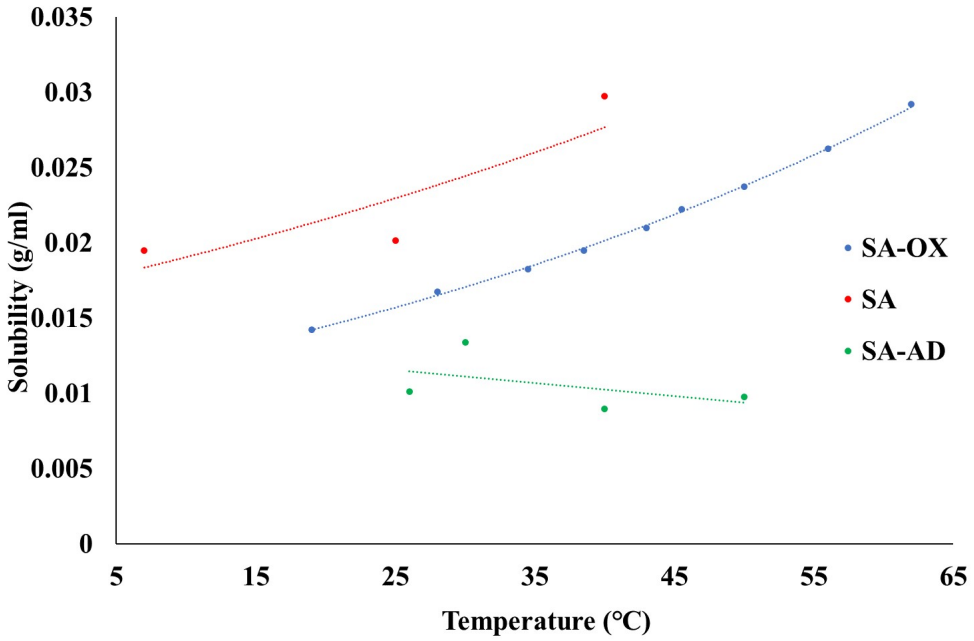

Figure 5-24: The solubility curves of SA, SA-OX and SA-AD in water.

The solubility curve of the marketed form, SAS (trade name, Proventil HFA) was measured using observational methods and compared to that of SA, SA-OX and SA-AD. The marketed salt formulation, SAS, is seen to be substantially more soluble than the other multi-component complexes (figure 5-25).

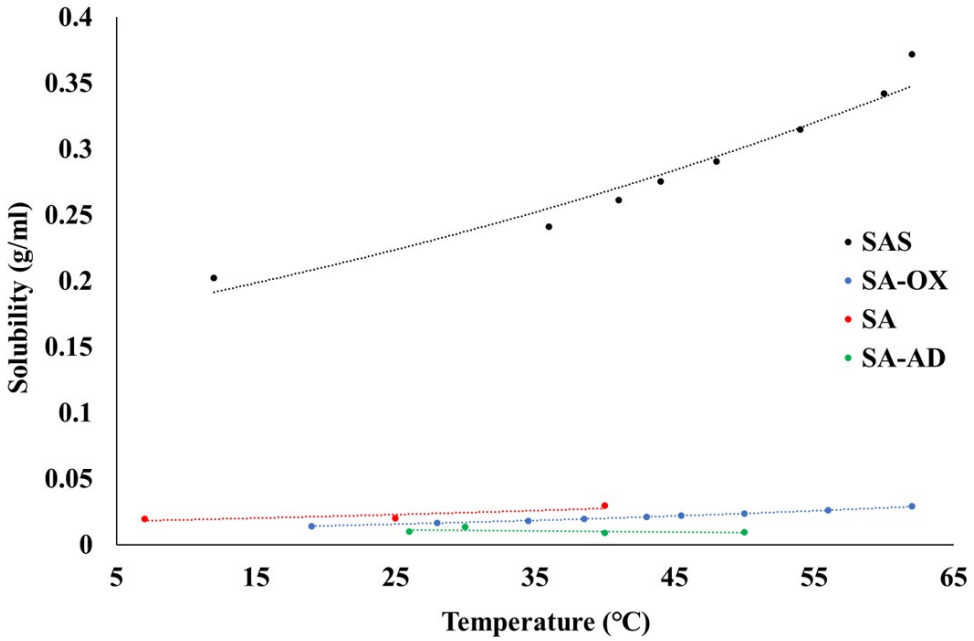

Figure 5-25: The solubility curves of SA, SA-OX and SA-AD compared to SAS in water.

5.7 Investigating the structural nature of SA and its multi-component complexes

The structural nature of solid forms SA, SA-OX, SA-SU and SA-AD was characterised by several methods. X-ray crystallography and ^{1}H NMR spectroscopy were used to determine the molecular structure of each solid form. A delocalisation study was used to investigate the interactions between the two components and to identify if the complexes were neutral or molecular ionic complexes (also known as co-crystalline salts). The determined crystal structures of SA and SA-AD in this work are compared to the structures of the same solid form previously determined and available in the CSD.

5.7.1 The structure of SA

The crystal structure of SA was reported by Beale and Grainger[178] in 1972 (CSD code = BHHPHE) to crystallise in the orthorhombic, centrosymmetric, space group Pbca. Figure 5-26a shows the asymmetric unit, found to contain one molecule of SA. The packing of SA, viewed along the b axis, shows a layered arrangement of the aromatic groups which stack in pairs with branched *tert*-butyl groups meeting in the middle (figure 5-26b).

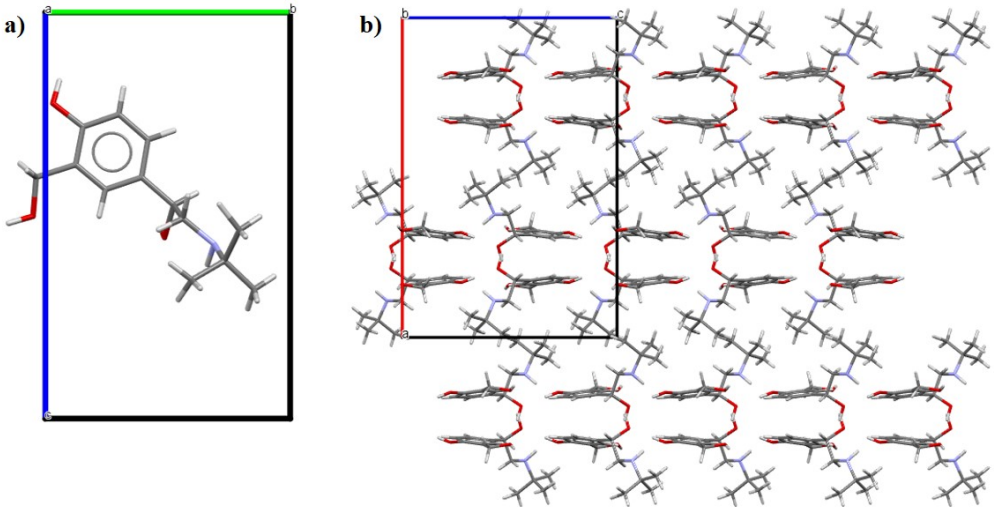

Figure 5-26: The structure of SA showing (a) the asymmetric unit viewed along the a axis and (b) the packing arrangement viewed along the b axis.

The presence of crystallographic disorder is not reported in the crystal structure of SA. To confirm this, the structure of SA was redetermined in this work and modelled with and without multiple site occupancies enforced onto the *C-OH group. A weak cluster of electron density (0.7 e Å^{-3}) was found in a reasonable location for a minor occupancy position to be modelled (figure 9-26 in the Appendix). Table 5.7 shows the refinement parameters for SA modelled with full and partial occupancy positions at the *C-OH chiral centre.

Table 5.7: The unit cell and refinement parameters of SA refined with and without multiple site occupancies.

complex code	**SA (full occupancy)**	**SA (multiple occupancies)**
formula	$C_{13}H_{21}N_1O_3$	$C_{13}H_{21}N_1O_3$
g mol^{-1}	239.31	239.31
T (K)	150 (10)	150 (10)
radiation	Cu Kα($\lambda = 1.54184$)	Cu Kα($\lambda = 1.54184$)
2θ range (^{o})	8.274 to 146.194	8.274 to 146.15
crystal system	orthorhombic	orthorhombic
space group	Pbca	Pbca
a (Å)	8.7871(3)	8.7872(3)
b (Å)	14.4645(5)	14.4664(6)
c (Å)	21.3744(7)	21.3745(8)
$\alpha(^o)$	90	90
$\beta(^o)$	90	90
$\gamma(^o)$	90	90
volume (Å^3)	2716.72(16)	2717.11(18)
Z	8	8
density (g cm^3)	1.170	1.170
$\mu(mm^{-1})$	0.668	0.668
completeness (%)	98.8	99.8
reflections collected	6797	6797
independent reflections	2674	2674
data/restraints/parameters	2674/0/170	2674/7/181
R int	0.0385	0.0364
GooF	1.123	1.112
R_1 (obs)	0.1088	0.1130
R_1 (all)	0.1235	0.1244
wR_2 (all)	0.3300	0.3354
$\rho_{max,min}$ (e Å^{-3})	0.78/-0.68	0.72/-0.51
atomic occupancy	-	0.12(5) : 0.88(5)

Upon refinement of multiple site occupancies, a minor position of 0.12(5) was seen. No significant differences were observed between the refinement parameters of the two models in table 5.7. However, when refined with multiple site occupancies, a CHECK CIF alert (level A) reading "ADP of Atom O3A is N.P.D. or nearly 2D", suggested that the site occupancies should not be split. No dynamic disorder (thermal motion) was observed around the *C-OH group. Figure 5-27 shows the size of the ellipsoids in the structure of SA refined without multiple site occupancies (a) and with multiple site occupancies (b). In both cases, the elongation of ellipsoids, corresponding to thermal motion, was only observed in the tert-butyl group and not in the *C8-O3-H region. Furthermore, a significantly small angle of 19(3)^o between the atoms O3a-C8-O3 in b was measured. This shows a significantly close proximity between the multiple site occupants which seem to almost merge into a single site. These observations suggested that the chiral centre (*C-OH) of SA has a chemical occupancy value of one. This is in agreement with the model published by Beale and Grainger[178] and confirms the previous finding that SA does not show signs of crystallographic disorder as a single entity.

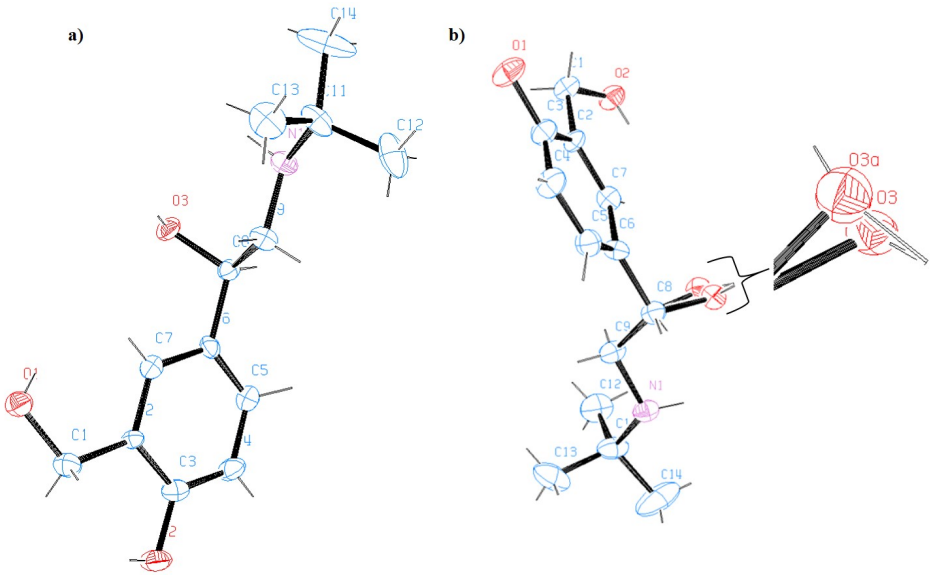

Figure 5-27: The structure of SA showing the size of ellipsoids in labelled atoms refined with (b) and without (a) multiple site occupancies.

5.7.2 The structure of SA-OX

SA-OX is a novel solid form discovered in this work. The multi-component complex crystallises in the monoclinic, centrosymmetric, space group $P2_1/n$. Figure 5-28a displays the asymmetric unit of SA-OX, found to contain a molecule of SA alongside half a molecule of OX (salbutamol hemi-oxalate). Multiple site occupancies are observed around the chiral centre (*C-OH) of SA, labelled O6, O6A C8 and C8A, showing that a disordered complex has been produced, one of the original aims of the co-crystallisation investigation. Figure 5-28b displays the packing arrangement in the complex, viewed along the a axis. Chains of SA molecules are seen to assemble between chains of OX molecules.

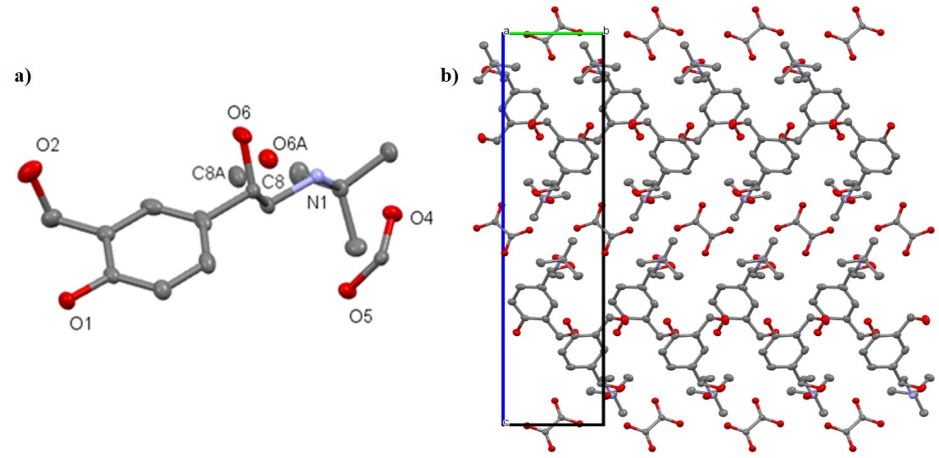

Figure 5-28: The structure of SA-OX showing (a) labelled atoms and (b) the packing arrangement viewed along the a axis.

The ^{1}H NMR spectroscopy spectrum of SA-OX (figure 9-27 in the Appendix) shows hydrogen environments for SA and not OX due to ion exchange. The ratio of multi-components could therefore not be calculated; however, an API:co-former ratio of 2:1 is evident from the crystallographic data collected.

The hydrogen bond framework in SA-OX is displayed in figure 5-29. The two components are linked by five hydrogen bonds. Two of the hydrogen bonds are charge assisted and proton transfer occurs between a NH_2^+ group and an oxalate ion (hydrogen bonds 1 and 2). Hydrogen bonds 2, 3 are of interest, appearing to be bifurcated hydrogen bonds (also known as three-centered interactions). A bifurcated hydrogen bond describes a configuration in which two or more hydrogen bond acceptors are in close proximity and can simultaneously accept the same hydrogen bond donor group; this type of bond is common in X-ray structures.[189] One element of this bifurcated hydrogen bond involves the disordered *C-OH group in SA. The competition to interact with the same donor atom may influence the presence of crystallographic disorder in SA-OX.

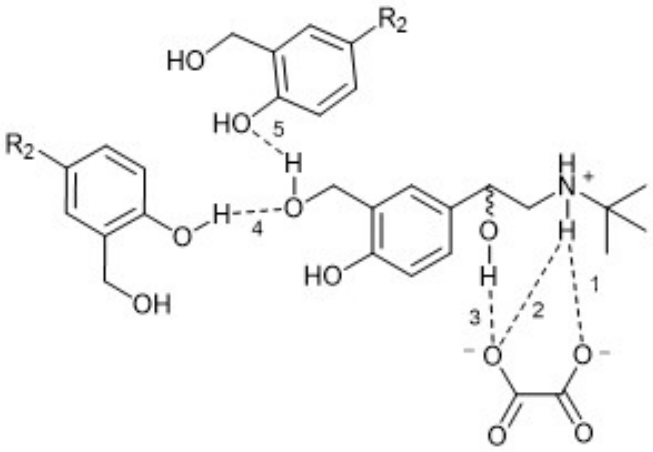

Figure 5-29: The hydrogen bonding frame work in SA-OX.

Table 5.8 shows the distances and angles of the six hydrogen bonds measured in SA-OX at 150 K. The tables relate to the atom labels in figure 5-28a and the labelled hydrogen bonds in figure 5-29.

Table 5.8: The hydrogen bond distance and angles measured in SA-OX at 150 K.

Hydrogen bond distances and angles in salbutamol oxalate at 150 K					
Hydrogen bond	**D-H···A**	**d(D-H) (Å)**	**d(H···A) (Å)**	**d(D···A) (Å)**	**<(DHA) (º)**
1	N1-H···O4[a]	1.93(2)	1.90(2)	2.8164(18)	166.9(19)
2	N1-H···O5	0.88(2)	1.95(2)	2.8215(18)	171(2)
3	O6-H···O5 [b]	0.87(3)	1.97(3)	2.8370(19)	175(3)
4	O2-H···O1[c]	0.85(3)	1.78(3)	2.6241(19)	172(3)
5	O1-H···O2[d]	0.90(3)	2.02(3)	2.8667(17)	157(2)

[a] +X,1+Y,+Z [b] 1-X,2-Y,-Z [c] +X,-1+Y,+Z [d] -1/2-X,1/2+Y,-1/2-Z

Evidence of proton transfer was gathered to support the conclusion that a molecular ionic complex is formed. The bond lengths of a localised co-crystal, monobasic and full oxalate ion were measured in multi-component complexes that contained an OX group in the CSD. The results were compared to the bond lengths of SA-OX, shown in table 5.9. The study suggests that SA-OX contains a fully delocalised oxalate ion. A short C-O bond length of 1.250(3) Å was observed and provided further evidence of proton transfer, which is also supported from the large pKa difference of the two components. The amino group in SA has a pKa of 10.3 and OX a pK_{a1} of 1.36 and pK_{a2} of 4.1.

Table 5.9: The bond lengths of OX when the complex is localised, monobasic and a fully ionised oxalate ion.

CSD code	**delocalisation**	**bond length (Å)**		
		C-OH	**C=O**	**C-O⁻**
OXALAC05	localised	1.303 (2)	1.218 (2)	-
AYUMEN	localised	1.307 (1)	1.199 (1)	-
ATOXAL04	monobasic	1.294(3)	1.243(4) and 1.222(4)	1.258(3)
BAHOXH01	oxalate ion	-	1.232(1)	1.268(2)
SA-OX	oxalate ion	-	1.244(3)	1.250(3)

*OXALAC05 is oxalic acid as a single entity, AYUMEN, ATOXAL04 and BAHOXH01 are multi-component complexes that contain oxalic acid.

5.7.3 The structure of SA-SU

SA-SU is a novel solid form discovered in this work and was found to be a solvate. The multi-component complex crystallises in the triclinic, centrosymmetric, space group $P\bar{1}$. Figure 5-30 displays the asymmetric unit of SA-SU, showing two molecules of SA alongside one molecule of SU and one molecule of EtOH (salbutamol succinate ethanol solvate). Crystallographic disorder around the chiral centre (*C-OH) of SA is observed in one of two molecules; the disordered O atoms are labelled O5 and O5A. The ^{1}H NMR spectroscopy spectrum of SA-SU (figure 9-28 in the Appendix) shows hydrogen environments for SA, SU and EtOH with a 1 : 2 : 0.08 ratio. However, this does not represent the ratio of components in the multi-component complex as the bulk material was found to be impure and contain SA alongside SA-SU (discussed in section 5.4.2). An API : co-former : solvent ratio of 2:1:1 is determined from the crystallographic data collected.

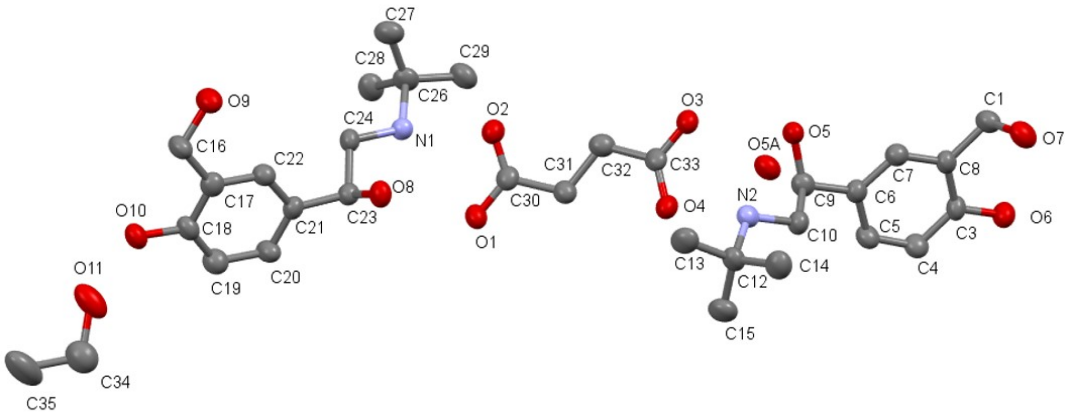

Figure 5-30: The structure of solvated SA-SU showing labelled atoms.

Figure 5-31 displays the packing arrangement in the complex, viewed along the a axis. Four SA molecules are seen to assemble alongside two molecules of SU.

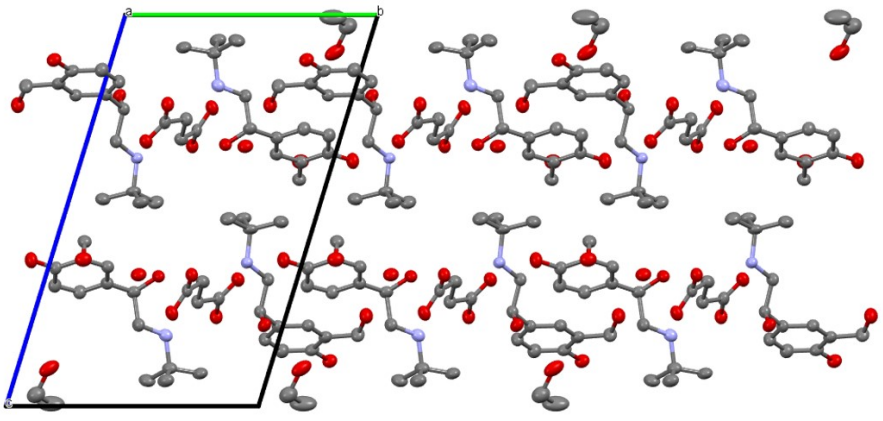

Figure 5-31: The packing arrangement of SA-SU, viewed along the a axis.

The hydrogen bond framework in SA-SU is displayed in figure 5-32. The three components are linked by nine hydrogen bonds. Three of the hydrogen bonds are charge assisted and proton transfer occurs between a NH_2^+ group and a succinate ion (hydrogen bonds 3, 7 and 8). In this case, no bifurcated hydrogen bonds (as observed in the hydrogen bond framework of SA-OX)

are seen in the framework of SA-SU. Table 5.10 shows the distances and angles of the nine hydrogen bonds in SA-SU at 150 K. The tables relate to the atom labels in figure 5-30 and the labelled hydrogen bonds in figure 5-32. EtOH was found to be part of the framework; EtOH molecules form two hydrogen bonds with SA (hydrogen bond 4 and 5 in table 5.10).

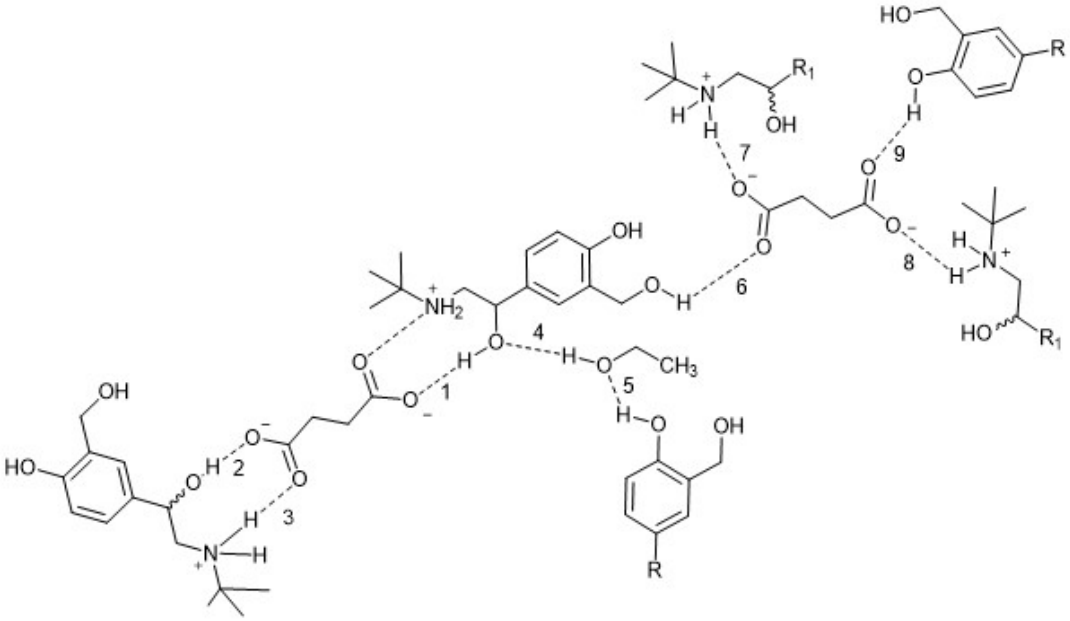

Figure 5-32: The hydrogen bonding framework in SA-SU.

Table 5.10: The hydrogen bond distance and angles measured in SA-SU at 150 K.

Hydrogen bond	D-H···A	d(D-H) (Å)	d(H···A) (Å)	d(D···A) (Å)	<(DHA) (º)
1	O8-H···O1	1.09(8)	1.57(8)	2.646(8)	173(7)
2	O5-H···O3	0.95(7)	1.84(7)	2.735(8)	156(6)
3	N2-H···O4	0.89	1.85	2.738(9)	175.1
4	O11-H···O8 [a]	0.82	1.90	2.713(9)	173.2
5	O10-H···O11	0.82	1.86	2.675(9)	175.9
6	O9-H···O4 [b]	0.82	1.93	2.712(8)	160.4
7	N1-H···O3 [a]	0.89	1.92	2.805(8)	173.7
8	N2-H···O1 [c]	0.89	1.91	2.792(9)	171.1
9	O6-H···O2 [d]	0.82	1.98	2.787(8)	169.5

[a] -1+X,+Y,+Z [b] -1+X,-1+Y,+Z [c] 1+X,+Y,+Z [d] 1+X,1+Y,+Z

* Measurements reported in the absence of an error contain a hydrogen atom that was fixed in an idealised position.

Evidence of proton transfer was gathered that supported the formation of a molecular ionic complex. The bond lengths of a localised co-crystal, monobasic and full succinate ion were measured in multi-component complexes that contained an SU group in the CSD. These were compared to the bond lengths in SA-SU; table 5.11 summarises the results. The study suggests that SA-SU contains a fully delocalised succinate ion. A short C-O bond length of 1.271(9) Å was observed and provided evidence supporting proton transfer. Further support for proton transfer is suggested from the large pKa difference of the two components; the amino group in SA has a pKa of 10.3 and SU a pK_{a1} of 4.21 and pK_{a2} of 5.64.

Table 5.11: The bond lengths of SU when the complex is localised, monobasic and a full succinate ion.

CSD code	**delocalisation**	**bond length (Å)**		
		C-OH	**C=O**	**C-O$^-$**
SUCACB07	localised	1.297(5)	1.231(6)	-
DUFJIA	localised	1.312(2)	1.221(3)	-
MEQPON01	monobasic	1.312(2)	1.221(1) and 1.223(1)	1.293(2)
ORUXAB	succinate ion	-	1.253(2)	1.274(1)
SA-SU	succinate ion	-	1.24(1) and 1.26(1)	1.271(9)

*SUCACB07 is succinic acid as a single entity, DUFJIA, MEQPON01 and ORUXAB are multi-component complexes that contain succinic acid.

5.7.3.1 Comparing the structure of SA-SU solvated with MeOH and EtOH

The crystal structure of salbutamol succinate methanol solvate (SA-SU-MeOH) [182] reported in the CSD (CSD code= ORUXAB) was compared to the novel structure of salbutamol succinate ethanol solvate (SA-SU-EtOH) discovered in this work.

The crystal structure of SA-SU-MeOH contains additional symmetry to SA-SU-EtOH, crystallising in the monoclinic, centrosymmetric, space group $P2_1/n$ (compared to the triclinic $P\bar{1}$ unit cell of the ethanol solvate). The asymmetric unit of SA-SU-MeOH has the same API: co-former ratio of components as that seen in SA-SU-EtOH. However, a 2:1:4 ratio of multi-components (one molecule of SA alongside half a molecule of SU and two molecules of MeOH) is seen in SA-SU-MeOH compared to the 2:1:1 ratio in SA-SU-EtOH. The structure of SA-SU-MeOH thus contains additional solvent molecules and interactions than SA-SU-EtOH; the four-fold increase of solvate molecules in SA-SU-MeOH leads to the formation of solvent-solvent interactions, not observed between the solvent molecules in SA-SU-EtOH. No crystallographic disorder was reported in SA-SU-MeOH, however this may be an oversight since disorder is observed in every other dicarboxylic acid multi-component system of SA.

In the case of SA-SU-MeOH, there are seven hydrogen bonds (figure 5-33). Two of these are SA-SA interactions (hydrogen bonds 3 and 4), three are SA-SU interactions (hydrogen bonds 1, 2 and 5), one is a SA-solvate interaction (hydrogen bond 6) and one is a solvent-solvent interaction (hydrogen bond 7). Similarly to SA-SU-EtOH no hydrogen bonds are seen to be in competition to interact with the same donor atom in the succinate ion, as observed in the hydrogen bond framework of SA-OX. In addition, the same assembly of molecular synthons

is observed between the amine and alcohol group in SA and the carboxylic acid group in SU. This assembly is also observed in SA-OX between SA and OX.

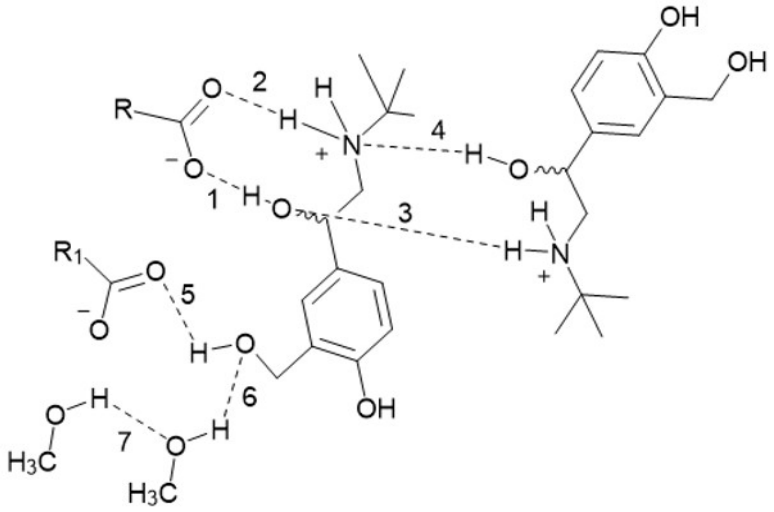

Figure 5-33: The hydrogen bonding framework in SA-SU.

5.7.4 The structure of SA-AD

The crystal structure of SA-AD refined in this work is in good agreement with the structure in the CSD (CSD code= ORUWUU).[182] The multi-component complex crystallises in the triclinic, centrosymmetric, space group $P\bar{1}$. Figure 5-34a displays the asymmetric unit with a molecule of SA alongside half of a molecule of an adipate ion and half a localised molecule of AD (salbutamol adipate adipic acid). Figure 5-34b displays the packing arrangement of SA-AD, viewed along the a axis; chains of SA molecules are seen to assemble between chains of the co-former molecules, AD.

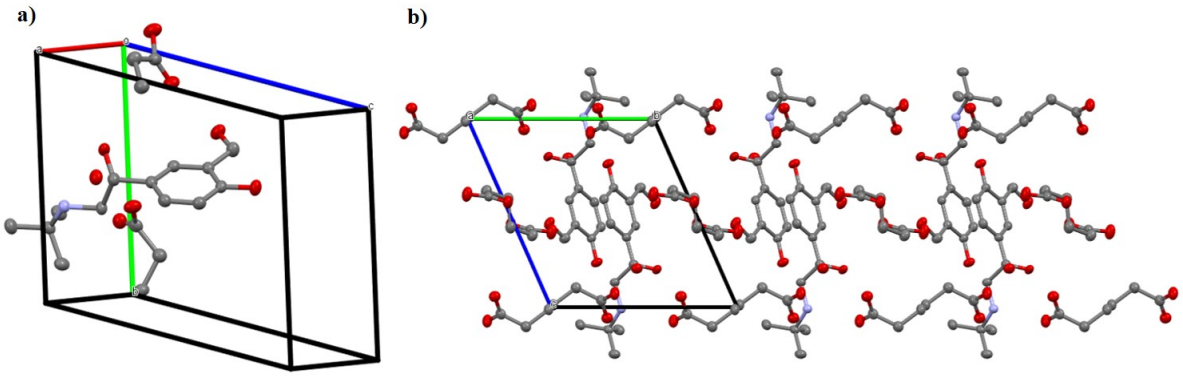

Figure 5-34: The unit cell and structure of SA-AD including a) the asymmetric unit and b) the packing arrangement viewed along the a axis.

Crystallographic disorder was observed in the refinement of both SA-AD structures, with multiple site occupancies observed at the chiral centre (*C-OH) of SA. A significant difference in occupancy values was found between the two determined crystal structures. The structure refined in this work showed a minor occupancy position of 0.309(5) at 150 K compared to the structure reported in the CSD, which reported a minor occupancy position of 0.209 at 100

K;[182] both multi-component complexes were produced by solvent evaporation. The difference in chemical occupancy at different acquisition temperatures may suggest that the nature of disorder in SA-AD is dynamically driven. Alternatively, the chemical occupancy position may be dependent on the crystallisation parameters. The influence of crystallisation parameters on the resultant disorder occupancy is of interest to the aim of this thesis and is studied in chapter 6.

Hydrogen bonds are a key intermolecular interaction for the formation of the multi-component complex (figure 5-35). There are six hydrogen bonds, four of which are SA-adipate (blue) interactions (hydrogen bonds 1, 2, 3 and 4) and two are SA-adipic acid (red) interactions (hydrogen bonds 5 and 6). Similarly to SA-OX and SA-SU, the same assembly of molecular synthons is observed between the amine and alcohol group in SA and the carboxylic acid group in AD. No bifurcated hydrogen bonds (as observed in the framework of SA-OX) are seen in the framework of SA-AD.

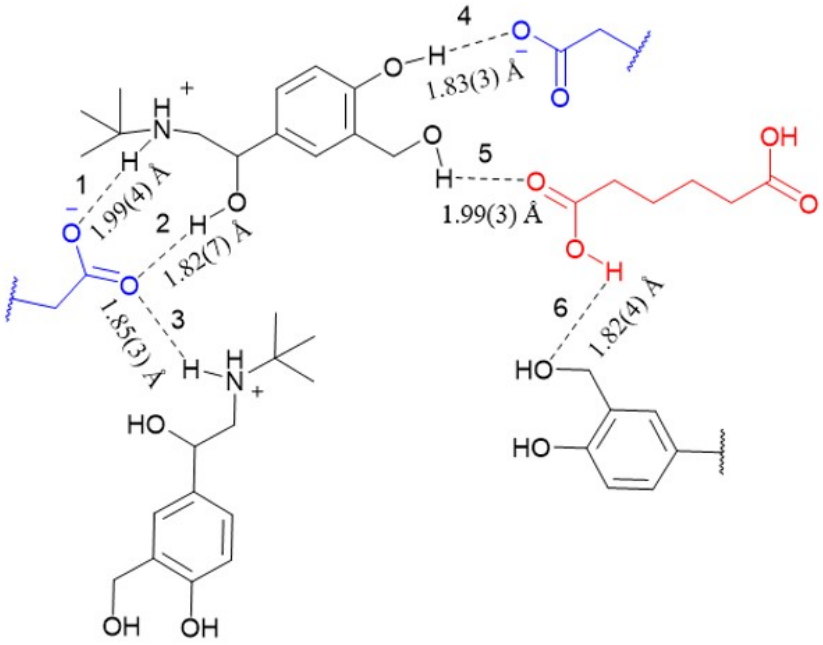

Figure 5-35: The hydrogen bonding framework in SA-AD.

5.8 Structural informatics assessment

5.8.1 Comparing the crystal structure and crystallographic disorder

The chiral center (*C-OH) of SA exhibits crystallographic disorder over two positions in all of the multi-component complexes studied in this chapter. In the case of SA-SU and SA-AD, multiple site occupancies were found in the hydroxyl group of the chiral centre. An extension of this was observed in SA-OX, in which case multiple site occupancies were found in the sp^3 carbon atom attached to the hydroxyl group of the chiral centre. The resultant site occupancies of each solid form were compared against co-former chain length, the $O_{major} - C_{major}$ bond distance and the $O_{major} - C_{major} - O_{minor}$ angle (table 5.12). For completeness, the model of SA modelled with multiple site occupancies is included in table 5.12, although it was concluded (see above, section 5.7.1) that SA does not show clear signs of crystallographic disorder as a single entity.

Table 5.12: The minor occupancy positions and measured bond distances and angles in SA and multi-component complexes SA-OX, SA-SU and SA-AD.

solid form	**chain length**	**minor occupancy**	**distance C-O (Å)**	**angle (^{o})** *a*	**density (g cm^3)**
SA *b*	-	0.12(5)	1.429(9)	19(3)	1.170
SA-OX *b*	2	0.148(4)	1.417(3)	45.0(5)	1.321
SA-SU *b*	4	0.129(18)	1.40(1)	78(2)	1.226
SA-AD *b* (this work)	6	0.316(5)	1.302(7)	94.2(3)	1.322
SA-AD *c* (ORUWUU)	6	0.209	1.388(2)	95.4(3)	-

a the angle measured between $O_{major} - C_{major} - O_{minor}$
b acquisition temperature = 150 K
c acquisition temperature= 100 K

The assessment revealed significant differences between the multiple site occupancies determined in each solid form. The minor position values were broadly found to increase as a function of co-former chain length. However, a weak correlation between the co-former chain length and O-H disorder occupancy was observed. A coefficient of determination (R^2) of 0.6297 was calculated (figure 9-29 in the Appendix). Moreover, significant differences in the angle of the major and minor position was observed. The angle was found to increase as a function of co-former chain length, with a stronger correlation between the co-former chain length and $O_{major} - C_{major} - O_{minor}$ angle observed; a coefficient of determination (R^2) of 0.9841 was calculated for chain length as a function of O-C-O angle (figure 9-29 in the Appendix). A slight difference was observed between the $O_{major} - C_{major}$ distance in each solid form. A typical C-O bond length in an alcohol is 1.427 Å, whereas this bond length is shorter in each of the co-crystals studied here.[190] This suggests that there is a level of strain in the $O_{major} - C_{major}$ bonds for SA-AD, the extent of which appears to decrease as the dicarboxylic acid chain length decreases in the multi-component complexes studied. No significant differences were seen in packing density that would correlate to the increase or decrease of disorder.

It is important to note that this study assumes the crystallographic disorder in every single

crystal in a batch is identical; this is a common misconception and a simplified view. To gain information about the overall arrangement (including disorder) of a structure in the bulk more than one single crystal needs to be studied from a batch. The development of a methodology to overcome this limitation is described in chapter 6.

5.8.2 Comparing the amount of free space

Molecules tend to pack closely to one another in crystals to maximise intermolecular contacts. It is rare to find crystal structures with large voids (larger than 25 Å^3)[191] or open channels since solvent molecules usually fill in these gaps. This study does not aim to discover large voids in a structure, but focuses on subtle differences in void space between the multi-component complexes of SA studied in the chapter. A looser crystal packing may favour weaker intermolecular interactions, leading to an increase in crystallographic disorder.

The size probe radius needed before voids were observed was calculated for each solid form via two different models: 1) no edits were made to the structures and the disorder occupancy positions were left untouched; and 2) all atoms that held a minor occupancy position were deleted. Table 5.13 displays the results for each model.

For voids to be observed under model 1, an experimentally relevant size probe radius needed to be as low as 1.2 Å for SA, 0.9 Å for SA-OX, 1.2 Å for SA-SU and 0.6-0.7 Å for SA-AD. No voids of a significantly different sizes were found in any of the crystal structures under model 2; in this case, no changes in probe radius size were seen for SA, SA-SU and the published form of SA-AD. The slight change in probe radius size indicated for SA-OX and SA-AD under model 1 (this work) is not considered significant as the size probe radius observed in each form is no larger than that of a Hydrogen atom (1.17 Å);[191] it was concluded that the CCDC tool used may not be applicable for this type of analysis. No evidence was gathered in this study to suggest that a looser crystal packing leads to an increase in crystallographic disorder in the solid forms investigated.

Table 5.13: The size probe radius needed before voids are observed in multi-component complexes of SA.

solid form	**chain length**	**minor occupancy**	**model 1 radius (Å)**[a]	**model 2 radius (Å)**[b]
SA[c]	-	0.12(5)	1.2	1.2
SA-OX[c]	2	0.148(4)	0.9	1.2
SA-SU[c]	4	0.129(18)	1.2	1.2
SA-AD[c] (this work)	6	0.316(5)	0.6	0.8
SA-AD[d] (ORUWUU)	6	0.209	0.7	0.7

[a] no edits were made to the structure
[b] all minor occupancy atoms were deleted
[c] acquisition temperature = 150 K
[d] acquisition temperature= 100 K

5.9 Conclusion

The work presented in this chapter investigated the co-crystallisation of pharmaceutically relevant SA with dicarboxylic acids to facilitate the study of the effect of small changes in the molecular nature of the co-former (chain length) on the resulting crystal structure, with a focus on crystallographic disorder. Four solid forms have been presented with respect to their selective isolation, bulk properties and crystal structures. Moreover, the crystallographic disorder in each of these complexes was studied and compared.

SA-OX was selectively isolated from evaporative, cooling and slurrying crystallisation methods. Crystallographic data collection identified the crystal structure of SA-OX to be salbutamol hemi-oxalate. The multi-component complex crystallised in the monoclinic, centrosymmetric, space group $P2_1/n$. Multiple site occupancies were observed around the chiral centre (*C-OH) of SA with a minor position occupancy of 0.148(4). The solid form has a melting point of 195^{o}C and was stable at an elevated temperature of 70^{o}C and at a relative humidity of 10% and 80% for at least six weeks.

Efforts to isolate SA-SU selectively were unsuccessful by evaporative, cooling, slurrying and grinding crystallisation methods. Crystallographic data collection identified the crystal structure of SA-SU to be salbutamol succinate ethanol solvate. The multi-component complex crystallises in the triclinic, centrosymmetric, space group $P\bar{1}$. Multiple site occupancies were observed around the chiral centre (*C-OH) of SA with a minor position occupancy of 0.129(18). A melting point of 110^{o}C was found for SA-SU. Stability testing showed desolvation of the solid form after one week when held at an elevated temperature of 70^{o}C and relative humidity of 10%. The solvated form was stable after a week held at a relative humidity of 80%.

The novel solid form, SA-GL, was successfully formed as a polycrystalline material under evaporative, cooling and slurrying crystallisation methods. The crystal structure of this phase was not obtained in this work. Two different forms were identified in the bulk material, SA-GL-X and SA-GL-Y. A melting point of 144^{o}C was found for form SA-GL-X and a melting point of 180^{o}C was found for form SA-GL-Y. Stability testing showed a transition of the solid form to an unknown phase after one week held at an elevated temperature of 70^{o}C and relative humidity of 10% and 80%.

A published form, SA-AD, was selectively isolated from evaporative, cooling, slurrying and grinding crystallisation methods under a 1:1 stoichiometric ratio of SA and AD. Multiple site occupancies were observed around the chiral centre (*C-OH) of SA-AD with a minor position occupancy of 0.316(5). A melting point of 164^{o}C was measured for the solid form. The stoichiometric ratio of components used under evaporative crystallisation was found to have a large influence on the crystallinity of the resultant material. The amorphisation of SA-AD was observed under a 2:1 ratio, while crystalline SA-AD was produced under a 1:1 ratio; however, crystalline material was produced from other crystallisation methods (cooling and slurrying) with a 2:1 ratio. These 2:1 experiments yielded a new solid form, form-X. Recrystallisation of SA-AD to form-X suggested it may be a polymorphic form. The structure of this form was unidentified in this work; single crystals of form-X were crystallised but were found unsuitable

for in-house data collection, but a melting point of 175^{o}C was seen for form-X by DSC. Stability testing showed that crystalline SA-AD was stable when held at a relative humidity of 10% and 80% for at least six weeks but transformed into an amorphous state at elevated temperature of 70^{o}C. Amorphous SA-AD was stable in an amorphous state at an elevated temperature of 70^{o}C and at a relative humidity of 10% and 80% for at least six weeks.

The crystal structure of SA was re-collected in this work and is in agreement with the previously published structure. There was no convincing evidence of crystallographic disorder in SA as a single entity.

A structural informatics assessment revealed significant differences between the occupancies of the multiple site positions. The minor position values were found to increase slightly as a function of co-former chain length with a relatively poor correlation. A more significant difference between the angle of the major and minor position was observed; this angle was found to increase as a function of co-former chain length. A study that modeled the size probe radius needed before voids were observed in the structure found no evidence to suggest a looser crystal packing may lead to an increase in crystallographic disorder for the solid forms studied.

Overall, crystallographic disorder was found in all of the multi-component complexes of SA studied. The results in this chapter were used to find a suitable new multi-component complex of SA that contains crystallographic disorder to study further in chapter 6, alongside the disorder in SAS. SA-OX was selected as the best model system for that purpose. The doubly ionised oxalate ion in SA-OX has a delocalised charge spread across the molecule, similar to the sulfate ion in SAS, which also has charge delocalisation across the molecule.

The characterisation of crystallographic disorder in pharmaceuticals through time-averaged structures is a valuable starting point in the ultimate joint goal in industry and academia in the development of materials such as these; to achieve a high level of control of physical properties in pharmaceuticals. Such an ambitious goal is only achievable through an in-depth understanding of the molecular structure to gain the knowledge needed to design and develop new drugs. This aspect of the work presented is explored further in Chapter 6.

Chapter 6

Elucidating the nature of disorder in salbutamol sulfate and salbutamol oxalate with single crystal X-ray diffraction and bulk analysis methods.

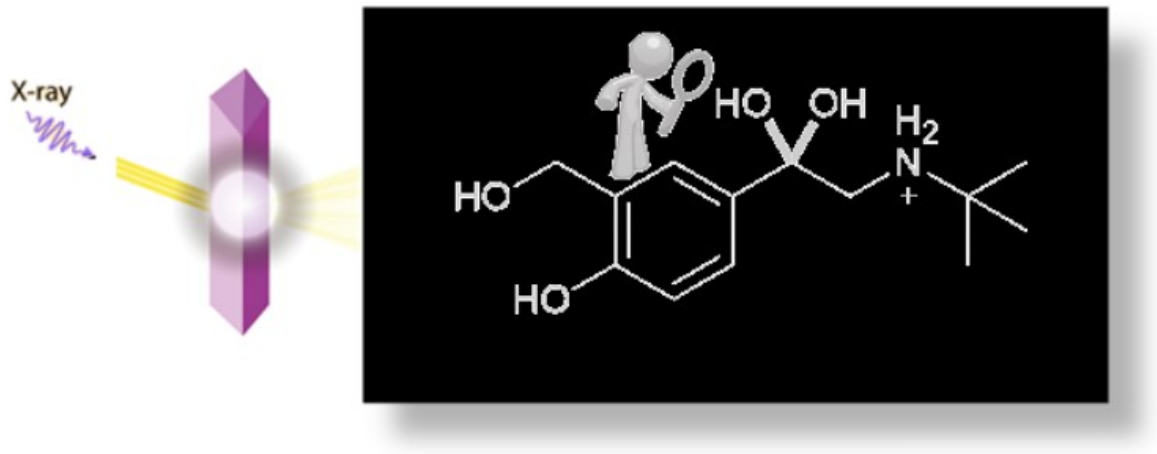

Parts of this chapter have been included in the following article submitted for publication:

A. J. Al-Ani, P.M.J Szell, Z. Rehman, H. Blade, H. P. Wheatcroft, L. P Hughes, S. P. Brown, C. C. Wilson, Combining X-ray and NMR Crystallography to Explore the Crystallographic Disorder in Salbutamol Oxalate, *Cryst. Growth Des.*, 2021

6.1 Introduction

The characterisation of crystallographic disorder in pharmaceuticals is not a new field, in terms of moving beyond idealised atom positions in a crystal structure, though this is still generally via time-averaged X-ray diffraction methods. Crystal structure solution and refinement can provide information on disorder in a structure from the presence of secondary atomic positions with fractional occupancies, sizes of refined anisotropic thermal parameters and the presence of unusual bond lengths and angles.[165] Resolving disorder in this way in one single crystal, as traditionally carried out, is important but arguably an over simplified view. Single crystal-to-single crystal variations are rarely studied and the ability to distinguish subtle changes of disorder across a bulk material at the molecular level is a challenge. The characterisation of disorder in one single crystal does not consider disordered variants (unless fixed by symmetry) or how disorder may vary between crystallites in the bulk powder. Characterising variations in disorder between single crystals is important for the consistent manufacturing of drug compounds; variations of disorder between crystals could affect the properties of a solid form.[92,192] The characterisation of crystallographic disorder of an individual crystal via SCXRD methods alone is not a fully representative characterisation tool to understand such variations.

Failure to note this level of structural detail has led to consequences in the understanding (and therefore control) of previous pharmaceutical compounds. In the case of Eniluracil,[93] a detailed study that looked into the molecular level with X-ray crystallography (four single crystals) and the bulk powder with solid-state nuclear magnetic resonance spectroscopy (SS-NMR spectroscopy) accounted for previous manufacturing challenges. Structural variations previously seen in Eniluracil were confirmed to be due to variable degrees of disorder rather than what was thought to be polymorphism when under development by GlaxoSmithKline in the 1990s. Forewarning of a disordered structure could have aided the experimental development of Eniluracil and helped to explain ambiguities in the X-ray data. Here, the importance of pairing SCXRD with one or more bulk analysis methods to elucidate the nature of disorder is highlighted. To fully understand the depth of this methodology, more well-characterised examples are needed. This level of structural detail will become important to the drug development process when it can be linked to pharmaceutical properties. When this is the case, similar guidelines to those applied for the control of polymorphism can be extended to cases of solid forms with structural disorder. Furthermore, it is of interest from a legal perspective, since it is not clear how disordered variants might be considered in a patent.

6.1.1 Project aim

Aim: To gather a portfolio of data in order to study single crystal-to-single crystal variations in disorder via structural refinement by X-ray crystallography (molecular level) and correlate the results with bulk analysis methods (bulk powder level).

The research in this chapter is the first, to the author's knowledge, to take a systematic approach to the characterisation of solid-state disorder in samples of pharmaceutically relevant model systems- multi component complexes of SA. It focuses on comparing and contrasting repeats, instead of characterising one single crystal with the assumption that each single crystal

is representative of all the single crystals in a batch. A portfolio of crystallographic data was collected for two APIs known to host disorder in the form of multiple site occupancy positions. The research conducted in this chapter pairs SCXRD with bulk analysis techniques to understand the nature of disorder. Furthermore, variations in disorder between single crystals in a batch are quantified, a factor which may be highly dependent on the exact crystallisation conditions utilised.[92] The effects of several different crystallisation and process parameters are investigated including temperature, rate of crystallisation and concentration.

6.1.2 Model API systems investigated

The API SA, figure 6-1a, is as a bronchodilator used in the treatment of asthma.[180] Multi-component complexes of SA were chosen as model systems in this work as they display signs of structural disorder and contain common attributes of current APIs used in pharmaceutical drugs: chiral organic molecules that are marketed in a salt or co-crystalline formation.[3] Figure 6-1b displays the hemi-sulfate salt, SAS (commercially known as Albuterol), a marketed form of SA. The thermodynamically stable polymorph, form I, of SAS is marketed as a racemate, with the (R)-isomer as the active form. One other metastable form exists, form II. The polymorphs are easily identified through different morphologies, form I has an elongated prismatic habit and form II a short plate like habit.[193] The racemic, thermodynamically stable form of SAS was one of the target model systems in this study alongside a second model system, SA-OX (figure 6-1c). SA-OX is a novel co-crystalline salt of SA discovered in this work (see chapter 5). Oxalic acid was chosen as a secondary component of interest due to its similarities to the sulfate group anion in SAS. The oxalate anion has a delocalised charge spread across the molecule. This is similar to the sulfate anion which has direct charge delocalisation across the molecule.

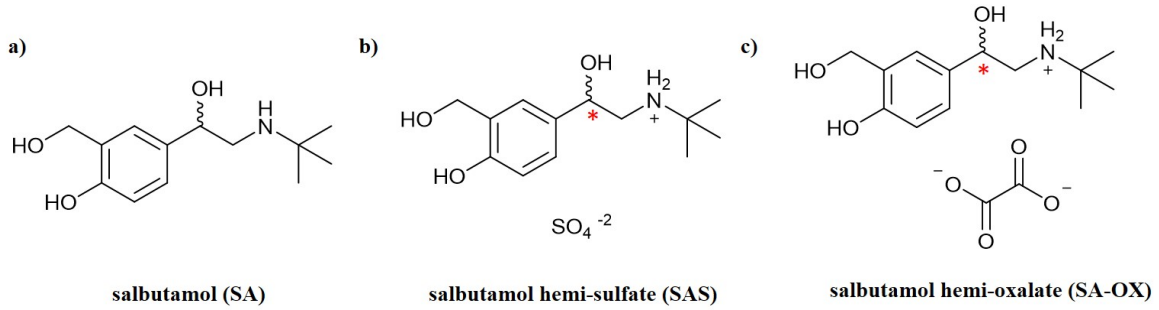

Figure 6-1: The chemical structure of salbutamol, salbutamol hemi-sulfate and salbutamol hemi-oxalate.

6.1.2.1 Disorder in the published structures of SAS

The crystal structure of SAS was reported by Leger et al[179] in 1978 (CSD code = SALBUT) to crystallise in the non-centrosymmetric space group Cc. The *C-OH region (see red asterisk in figure 6-1b) was found to be disordered over two equal positions. An additional symmetry operation in the crystal structure was later reported in 2010 by Xie et al[194] (CSD code = SALBUT01). The revised structure of SAS possessed an inversion centre and crystallised in the centrosymmetric space group C2/c. In this case, no disorder was reported around the

*C-OH region but the sulfate anion was found to be disordered by symmetry. Identifying the correct space group is a key factor in crystallography and a requirement for gaining accurate crystal structure data. A common error for incorrect crystal structure determination is missed symmetry causing refinements to be carried out in an incorrect space group;[195] structural refinement in the wrong space group can lead to a disordered crystal structure. An investigation into determining the correct space group of SAS was therefore conducted as part of the current work to ensure the structure is truly disordered.

6.2 Preparation of material and crystallographic data collection

SAS was obtained from Tokyo Chemical Industry, OX and (R)-SA HCl were obtained from Sigma-Aldrich, SA was isolated from SAS (see section 5.2.1 in chapter 5) and solvents methanol (MeOH), acetone (Ace) and hexane (hx) were obtained from VWR.

6.2.1 Solubility measurements

6.2.1.1 Solubility measurements of SAS

The solubility of SAS in MeOH and a binary solvent system of MeOH and water (1:1) was determined using gravimetric methods. The methodology described in section 3.2.1.1 was used to conduct these solubility measurements. The measured solubility curves (figure 9-30 in the Appendix) were used as a guide when planning crystallisation experiments and as a method of calculating the saturation of solution (or concentration) of each experiment at a certain temperature.

6.2.1.2 Solubility measurements of SA-OX

The solubility of SA-OX in water was determined using observational methods. The methodology described in section 3.2.1.2 was used to conduct the solubility measurements. The measured solubility curve (figure 9-31 in the Appendix) was used as a guide when planning crystallisation experiments and as a method of calculating the saturation of solution of each experiment at a certain temperature.

6.2.2 CD measurements

The molar ellipticity, a value independent of concentration, was calculated with the software package Chirascan Q100. The raw data (in mdeg) was converted to molar ellipticity by inputting the concentration of solution and path length. The concentration of each material dissolved in water was calculated using the Beer-Lambert law. In order to calculate the concentration of solution a molar extinction coefficient was needed for each material analysed. A Chirascan Circular Dichroism Spectrometer was used to obtain a UV-Vis spectrum and measure the absorbance maxima from a solution of known concentration. The Beer-Lambert law was then used to calculate the molar extinction coefficient, all calculations are available in the

Appendix, see figure 9-32. Molar extinction coefficients of 1687.25, 1894.94 and 1658.98 L mol^{-1} cm^{-1} were calculated for SA, SA-OX and (R)-SA-OX respectively.

6.2.3 Crystallisation conditions screen for well diffracting single crystals

A screening process was conducted in order to identify a set of conditions that could deliver single crystals of good quality for SCXRD experiments, a key tool for the quantification of structural disorder in this work. The most desirable set of conditions identified in this screening study was used to collect a portfolio of SCXRD data for SAS and SA-OX.

6.2.3.1 Crystallisation conditions screen for SAS

The influence of crystallisation method, solvent system and temperature was explored for SAS. Evaporative, cooling and vapor diffusion methods were screened for the crystallisation of high quality single crystals of SAS. The effects of three different solvent systems were investigated under evaporative and cooling crystallisation; these were water, MeOH and a binary solvent system of MeOH and water (1:1). The effect of two different anti-solvent systems, Ace and hx, was explored via vapour diffusion with MeOH. A saturated solution of SAS in the corresponding solvent system was used for each experiment. The temperature of saturation was based on the highest temperature at which each experiment was held (i.e. 40, 20 or 4^{o}C). Table 6.1 displays a summary of the results and figure 6-2 shows optical microscopy images of the resultant batches of crystals obtained.

Table 6.1: Crystallisation conditions screen for good quality crystals of SAS.

method	**solvent system**	**temperature (^{o}C)**	**stirring (rpm)**	**material obtained**
evaporative crystallisation	MeOH and water (1:1)	40, 20, 4	x	single crystals
	water	40, 20, 4	x	single crystals
	MeOH	40, 20, 4	x	single crystals
cooling crystallisation[a]	MeOH and water (1:1)	40-4	x	single crystals[b]
	water	40-4	x	x
	MeOH	40-4	x	x
	MeOH and water (1:1)	40-4	100	poly-crystallites
	water	40-4	100	poly-crystallites
	MeOH	40-4	100	poly-crystallites
vapour diffusion	MeOH and hx	40, 20	x	single crystals
	MeOH and hx	4	x	x
	MeOH and Ace	20	x	x

[a] a range of cooling rates (0.01-5 ^{o}C /min) and stirring methods (over head and magnetic bottom stirring) were investigated.
[b] a cooling rate of 1^{o}C /min and a dwell time of 120 h at 4^{o}C was used to obtain this material.

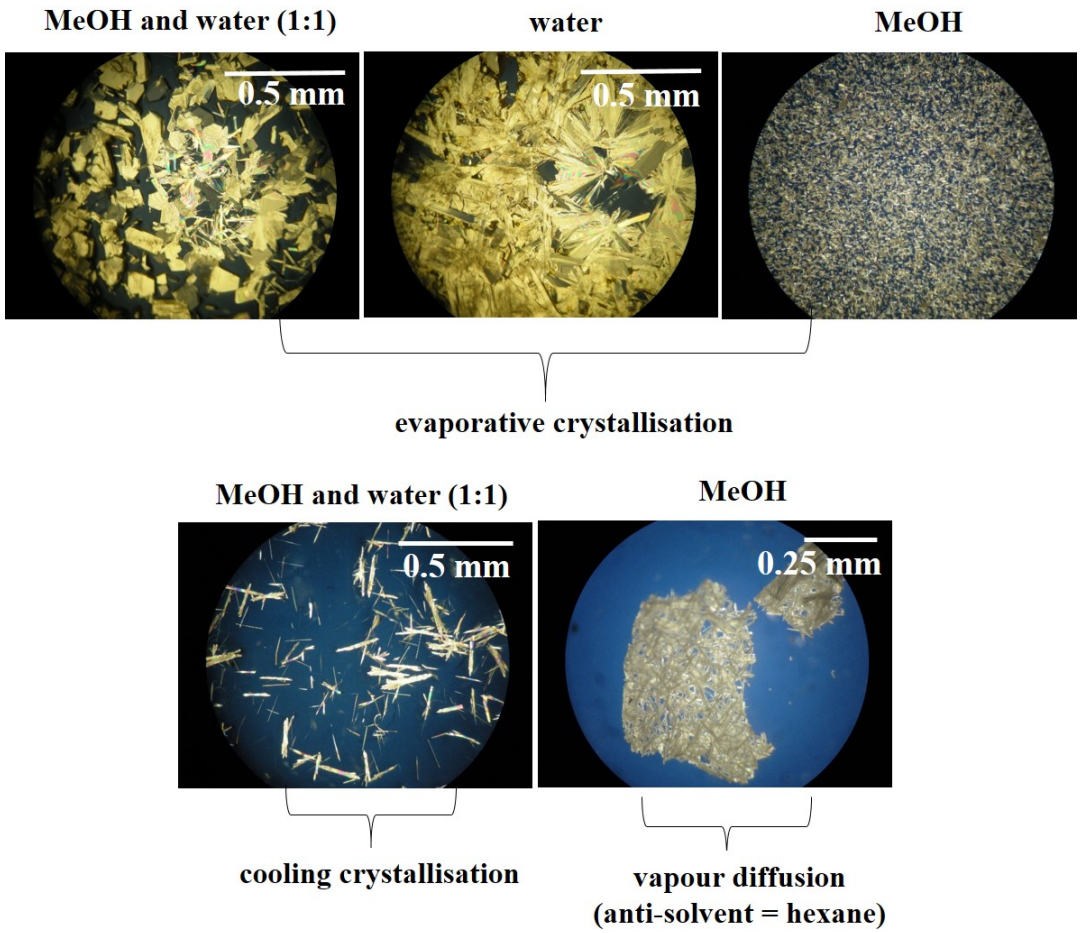

Figure 6-2: Microscope images of experimental batches containing crystals of SAS, obtained under different crystallisation methods and solvents.

Desirable crystals for SCXRD were gained under evaporative crystallisation from a binary solvent system of MeOH and water (1:1). The temperature of crystallisation did not seem to alter the crystal quality under these conditions. The crystals of SAS used to collect a portfolio of SCXRD data were thus prepared under evaporative crystallisation from MeOH and water (1:1).

The bulk material from each experiment of interest was characterised by PXRD to identify the solid form (figure 6-3). The thermodynamically stable form of SAS (CSD code = SALBUT) was crystallised under each experiment apart from vapor diffusion methods using MeOH and hx, where a new solid form was identified. Further characterisation of the new solid form by DSC showed the loss of solvent at 80^{o}C (onset), suggesting solvate formation, alongside the melting point of SAS at 165^{o}C (onset) (figure 9-33 in the Appendix). The crystal structure of this new solid form could not be determined with in-house X-ray diffractometers. It is predicted that the new structure is a solvated form of SAS with MeOH or hx incorporated into the crystal structure.

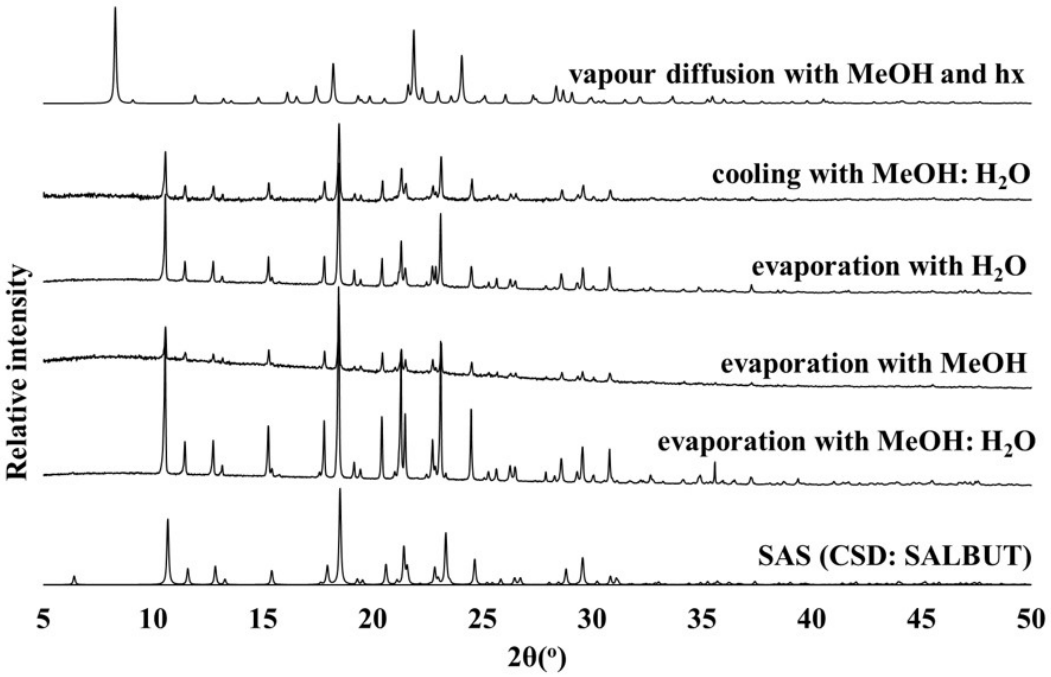

Figure 6-3: PXRD traces for the crystallisation conditions screen with SAS.

6.2.3.2 Crystallisation conditions screen for SA-OX

The influence of solvent system was explored with evaporative crystallisation for the formation of good quality single crystals of SA-OX. In this case, evaporative crystallisation was the main focus since crystals of SAS, used to collect a portfolio of data, were also prepared under evaporative crystallisation methods. A saturated solution of the two components (a 1:1 molar ratio of SA and OX), in the corresponding solvent system, was used for each experiment. The temperature of saturation was based on the highest temperature at which each experiment was held (i.e. 50, 30 or 20^{o}C). Table 6.2 displays a summary of the results obtained and figure 6-4 displays optical microscopy images of the crystals obtained. The material from each experiment was characterised by PXRD to identify the solid form (figure 9-34 in the Appendix). The target form, SA-OX, was found in the product material of each experiment and SA was found alongside the target form in the binary solvent system of EtOH and water (1:1).

Table 6.2: Evaporative crystallisation conditions screen for good quality crystals of SA-OX.

starting material	**solvent system**	**temperature[a] (^{o}C)**	**solid form(s)**	**material obtained**
SA and OX (1:1)	water	50 ,30, 20	SA-OX	single crystals
	EtOH	50 ,30, 20	SA-OX	poorly crystalline
	EtOH and water	50 ,30, 20	SA-OX, SA	single crystals

[a] The same solid form and type of material was obtained under each temperature investigated.

Desirable crystals for SCXRD were gained from water via evaporative crystallisation; crystallisation temperature did not seem to alter the crystal quality. Henceforth, crystals of SA-OX were prepared under evaporative methods from water.

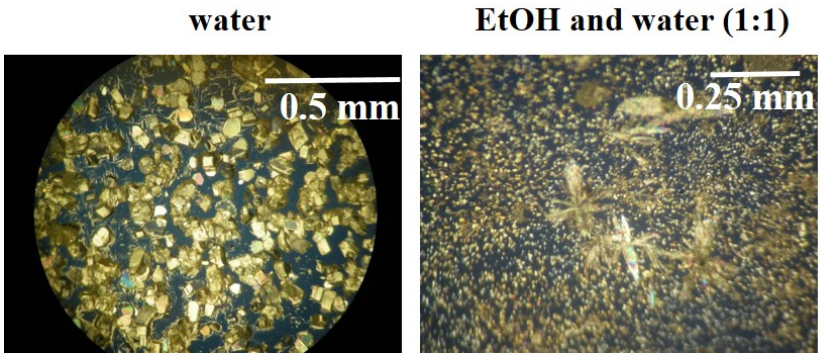

Figure 6-4: Microscope images of experimental batches containing crystals of SA-OX, obtained under evaporative crystallisation with different solvent systems.

6.2.4 Sample preparation to gather a portfolio of crystallographic data

The impact of crystallisation conditions on the degree of disorder observed in SAS and SA-OX was investigated. Three different crystallisation parameters were explored to gain an insight into the single crystal-to-single crystal variations of disorder; a factor which may be dependent on the exact crystallisation conditions used. Material was prepared under evaporative crystallisation and each sample was held at a different temperature, rate of crystallisation and different concentrations (saturation of solution at a set temperature). For temperature control, vials containing the crystallisation media were placed into a jacketed hotplate at a set temperature or a fridge set at 4^{o}C. The rate of crystallisation, at a set temperature, was controlled by the alteration of pressure and surface area. A fan was used to increase pressure (see figure 3-1 in section 3.1.1) and a vial lid was used to decrease surface area (no lid, lid with 10 holes and a lid with 1 hole). The rate of crystallisation is an approximate value and refers to crystallisation until dryness, a value manually determined by eye. Solutions with different concentrations were made by decreasing the amount of solute in solution by a factor of 2 (a saturation of 50%) and a factor of 4 (a saturation of 25%). At a concentration of 100%, a solution was saturated at a set temperature (based on solubility data).

6.2.4.1 SAS sample preparation

Twelve samples of SAS were prepared under evaporative crystallisation at a set temperature of 40, 20 or 4^{o}C and set crystallisation rate of 3-5 days, 11-14 days or 30-32 days. Each solution (3 mL) was placed into a 7 mL glass vial for crystallisation to occur. The concentration of solution was based on the temperature of saturation. A solution of 100% saturation was made by dissolving 0.21 g/mL of SAS at 40^{o}C, 0.18 g/mL of SAS at 20^{o}C and 0.12 g/mL of SAS at 4^{o}C in a binary solvent mixture of MeOH and water (1:1). The weights of SAS were based on measured solubility data (figure 9-30 in the Appendix). The concentration of each sample for evaporative crystallisation was then set at 100%, 50% or 25% as described above. Table 6.3 shows the conditions used to prepared each of the twelve samples investigated in this work.

Table 6.3: The experimental parameters explored the variation of structural disorder in SAS.

sample	temperature (^{o}C)	rate (days)	concentration (%)
SAS-1	40	3-5	100
SAS-2	40	11-14	100
SAS-3	40	3-5	50
SAS-4	40	3-5	25
SAS-5	20	3-5	100
SAS-6	20	11-14	100
SAS-7	20	3-5	50
SAS-8	20	3-5	25
SAS-9	4	11-14	100
SAS-10	4	30-32	100
SAS-11	4	30-32	50
SAS-12[a]	4	30-32	25

[a] crystallographic data collection was unsuccessful due to poorly diffracting crystals.

6.2.4.2 SA-OX sample preparation

Five samples of SA-OX were prepared under evaporative crystallisation at a set temperature of 50, 30 or 20^{o}C and set crystallisation rate of $\leq$ 1 day, 3-4 days and 40 days. Each solution (3 mL) was placed into a 7 mL glass vial for crystallisation to occur. The concentration of solution was set at 100% for each sample. A solution of 100% saturation was made by dissolving 0.023 g/mL at 50^{o}C, 0.016 g/mL at 30^{o}C and 0.014 g/mL at 20^{o}C of a 1:1 molar ratio of SA and OX in water. The weights were based on solubility data measured for the co-crystal, SA-OX (figure 9-31 in the Appendix). Table 6.4 shows the conditions used to prepared each of the five samples investigated in this work.

Table 6.4: The experimental parameters explored the variation of structural disorder in SA-OX.

sample	temperature (^{o}C)	rate (days)	concentration (%)
SAOX-1	50	$\leq$1	100
SAOX-2	30	3-4	100
SAOX-3	20	$\leq$1	100
SAOX-4	20	3-4	100
SAOX-5	20	40	100

6.2.5 Single crystal X-ray diffraction experiments of SAS and SA-OX samples

At least three single crystals (labelled trial #1, #2, #3, etc.) were analysed from a sample batch of SAS (samples SAS-1 to SAS-11) and SA-OX (samples SAOX-1 to SAOX-5). Crystallographic disorder was determined for each crystal analysed and the relative site occupancies of the minor phase determined. A Rigaku Oxford Diffraction SuperNova and Xcalibur diffractometer were used for data collection of all crystals in this chapter at 150 K or 298 K, with a Cu-Kα (λ = 1.54045 Å) or Mo-Kα (λ = 0.71073 Å) X-ray source. All crystal structures were solved by direct methods using SHELXS-2013[143] and refined using SHELXL-2015[144] with the software package Olex2.[145] Isotropic displacement parameters were used for the refinement of atoms with multiple site occupancies. Following this, refinement under anisotropic displacement parameters (ADPs) were conducted with free site occupancy factors. All hydrogen atoms were refined freely where possible; if the position of a hydrogen atom was unclear, constraints were used to fix hydrogen atoms in an idealised position based on a riding model.

The crystallographic data collected for samples of SAS are shown in tables 6.5 to 6.15. Each table presents the crystal data and structure refinement of at least three single crystals isolated from a sample batch. Each single crystal analysed was chosen at random and from different areas of the bulk material.

The crystallographic data collected for samples of SA-OX are shown in tables 6.16 to 6.20. Each table presents the crystal data and structure refinement of three single crystals isolated from a sample batch. As with the samples of SAS, each single crystal analysed was chosen at random and from different areas of the bulk material.

Table 6.5: The crystallographic data collected for sample SAS-1

sample SAS-1	**#1**	**#2**	**#3**	**#4**
formula	$C_{13}H_{22}N_1O_5S_{0.5}$	$C_{13}H_{22}N_1O_5S_{0.5}$	$C_{13}H_{22}N_1O_5S_{0.5}$	$C_{13}H_{22}N_1O_5S_{0.5}$
g mol^{-1}	288.34	288.34	288.34	288.34
T (K)	150.00 (10)	150.00 (10)	150.02 (10)	149.8(4)
radiation	Cu Kα($\lambda = 1.54184$)	Cu Kα($\lambda = 1.54184$)	Mo Kα($\lambda = 0.71073$)	Cu Kα($\lambda = 1.54184$)
2θ range (^{o})	6.412 to 146.178	6.412 to 146.226	6.768 to 52.742	6.396 to 146.974
crystal system	monoclinic	monoclinic	monoclinic	monoclinic
space group	C2/c	C2/c	C2/c	C2/c
a (Å)	27.9012(4)	27.9006(6)	27.8808(12)	27.9463(7)
b (Å)	6.18160(10)	6.18400(10)	6.1696(2)	6.1853(2)
c (Å)	16.7774(3)	16.7561(4)	16.7758(8)	16.7642(5)
$\alpha(^o)$	90	90	90	90
$\beta(^o)$	98.814(2)	98.807(2)	98.889(4)	98.548(3)
$\gamma(^o)$	90	90	90	90
volume ($Å^3$)	2859.49(8)	2856.97(10)	2851.0(2)	2865.61(15)
Z	8	8	8	8
density (g cm^3)	1.340	1.341	1.344	1.337
$\mu(mm^{-1})$	1.500	1.501	0.172	1.497
completeness (%)	99.9	99.8	98.6	99.8
reflections collected	14438	14181	6468	12838
independent reflections	2870	2867	2907	2883
R int	0.0344	0.0343	0.0333	0.0342
GooF	1.094	1.061	1.029	1.058
R_1 (obs)	0.0509	0.0477	0.0457	0.0513
R_1 (all)	0.0518	0.0498	0.0650	0.0550
wR_2 (all)	0.1332	0.1282	0.1149	0.1363
$\rho_{max,min}$ (e $Å^{-3}$)	0.49/-0.45	0.45/-0.38	0.46/-0.31	0.52/-0.41
atomic occupancy (*C-OH)	0.123(4) : 0.877(4)	0.093(5) : 0.907(5)	0.153(3) : 0.847(3)	0.155(5) : 0.845(5)
atomic occupancy (SO_4)	0.5 : 0.5	0.5 : 0.5	0.5 : 0.5	0.5 : 0.5

Table 6.6: The crystallographic data collected for sample SAS-2

sample SAS-2	**#1**	**#2**	**#3**
formula	$C_{13}H_{22}N_1O_5S_{0.5}$	$C_{13}H_{22}N_1O_5S_{0.5}$	$C_{13}H_{22}N_1O_5S_{0.5}$
g mol^{-1}	288.34	288.34	288.34
T (K)	150.00 (10)	150.00 (10)	150.00 (10)
radiation	Cu Kα($\lambda = 1.54184$)	Cu Kα($\lambda = 1.54184$)	Cu Kα($\lambda = 1.54184$)
2θ range (^{o})	10.692 to 147.154	10.684 to 143.76	10.682 to 143.776
crystal system	monoclinic	monoclinic	monoclinic
space group	C2/c	C2/c	C2/c
a (Å)	27.9121(12)	27.8831(6)	27.8694(8)
b (Å)	6.1836(3)	6.18559(14)	6.18860(19)
c (Å)	16.7424(10)	16.7563(4)	16.7609(6)
$\alpha(^o)$	90	90	90
$\beta(^o)$	98.741(5)	98.764(2)	98.821(3)
$\gamma(^o)$	90	90	90
volume (Å^3)	2856.1(3)	2856.26(12)	2856.61(16)
Z	8	8	8
density (g cm^3)	1.341	1.341	1.341
$\mu(mm^{-1})$	1.502	1.502	1.501
completeness (%)	99.5	99.9	99.9
reflections collected	7365	4886	4531
independent reflections	2873	2763	2753
R int	0.0213	0.0146	0.0255
GooF	1.034	1.040	1.027
R_1 (obs)	0.0604	0.0394	0.0457
R_1 (all)	0.0653	0.0441,	0.0543
wR_2 (all)	0.1900	0.1069	0.1226
$\rho_{max,min}$ (e Å^{-3})	0.87/-0.61	0.39/-0.33	0.31/-0.40
atomic occupancy (*C-OH)	0.064(6) : 0.936(6)	0.040(3) : 0.960(3)	0.084(4) : 0.916(4)
atomic occupancy (SO_4)	0.5 : 0.5	0.5 : 0.5	0.5 : 0.5

Table 6.7: The crystallographic data collected for sample SAS-3

sample SAS-3	**#1**	**#2**	**#3**
formula	$C_{13}H_{22}N_1O_5S_{0.5}$	$C_{13}H_{22}N_1O_5S_{0.5}$	$C_{13}H_{22}N_1O_5S_{0.5}$
g mol^{-1}	288.34	288.34	288.34
T (K)	150.00 (10)	150.00 (10)	150.00 (10)
radiation	Mo Kα($\lambda = 0.71073$)	Mo Kα($\lambda = 0.71073$)	Cu Kα($\lambda = 1.54184$)
2θ range (^{o})	5.916 to 60.464	5.916 to 60.884	6.408 to 142.584
crystal system	monoclinic	monoclinic	monoclinic
space group	C2/c	C2/c	C2/c
a (Å)	27.8845(14)	27.8756(12)	27.9180(10)
b (Å)	6.1771(2)	6.1715(2)	6.1796(2)
c (Å)	16.7656(9)	16.7549(8)	16.7741(7)
$\alpha(^o)$	90	90	90
$\beta(^o)$	98.896(5)	98.856(4)	98.800(4)
$\gamma(^o)$	90	90	90
volume (Å^3)	2853.0(2)	2848.1(2)	2859.83(19)
Z	8	8	8
density (g cm^3)	1.343	1.345	1.339
$\mu(mm^{-1})$	0.171	0.172	1.500
completeness (%)	99.9	99.9	100
reflections collected	7043	6845	4499
independent reflections	3647	3653	2710
R int	0.0222	0.0235	0.0185
GooF	1.108	1.102	1.128
R_1 (obs)	0.0531	0.0523	0.0458
R_1 (all)	0.0640	0.0646	0.0489
wR_2 (all)	0.1217	0.1281	0.1160
$\rho_{max,min}$ (e Å^{-3})	0.34/-0.33	0.33/-0.34	0.35/-0.27
atomic occupancy (*C-OH)	0.167(4) : 0.833(4)	0.163(4) : 0.837(4)	0.159(4) : 0.841(4)
atomic occupancy (SO_4)	0.5 : 0.5	0.5 : 0.5	0.5 : 0.5

Table 6.8: The crystallographic data collected for sample SAS-4

sample SAS-4	**#1**	**#2**	**#3**
formula	$C_{13}H_{22}N_1O_5S_{0.5}$	$C_{13}H_{22}N_1O_5S_{0.5}$	$C_{13}H_{22}N_1O_5S_{0.5}$
g mol^{-1}	288.34	288.34	288.34
T (K)	150.00 (10)	150.00 (10)	150.00 (10)
radiation	Cu Kα($\lambda = 1.54184$)	Cu Kα($\lambda = 1.54184$)	Cu Kα($\lambda = 1.54184$)
2θ range (^{o})	6.414 to 146.16	6.406 to 146.2	10.684 to 146.468
crystal system	monoclinic	monoclinic	monoclinic
space group	C2/c	C2/c	C2/c
a (Å)	27.8908(7)	27.9200(5)	27.9651(13)
b (Å)	6.18040(15)	6.18034(11)	6.1808(2)
c (Å)	16.7710(4)	16.7571(3)	16.7480(7)
$\alpha(^o)$	90	90	90
$\beta(^o)$	98.814(2)	98.7703(18)	98.598(4)
$\gamma(^o)$	90	90	90
volume (Å^3)	2856.78(12)	2857.71(9)	2862.3(2)
Z	8	8	8
density (g cm^3)	1.341	1.340	1.338
$\mu(mm^{-1})$	1.501	1.501	1.498
completeness (%)	99.8	99.9	98.3
reflections collected	7302	7180	7011
independent reflections	2864	2836	2830
R int	0.0293	0.0241	0.0297
GooF	1.056	1.029	1.029
R_1 (obs)	0.049	0.0493	0.0527
R_1 (all)	0.0548	0.0523	0.0602
wR_2 (all)	0.1358	0.1358	0.1497
$\rho_{max,min}$ (e Å^{-3})	0.37/-0.38	0.40/-0.33	0.43/-0.36
atomic occupancy (*C-OH)	0.130(4) : 0.870(4)	0.129(4) : 0.871(4)	0.138(5) : 0.862(5)
atomic occupancy (SO_4)	0.5 : 0.5	0.5 : 0.5	0.5 : 0.5

Table 6.9: The crystallographic data collected for sample SAS-5

sample SAS-5	**#1**	**#2**	**#3**	**#4**
formula	$C_{13}H_{22}N_1O_5S_{0.5}$	$C_{13}H_{22}N_1O_5S_{0.5}$	$C_{13}H_{22}N_1O_5S_{0.5}$	$C_{13}H_{22}N_1O_5S_{0.5}$
g mol^{-1}	288.34	288.34	288.34	288.34
T (K)	150.00 (10)	150.00 (10)	150.00 (10)	149.8(4)
radiation	Mo Kα($\lambda = 0.71073$)	Mo Kα($\lambda = 0.71073$)	Cu Kα($\lambda = 1.54184$)	Cu Kα($\lambda = 1.54184$)
2θ range (^{o})	5.336 to 60.16	5.33 to 60.694	6.412 to 142.934	6.408 to 143.068
crystal system	monoclinic	monoclinic	monoclinic	monoclinic
space group	C2/c	C2/c	C2/c	C2/c
a (Å)	27.8288(15)	27.8744(14)	27.9008(4)	27.9150(4)
b (Å)	6.1749(3)	6.1793(3)	6.18235(9)	6.18063(7)
c (Å)	16.7722(10)	16.7864(9)	16.7680(3)	16.7643(3)
$\alpha(^o)$	90	90	90	90
$\beta(^o)$	98.816(5)	98.838(5)	98.8542(15)	98.7839(15)
$\gamma(^o)$	90	90	90	90
volume ($Å^3$)	2848.1(3)	2857.0(2)	2857.89(8)	2858.45(7)
Z	8	8	8	8
density (g cm^3)	1.345	1.341	1.340	1.340
$\mu(mm^{-1})$	0.172	0.171	1.501	1.500
completeness (%)	99.9	99.9	100	100
reflections collected	7304	8290	8431	9510
independent reflections	3669	3732	2758	2773
R int	0.0235	0.0316	0.0289	0.0316
GooF	1.093	1.147	1.045	1.035
R_1 (obs)	0.0531	0.0565	0.0456	0.0434
R_1 (all)	0.0622	0.0668	0.0478	0.0477
wR_2 (all)	0.1293	0.1395	0.1261	0.1232
$\rho_{max,min}$ (e $Å^{-3}$)	0.44/-0.39	0.38/-0.35	0.42/-0.32	0.36/-0.33
atomic occupancy (*C-OH)	0.161(4) : 0.839(4)	0.163(4) : 0.837(4)	0.104(4) : 0.896(4)	0.103(4) : 0.897(4)
atomic occupancy (SO_4)	0.5 : 0.5	0.5 : 0.5	0.5 : 0.5	0.5 : 0.5

Table 6.10: The crystallographic data collected for sample SAS-6

sample SAS-6	**#1**	**#2**	**#3**	**#4**
formula	$C_{13}H_{22}N_1O_5S_{0.5}$	$C_{13}H_{22}N_1O_5S_{0.5}$	$C_{13}H_{22}N_1O_5S_{0.5}$	$C_{13}H_{22}N_1O_5S_{0.5}$
g mol^{-1}	288.34	288.34	288.34	288.34
T (K)	150.00 (10)	150.0(10)	150.01 (10)	150.00(10)
radiation	Cu Kα($\lambda = 1.54184$)	Cu Kα($\lambda = 1.54184$)	Cu Kα($\lambda = 1.54184$)	Cu Kα($\lambda = 1.54184$)
2θ range (^{o})	6.41 to 146.084	6.41 to 146.112	6.41 to 144.644	6.412 to 146.13
crystal system	monoclinic	monoclinic	monoclinic	monoclinic
space group	C2/c	C2/c	C2/c	C2/c
a (Å)	27.9065(5)	27.9101(5)	27.9076(6)	27.9000(6)
b (Å)	6.18389(10)	6.18259(10)	6.18271(13)	6.18313(13)
c (Å)	16.7638(3)	16.7598(3)	16.7652(4)	16.7604(4)
$\alpha(^o)$	90	90	90	90
$\beta(^o)$	98.8260(17)	98.8216(18)	98.824(2)	98.8468(19)
$\gamma(^o)$	90	90	90	90
volume (Å^3)	2858.69(9)	2857.81(9)	2858.51(11)	2856.94(11)
Z	8	8	8	8
density (g cm^3)	1.340	1.340	1.340	1.341
$\mu(mm^{-1})$	1.500	1.501	1.500	1.501
completeness (%)	99.7	99.7	100	100
reflections collected	7257	7166	12115	7555
independent reflections	2862	2859	2829	2862
R int	0.0201	0.0215	0.0244	0.0279
GooF	1.060	1.053	1.057	1.041
R_1 (obs)	0.0436	0.0404	0.0382	0.0415
R_1 (all)	0.0450	0.0428	0.0396	0.0433
wR_2 (all)	0.1136	0.1091	0.0986	0.1124
$\rho_{max,min}$ (e Å^{-3})	0.37/-0.55	0.43/-0.30	0.39/-0.31	0.50/-0.29
atomic occupancy (*C-OH)	0.107(4) : 0.893(4)	0.122(4) : 0.878(4)	0.123(3) : 0.877(3)	0.113(4) : 0.887(4)
atomic occupancy (SO_4)	0.5 : 0.5	0.5 : 0.5	0.5 : 0.5	0.5 : 0.5

Table 6.11: The crystallographic data collected for sample SAS-7

sample SAS-7	**#1**	**#2**	**#3**	**#4**
formula	$C_{13}H_{22}N_1O_5S_{0.5}$	$C_{13}H_{22}N_1O_5S_{0.5}$	$C_{13}H_{22}N_1O_5S_{0.5}$	$C_{13}H_{22}N_1O_5S_{0.5}$
g mol^{-1}	288.34	288.34	288.34	288.34
T (K)	150 (10)	113(20)	150.02 (10)	149.8(4)
radiation	Mo Kα($\lambda = 0.71073$)	Mo Kα($\lambda = 0.71073$)	Mo Kα($\lambda = 0.71073$)	Mo Kα($\lambda = 0.71073$)
2θ range (^{o})	7.084 to 60.546	5.928 to 59.06	6.118 to 58.19	6.124 to 58.36
crystal system	monoclinic	monoclinic	monoclinic	monoclinic
space group	C2/c	C2/c	C2/c	C2/c
a (Å)	27.9015(10)	27.827(2)	27.879(2)	27.8674(16)
b (Å)	6.1782(2)	6.1714(4)	6.1764(4)	6.1678(3)
c (Å)	16.7717(6)	16.7390(13)	16.7567(13)	16.7358(10)
$\alpha(^o)$	90	90	90	90
$\beta(^o)$	98.867(3)	98.911(7)	98.840(7)	98.819(6)
$\gamma(^o)$	90	90	90	90
volume (Å^3)	2856.57(17)	2839.9(4)	2851.1(4)	2842.6(3)
Z	8	8	8	8
density (g cm^3)	1.415	1.349	1.344	1.349
$\mu(mm^{-1})$	0.180	0.172	0.172	0.172
completeness (%)	99.8	99.9	100	99.9
reflections collected	19950	6652	6626	6739
independent reflections	3904	3319	3316	3301
R int	0.0268	0.0462	0.0486	0.0303
GooF	1.124	1.035	1.032	1.047
R_1 (obs)	0.0519	0.0541	0.0599	0.0488
R_1 (all)	0.0612	0.0875	0.1173	0.0722
wR_2 (all)	0.1242	0.1250	0.1341	0.1207
$\rho_{max,min}$ (e Å^{-3})	0.47/-0.32	0.31/-0.37	0.21/-0.33	0.36/-0.42
atomic occupancy (*C-OH)	0.165(5) : 0.831(6)	0.163(4) : 0.837(4)	0.145(4) : 0.855(4)	0.188(4) : 0.812(4)
atomic occupancy (SO_4)	0.5 : 0.5	0.5 : 0.5	0.5 : 0.5	0.5 : 0.5

Table 6.12: The crystallographic data collected for sample SAS-8

sample SAS-8	**#1**	**#2**	**#3**
formula	$C_{13}H_{22}N_1O_5S_{0.5}$	$C_{13}H_{22}N_1O_5S_{0.5}$	$C_{13}H_{22}N_1O_5S_{0.5}$
g mol^{-1}	288.34	288.34	288.34
T (K)	150.00(10)	150.01(10)	150.00(10)
radiation	Mo Kα($\lambda = 0.71073$)	Cu Kα($\lambda = 1.54184$)	Cu Kα($\lambda = 1.54184$)
2θ range (^{o})	5.924 to 61.034	6.412 to 146.242	6.41 to 142.336
crystal system	monoclinic	monoclinic	monoclinic
space group	C2/c	C2/c	C2/c
a (Å)	27.8390(13)	27.9057(4)	27.9083(6)
b (Å)	6.1658(2)	6.17601(7)	6.17785(12)
c (Å)	16.7444(8)	16.7737(3)	16.7813(3)
$\alpha(^o)$	90	90	90
$\beta(^o)$	98.847(4)	98.8596(14)	98.822(2)
$\gamma(^o)$	90	90	90
volume (Å^3)	2840.0(2)	2856.39(7)	2859.09(10)
Z	8	8	8
density (g cm^3)	1.349	1.341	1.340
$\mu(mm^{-1})$	0.172	1.502	1.500
completeness (%)	99.9	99.8	98.3
reflections collected	7384	7660	4869
independent reflections	3700	2865	2713
R int	0.0227	0.0295	0.0202
GooF	1.052	1.063	1.072
R_1 (obs)	0.0521	0.0488	0.0414
R_1 (all)	0.0694	0.0507	0.0484
wR_2 (all)	0.1224	0.1312	0.1079
$\rho_{max,min}$ (e Å^{-3})	0.37/-0.37	0.36/-0.40	0.30/-0.38
atomic occupancy (*C-OH)	0.166(4) : 0.834(4)	0.163(5) : 0.837(5)	0.166(4) : 0.834(4)
atomic occupancy (SO_4)	0.5 : 0.5	0.5 : 0.5	0.5 : 0.5

Table 6.13: The crystallographic data collected for sample SAS-9

sample SAS-9	**#1**	**#2**	**#3**
formula	$C_{13}H_{22}N_1O_5S_{0.5}$	$C_{13}H_{22}N_1O_5S_{0.5}$	$C_{13}H_{22}N_1O_5S_{0.5}$
g mol^{-1}	288.34	288.34	288.34
T (K)	150.01(10)	150.00(10)	150.00(10)
radiation	Cu Kα($\lambda = 1.54184$)	Cu Kα($\lambda = 1.54184$)	Cu Kα($\lambda = 1.54184$)
2θ range (^{o})	10.682 to 143.006	6.41 to 143.066	6.406 to 146.428
crystal system	monoclinic	monoclinic	monoclinic
space group	C2/c	C2/c	C2/c
a (Å)	27.8986(7)	27.9088(7)	27.9213(5)
b (Å)	6.17776(13)	6.17585(12)	6.17840(9)
c (Å)	16.7629(4)	16.7761(4)	16.7636(3)
$\alpha(^o)$	90	90	90
$\beta(^o)$	98.838(2)	98.845(2)	98.7993(17)
$\gamma(^o)$	90	90	90
volume (Å^3)	2854.81(12)	2857.15(11)	2857.83(9)
Z	8	8	8
density (g cm^3)	1.342	1.341	1.340
$\mu(mm^{-1})$	1.502	1.501	1.501
completeness (%)	99.9	100	98.3
reflections collected	8181	8838	14077
independent reflections	2744	2759	2871
R int	0.0221	0.0328	0.0228
GooF	1.079	1.074	1.110
R_1 (obs)	0.0422	0.0445	0.0429
R_1 (all)	0.0442	0.0489	0.0438
wR_2 (all)	0.1084	0.1108	0.1066
$\rho_{max,min}$ (e Å^{-3})	0.34/-0.44	0.30/-0.40	0.38/-0.36
atomic occupancy (*C-OH)	0.139(4) : 0.861(4)	0.165(4) : 0.835(4)	0.154(4) : 0.846(4)
atomic occupancy (SO_4)	0.5 : 0.5	0.5 : 0.5	0.5 : 0.5

Table 6.14: The crystallographic data collected for sample SAS-10

sample SAS-10	**#1**	**#2**	**#3**	**#4**
formula	$C_{13}H_{22}N_1O_5S_{0.5}$	$C_{13}H_{22}N_1O_5S_{0.5}$	$C_{13}H_{22}N_1O_5S_{0.5}$	$C_{13}H_{22}N_1O_5S_{0.5}$
g mol^{-1}	288.34	288.34	288.34	288.34
T (K)	150.00(10)	150.01(10)	150.00(10)	150.01(10)
radiation	Cu Kα($\lambda = 1.54184$)	Cu Kα($\lambda = 1.54184$)	Cu Kα($\lambda = 1.54184$)	Cu Kα($\lambda = 1.54184$)
2θ range (^{o})	6.412 to 145.55	6.406 to 146.068	6.412 to 146.37	6.412 to 145.828
crystal system	monoclinic	monoclinic	monoclinic	monoclinic
space group	C2/c	C2/c	C2/c	C2/c
a (Å)	27.9017(5)	27.9254(9)	27.8989(4)	27.8976(7)
b (Å)	6.17975(12)	6.1743(2)	6.18110(6)	6.18100(16)
c (Å)	16.7698(3)	16.7802(5)	16.7700(2)	16.7766(4)
$\alpha(^o)$	90	90	90	90
$\beta(^o)$	98.8335(19)	98.845(3)	98.8458(12)	98.850(2)
$\gamma(^o)$	90	90	90	90
volume (Å^3)	2857.24(10)	2858.84(17)	2857.52(6)	2858.43(13)
Z	8	8	8	8
density (g cm^3)	1.337	1.331	1.340	1.340
$\mu(mm^{-1})$	1.501	1.500	1.501	1.500
completeness (%)	99.7	99.3	100	100
reflections collected	7174	7350	13565	6485
independent reflections	2848	2852	2856	2835
R int	0.0297	0.0341	0.0273	0.0234
GooF	1.061	1.164	1.068	1.159
R_1 (obs)	0.0549	0.0620	0.0413	0.0523
R_1 (all)	0.0560	0.0636	0.0422	0.0539
wR_2 (all)	0.1438	0.1561	0.1050	0.1287
$\rho_{max,min}$ (e Å^{-3})	0.55/-0.46	0.35/-0.31	0.38/-0.40	0.39/-0.45
atomic occupancy (*C-OH)	0.133(5) : 0.867(5)	0.190(6) : 0.810(6)	0.131(4) :0.869(4)	0.164(5) : 0.836(5)
atomic occupancy (SO_4)	0.5 : 0.5	0.5 : 0.5	0.5 : 0.5	0.5 : 0.5

Table 6.15: The crystallographic data collected for sample SAS-11

sample SAS-11	**#1**	**#2**	**#3**
formula	$C_{13}H_{22}N_1O_5S_{0.5}$	$C_{13}H_{22}N_1O_5S_{0.5}$	$C_{13}H_{22}N_1O_5S_{0.5}$
g mol^{-1}	288.34	288.34	288.34
T (K)	150.01(10)	150.00(10)	150.01(10)
radiation	Cu Kα($\lambda = 1.54184$)	Mo Kα($\lambda = 0.71073$)	Cu Kα($\lambda = 1.54184$)
2θ range (^{o})	6.406 to 145.798	5.91 to 61.118	6.406 to 145.798
crystal system	monoclinic	monoclinic	monoclinic
space group	C2/c	C2/c	C2/c
a (Å)	27.9235(5)	27.9086(9)	27.9235(5)
b (Å)	6.17276(12)	6.1779(2)	6.17276(12)
c (Å)	16.7963(3)	16.7629(5)	16.7963(3)
$\alpha(^o)$	90	90	90
$\beta(^o)$	98.8103(17)	98.850(3)	98.8103(17)
$\gamma(^o)$	90	90	90
volume ($Å^3$)	2860.93(9)	2855.79(17)	2860.93(9)
Z	8	8	8
density (g cm^3)	1.340	1.341	1.340
$\mu(mm^{-1})$	1.499	0.171	1.499
completeness (%)	99.7	89.3	99.7
reflections collected	7264	5137	7264
independent reflections	2856	3221	2856
R int	0.0307	0.0190	0.0307
GooF	1.099	1.055	1.099
R_1 (obs)	0.0550	0.0459	0.0550
R_1 (all)	0.0588	0.0566	0.0588
wR_2 (all)	0.1471	0.1241	0.1471
$\rho_{max,min}$ (e $Å^{-3}$)	0.36/-0.35	0.40/-0.29	0.36/-0.35
atomic occupancy (*C-OH)	0.213(5) : 0.787(5)	0.163(4) : 0.837(4)	0.213(5) : 0.787(5)
atomic occupancy (SO_4)	0.5 : 0.5	0.5 : 0.5	0.5 : 0.5

Table 6.16: The crystallographic data collected for sample SA-OX-1

sample SA-OX 1	**#1**	**#2**	**#3**
formula	$C_{14}H_{22}N_1O_5$	$C_{14}H_{22}N_1O_5$	$C_{14}H_{22}N_1O_5$
g mol^{-1}	284.32	284.32	284.32
T (K)	150.00(10)	150.00 (10)	150.00 (10)
radiation	Cu Kα($\lambda = 1.54184$)	Cu Kα($\lambda = 1.54184$)	Cu Kα($\lambda = 1.54184$)
2θ range (^{o})	10.694 to 147.296	10.704 to 147.144	10.692 to 145.99
crystal system	monoclinic	monoclinic	monoclinic
space group	P21/n	P21/n	P21/n
a (Å)	8.40511(19)	8.3986(3)	8.4075(4)
b (Å)	6.20065(14)	6.20228(16)	6.2047(2)
c (Å)	27.6803(6)	27.6418(8)	27.6621(12)
$\alpha(^o)$	90	90	90
$\beta(^o)$	97.211(2)	97.154(3)	97.178(4)
$\gamma(^o)$	90	90	90
volume (Å^3)	1431.21(6)	1428.66(7)	1431.71(10)
Z	4	4	4
density (g cm^3)	1.320	1.322	1.319
$\mu(mm^{-1})$	0.829	0.830	0.829
completeness (%)	99.7	99.7	99.7
reflections collected	7324	7104	7435
independent reflections	2880	2879	2856
R int	0.0392	0.0325	0.0390
GooF	1.021	1.073	1.039
R_1 (obs)	0.0469	0.0444	0.0521
R_1 (all)	0.0561	0.0513	0.0622
wR_2 (all)	0.1234	0.1174	0.1402
$\rho_{max,min}$ (e Å^{-3})	0.35/-0.31	0.33/-0.26	0.36/-0.26
atomic occupancy (*C-OH)	0.161(6) : 0.839(6)	0.121(5) : 0.879(5)	0.132(6) : 0.868(6)

Table 6.17: The crystallographic data collected for sample SA-OX-2

sample SA-OX 2	**#1**	**#2**	**#3**
formula	$C_{14}H_{22}N_1O_5$	$C_{14}H_{22}N_1O_5$	$C_{14}H_{22}N_1O_5$
g mol^{-1}	284.32	284.32	284.32
T (K)	150.00(10)	150.00 (10)	150.00 (10)
radiation	Cu Kα($\lambda = 1.54184$)	Cu Kα($\lambda = 1.54184$)	Cu Kα($\lambda = 1.54184$)
2θ range (^{o})	10.692 to 146.782	10.7 to 147.116	10.702 to 147.326
crystal system	monoclinic	monoclinic	monoclinic
space group	P21/n	P21/n	P21/n
a (Å)	8.4069(2)	8.40076(19)	8.4006(4)
b (Å)	6.20466(16)	6.20553(14)	6.2011(3)
c (Å)	27.6775(8)	27.6588(6)	27.6450(14)
$\alpha(^o)$	90	90	90
$\beta(^o)$	97.215(3)	97.177(2)	97.178(4)
$\gamma(^o)$	90	90	90
volume (Å^3)	1432.29(7)	1430.59(5)	1428.83(12)
Z	4	4	4
density (g cm^3)	1.319	1.320	1.322
$\mu(mm^{-1})$	0.828	0.829	0.830
completeness (%)	99.8	99.7	99.8
reflections collected	7492	7982	7289
independent reflections	2878	2877	2881
R int	0.0301	0.0227	0.0570
GooF	1.044	1.067	1.071
R_1 (obs)	0.0440	0.0386	0.0514
R_1 (all)	0.0501	0.0412	0.0633
wR_2 (all)	0.1107	0.0979	0.1298
$\rho_{max,min}$ (e Å^{-3})	0.35/-0.29	0.34/-0.30	0.37/-0.29
atomic occupancy (*C-OH)	0.153(5) : 0.847(5)	0.148(4) : 0.52(4)	0.165(6) : 0.835(6)

Table 6.18: The crystallographic data collected for sample SA-OX-3

sample SA-OX 3	**#1**	**#2**	**#3**
formula	$C_{14}H_{22}N_1O_5$	$C_{14}H_{22}N_1O_5$	$C_{14}H_{22}N_1O_5$
g mol^{-1}	284.32	284.32	284.32
T (K)	150.01(10)	150.00 (10)	150.01 (10)
radiation	Cu Kα($\lambda = 1.54184$)	Cu Kα($\lambda = 1.54184$)	Cu Kα($\lambda = 1.54184$)
2θ range (^{o})	10.702 to 147.202	10.7 to 147.512	10.698 to 146.018
crystal system	monoclinic	monoclinic	monoclinic
space group	P21/n	P21/n	P21/n
a (Å)	8.3996(2)	8.4010(3)	8.40282(16)
b (Å)	6.20369(16)	6.2001(2)	6.20170(14)
c (Å)	27.6549(6)	27.6519(9)	27.6617(6)
$\alpha(^o)$	90	90	90
$\beta(^o)$	97.214(2)	97.211(3)	97.1873(19)
$\gamma(^o)$	90	90	90
volume (Å^3)	1429.65(6)	1428.90(8)	1430.17(5)
Z	4	4	4
density (g cm^3)	1.321	1.322	1.320
$\mu(mm^{-1})$	0.830	0.830	0.830
completeness (%)	99.8	99.6	99.8
reflections collected	7185	7518	7721
independent reflections	2881	2878	2854
R int	0.0231	0.0285	0.0279
GooF	1.076	1.048	1.060
R_1 (obs)	0.0406	0.0459	0.0404
R_1 (all)	0.0448	0.0532	0.0450
wR_2 (all)	0.0991	0.1192	0.1011
$\rho_{max,min}$ (e Å^{-3})	0.34/-0.28	0.30/-0.23	0.33/-0.29
atomic occupancy (*C-OH)	0.148(4) : 0.852(4)	0.140(5) : 0.860(5)	0.160(5) : 0.840(5)

Table 6.19: The crystallographic data collected for sample SA-OX-4

sample SA-OX 4	**#1**	**#2**[a]	**#3**[a]
formula	$C_{14}H_{22}N_1O_5$	$C_{14}H_{22}N_1O_5$	$C_{14}H_{22}N_1O_5$
g mol^{-1}	284.32	284.32	284.32
T (K)	150.00(10)	150.00 (10)	150.01 (10)
radiation	Cu Kα($\lambda = 1.54184$)	Cu Kα($\lambda = 1.54184$)	Cu Kα($\lambda = 1.54184$)
2θ range (^{o})	10.7 to 147.414	10.712 to 146.218	10.696 to 145.974
crystal system	monoclinic	monoclinic	monoclinic
space group	P21/n	P21/n	P21/n
a (Å)	8.40087(19)	8.3917(6)	8.4048(5)
b (Å)	6.20198(16)	6.1940(3)	6.2098(2)
c (Å)	27.6590(5)	27.6272(18)	27.6314(14)
$\alpha(^o)$	90	90	90
$\beta(^o)$	97.195(2)	97.198(7)	97.222(5)
$\gamma(^o)$	90	90	90
volume (Å^3)	1429.74(6)	1424.69(15)	1430.69(12)
Z	4	4	4
density (g cm^3)	1.321	1.326	1.320
$\mu(mm^{-1})$	0.830	0.833	0.829
completeness (%)	99.4	99.6	99.8
reflections collected	7863	19404	7446
independent reflections	2873	2842	2854
R int	0.0233	0.2031	0.1004
GooF	1.063	1.039	1.043
R_1 (obs)	0.0415	0.0913	0.0952
R_1 (all)	0.0447	0.1355	0.1129
wR_2 (all)	0.1063	0.2879	0.2787
$\rho_{max,min}$ (e Å^{-3})	0.30/-0.33	0.45/-0.34	0.52/-0.46
atomic occupancy (*C-OH)	0.148(4) : 0.852(4)	0.183(12) : 0.817(12)	0.116(9) : 0.884(9)

[a] The crystallographic data collected is of poor quality and should be taken with caution.

Table 6.20: The crystallographic data collected for sample SA-OX-5

sample SA-OX 5	**#1**	**#2**	**#3**
formula	$C_{14}H_{22}N_1O_5$	$C_{14}H_{22}N_1O_5$	$C_{14}H_{22}N_1O_5$
g mol^{-1}	284.32	284.32	284.32
T (K)	150.00(10)	150.00 (10)	150.00 (10)
radiation	Cu Kα($\lambda = 1.54184$)	Cu Kα($\lambda = 1.54184$)	Cu Kα($\lambda = 1.54184$)
2θ range (^{o})	10.698 to 145.952	10.692 to 10.694	10.694 to 146.202
crystal system	monoclinic	monoclinic	monoclinic
space group	P21/n	P21/n	P21/n
a (Å)	8.40267(13)	8.40766(14)	8.4053(2)
b (Å)	6.21008(10)	6.20953(10)	6.20994(18)
c (Å)	27.6267(4)	27.6142(4)	27.6194(7)
$\alpha(^o)$	90	90	90
$\beta(^o)$	97.2135(14)	97.2227(15)	97.229(3)
$\gamma(^o)$	90	90	90
volume (Å^3)	1430.18(4)	1430.23(4)	1430.18(7)
Z	4	4	4
density (g cm^3)	1.320	1.320	1.320
$\mu(mm^{-1})$	0.830	0.830	0.830
completeness (%)	97.9	99.9	99.9
reflections collected	6563	7921	4990
independent reflections	2798	2849	2806
R int	0.0192	0.0231	0.0243
GooF	1.075	1.096	1.053
R_1 (obs)	0.0379	0.0417	0.0447
R_1 (all)	0.0397	0.0449	0.0536
wR_2 (all)	0.0953	0.1049	0.1121
$\rho_{max,min}$ (e Å^{-3})	0.28/-0.25	0.59/-0.38	0.34/-0.30
atomic occupancy (*C-OH)	0.096(4) : 0.904(4)	0.221(14) : 0.779(14)	0.212(16) : 0.788(16)

6.3 Space group determination of SAS

Crystallographic data collected from sample SAS-7, trial #4, was refined in the two previously reported space groups for the SAS structure, Cc and C2/c (table 6.21). A centrosymmetric crystal structure was found with a $|E^2-1|$ value of 1.037 (figure 9-35 in the Appendix). Refinement under non-centrosymmetric space group Cc afforded a Flack parameter of 0.5(3). Such a value suggests a configuration that is halfway between two forms and indicates that both enantiomers are present in equal proportions. PLATON, a single crystal structure validation program, found missed symmetry when the data was modelled in space group Cc and suggested space group C2/c.

Table 6.21: The refinement parameters of SAS refined in space group C2/c and Cc.

space group	**C2/c**	**Cc**
formula	$C_{13}H_{22}N_1O_5S_{0.5}$	$C_{26}H_{44}N_2O_{10}S_1$
g mol^{-1}	288.34	576.69
T (K)	136(6)	136(6)
radiation	Mo Kα($\lambda = 0.71073$)	Mo Kα($\lambda = 0.71073$)
2θ range (^{o})	6.124 to 58.36	6.124 to 58.36
crystal system	monoclinic	monoclinic
space group	C2/c	Cc
a (Å)	27.8674(16)	27.8674(16)
b (Å)	6.1678(3)	6.1678(3)
c (Å)	16.7358(10)	16.7358(10)
$\alpha(^o)$	90	90
$\beta(^o)$	98.819(6)	98.819(6)
$\gamma(^o)$	90	90
volume (Å^3)	2842.6(3)	2842.6(3)
Z	8	4
density (g cm^3)	1.349	1.348
$\mu(mm^{-1})$	0.172	0.172
completeness (%)	99.9	99.9
reflections collected	6739	6739
independent reflections	3301	4511
data/restraints/parameters	3301/1/223	4511/10/404
R int	0.0303	0.0322
GooF	1.047	1.044
R_1 (obs)	0.0488	0.0444
R_1 (all)	0.0722	0.0647
wR_2 (all)	0.1207	0.1196
$\rho_{max,min}$ (e Å^{-3})	0.36/-0.42	0.25/-0.39
flack parameter	-	0.5(3)
atomic occupancy of *C-OH	0.188(4) : 0.812(4)	0.333(7) : 0.667(7)
atomic occupancy of SO_4[a]	0.5 : 0.5	0.5 : 0.5

[a] atomic positions are fixed by symmetry

Figure 6-5 shows the structure of SAS refined in the two space groups, C2/c (a) and Cc (b). The dashed line in figure 6-5b shows missed symmetry in the structural model in the form of an inversion centre. This comparison confirmed the assignment of space group C2/c to SAS in this work.

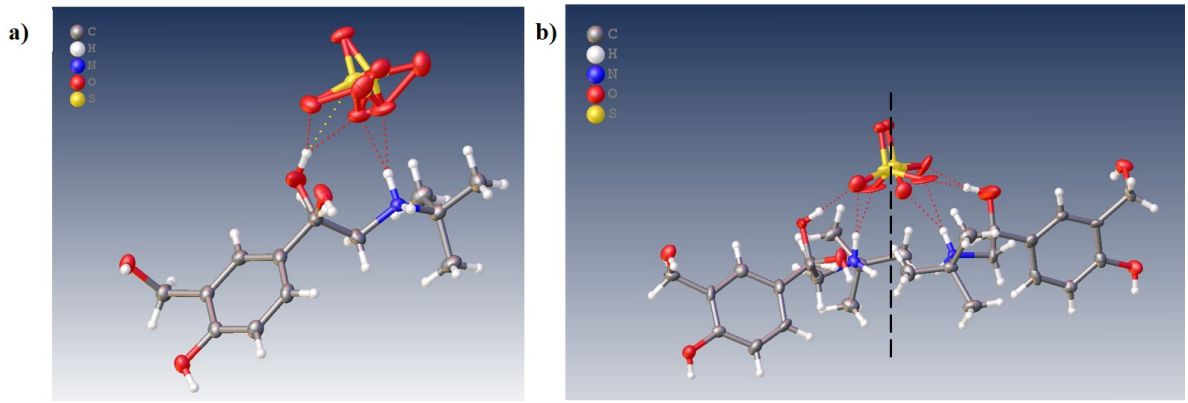

Figure 6-5: The structure of SAS refined in space group (a) C2/c and (b) Cc.

6.4 An investigation into the nature of disorder in SAS

6.4.1 The nature of disorder in the crystal structure

Two regions of structural disorder are seen in the crystal structure of SAS, when modelled in space group C2/c. Multiple atomic occupancies with a major and minor phase are observed around the *C-OH region, labelled O3 and O3A in figure 6-6a, and appear to be free of symmetry. An angle of 90.6(3)^o is seen between the disordered atoms comprising the major and minor phase (O3-C8-03A). In addition, the sulfate anion is disordered over an inversion centre. In this case, the occupancies of the atomic positions of the sulfate anion are restricted by the symmetry operator to be 0.5. Figure 6-6b shows the inversion centres (black spheres) in the unit cell of SAS, some of which are located in the centre of each sulfate anion.

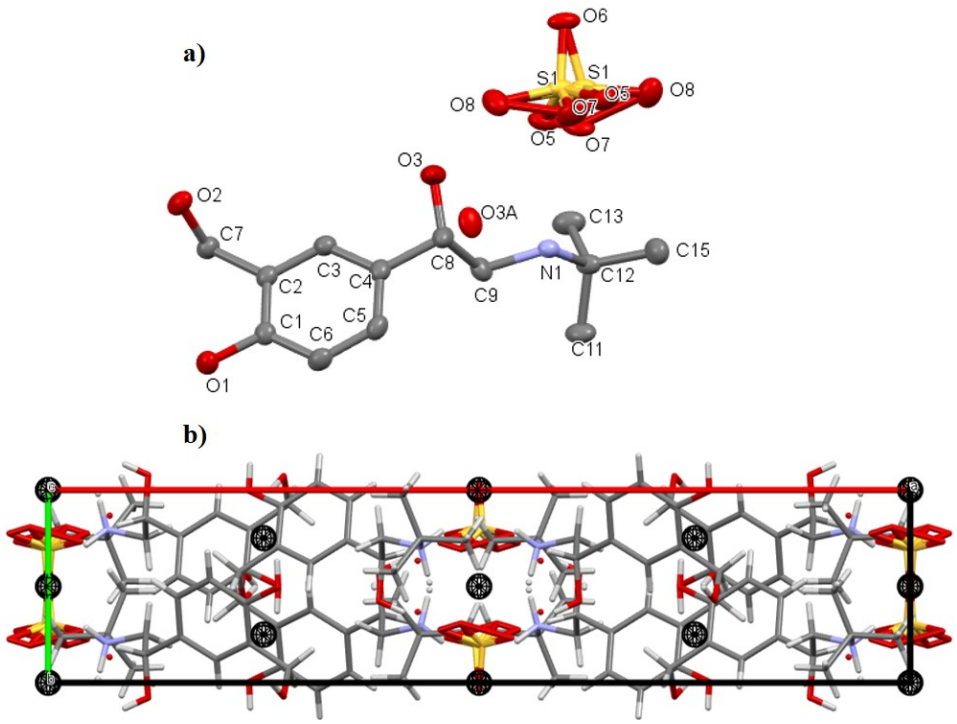

Figure 6-6: The structure of SAS, showing (a) labelled atoms and (b) the packing arrangement with symmetry operations, black spheres show the location of inversion centres.

The disordered *C-OH region in SAS was the main focus of this study. The free nature of the occupancies of the major and minor phase suggested the potential for single crystal-to-single crystal variations.

6.4.2 Variable temperature X-ray studies

Variable temperature X-ray diffraction experiments were performed to investigate the nature of the disorder in SAS (i.e. static, temperature-dependent static, or dynamic). Variable temperature experiments were performed on the same single crystal (sample SAS-2, trial #3); data were collected at 298 K, followed by data collection at 150 K immediately after the first acquisition temperature run. Table 6.22 shows the refinement parameters of each data set. A minor phase with an atomic occupancy of 0.084(4) was seen at 150 K and 298 K; this suggests that the major and minor phases are independent of temperature. On this evidence, the disorder observed in the crystal structure of SAS is therefore static in nature.

Table 6.22: The unit cell and refinement parameters of sample SAS-2 trial #3, refined at 150 K and 298 K.

acquisition temperature	**150 K**	**298 K**
formula	$C_{13}H_{22}N_1O_5S_{0.5}$	$C_{13}H_{22}N_1O_5S_{0.5}$
g mol^{-1}	288.34	288.34
T (K)	150.00(10)	298.00(10)
radiation	Cu Kα(λ = 1.54184)	Cu Kα(λ = 1.54184)
2θ range (^{o})	10.682 to 143.776	10.59 to 143.77
crystal system	monoclinic	monoclinic
space group	C2/c	C2/c
a (Å)	27.8694(8)	28.0450(10)
b (Å)	6.18860(19)	6.18631(17)
c (Å)	16.7609(6)	16.9074(6)
$\alpha(^o)$	90	90
$\beta(^o)$	98.821(3)	98.806(3)
$\gamma(^o)$	90	90
volume (Å^3)	2856.61(16)	2898.77(17)
Z	8	8
density (g cm^3)	1.341	1.321
$\mu(mm^{-1})$	1.501	1.480
completeness (%)	99.9	99.9
reflections collected	4531	4958
independent reflections	2753	2803
R int	0.0255	0.0230
GooF	1.027	1.032
R_1 (obs)	0.0457	0.0503
R_1 (all)	0.0543	0.0615
wR_2 (all)	0.1226	0.1464
$\rho_{max,min}$ (e Å^{-3})	0.31/-0.40	0.27/-0.30
atomic occupancy of *C-OH	0.084(4) : 0.916(4)	0.084(5) : 0.916(5)
atomic occupancy of SO_4[a]	0.5 : 0.5	0.5 : 0.5

[a] atomic positions are fixed by symmetry

6.5 An investigation into the nature of disorder in SA-OX

6.5.1 The nature of disorder in the crystal structure

The crystal structure of SA-OX is novel to this work and is presented in chapter 5, section 5.7.2. The refined structure displayed a similar case of structural disorder in the molecule of salbutamol as that observed in SAS. Multiple atomic occupancies with a major and minor phase are observed around the *C-OH region. In this solid form the disorder extends onto the C atom of the *C-OH region (see O6, O6A, C8 and C8A in figure 6-7). A significantly smaller angle of 46.3(5)^o is seen between the groups of the major and minor phase (O6-C8-06A) of SA-OX compared to an angle of 90.6(3)^o in SAS (O3-C8-03A in figure 6-6). No disorder is seen in the oxalate molecule.

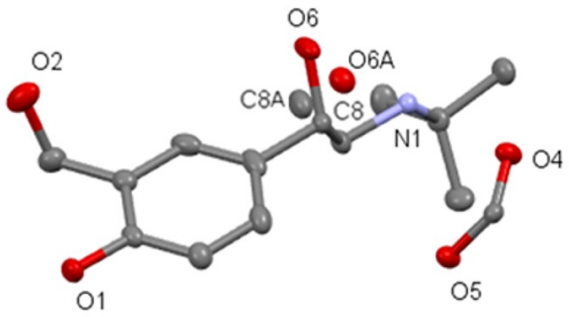

Figure 6-7: The structure of SA-OX showing labelled atoms.

6.5.2 Variable temperature X-ray studies

Variable temperature X-ray diffraction experiments were performed to investigate the nature of the disorder in SA-OX (i.e. static, temperature-dependent static, or dynamic). Variable temperature experiments were performed on the same single crystal (sample SAOX-3, trial #2); data were collected at 298 K, followed by data collection at 150 K immediately after the first acquisition temperature run. Table 6.23 shows the refinement parameters of each data set. A minor phase with an atomic occupancy of 0.140(5) was seen at 150 K and 0.134(8) at 298 K; these values are within error of one another and suggests that the major and minor phase occupancies are independent of temperature. Thus, on this evidence the disorder in SA-OX is also static in nature.

Table 6.23: The refinement parameters of sample SAOX-3 trial #2, refined at 150 K and 298 K.

acquisition temperature	**150 K**	**289 K**
formula	$C_{14}H_{22}N_1O_5$	$C_{14}H_{22}N_1O_5$
g mol^{-1}	284.32	284.32
T (K)	150.01 (10)	298.09 (15)
radiation	Cu K$\alpha(\lambda = 1.54184)$	Cu K$\alpha(\lambda = 1.54184)$
2θ range (^{o})	10.7 to 147.512	10.612 to 147.718
crystal system	monoclinic	monoclinic
space group	$P2_1/n$	$P2_1/n$
a (Å)	8.4010(2)	8.4844(8)
b (Å)	6.2001(2)	6.2472(6)
c (Å)	27.6519(9)	27.619(2)
$\alpha(^o)$	90	90
$\beta(^o)$	97.211(3)	96.832(9)
$\gamma(^o)$	90	90
volume (Å^3)	1428.90(8)	1453.5(2)
Z	4	4
density (g cm^3)	1.322	1.299
$\mu(mm^{-1})$	0.830	0.816
completeness (%)	99.6	95.3
reflections collected	7518	6899
independent reflections	2878	2809
R int	0.0285	0.0667
GooF	1.048	1.121
R_1 (obs)	0.0459	0.0677
R_1 (all)	0.0532	0.0950
wR_2 (all)	0.1192	0.2585
$\rho_{max,min}$ (e Å^{-3})	0.30/-0.23	0.52/-0.53
atomic occupancy	0.140(5) : 0.860(5)	0.134(8) : 0.866(10)

6.6 Single crystal-to-single crystal variations in the minor phase occupancy

Disclaimer: *All SS-NMR spectroscopy studies characterising samples in this section were conducted by Dr. Steven Brown, Warwick University, as part of a research collaboration between the University of Bath, Warwick University and AstraZeneca. Material preparation for SS-NMR spectroscopy experiments was conducted by the author. The same sample batches (SAOX-1, SAOX-2 and SAOX-4) were characterised by X-ray crystallography and SS-NMR spectroscopy. Sample batches of SAS were not characterised by SS-NMR spectroscopy due to issues with confidentiality. Characterisation and the interpretation of all SS-NMR spectroscopy samples and data was conducted by Warwick University and AstraZeneca and not the author of this work.*

The characterisation of single crystal-to-single crystal structural variations in a bulk sample is important, as variations in disorder between multiple crystals could potentially cause inconsistencies within manufacturing, since disorder may influence a material's physical properties.[92,192] This study aims to determine variations in disorder on a molecular scale (single crystal-to-single crystal) and compare it to variations observed in the bulk powder. X-ray crystallography was used as a tool for the crystal-to-crystal quantification of disorder in SAS and SA-OX. While the analysis of 3-4 single crystals is not fully representative of the bulk material, it does provide a valuable insight into the variation of disorder between single crystals in a batch. SS-NMR spectroscopy was used to characterise disorder in the bulk powder of SA-OX via assessing the relative population of molecules in distinct conformations, i.e. the major and minor phases. The combination of X-ray crystallography and SS-NMR spectroscopy methods is an important tool for understanding the nature of disorder in a material at a local scale (when viewed by NMR) and longer-range periodic scale (when viewed by crystallography).

6.6.1 Single crystal-to-single crystal variations in SAS

The minor phase occupancy of at least three single crystals isolated from sample batches was determined from each crystallised sample of SAS (SAS-1 to SAS-11 in table 6.3, section 6.2). Table 6.24 displays the minor phase occupancies of each single crystal, the average minor phase occupancy, as a percentage, of each single crystal analysed in a sample and the observed range of occupancies in a sample. The standard uncertainties for all of the X-ray experiments in table 6.24 indicate consistently precise determinations for each sample. The minor phase occupancy value as a function of crystallisation temperature, rate and concentration is discussed below.

Table 6.24: The minor phase values recorded from crystallised samples of SAS (SAS-1 to SAS-11)

sample	**speed of crystallisation**	**minor phase occupancy**				**average (%)**	**range observed (%)**
40^{o}C, concentration = 100%							
SAS-1	3-5 days	0.093(5)	0.123(4)	0.153(3)	0.155(5)	13.1	15.5-9.3
SAS-2	11-14 days	0.084(4)	0.040(3)	0.064(6)	-	6.2	8.4-4.0
20^{o}C, concentration = 100%							
SAS-5	3-5 days	0.161(4)	0.163(4)	0.104(4)	0.103(4)	13.2	16.3-10.3
SAS-6	11-14 days	0.107(4)	0.122(4)	0.123(3)	0.113(4)	11.6	12.3-10.7
4^{o}C, concentration = 100%							
SAS-9	11-14 days	0.139(4)	0.165(4)	0.154(4)	-	15.3	16.5-13.9
SAS-10	30-32 days	0.133(5)	0.190(6)	0.131(4)	0.164(5)	15.5	19.0-13.1
40^{o}C, concentration= 50%							
SAS-3	3-5 days	0.167(4)	0.163(4)	0.159(4)	-	16.3	16.7-15.9
20^{o}C, concentration = 50%							
SAS-7	3-5 days	0.165(5)	0.163(4)	0.145(4)	0.188(4)	16.5	18.8-14.5
4^{o}C, concentration = 50%							
SAS-11	30-32 days	0.213(5)	0.213(5)	0.163(4)	-	19.6	21.3-16.3
40^{o}C, concentration = 25%							
SAS-4	3-5 days	0.130(4)	0.129(4)	0.138(5)	-	13.2	13.8-12.9
20^{o}C, concentration = 25%							
SAS-8	3-5 days	0.166(4)	0.163(5)	0.166(4)	-	16.5	16.6-16.3

Figure 6-8 and figure 6-9 show a visual summary of the results obtained in this study. In these figures, the average minor phase occupancies found in a sample are shown with grey boxes and the range of disorder observed in a sample is represented by black bars (in this case the black "error" bars do not show the standard uncertainties of X-ray data).

6.6.1.1 The influence of crystallisation rate

Under a concentration of 100% and a set temperature of 40^{o}C (samples SAS-1 and SAS-2), the rate of crystallisation had an influence on the minor phase occupancies in single crystals of SAS (figure 6-8). A 2-fold increase was found for the average minor phase value under a crystallisation rate of 3-5 days, ≈13%, compared to 11-14 days, ≈6%. The range of disorder occupancies from the average value was found to be similar for these experiments +/- ≈2 to 3%.

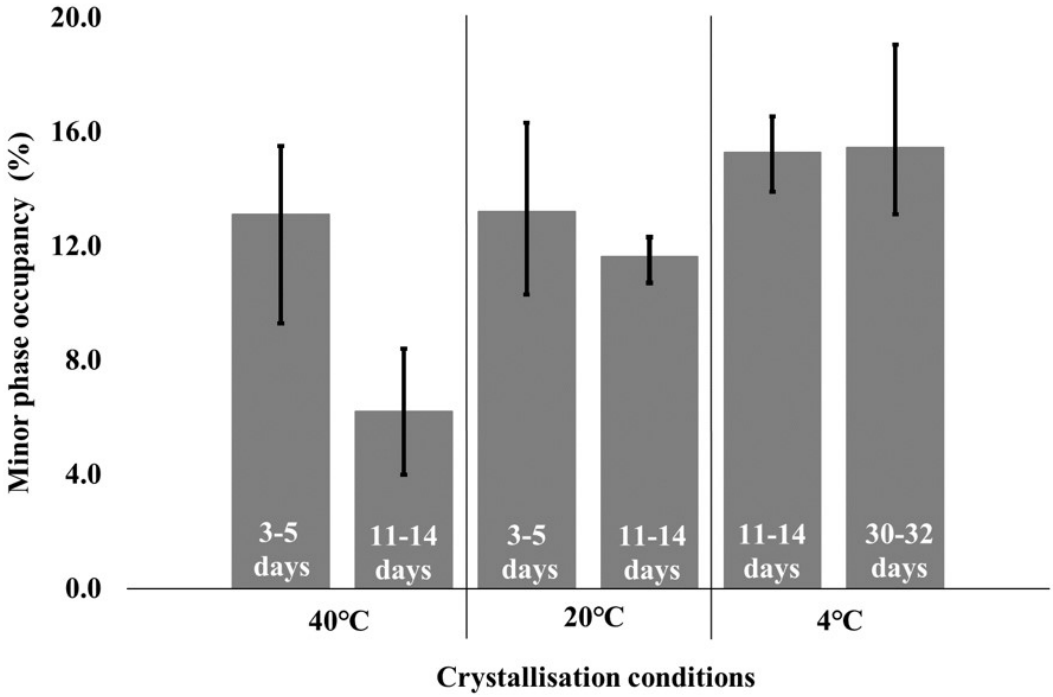

Figure 6-8: The average and range of minor phase occupancies in single crystals of SAS as a function of crystallisation conditions, with a focus on rate.

At a lower set temperature of 20^{o}C and 4^{o}C and a concentration of 100%, the rate of crystallisation did not show any significant influence on the minor phase occupancies found in single crystals of SAS (figure 6-8). In both cases, the average minor phase occupancy was approximately the same and within the distribution range of all four of the samples investigated in table 6-8. At 20^{o}C, an average minor occupancy of ≈ 12% (+/- ≈1%) and 13% (+/- ≈3%) were obtained under a crystallisation rate of 11-14 days and 3-5 days respectively. At 4^{o}C, an average minor occupancy of ≈ 15% were obtained under a crystallisation speed of 11-14 days (+/- ≈1.4%) and 30-32 days (+/- ≈3%) respectively. The experiments at a lower set temperature of 20^{o}C and 4^{o}C (samples SAS-5, SAS-6, SAS-9 and SAS-10) show different observed ranges of disorder. However, all of the minor phase values for each of these experiments are within each other's distribution range. It is possible that the analysis of a larger data set (more

than four single crystals per sample) would show consistent values of the average minor phase and observed range of disorder in samples SAS-5, SAS-6, SAS-9 and SAS-10.

6.6.1.2 The influence of crystallisation temperature

Under a concentration of 100% and a set crystallisation rate, the temperature of crystallisation seems to have a small influence on the minor phase occupancies seen in single crystals of SAS (figure 6-9). At a set rate of 11-14 days a higher crystallisation temperature yielded crystals with a lower average minor phase occupancy; this value increases as the temperature of crystallisation decreases (40^oC = 6.2%, 20^oC = 11.6% and 4^oC = 15.3%). In this case, the minor phase occupancies for each sample are not within the distribution range of each experiment and do appear to be significantly different. The same trend is not observed at a set crystallisation rate of 3-5 days (40^oC = 13.1% and 20^oC = 13.2%); in this case the minor phase values for each sample and the range of values observed (9-16%) are consistent. A slightly higher average minor phase occupancy of 15.5% and range of 19.0-13.1% was found under 4^oC at a set crystallisation rate of 30-32 days (figure 6-9). However, the distribution range of values observed are not too dissimilar to the ranges observed at other temperatures. The collection of additional data on samples that take 30-32 days to crystallise at 40^oC and 20^oC would be required for further comments to be made on this data set.

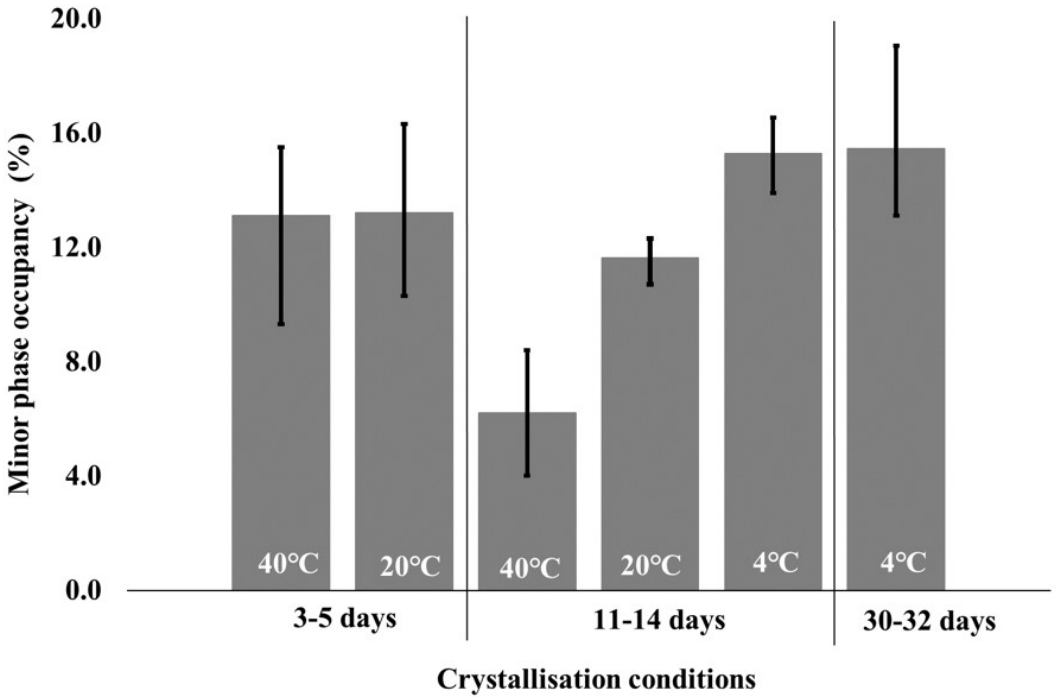

Figure 6-9: The average and range of minor phase occupancies in single crystals of SAS as a function of crystallisation conditions, with a focus on temperature.

6.6.1.3 The influence of concentration

At a set rate and temperature of crystallisation, the concentration does not have a significant influence on the average minor phase occupancies of each sample (figure 6-10). Small differences were observed, however the values for each sample are within the distribution range of each

experiment (apart from a concentration of 25% at 40^{o}C) and may not be different in the analysis of a larger data set (see dashed red line in figure 6-10). Comparing the observed range in each sample suggests that a lower concentration of crystallisation (i.e. 25%) has more consistent minor phase occupancy value, with a significantly smaller variation range observed. A range of 13.8-12.9% (+0.56% an -0.34% from the average value) was found at 40^{o}C (SAS-4) and 16.6-16.3% (+0.10% and -0.20% from the average value) at 20^{o}C (SAS-8). This is a significantly lower distribution range than at higher concentrations of crystallisation (e.g. 100%, where an observed range of +/- 2-3% from the average value was seen).

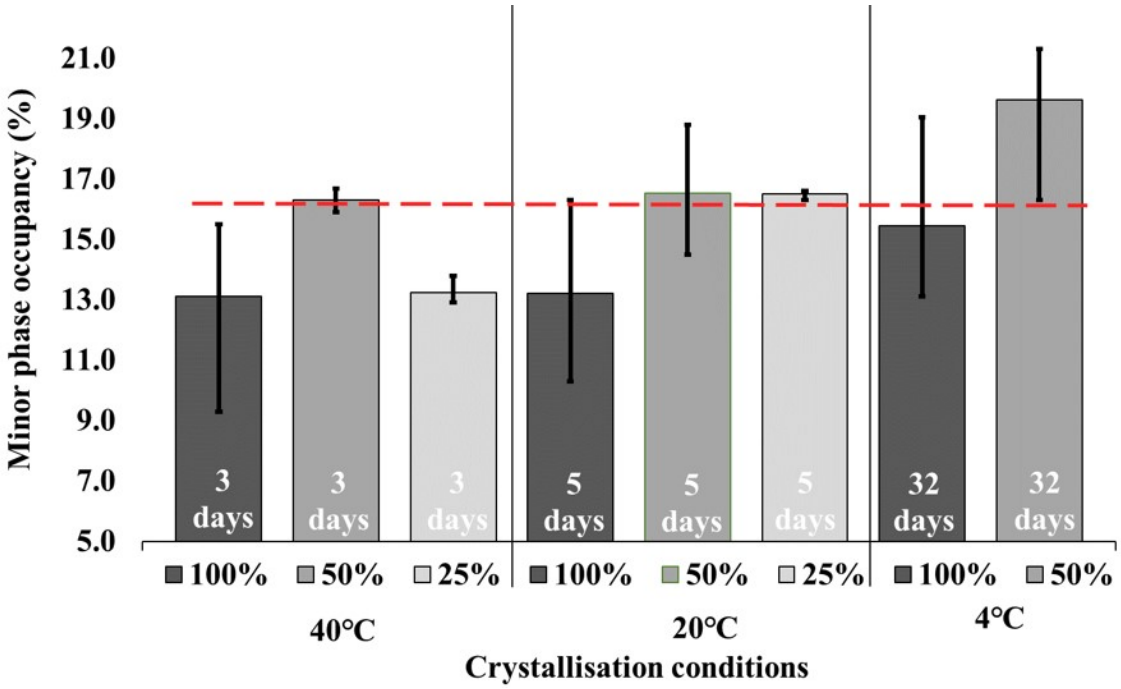

Figure 6-10: The average and range of minor phase occupancies in single crystals of SAS as a function of crystallisation conditions, with a focus on concentration.

6.6.1.4 The overall influence of crystallisation conditions

The portfolio of X-ray data collected for SAS does not show a significant influence on the relative minor phase occupancy seen in each sample as a function of crystallisation temperature, rate and concentration. Single crystal-to-single crystal variations in each sample are observed in this study. The average minor phase occupancy can differ significantly between samples. The lowest average minor occupancy seen between samples was 6.2% (SAS-2) and the highest average minor occupancy seen was 19.6% (SAS-11). Studies on the observed range seen in each sample suggest that these values are significantly different from one another; the highest occupancy range observed in a sample was 15.5-9.3% (+2.39% and -3.81% from the average value) in SAS-1, and the lowest range observed was 16.6-16.3% (+0.1% and -0.2% from the average value) in SAS-8.

6.6.1.5 The influence of crystal growth rates during crystallisation

This study was extended to look at the influence of crystal growth rates during crystallisation. The point at which nucleation was first seen by eye was recorded (start of crystal growth) and the point at which the crystallisation solvent had evaporated to dryness was recorded (finish of crystal growth) for samples held at 40^{o}C (SAS-1, SAS-3 and SAS-4), 20^{o}C (SAS-5, SAS-7 and SAS-8) and 4^{o}C (SAS-10 and SAS-11). Three identical batches were set up for each sample and an average value was recorded for each of the three sample batches studied. This study looks at the appearance of the first nuclei crystallising under different concentrations and temperatures and is of importance since there was no form of agitation during crystallisation. The absence of mixing could cause a gradient difference or shear effects which may lead to a difference in nucleation kinetics between samples.[196] Figure 6-11 displays a graph of the data obtained. In the graph a solid line, a dashed line, and a dotted line are used to guide the eye and correspond to experiments with a set temperature of 40^{o}C, 20^{o}C and 4^{o}C respectively.

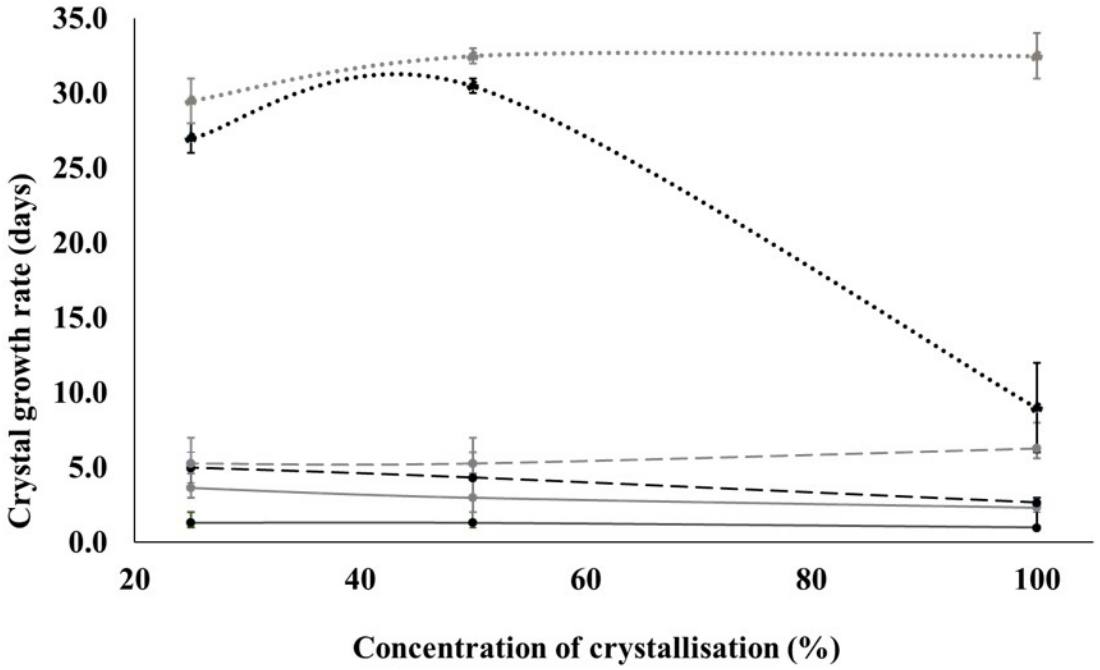

Figure 6-11: Crystal growth rates during crystallisation of SAS under different concentrations at set temperatures of 40^{o}C (solid line), 20^{o}C (dashed line) and 4^{o}C (dotted line). The data points recorded for the start of nucleation are in black and the data points recorded for solvent evaporation to dryness are in grey.

Linear growth rates are seen for the start and finish of crystal growth, under a 100%, 50% and 25% concentration of crystallisation at 40^{o}C (solid line) and 20^{o}C (dashed line). This finding is in good agreement with the single crystal-to-single crystal X-ray data obtained in this study; the concentration of crystallisation did not have an influence on the average minor phase occupancies of each sample. The finding of linear growth rates correlates with the X-ray data as no significant difference in the rate of nucleation and crystal growth were seen for samples of SAS with different concentrations. At 4^{o}C (black dotted line), a significant

difference was seen for the point at which nucleation was first observed in a sample of 100% concentration (≈9 days) compared to a sample of 50% and 25% concentration (≈30 days). All of the samples held at a temperature of 4^{o}C were stored in a fridge, an environment which may have different humidity and moisture levels in the air than the bench top environment that all of the samples held at a temperature of 40^{o}C and 20^{o}C were stored. Although there may be a difference in nucleation kinetics between samples held in a fridge (at 4^{o}C) compared to those held on a bench top (at 40^{o}C and 20^{o}C), no differences in the minor phase occupancy in single crystals of SAS correlate to this finding. The rate of solvent evaporation until dryness at 4^{o}C (grey dotted line) was found to be more consistent and an almost linear growth rate was found under a concentration of 100%, 50% and 25%.

6.6.1.6 Investigating the distances and angles of relevant functional groups.

The aim of this study was to identify any deformations or strain in the structures that may be required to improve interactions in the minor phase regions. The distances and angles around the disordered *C-OH region were measured for most of the sample trials (SAS-1 to SAS-8) characterised by SCXRD, table 6.25 displays a summary of the results in order of minor phase occupancy value (low to high). A distance range of 1.40-1.37 Å was measured between C8 and O3 atoms (figure 6-12) and a subtle correlation between the distance and site occupancies were found. The measured distances between C8 and O3 atoms (major phase atoms) were found to decrease slightly as the minor occupancy increased. For example, a lower minor phase occupancy of 4.0% had a longer C8 to O3 distance of 1.406(2) Å, a medium minor phase occupancy of 14.4% had a C8 and O3 distance of 1.385(3) Å and a higher minor phase occupancy of 21.3% had a C8 and O3 distance of 1.379(3) Å. The C8 to O3 distance in an ordered structure of SA (as a single entity), published in the CSD (BHHPHE), is 1.432 Å and is good agreement with the distance measured in the ordered structure of SA determined in this work of 1.430(5) Å (see chapter 5, section 5.7.1 for more details).

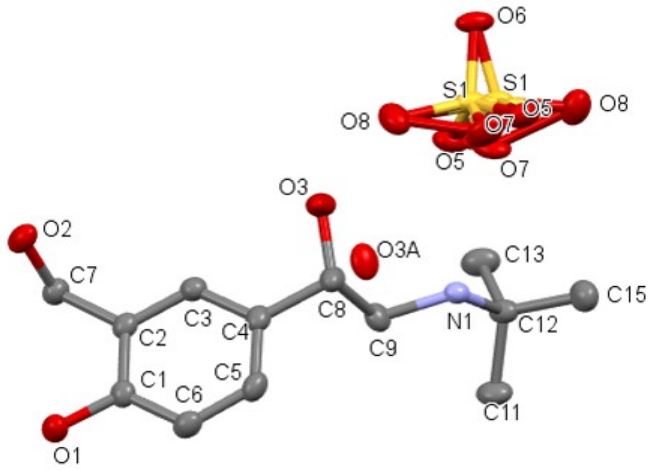

Figure 6-12: The structure of SAS, showing labelled atoms.

The findings discussed suggest that the minor phase occupancy in crystal structures of SAS increases slightly as the C8 and O3 bond length becomes shorter and more strained. The parameters measured for the C8 and O3A bond length and O3A-C8-O3 angles are not signifi-

cantly different from each other. As would be expected for refined parameters involving atomic sites with different levels of occupancy, large differences in the standard uncertainty values were seen between atom distances of the major phase (O3-C8) and minor phase (O3A-C8). Lower standard uncertainties between 0.002 and 0.004 were seen in the measured distances of O3-C8, compared to significantly higher standard uncertainties of 0.006 and 0.015 for the distances of O3A-C8.

Table 6.25: The distance and angles measured in SAS samples (at 150 K) in order of minor phase value.

Sample and trial number	Minor phase (%)	Distances (Å) and angles (°)		
		O3-C8	O3A-C8	O3A-C8-O3
SAS-2 #2	4.0	1.406(2)	1.352(15)	89.3(12)
SAS-1 #1	9.9	1.394(2)	1.305(12)	90.9(7)
SAS-5 #4	10.2	1.392(2)	1.286(10)	92.0(6)
SAS-5 #3	10.3	1.394(2)	1.284(10)	91.6(6)
SAS-6 #2	12.1	1.391(2)	1.291(10)	92.9(6)
SAS-6 #3	12.3	1.391(2)	1.292(10)	92.0(6)
SAS-4 #2	12.9	1.387(3)	1.297(10)	92.2(6)
SAS-4 #1	13.0	1.391(2)	1.306(9)	91.9(6)
SAS-4 #3	13.6	1.390(3)	1.277(8)	91.3(5)
SAS-9 #1	13.7	1.391(2)	1.308(8)	92.0(5)
SAS-7 #3	14.4	1.385(3)	1.282(11)	89.8(6)
SAS-1 #3	15.4	1.391(3)	1.271(10)	91.6(5)
SAS-1 #4	15.5	1.386(3)	1.299(9)	92.2(6)
SAS-9 #3	15.6	1.384(3)	1.301(9)	90.8(5)
SAS-3 #3	15.9	1.384(3)	1.301(9)	90.8(5)
SAS-5 #1	16.1	1.387(3)	1.297(7)	90.2(5)
SAS-5 #2	16.2	1.386(2)	1.296(7)	89.9(4)
SAS-7 #2	16.3	1.388(3)	1.298(8)	90.3(5)
SAS-3 #2	16.3	1.384(2)	1.295(7)	90.8(4)
SAS-8 #2	16.3	1.385(2)	1.295(7)	92.6(4)
SAS-9 #2	16.5	1.385(2)	1.295(7)	91.6(4)
SAS-8 #1	16.6	1.384(2)	1.291(7)	90.3(4)
SAS-3 #1	16.7	1.385(3)	1.297(7)	90.2(4)
SAS-8 #3	16.7	1.385(3)	1.297(7)	90.2(4)
SAS-7 #4	18.8	1.382(3)	1.290(6)	90.6(4)
SAS-10 #2	19.0	1.379(4)	1.304(10)	92.1(6)
SAS-11 #2	21.3	1.379(3)	1.299(7)	92.6(5)

6.6.2 Single crystal-to-single crystal variations in SA-OX

The occupancies of the minor phase position found in three different single crystals in a batch were recorded for each crystallised sample of SA-OX (SAOX-1 to SAOX-5 in table 6.4, section 6.2). Table 6.26 displays the minor phase occupancies for each single crystal, the average minor phase occupancies calculated as a percentage of each single crystal analysed and the distribution range observed. The minor phase occupancy as a function of crystallisation temperature and rate are discussed below.

Table 6.26: The minor phase occupancy values recorded from crystallised samples of SA-OX (SAOX-1 to SAOX-5).

sample	**rate (day(s))**	**minor phase occupancy**			**average (%)**	**range observed (%)**
50^{o}C, concentration = 100%						
SAOX-1	≤1	0.161(6)	0.121(5)	0.132(6)	13.8	16.1-12.1
30^{o}C, concentration = 100%						
SAOX-2	3-4	0.153(5)	0.148(4)	0.165(6)	15.5	16.5-14.8
20^{o}C, concentration = 100%						
SAOX-3	≤1	0.148(4)	0.140(5)	0.160(5)	14.9	16.0-14.0
SAOX-4	3-4	0.148(4)	0.183(12)	0.116(9)	14.9	18.3-11.6
SAOX-5	40	0.096(4)	0.221(14)	0.212(16)	17.6	22.1-9.6

Figure 6-13 and figure 6-14 show a visual summary of the results obtained in this study. In these figures, the average minor phase occupancies found from single crystal-to-single crystal analysis of samples is shown with grey boxes and the observed range of disorder from each crystal in the data set is represented by black bars (in this case the black "error" bars do not show the standard uncertainties of X-ray data).

6.6.2.1 The influence of crystallisation rate

Under a concentration of 100% and a set temperature of 20^{o}C (samples SAOX-3, SAOX-4 and SAOX-5), the rate of crystallisation does not have an influence on the average minor phase occupancy. An average minor phase of ≈15-17% was found in all samples. The range of disorder was found to increase as the rate of crystallisation decreased. A small distribution range of 16.0-14.0% (+/- ≈1% from the average value) was found after ≤1 day which increased to a larger distribution range of 18.3-11.6 (+/- ≈3% from the average value) after 3-4 days and 22.1-9.6 (+≈4%, - ≈8% from the average value) after 40 days (figure 6-13).

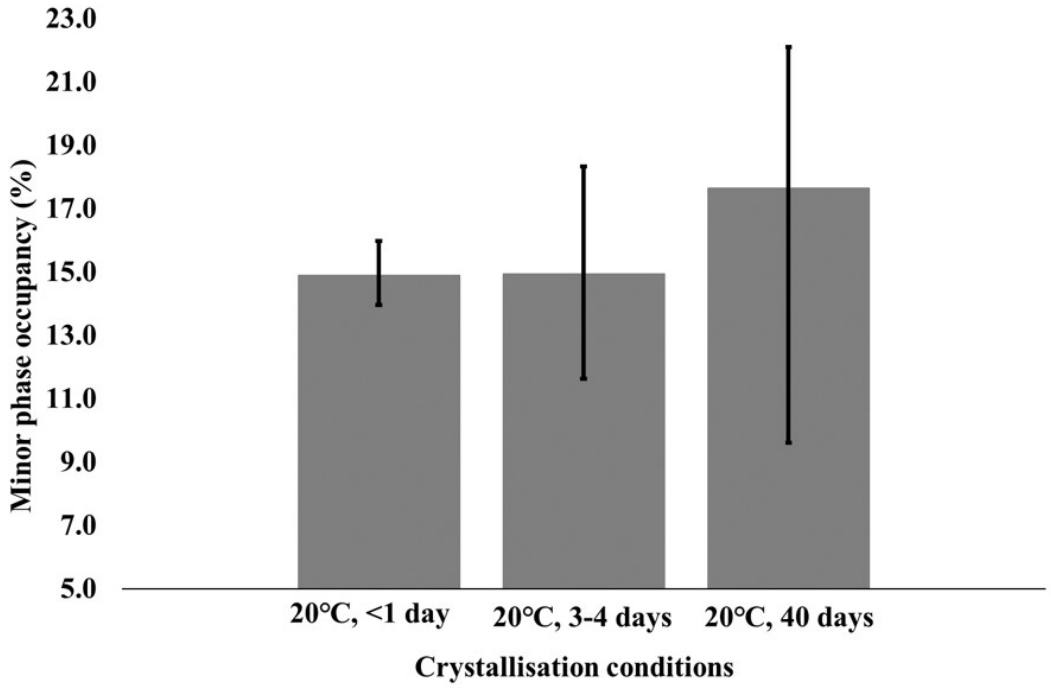

Figure 6-13: Minor phase occupancy in crystals of SA-OX as a function of crystallisation conditions with a focus on speed of crystallisation.

6.6.2.2 The influence of crystallisation temperature

Under a set crystallisation rate of 1-4 days and crystallisation temperatures ranging across 50, 30 and 20^{o}C, relatively consistent results were again found between each sample. Average minor phase occupancies of approximately 14-15% were found, with a distribution range of +/- ≈1-4% and all of the minor phase occupancies for these experiments are within each other's distribution range (figure 6-14). From this, it might be expected that the analysis of a larger data set (more than three single crystals per sample) would show consistent values of the average minor phase and distribution range in samples SAOX-1, SAOX-2 and SAOX-3.

6.6.2.3 The overall influence of crystallisation conditions

The portfolio of X-ray data collected for SA-OX does not show a significant influence on the average relative minor disorder phase seen in each sample as a function of crystallisation temperature and rate. The average minor phase value differs only slightly between samples with a lowest average minor phase of 13.8% (SAOX-1) and a highest average minor phase of 17.6% (SAOX-5) observed between the samples. However, individual single crystal-to-single crystal variations in each sample are observed in this study; studies on the range of disorder observed in each sample showed large differences between the consistency of disorder. The highest range observed in a sample was 22.1-9.6 (+4.5% and -8.0% from the average value) in sample SAOX-5 and the lowest range observed was 16.5-14.8 (+1.0% and -0.7% from the average value) in sample SAOX-2.

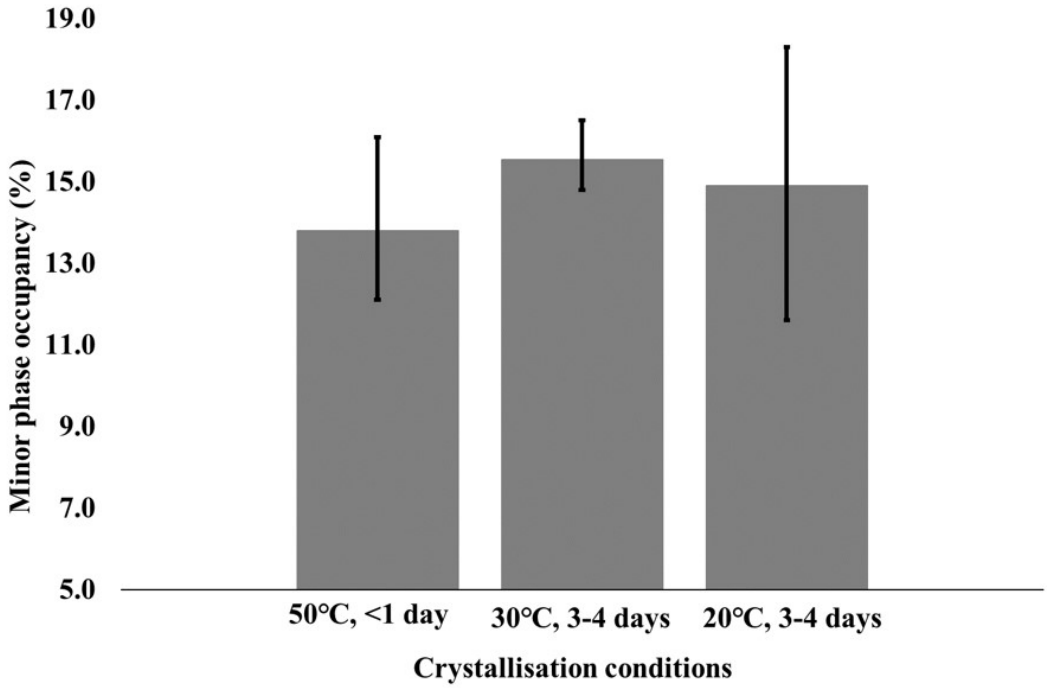

Figure 6-14: Minor phase occupancy in crystals of SA-OX as a function of crystallisation conditions with a focus on temperature of crystallisation.

6.6.2.4 Bulk analysis of the minor phase via SS-NMR

One aim of this work was to combine a bulk analysis technique, such as SS-NMR spectroscopy, with SCXRD to help close the gap between the characterisation of disorder in single crystals and the bulk material. SS-NMR spectroscopy experiments were conducted by Warwick University on samples SAOX-1, SAOX-2 and SAOX-4 to confirm and quantify the minor phase occupancies found in the bulk powder. Table 6.27 contains a comparison of the results including a summary of the SS-NMR spectroscopy results reported by the collaborators at Warwick University and of the X-ray data collected by the author.

Table 6.27: The minor phase values recorded from X-ray and SS-NMR spectroscopy characterisation of crystallised SA-OX samples (SAOX-1, SAOX-2 and SAOX-4).

sample	**X-ray average (%)**	**X-ray range observed (%)**	**NMR minor phase (%)**
SAOX-1	13.8	16.1-12.1	12 +/-3
SAOX-2	15.5	16.5-14.8	11 +/-2
SAOX-4	14.9	18.3-11.6	9 +/-3

The relative amount of disorder in the bulk, measured by SS-NMR spectroscopy, seems to be consistent across all three samples of SA-OX, and is in good agreement with the X-ray results. Similar minor phase values of 9-12% (+/- 3) were found by SS-NMR spectroscopy in the bulk powder of each sample that are close to the average minor phase occupancies found in single crystals of 13-15 %, by X-ray crystallography. SCXRD paired with SS-NMR spectroscopy confirms that crystallisation temperature and rate do not appear to influence the

relative minor disorder phase seen in each sample. The SS-NMR spectroscopy results from the bulk samples support the conclusion drawn from the X-ray data that a larger data set (more than three single crystals per sample) would be expected to show consistent values of the average minor phase and distribution range in samples SAOX-1, SAOX-2 and SAOX-4.

Variable temperature SS-NMR spectroscopy experiments indicate that the relative major and minor phase populations are slightly dependent on data collection temperature. Experiments interpreted by collaborators at Warwick University reported a slight increase in the peak intensity due to the minor site as the temperature was reduced. Variable temperature X-ray crystallography experiments (discussed in section 6.5.2), in contrast, do not show a temperature dependence in single crystals of SA-OX; the refined disorder site occupancies were found to be within error at the two temperatures (150 K and 298 K) and thus independent of acquisition temperature within the precision of the crystallographic determination. The discrepancy between temperature dependence between data collected by SS-NMR spectroscopy and X-ray crystallography could be caused by the restraints imposed on the X-ray data during data refinement. It is possible that the nature of disorder may have been masked by the removal of unusual features to meet CIF requirements; similarity restraints on bond lengths, angles and on displacement parameters (SAME / SADI and SIMU) were used in the refinement of SA-OX.

This investigation highlights the importance of combining SCXRD with SS-NMR spectroscopy. X-ray crystallography can provide a detailed picture of how the molecules arrange in the solid-state on a molecular level and SS-NMR spectroscopy can provide information on the larger (bulk powder) level. Finding a method that can analyse disorder in a bulk material that can be compared with the disorder observed in a single crystal can help with many research applications; this would be especially relevant in materials where disorder may change the physical properties.

6.6.3 Eliminating enantiomeric excess as the cause of multiple site occupancies

SA-OX crystallises in space group $P2_1/n$ which suggests that the crystals are a racemic mixture and the multiple site occupancies observed in the structure are due to a major and minor phase. In the case of a batch of crystals with an enantiomeric excess (ee), two different crystal forms would be identified, each crystallising in a separate non-centrosymmetric space group. For example, with an excess of 80:20, 80% of the crystals would crystallise with one handedness and 20% of crystals would separately crystallise with the other handedness. Technically, the presence of two different enantiomers should not cause multiple site occupancy positions within a crystal structure. However, if the two forms were to co-crystallise and become superimposed, the crystals would display apparent disorder in the case where the two forms can co-crystallise in a centrosymmetric space group.

CD spectroscopy was used as a method to identify the ee in a single crystal of SA-OX (sample SAOX-1, trial #2), the bulk material of SA-OX (sample SAOX-1), the bulk material of SA and the bulk material of a pure enantiomer, (R)-SA HCl, that was obtained from Sigma-Aldrich.

A racemic mixture has an ee of 0% and a single pure enantiomer has an ee of 100%. CD spectroscopy can discriminate between a solution containing a racemic mixture and an achiral solution by measuring the difference in absorption of left and right circularly polarised light. A molar ellipticity of zero (within background noise) was found by CD spectroscopy in a single crystal of SA-OX, the bulk material of SA-OX and the bulk material of SA (the grey, yellow and orange traces in figure 6-15). This result corresponds to a racemic mixture, as equal amounts of left and right circularly polarised light were measured. As expected, a significant and consistent negative molar ellipticity was found for the pure enantiomer, (R)-SA HCl (the dark blue trace in figure 6-15); in this case, only one handiness of circularly polarised light was measured.

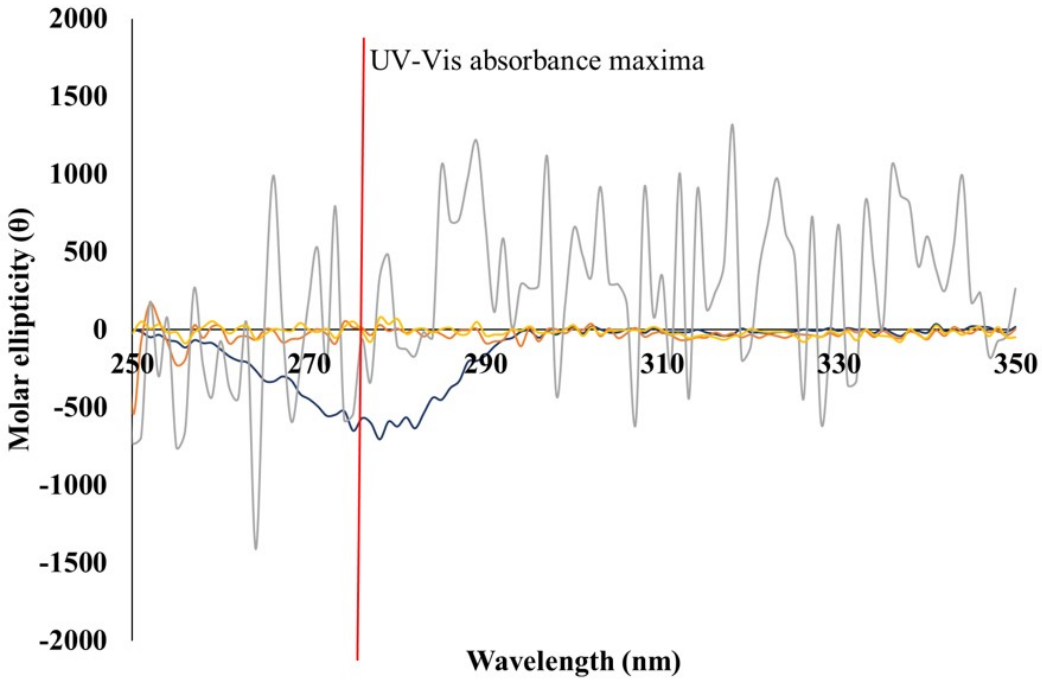

Figure 6-15: Material characterisation by CD, showing the molar ellipticity trace obtained for a single crystal of SA-OX (grey), the bulk powder of SA-OX (yellow), the bulk powder of SA (orange) and the bulk powder of pure enantiomer, (R)-SA HCl (dark blue). The UV-Vis absorbance maxima obtained for each material is highlighted by a red line.

This study confirmed that the single crystals of SA-OX analysed by SCXRD are racemic mixtures and that the disorder observed in the crystals is not due to the co-crystallisation of two different enantiomers. This conclusion is also supported by the variable temperature SS-NMR spectroscopy experiments that found a temperature dependence of the occupancies, eliminating the possibility that ee is the cause of the disorder in SA-OX (the ee of a material is independent of temperature).

6.7 Conclusion

The work presented in this chapter investigated the single crystal-to-single crystal variations in disorder of two pharmaceutically relevant model systems, SAS and SA-OX. Variations in disorder were studied at the molecular level, via X-ray crystallography, and at the bulk powder level with SS-NMR spectroscopy and CD spectroscopy. A portfolio of crystallographic data was collected to understand the nature of the disorder present (i.e. static or dynamic) and to quantify the variation of disorder observed in samples prepared under different crystallisation conditions; the effect of temperature, rate of crystallisation and concentration were investigated.

An investigation into the space group of SAS was conducted after conflicting results were found in the literature. This was an important step to ensure that accurate crystal structure data was reported in the study and that any disorder observed was not down to refinement in an incorrect space group with missed symmetry. From this study, the centrosymmetric space group C2/c was confirmed and assigned to SAS. SA-OX is a novel solid form discovered in this work (see chapter 5) and found to crystallise in centrosymmetric space group $P2_1/n$. Both SAS and SA-OX were found to have multiple site occupancies with a major and minor phase around the chiral centre of SA; the disorder found in this region was the main focus of this study.

The nature of disorder was investigated with variable temperature single crystal X-ray diffraction experiments. The disorder observed in the crystal structure of SAS was found to be static in nature. A minor phase with an atomic occupancy of 0.084(4) was seen at both 150 K and 298 K, suggesting that the observed disorder is independent of temperature and is not driven by dynamics. A similar result was seen for SA-OX; a minor phase with a site occupancy of 0.140(5) was seen at 150 K and a site occupancy of 0.134(8) at 298 K. The occupancy values are within error of one another suggesting that the disorder is independent of temperature and thus static in nature. Variable temperature SS-NMR spectroscopy experiments (conducted at Warwick University) that investigated the nature of disorder in the bulk powder of SA-OX indicated that the major and minor populations were slightly dependent on temperature, showing some discrepancy between the temperature dependence from the data collected by X-ray crystallography. It was reasoned that this slight temperature dependence of disorder may have been masked in the X-ray data by the removal of unusual features with restraints to meet CIF requirements.

The portfolio of X-ray data collected for SAS and SA-OX may have shown individual single crystal-to-single crystal variations. However, the cause and effect of such variations remains unknown. The findings of this study hinted at the possibility of a trend. In some samples a potential consistency is potentially seen between samples of SA-OX, particularly between SAOX-1 to SAOX-4. Between these samples the lowest average minor occupancy calculated from three single crystals in a sample was 13.8% and the highest was 15.5%. On the other hand, this result is not reproduced across another model system, SAS, in which case a much larger range of average minor occupancy values were observed. The lowest average minor occupancy calculated from 3-4 single crystals in a sample was 6.2% and the highest was 19.6%. Clearly

this is a complex problem; the systematic approach of analysing up to four single crystals used in this work is able to highlight a possible trend but is unable to confirm this or resolve its cause. Such trends can be further developed with the use of a synchrotron source to gain a more representative data set; advanced synchrotron methods are able to analyse up to 100 crystals simultaneously in a short amount of time.

The influence of crystallisation conditions on APIs with multiple site occupancies has been investigated for other disordered structures in the literature. A similar finding was seen in enilu-racil;[93] in this case no significant differences were seen between the site occupancies for samples crystallised under evaporative methods with different procedures. In contrast, 5-chlorouracil[197] presents a case where the site occupancies were found to depend on the procedure used under evaporative crystallisation. It is still unknown why the disorder in some molecules is sensitive to the crystallisation procedures used but not others. Further investigations are required to fill this gap in scientific knowledge.

The work conducted in this chapter did successfully confirm that disorder in each single crystal is not identical and can hold a large range of major and minor site occupancies. Individual single crystal-to-single crystal variations in the determined disorder were seen for both SAS and SA-OX. In SAS, larger variations of disorder were found in some samples and smaller variations in others. The highest occupancy range observed in a sample was 15.5-9.3% and the lowest was 16.6-16.3%. In SA-OX, the highest ranges observed in a sample was 22.1-9.6% and the lowest range observed was 16.5-14.8%. This finding highlights the importance of analysing the extent of variation in disorder between crystals within and between batches. Knowing the cause and effect of variations in disorder is a powerful tool that could be used to gain a higher level of control over the solid form and for the potential of tuning the physical properties of pharmaceuticals (if disorder is found to have an effect on them).

X-ray crystallography experiments were combined with SS-NMR spectroscopy experiments to quantify the major and minor phases in the bulk powder of SA-OX in-addition to single crystals. The relative amount of disorder found in the bulk material was found to be in good agreement with the average minor phase occupancies calculated by the X-ray crystallography experiments. Similar minor phase values of 9-12% (+/- 3) were found by SS-NMR spectroscopy in the bulk powder of each sample investigated, which are close to the average minor phase occupancies found in single crystals by SCXRD (13-15%).

A molar ellipticity of zero was found by CD spectroscopy in a single crystal of SA-OX, the bulk material of SA-OX and the bulk material of SA. This study confirmed that the single crystals of SA-OX analysed by SCXRD are racemic mixtures and that the disorder observed in the crystals is not due to the co-crystallisation of two different enantiomers. The result is in good agreement with variable temperature SS-NMR spectroscopy experiments that showed the minor phase populations in SA-OX were slightly temperature dependent, eliminating the possibility of ee causing disorder in SA-OX.

Overall, the results presented in this chapter increase our understanding of the presence of disorder in solid-state materials and can aid the characterisation and prediction of these dis-

ordered materials and their properties in the future development of pharmaceuticals. This investigation highlights the importance of pairing X-ray crystallography with a bulk analysis technique, such as SS-NMR spectroscopy. The combination of both methods can help to provide a more detailed picture of how the solid-state structure is organised at the molecular level and at larger (bulk powder) scale.

Chapter 7

A potential method for quantifying the degree of short-range ordering in crystals: diffuse scattering study of Phloroglucinol Dihydrate.

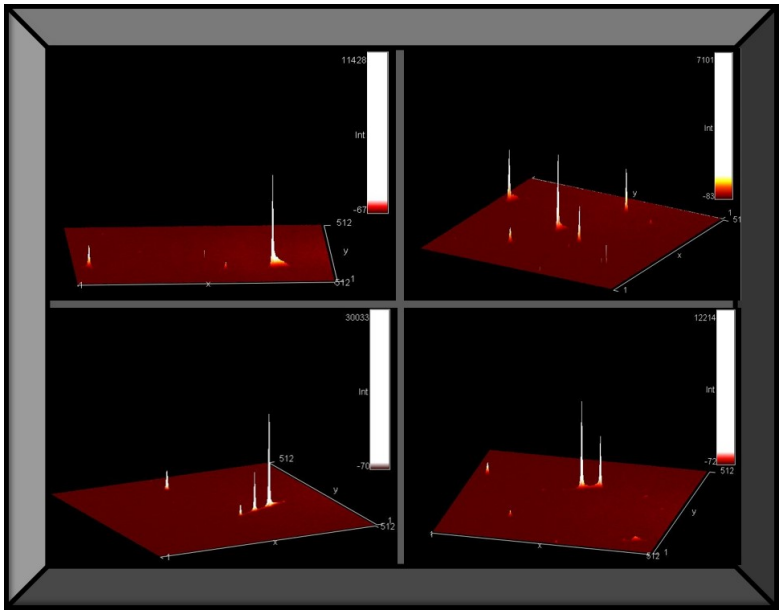

The work presented in this chapter is an extension of the following Masters student project, supervised by the author:

C. J. G. Wilson, Controlling Crystallographic Disorder and Polymorphism within Batch and Continuous Crystallisation of Active Pharmaceutical Ingredients, University of Bath, Department of Chemistry, MSci Research Dissertation, 2020.

The work conducted by the student focused on the optimisation of crystallisation parameters to gain well diffracting single crystals under different methods.

7.1 Introduction

Crystal structure determination by X-ray crystallography identifies the average atomic positions and thermal parameters of atoms in the molecules in a solid form. There are two distinct scattering types that can be considered, Bragg and diffuse. The scattering intensities of Bragg reflections can give information on disordered crystalline materials and can indicate the nature of the average disorder in a material (e.g. static or dynamic disorder) from site occupancy refinements or the size and shape of thermal ellipsoids. Diffuse scattering, on the other hand, results from imperfections in a crystal structure caused by some degree of short-range ordering, typically over regions longer than that of a unit cell (a few unit cells).[198] It tends to be weaker, more difficult to measure and to interpret, particularly in molecular systems.

The phenomenon of diffuse scattering has been known since the earliest years of X-ray diffraction. Yet, the development of a well-established methodology that can be used to interpret and analyse diffuse scattering (from non-synchrotron sources) significantly lags behind the development of crystal structure determination.[199] As noted above, diffuse scattering intensities are generally weaker than Bragg reflections, which makes interpretation and analysis more demanding and time consuming. This challenge includes the basic element tackled here, of quantifying the extent of diffuse scattering in crystals from the diffraction data obtained. Studies into controlling and predicting the extent and the variation of disorder between individual single crystals of organic materials are rare and the subject has been poorly explored. In terms of attempting to model the measured diffuse scattering, computer simulations can be used to gain a more in-depth understanding of the disorder in crystal structures.[200,201] However, these methods often require significant expertise and are not transferable between target systems;[165] in particular, they are very infrequently applied to molecular systems to date. A more accessible, transferable, set of methods would allow for the routine analysis of structures that show signs of diffuse scattering.

7.1.1 Project aim

Aim: To study the extent of diffuse scattering observed in crystals of phloroglucinol dihydrate (PhG dihydrate) via a newly-developed counting spots method and to study single crystal-to-single crystal variations in samples.

The research in this chapter looks to establish a method of quantifying the extent of diffuse scattering in a material by a simple observational method that does not require modelling or the use of computer simulations. The quantification of diffuse scattering in a material is an important first step for the potential later development of a more advanced methodology that can help to control and predict the extent of disorder; such a methodology would be a tool that could be used to tune the physical properties of pharmaceuticals in the future. A visual representation of diffuse scattering can usually be seen in the raw frames of the crystallographic data collected. A novel "counting spots" method is tested in this work that counts all of the visual signs of diffuse scattering (Bragg reflections with 'tails' and 'streaks'). The presence of streaked Bragg reflections is regarded as evidence of stacking disorder and can therefore be used to quantify the extent of disorder in a crystal.

A portfolio of crystallographic data was collected for an API known to show signs of stacking disorder, PhG dihydrate. Multiple samples were studied to investigate the degree of disorder seen in a batch as a function of crystallisation method. Understanding the influence of crystallisation conditions on disorder is an additional factor to consider in attempting to gain control of disordered materials in the future.

7.1.2 Model API system investigated

The dihydrate of phloroglucinol (figure 7-2a) is the target system investigated in this chapter. Phloroglucinols have a broad spectrum of therapeutic effects and can be used for their antiviral, antibacterial and antifungal activities.[202] The crystal structure of PhG dihydrate was first reported in 1957[203] (CSD code = PHGLOH) and is known to show strong streaks of diffuse scattering in its diffraction pattern.[165,203,204] A layered packing arrangement (figure 7-1b) is seen in the crystal structure formed by corrugated layers of chains (figure 7-1a).

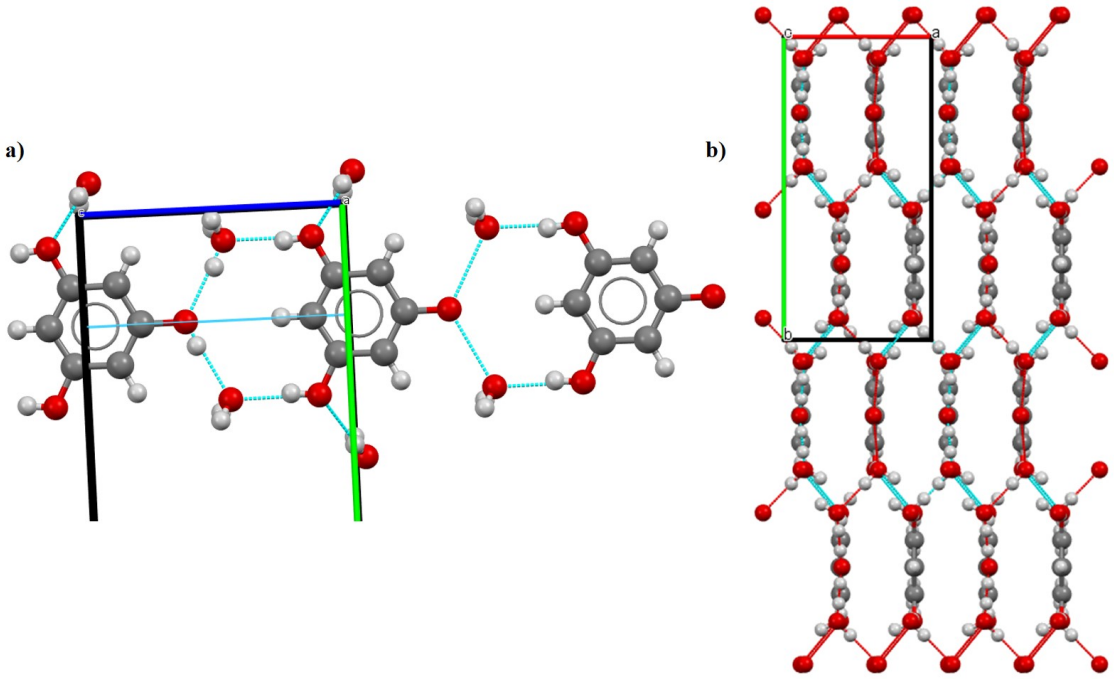

Figure 7-1: The hydrogen bonded chains in PhG-dihydrate form the CSD entry PHGLOH02. (a) viewed along the c axis and (b) corrugated layers of hydrogen bonded chains.

The crystal structure of PhG dihydrate is disordered by symmetry; a mirror plane found in the centre of a phlorglucinol molecule dictates disorder in a hydroxyl (OH) group (figure 7-2b). The hydrogen atom in this hydroxyl group is disordered over two positions, restricted by symmetry to have 0.5 occupancy. At a local level, one of these hydrogen atoms must occupy one of these two positions. A hydrogen atom in the water molecule is also disordered in similar fashion over two positions. Locally, this disorder will be correlated with the OH disorder; the water molecules in PhG dihydrate are linked through hydrogen bond chains which leads to a domino effect of disorder in the structure, as seen in figure 7-2c.

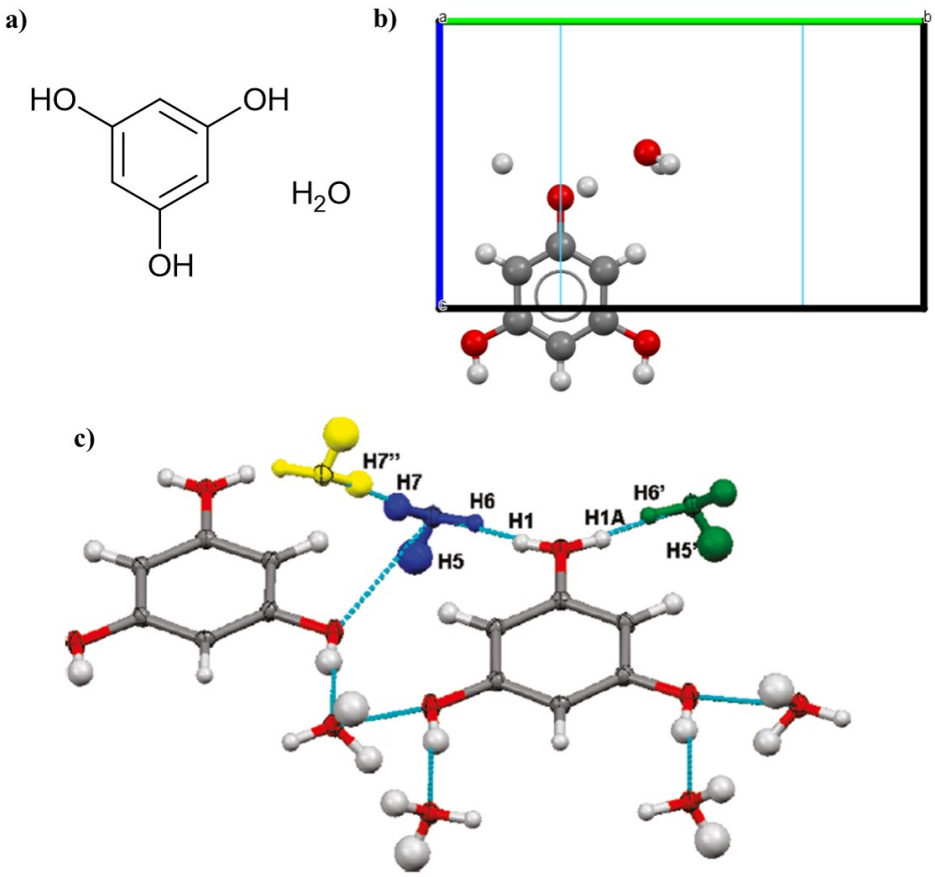

Figure 7-2: PhG-dihydrate, showing (a) the structure, (b) a mirror plane in the centre of the molecule (from the CSD entry PHGLOH02) and (c) a domino effect on hydrogen bonded chains caused by disorder in the structure, showing symmetry equivalent water molecules. Image c is taken from a publication by Thomas et al.[165]

Strong diffuse scattering streaks are observed in the diffraction pattern of PhG dihydrate, suggesting that local structure is generated, *via* hydrogen bonding that is cooperative over distances longer than that of the unit cell.[165] The work in this study does not aim to investigate the cause of disorder and diffuse scattering in PhG dihydrate. It focuses instead on quantifying by observational methods the degree of diffuse scattering (and therefore short-range ordering) in single crystals and looks at single crystal-to-single crystal variations in disorder.

7.2 Preparation of material and crystallographic data collection

PhG dihydrate was obtained from Tokyo Chemical Industry and solvents ethyl acetate (EtOAc) and hexane (hx), were obtained from VWR.

7.2.1 Solubility measurements

Solubility measurements of PhG dihydrate in EtOAc were made using gravimetric methods using the methodology described in section 3.2.1.1. The measured solubility curves (figure 9-36 in the Appendix) were used as a guide when planning crystallisation experiments.

7.2.2 Sample preparation to gather a portfolio of crystallographic data

The impact of crystallisation method on the degree of diffuse scattering seen in crystals of PhG dihydrate was investigated. Three different crystallisation methods were explored to gain an insight into the single crystal-to-single crystal variations in disorder. Material was prepared under evaporative, cooling and vapour diffusion crystallisation methods.

7.2.2.1 Evaporative crystallisation

A solution that contained 0.05 g of PhG dihydrate in 2 mL of EtOAc was placed into a 7 mL glass vial and held at room temperature until the solvent had evaporated to dryness. Ten holes were pierced into the vial lid to ensure slow evaporation of solvent.

7.2.2.2 Cooling crystallisation

A solution that contained 3.75 g of PhG dihydrate in 25 mL of EtOAc was placed into a 50 mL round bottom flask. The concentration of solution was saturated at 40^{o}C and was based on the measured solubility curve of PhG dihydrate. The solution was heated to 10^{o}C above the temperature of saturation and held for 10 minutes while being stirred at 700 rpm. The stirring was turned off and the solution was cooled at 1^{o}C/ min to a temperature of 4^{o}C and then held for 12 hours to promote crystal growth.

7.2.2.3 Vapour diffusion

A saturated solution that contained 0.07 g of PhG dihydrate in 1 mL of EtOAc was placed into a 1.5 mL glass vial and left unsealed. The 1.5 mL vial was then placed into a sealed 10 mL glass vial that contained 3 mL of anti-solvent (hx) and held at room temperature until crystallisation occurred.

7.2.3 Single crystal X-ray diffraction experiments

At least three single crystals (labelled trial #1, #2, #3, etc.) were analysed from a batch of PhG dihydrate crystallised under each of evaporative, cooling and vapour diffusion methods. Crystallographic disorder was determined for each crystal analysed and the degree of diffuse scattering seen in a single crystal was determined using the counting spots method discussed below. A Rigaku Oxford Diffraction SuperNova diffractometer was used for data collection from all crystals in this chapter, with a Cu-Kα (λ = 1.54045 Å) X-ray source at 150 K. All crystal structures were solved by direct methods using SHELXS-2013[143] and refined using SHELXL-2015[144] with the software package Olex2.[145] Isotropic displacement parameters were used for the refinement of atoms with multiple site occupancies. Following this, refinement under anisotropic displacement parameters (ADPs) were conducted with sites with multiple occupancies fixed to 0.5. All hydrogen atoms were refined freely where possible, if the position of a hydrogen atom was unclear, constraints were used to fixed hydrogen atoms in an idealised position based on a riding model.

The crystallographic data collected for samples of PhG dihydrate are shown in tables 7.1, 7.2 and 7.3. Each table presents the crystal data and structure refinement of at least three single crystals isolated from a sample batch. Each single crystal analysed was chosen at random and from different areas of the bulk material. The hydrogen atoms referred to in these tables are labelled in figure 7-2c.

Table 7.1: The crystallographic data collected for PhG-dihydrate crystallised under evaporative methods.

evaporative crystallisation	**#1**	**#2**	**#3**
formula	$C_3H_5O_{2.5}$	$C_3H_5O_{2.5}$	$C_3H_5O_{2.5}$
g mol^{-1}	81.07	81.07	81.07
T (K)	150.00(10)	150.00 (10)	150.01(10)
radiation	Cu Kα($\lambda = 1.54184$)	Cu Kα($\lambda = 1.54184$)	Cu Kα($\lambda = 1.54184$)
2θ range (^{o})	12.802 to 145.98	12.81 to 146.178	12.802 to 144.9
crystal system	orthorhombic	orthorhombic	orthorhombic
space group	Pnma	Pnma	Pnma
a (Å)	6.6135(2)	6.6076(4)	6.6195(3)
b (Å)	13.5317(4)	13.5273(8)	13.5317(7)
c (Å)	8.0439(2)	8.0392(5)	8.0442(3)
$\alpha(^o)$	90	90	90
$\beta(^o)$	90	90	90
$\gamma(^o)$	90	90	90
volume (Å^3)	719.86(4)	718.57(8)	720.54(6)
Z	8	8	8
density (g cm^3)	1.505	1.499	1.504
$\mu(mm^{-1})$	1.148	1.150	1.147
completeness (%)	100.0	99.9	100.0
reflections collected	4727	4984	5670
independent reflections	745	742	745
R int	0.0237	0.0460	0.0346
GooF	1.129	1.086	1.061
R_1 (obs)	0.0338	0.0467	0.0420
R_1 (all)	0.0352	0.0526	0.0459
wR_2 (all)	0.0991	0.1335	0.1257
$\rho_{max,min}$ (e Å^{-3})	0.25/-0.35	0.40/-0.27	0.38/-0.23
atomic occupancy of H 1, 1A, 5 and 6	0.5 : 0.5	0.5 : 0.5	0.5 : 0.5

Table 7.2: The crystallographic data collected for PhG-dihydrate crystallised under cooling methods.

cooling crystallisation	**#1**	**#2**	**#3**	**#4**
formula	$C_3H_5O_{2.5}$	$C_3H_5O_{2.5}$	$C_3H_5O_{2.5}$	$C_3H_5O_{2.5}$
g mol^{-1}	81.07	81.07	81.07	81.07
T (K)	150.00(10)	150.00 (10)	149.91(13)	150.00 (10)
radiation	Cu Kα($\lambda = 1.54184$)	Cu Kα($\lambda = 1.54184$)	Cu Kα($\lambda = 1.54184$)	Cu Kα($\lambda = 1.54184$)
2θ range (^{o})	12.81 to 146.086	12.798 to 146.9	12.804 to 145.784	12.804 to 145.99
crystal system	orthorhombic	orthorhombic	orthorhombic	orthorhombic
space group	Pnma	Pnma	Pnma	Pnma
a (Å)	6.6112(7)	6.6132(3)	6.6087(3)	6.6127(3)
b (Å)	13.5315(15)	13.5280(5)	13.5287(6)	13.5334(6)
c (Å)	8.0377(7)	8.0491(3)	8.0438(3)	8.0420(4)
$\alpha(^o)$	90	90	90	90
$\beta(^o)$	90	90	90	90
$\gamma(^o)$	90	90	90	90
volume (Å^3)	719.05(13)	720.10(5)	719.17(5)	719.70(6)
Z	8	8	8	8
density (g cm^3)	1.498	1.505	1.507	1.506
$\mu(mm^{-1})$	1.149	1.148	1.149	1.149
completeness (%)	99.9	98.8	99.3	99.9
reflections collected	1718	1767	1648	1791
independent reflections	747	745	742	747
R int	0.0412	0.0248	0.0152	0.0174
GooF	1.055	1.100	1.100	1.160
R_1 (obs)	0.0547	0.0420	0.0350	0.0360
R_1 (all)	0.0685	0.0433	0.0374	0.0389
wR_2 (all)	0.1633	0.1195	0.1053	0.0987
$\rho_{max,min}$ (e Å^{-3})	0.48/-0.32	0.28/-0.25	0.26/-0.26	0.15/-0.32
atomic occupancy of H 1, 1A, 5 and 6	0.5 : 0.5	0.5 : 0.5	0.5 : 0.5	0.5 : 0.5

Table 7.3: The crystallographic data collected for PhG-dihydrate crystallised under vapour diffusion methods.

vapour diffusion crystallisation	**#1**	**#2**	**#3**	**#4**
formula	$C_3H_5O_{2.5}$	$C_3H_5O_{2.5}$	$C_3H_5O_{2.5}$	$C_3H_5O_{2.5}$
g mol^{-1}	81.07	81.07	81.07	81.07
T (K)	150.00(10)	150.00 (10)	149.91(13)	150.00 (10)
radiation	Cu Kα($\lambda = 1.54184$)	Cu Kα($\lambda = 1.54184$)	Cu Kα($\lambda = 1.54184$)	Cu Kα($\lambda = 1.54184$)
2θ range (^{o})	12.802 to 146.098	12.804 to 145.704	12.806 to 146.106	12.804 to 146.07
crystal system	orthorhombic	orthorhombic	orthorhombic	orthorhombic
space group	Pnma	Pnma	Pnma	Pnma
a (Å)	6.6124(3)	6.61590(10)	6.6134(2)	6.6135(2)
b (Å)	13.5300(6)	13.5280(3)	13.5233(4)	13.5250(3)
c (Å)	8.0452(3)	8.0433(2)	8.0434(3)	8.0443(2)
$\alpha(^o)$	90	90	90	90
$\beta(^o)$	90	90	90	90
$\gamma(^o)$	90	90	90	90
volume (Å^3)	719.77(5)	719.87(3)	719.36(4)	719.54(3)
Z	8	8	8	8
density (g cm^3)	1.506	1.505	1.506	1.497
$\mu(mm^{-1})$	1.148	1.148	1.149	1.148
completeness (%)	100	99.9	99.6	99.9
reflections collected	4899	4743	1821	4890
independent reflections	749	744	745	747
R int	0.0407	0.0237	0.0183	0.0234
GooF	1.159	1.154	1.100	1.130
R_1 (obs)	0.0359	0.0383	0.0449	0.0383
R_1 (all)	0.0396	0.0388	0.0476	0.0393
wR_2 (all)	0.1009	0.1036	0.1357	0.1049
$\rho_{max,min}$ (e Å^{-3})	0.17/-0.28	0.26/-0.36	0.32/-0.33	0.20/-0.44
atomic occupancy of H 1, 1A, 5 and 6	0.5 : 0.5	0.5 : 0.5	0.5 : 0.5	0.5 : 0.5

7.2.4 The counting spots method

Each crystallographic data frame collected was visualised manually and signs of diffuse scattering counted. Due to the complexity of the data, parameters were defined empirically by the author to regulate which visual signs should be included or excluded as evidence of diffuse scattering in each of the experimental data sets analysed. This chapter looks to summarise the initial development of the counting spots method for the quantification of diffuse scattering in a material and make an initial assessment of its potential. The scope of this project is to establish an important first step that can provide proof of concept for the later development of a more advanced methodology that can be taken further by image recognition experts and data analysts to automate the method and increase the accuracy and reliability.

Two parameters were defined that are known indicators of diffuse scattering: 1) the observation of a Bragg reflection with a tail, henceforth referred to as X; and 2) the observation of streaks between multiple Bragg reflections, henceforth referred to as Y. Examples of parameters X and Y are displayed in figure 7-3. Ambiguous cases were ignored in an attempt to increase the discrimination of the technique; figure 7-3 also displays examples of some ambiguous cases that were ignored in this work.

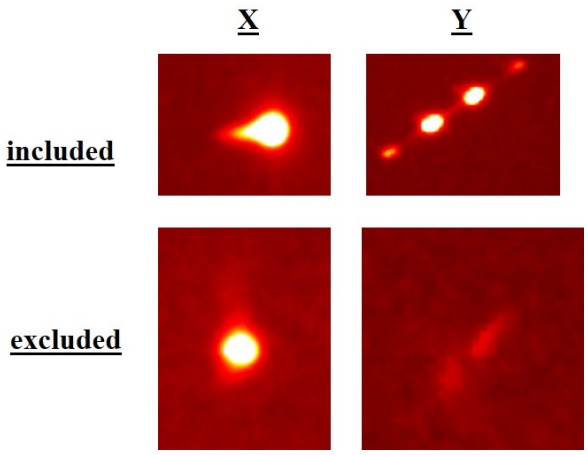

Figure 7-3: Examples of parameters X and Y, including (top) cases that were included in the counting spots method and (bottom) ambiguous cases that were excluded.

The number of occurrences of both X and Y per frame was recorded across all data collection frames. The overall sum of all incidences in each frame was calculated to give a number of occurrences of X and Y for each crystal investigated (summed as X+Y). This process was undertaken twice for each crystal and the average number of counts reported; the number of incidences counted for each frame was usually the same.

7.3 Establishing the counting spots method with PhG-dihydrate.

SCXRD is a precise, comprehensive analytical tool that is able routinely to detect the intensity of many thousands of Bragg reflections spread over large volumes of reciprocal space.[205] In contrast, few quantitative studies on diffuse scattering have been published in the literature. The presence of disorder in crystalline materials (including diffuse scattering) is not a rare occurrence. However, a considerable amount of early work (and indeed current work) by practicing crystallographers has neglected the study of disorder in molecular crystal structures by diffuse scattering methods, even when its presence is recognised, in many cases simply because its classification and interpretation is so difficult and under-established. This study aims to investigate a potential simple empirical method of quantifying the degree of diffuse scattering seen in single crystals of PhG dihydrate and hence determine (single crystal-to-single crystal) variations in associated disorder on a molecular scale.

The counting spots method, discussed in section 7.2.4, was used as a tool to quantify the degree of diffuse scattering seen in at least three single crystals isolated from samples that were crystallised under each of three different methods namely evaporative, cooling and vapour diffusion. Table 7.4 shows a summary of the results including the number of X, Y and the summed X+Y incidences counted in the crystallographic data frames of each single crystal analysed. The calculated average of X, Y and X+Y in 3-4 single crystals and the observed range of diffuse scattering seen is reported in the table.

Table 7.4: The number of incidences of parameters X, Y and X+Y found with the counting spots method.

crystallisation method	**trial**	**incidences recorded**			**average**			**range**[a]	
		X	**Y**	**X+Y**	**X**	**Y**	**X+Y**	**+ve**	**-ve**
evaporative	#1	53	40	93	72.7	48.7	121.3	51.7	28.3
	#2	63	35	98					
	#3	102	71	173					
cooling	#1	27	17	44	39.3	5.0	44.2	8.7	11.2
	#2	53	0	53					
	#3	32	1	33					
	#4	45	2	47					
vapour diffusion	#1	7	0	7	38.0	5.3	43.0	42.0	36.0
	#2	26	0	26					
	#3	64	21	85					
	#4	54	0	54					

[a]observed range of diffuse scattering seen in the summed parameter X + Y

The analysis of 3-4 single crystals may not fully represent the bulk material, but it can provide a valuable insight into the variation of disorder-related diffuse scattering between single crystals in a batch.

7.3.1 The influence of crystallisation method

More incidences of diffuse scattering defined by parameter X were generally seen compared to parameter Y in all of the single crystals analysed; this can clearly be expressed using the X : Y ratio. Crystals prepared under evaporative methods were found to afford single crystals with a relatively consistent X : Y ratio of 1.5 (+/- 0.3) : 1 (table 7.5). This consistency was not seen for crystals prepared under cooling and vapour diffusion methods, for which substantially varying ratios were found, albeit tending to have a higher value for the X : Y ratio (and a smaller number of diffuse scattering features overall, see below).

Table 7.5: The empirical ratio between parameters X and Y.

crystallisation method	**trial**	**incidences**		**X : Y**
		X	**Y**	**ratio**
evaporative	#1	53	40	1.3 : 1
	#2	63	35	1.8 : 1
	#3	102	71	1.4 : 1
cooling	#1	27	17	1.6 : 1
	#2	53	0	53 : 0
	#3	32	1	32 : 1
	#4	45	2	22.5 : 1
vapour diffusion	#1	7	0	7 : 0
	#2	26	0	26 : 0
	#3	64	21	3 : 1
	#4	54	0	54 : 0

Figure 7-4 shows a visual summary of the results obtained in this study. In this figure, the average number of incidences found for parameter X+Y from 3-4 single crystals in a batch is shown with grey boxes and the observed range of incidences for parameter X + Y is represented by black bars. On average, a larger number of diffuse scattering incidences was found in the data frames collected for crystals prepared under evaporative crystallisation. This value of 121 X+Y incidences can be compared to crystals prepared under cooling crystallisation and vapour diffusion methods which afforded similar incidences of diffuse scattering, averaging 44 and 43 X+Y incidences respectively.

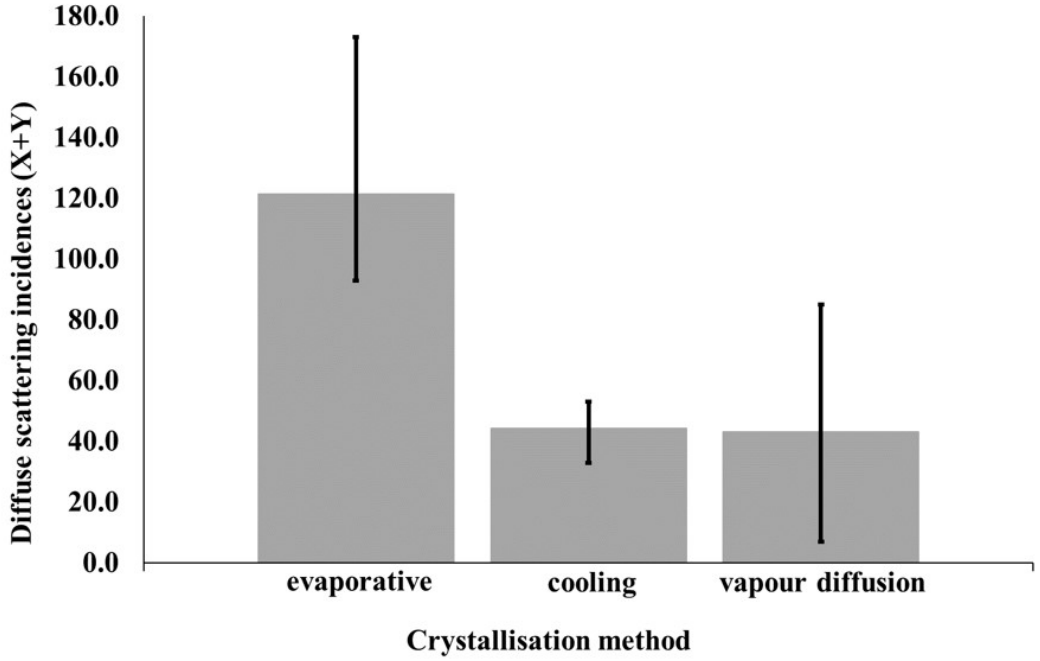

Figure 7-4: The number of incidences parameter X+Y were found to occur with the counting spots method in PhG-dihydrate as a function of crystallisation method.

As noted above, larger variations in the observed range of instances were found under evaporative and vapour diffusion methods. A distribution range of 173-93 summed incidences (+51 /- 28 from the average value) was found under evaporative methods and a range of 85-7 incidences (+42 /- 36 from the average value) under vapour diffusion methods. Cooling crystallisation afforded crystals that showed a significantly smaller distribution range of 53-33 incidences (+8 /- 11 from the average value). The data collected could suggest that under a crystallisation environment with a higher level of control, such as cooling crystallisation, the bulk powder contains crystals with similar degrees of disorder compared to those resulting from a crystallisation environment with lower levels of control, such as evaporative crystallisation or vapour diffusion. In this case, a Polar Bear Plus cooling crystallisation platform with temperature control and monitoring was used for all cooling crystallisations whereas evaporative and vapour diffusion crystallisations were left in an uncontrolled environment to crystallise (on a bench top at room temperature). These results are very preliminary; further studies are required to investigate if a high vs low controllable crystallisation environment is able to influence (and therefore control) the extent of disorder in crystalline materials.

7.3.2 Single crystal-to-single crystal variations

Single crystal-to-single crystal variations in the degree of diffuse scattering indicated by the simple empirical counting spots method were found between the single crystals analysed. The lowest degree of diffuse scattering seen in a single crystal was prepared under vapour diffusion methods (trial #1) with a summed number of 7 incidences (X+Y). In-contrast, the highest degree of diffuse scattering seen in a single crystal was from a sample prepared under evaporative methods (trial #3) with an X+Y sum of 173 incidences.

7.4 Conclusion

The work presented in this chapter investigated a simple empirical method of quantifying the extent of diffuse scattering in a material that does not require a sophisticated computational approach. The method devised counts the visual signs of diffuse scattering in crystallographic data frames collected by SCXRD. The streaked Bragg reflections targeted in this work are regarded as evidence of stacking disorder in a material and can therefore be used to quantify the extent of disorder in a single crystal. The variation in the extent of diffuse scattering seen between individual single crystals was investigated using a similar systematic approach as used in chapter 6. Multiple samples were studied to investigate the extent of disorder seen in crystals as a function of crystallisation method.

The counting spots method successfully identified and established a way of quantifying the amount of diffuse scattering incidences found in single crystals of PhG dihydrate. A portfolio of X-ray data was collected by SCXRD and was used to quantify empirically the degree of diffuse scattering in single crystals prepared under evaporative, cooling and vapour diffusion methods. The occurrences of defined parameters X (tails), Y (streaks) and the sum of these (X+Y) were manually counted in the crystallographic data frames collected for each single crystal analysed.

Single crystal-to-single crystal variations were seen between crystals prepared under different crystallisation methods. Crystals prepared under cooling crystallisation showed 44 incidences of parameter X+Y with a range of 53-33 incidences seen between single crystals in a batch. Vapour diffusion methods showed a similar value of 43 incidences and a larger range of 85-7 between single crystals. Evaporative methods were found to form crystals with a larger degree of diffuse scattering than crystals prepared under other crystallisation methods investigated. In this case a significantly higher number of incidences was counted (121) and a large range of 173-93 incidences were seen between single crystals. Although a larger diffuse scattering range was found between crystals prepared under evaporative methods, in that case the empirical ratio X : Y between the two types of diffuse feature was found to be relatively consistent between crystals. The empirical ratio X : Y for crystals prepared under cooling and vapour diffusion methods appeared to be random, despite having a smaller X+Y range.

Different variations in the amount of diffuse scattering incidences counted between single crystals of PhG dihydrate were seen. The lowest empirical total diffuse scattering features counted in a single crystal was 7 incidences (of summed parameter X+Y), whilst the highest degree was 173 incidences.

Overall, the crystallisation environment seems to have an influence on the extent of diffuse scattering found in a single crystal of PhG dihydrate. The cause and effect of this influence remains unknown and requires a more detailed investigation. The simple, empirical counting spots method was successful in the preliminary identification and quantification of diffuse scattering in PhG dihydrate; this can be linked to the degree of short-range ordering in a material. This work has begun the establishment of this empirical method and can provide a starting point for potential further development.

Chapter 8

Concluding remarks and future work

The work conducted in this thesis focused on gaining a more in-depth understanding of disorder and defects in pharmaceutical materials and contributed towards the development of new analytical tools for the characterisation and quantification of crystallographic disorder. The work presented looked at methods for gaining a higher level of control over the solid form; this is a factor that can allow the extraction of maximum value from pharmaceuticals by optimising the efficiency of drug development during the manufacturing process.

The work presented in Chapter 4 focused on gaining control over the crystallisation process via a novel method, electrospraying, to obtain elusive solid forms (structural) and to explore the resultant product qualities including particle attributes. Two solid forms were successfully crystallised under electrospraying, metastable PCM-II and a novel PCM-MCM co-crystal. Electrospraying has shown its potential for deployment in applications in pharmaceutical crystallisation and throughout the materials manufacturing industry. The method is able to provide a starting point for the development of difficult to crystallise solid forms including elusive multi-component complexes and polymorphic forms. Electrospraying has been shown to have the potential to gain a higher level of control over the crystallisation process and has the ability to switch between the production of solid forms selectively under different crystallisation parameters. The successful translation of electrosprayed co-crystal seeds into a more established cooling crystallisation platform shows the technique's potential as a seed manufacturing technology; this has been shown to be particularly powerful in this case as only the electrospray-produced seeds are able to be deployed in scaling up of crystallisation of the co-crystal material. The electrospray technique could thus be used in pharmaceutical manufacturing to discover and crystallise small batch elusive crystal seeds that are able to be integrated into a more established larger-scale crystallisation method. The production of novel and elusive solid forms can help to increase the diversity of solid forms in the pharmaceutical pipeline and in-turn increase pharmaceutical product innovation.

Electrospraying has been shown to form particles with a rough topography, a larger surface

area, and visible voids in the particle framework, which will influence their ability to be deployed, for example, as seeds. Figure 8-1 shows electrosprayed particles from this work and compares these particles to those prepared under a different method. The desired particle features obtained from electrospraying are not seen in the same solid form when prepared under different crystallisation methods; in the cases presented smooth particle surfaces are seen under cooling crystallisation and reaction coupling methods. This demonstrates that electrospraying is a technology capable of influencing the particle attributes of a material, a tool that is important in crystal engineering for desirable physical properties and downstream processing properties.

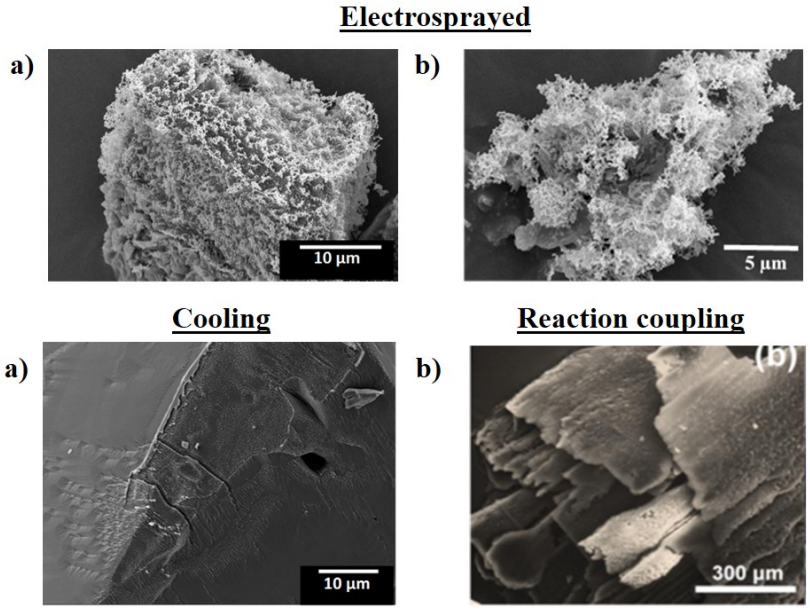

Figure 8-1: The topography of (a) PCM-MCM co-crystal and (b) PCM-II prepared under electrospraying and other crystallisation methods.
*The bottom right hand image was taken from a publication by Lee et al.[166]

The impact of the electrospraying parameters of voltage, flow rate and solvent volatility on the particle attributes of the resultant material would be a beneficial follow-on study. Such an investigation could explore if the framework of voids seen in electrosprayed particles is able to be controlled and engineered to desirable sizes and densities, for example; this could potentially lead to a QbD approach. Significant future work remains in terms of controlling the particle attributes of an electrosprayed material as part of a QbD approach. In order to reach this goal the answers to a number of questions need to be explored through further crystallisation experiments and a combination of microscopy techniques: 1) Are the sizes of individual voids uniform in the frameworks discovered and can crystal engineering be used to ensure uniformity and control void diameter?; 2) Can the density of voids present in the electrosprayed material be controlled, and what effect might this have on the particle properties?; 3) Can the voids be used as a host for a second component, possibly an amorphous material?

The work presented in Chapters 5, 6 and 7 contributes towards a long standing challenge, the ability to distinguish subtle changes of crystalline disorder across a bulk material at the molecular level. The work conducted certainly did not solve this problem but did contribute towards

the development of one aspect of the challenge. A series of molecular complexes of SA were identified in Chapter 5. For each complex in this chapter, different crystallisation methods and conditions were studied and the presence of crystallographic disorder was characterised. A similar type of disorder was found in each multi-component complex studied but significant differences were found between the multiple site occupancy values seen in each complex. The crystallisation of multiple complexes of a target API complex, such as SA, can be further investigated and used as a tool to measure and compare the physical properties of each individual complex and to relate any correlations seen with the structural attributes found in this study.

The results found in the study of disorder variations across multi-component complexes of SA in Chapter 5 are limited and assumed the crystallographic disorder in every single crystal in a batch is identical; this is the commonly made assumption in crystallographic disorder refinements and is a simplified view. A methodology was developed to overcome this limitation in Chapter 6. In this chapter a portfolio of information on single crystal-to-single crystal variations across a bulk material was gathered to understand the nature of disorder at the molecular level and correlate the results with a bulk analysis method, SS-NMR spectroscopy. The characterisation of multiple single crystals in a batch confirmed that disorder is inconsistent in individual crystals of SAS and SA-OX, large variations were found in site occupancies of both molecular complexes. This is a significant finding that highlights the importance of developing a tool that is able to probe disorder in the bulk as SCXRD is not necessarily a fully representative method to understand such variations. The combination of X-ray crystallography and SS-NMR spectroscopy to quantify the major and minor phases in the bulk was found to give generally good agreement. Similar average minor phase values were found in the bulk material for each of the three samples studied. A significant contrast was seen between the nature of disorder in SA-OX when investigated under variable temperature X-ray diffraction and variable temperature SS-NMR spectroscopy, with the latter showing some temperature dependence of the disorder; the conclusions on this in the X-ray diffraction refinements were found to be affected by the nature of the constraints applied in the refinement process. The contrasting result suggests that crystallographers should act with caution when using restraints in data refinement to meet CIF requirements as these may inadvertently mask potentially significant features in a crystal structure; in this case the affected feature (temperature dependence of disorder) might have the potential to be correlated with a bulk property of a material and utilised to fine tune the physical properties of a solid form.

The effect of crystallisation temperature, rate of crystallisation and concentration of solution on the degree of disorder was studied in Chapter 6. A large range of major and minor site occupancies were found for both of the target systems investigated, SAS and SA-OX. Individual single crystal-to-single crystal variations were seen and some conditions seemed to yield the crystallisation of batches with a higher level of consistency between the disorder across individual single crystals. However, the cause and effect of such variations and the level of consistency of variations between batches is still unknown. A method of characterising multiple site occupancies in a disordered material without the use of SCXRD is not yet available; even when site occupancy information can be obtained (not always possible and still difficult for molecular systems by PXRD, for example), bulk techniques will yield parameters averaged

over many crystals. The future establishment of such a method is of importance for characterising scaled-up crystalline powders and to help the correlation and exploitation of structural attributes for tuning physical properties in the future of drug development.

The broad diversity of different types of disorder in materials contributes to the difficulty of gaining control over disorder with a single strategy built for different types of disordered materials. Chapter 7 looked to address this challenge and used a similar type of systematic approach to that used in chapter 6 for the characterisation of multiple site occupancies, but this time focusing on quantification of the degree of disorder present, estimated direct from the diffuse scattering features present in the diffraction pattern. Both chapters focus on comparing and contrasting repeats instead of characterising one single crystal and aimed to quantify the variations of disorder seen in the bulk. Chapter 7 devised an empirical method of quantifying the extent of diffuse scattering in a material. A novel counting spots method was explored that does not require advanced computational methods. Visual signs of diffuse scattering in crystallographic data frames were counted manually to estimate the range of disorder seen between single crystals of a model system, PhG dihydrate. Variations in the amount of diffuse scattering incidences counted were seen between single crystals, but the cause and effect of this influence remains unknown; this is a similar result in terms of crystal-to-crystal variations as that found in Chapter 6. The work presented in Chapters 6 and 7 highlights the range of differences that can be seen between single crystals of the same structure and promotes the potential of developing methods to characterise and control disorder further. This work has begun the establishment of a simple, empirical counting spots method and has helped to provide a starting point for potential further development. The incorporation of image recognition software could be used to automate the counting spots method and increase its accuracy; the method is currently user dependent with a defined discriminatory cut off point for ambiguity around diffraction spots set by user observation. Utilisation of the counting spots method alongside routine crystal structure determination can provide quantitative information on diffuse scattering in addition to a detailed picture of the average disordered structure.

Looking towards the future development of the methods investigated in this doctoral thesis, a significant amount of high end instrumentation and expertise needs to be devoted to this. Facilities that can host bulk property characterisation such as powder flow with shear tester, compaction and dissolution testing would be advantageous to explore if the variations in disorder seen in crystals have an influence on a material's properties. Furthermore, material characterisation in a synchrotron facility would be advantageous to obtain a significantly larger portfolio of higher-quality structural data in a reasonable time frame, possibly focusing on determinations of structure and disorder in multiple very small single crystals. Data collection on a synchrotron source would help to confirm the conclusion that the analysis of a larger data set (more than three single crystals per sample) might show more consistent values of the average minor phase and distribution range than found in Chapter 6, through rapid synchrotron SCXRD experiments. The use of a synchrotron source could also help to promote a further study that looked into possibly correlated information relating to powder-diffraction line broadening and any strain contributions from disorder.

The ability to manipulate and utilise disorder in crystalline materials could bring innovation in the design and development of new pharmaceutical drug solid forms. A combination of four factors (two of which have been explored in this thesis) would help to develop such an ability: 1) gaining a higher control over the solid form and its structural attributes; 2) investigating single crystal-to-single crystal variations across a bulk material and correlated with a method such as SS-NMR spectroscopy; 3) linking structural attributes with physical properties in the bulk; and 4) data collection via an intense synchrotron source to help to create a (micro) crystal-by-crystal in-depth picture of an API and any crystallographic disorder it may host.

References

[1] H. Tung, E. L. Paul, M. Midler and J. A. McCauley, in *Crystallization of Organic Compounds: An Industrial Perspective.*, Wiley, United States of America, 2009, ch. 1, pp. 2–10.

[2] B. M. Couillaud, P. Espeau, N. Mignet and Y. Corvis, *ChemMedChem*, 2019, **14**, 8–23.

[3] M. J. Bryant, S. N. Black, H. Blade, R. Docherty, A. G. Maloney and S. C. Taylor, *Journal of Pharmaceutical Sciences*, 2019, **108**, 1655–1662.

[4] B. Y. Shekunov, P. Chattopadhyay, H. H. Tong and A. H. Chow, *Pharmaceutical Research*, 2007, **24**, 203.

[5] N. Schultheiss and A. Newman, *Crystal Growth and Design*, 2009, **9**, 2950–2967.

[6] K. T. Savjani, A. K. Gajjar and J. K. Savjani, *ISRN Pharmaceutics*, 2012, 195727.

[7] R. Hilfiker, S. M. De Paul and M. Szelagiewicz, in *Polymorphism: in the Pharmaceutical Industry*, Wiley -VCH, 2006, ch. 11, pp. 287–291.

[8] R. Hilfiker, *Polymorphism*, 2006, pp. 1–414.

[9] W. Beckmann, in *Crystallization: Basic Concepts and Industrial Applications*, Wiley -VCH, 2013, ch. 5, pp. 85–98.

[10] P. H. Stahl, C. G. Wermuth and International Union of Pure and Applied Chemistry., *Handbook of pharmaceutical salts : properties, selection, and use*, 2008, vol. 24, p. 374.

[11] P. H. Stahl and B. Sutter, in *Polymorphism: in the Pharmaceutical Industry*, Wiley -VCH, 2006, ch. 12, pp. 309–325.

[12] A. M. Healy, Z. A. Worku, D. Kumar and A. M. Madi, *Advanced Drug Delivery Reviews*, 2017, **117**, 25–46.

[13] M. Karimi-Jafari, L. Padrela, G. M. Walker and D. M. Croker, *Crystal Growth and Design*, 2018, **18**, 6370–6387.

[14] M. Descamps and J. Willart, in *Disordered Pharmaceutical Materials*, ed. M. Descamps, Wiley -VCH, 1st edn., 2016, ch. 1, pp. 1–51.

[15] W. Jones and M. Eddleston, in *Disordered Pharmaceutical Materials*, ed. M. Descamps, Wiley -VCH, 2016, ch. 3, pp. 85–99.

[16] W. Beckmann, in *Crystallization: Basic Concepts and Industrial Applications*, 2013, ch. 2, pp. 17–32.

[17] R. Davey and J. Garside, in *From Molecules to Crystallizers an Introduction to Crystallizationolecules to crystallizers*, Oxford University Press, 2000, ch. 3, pp. 15–25.

[18] R. Davey and J. Garside, in *From Molecules to Crystallizers an Introduction to Crystallization*, Oxford University Press, 2000, ch. 2, pp. 6–14.

[19] J. W. Mullin, in *Crystallization*, Butterworth-Heinemann, Oxford, UK, 2001, ch. 3, p. 125.

[20] A. S. Myerson and R. Ginde, in *Handbook of Industrial Crystallization*, 2nd edn., 2002, pp. 33–65.

[21] D. Erdemir, A. Y. Lee and A. S. Myerson, *Accounts of Chemical Research*, 2009, **42**, 621–629.

[22] J. Chen, B. Sarma, J. M. Evans and A. S. Myerson, *Crystal Growth and Design*, 2011, **11**, 887–895.

[23] S. Karthika, T. K. Radhakrishnan and P. Kalaichelvi, *Crystal Growth and Design*, 2016, **16**, 6663–6681.

[24] S. G. Agrawal and A. H. J. Paterson, *Chemical Engineering Communications*, 2015, **202**, 698–706.

[25] K. Roberts, R. Docherty and S. Taylor, in *Pharmaceutical Process Development: Current Chemical and Engineering Challenges*, ed. B. A. J and M. Williams, RSC Publishing, Cambridge, 2011, ch. 13, pp. 286–312.

[26] R. Davey and J. Garside, in *From Molecules to Crystallizers an Introduction to Crystallization*, Oxford University Press, 2000, ch. 4, pp. 26–35.

[27] J. W. Mullin, in *Crystallization*, Butterworth-Heinemann, Oxford, UK, 4th edn., 2001, ch. 6, pp. 216–284.

[28] R. Davey and J. Garside, in *From Molecules to Crystallizers an Introduction to Crystallization*, Oxford University Press, United States of America, 2000, ch. 5, pp. 36–43.

[29] H. Tung, E. L. Paul, M. Midler and J. A. McCauley, in *Crystallization of Organic Compounds: An Industrial Perspective.*, Wiley, 2009, ch. 2, pp. 13–44.

[30] G. Nichols, in *Polymorphism in the Pharmaceutical Industry*, Wiley -VCH, 2006, ch. 7, pp. 167–207.

[31] M. Vogt, K. Kunath and J. B. Dressman, *European Journal of Pharmaceutics and Biopharmaceutics*, 2008, **68**, 283–288.

[32] K. R. Vandana, Y. Prasanna Raju, V. Harini Chowdary, M. Sushma and N. Vijay Kumar, *Saudi Pharmaceutical Journal*, 2014, **22**, 283–289.

[33] H. Tung, E. Paul and M. Midler, in *Crystallisation of Organic Compounds*, Wiley, United States of America, 2009, ch. 8, pp. 167–178.

[34] H. Tung, E. Paul and M. Midler, in *Crystallisation of Organic Compounds*, Wiley, United States of America, 2009, ch. 7, pp. 137–166.

[35] G. G. Z. Zhang, R. F. Henry, T. B. Borchardt and X. Lou, *Journal of Pharmaceutical Sciences*, 2007, **96**, 990–995.

[36] D.-R. Chen and D. Y. H. Pui, *Aerosol Science and Technology*, 1997, **27**, 367–380.

[37] J. Wang, J. A. Jansen and F. Yang, *Electrospraying: Possibilities and Challenges of Engineering Carriers for Biomedical Applications—A Mini Review* , 2019, `https://www.frontiersin.org/article/10.3389/fchem.2019.00258`.

[38] S. K. Boda, X. Li and J. Xie, *Journal of Aerosol Science*, 2018, **125**, 164–181.

[39] M. Mirjalili and S. Zohoori, *Journal of Nanostructure in Chemistry*, 2016, **6**, 207–213.

[40] M. Aman Mohammadi, S. M. Hosseini and M. Yousefi, *Food Science & Nutrition*, 2020, **8**, 4656–4665.

[41] D. N. Nguyen, C. Clasen and G. Van den Mooter, *Journal of Pharmaceutical Sciences*, 2016, **105**, 2601–2620.

[42] G. A. Silva, *Surgical Neurology*, 2004, **61**, 216–220.

[43] R. L. Grimm and J. L. Beauchamp, *Journal of Physical Chemistry B*, 2005, **109**, 8244–8250.

[44] A. M. Gañán-Calvo, N. Rebollo-Muñoz and J. M. Montanero, *New Journal of Physics*, 2013, **15**, 033035.

[45] L. Wang and A. Ryan, in *Electrospinning for Tissue Regeneration*, ed. L. Bosworth and S. Downes, Woodhead Publishing, 2011, ch. 1, pp. 3–33.

[46] D. C. Taflin, T. L. Ward and E. J. Davis, *Langmuir*, 1989, **5**, 376–384.

[47] A. J. Al-Ani, C. Herdes, C. C. Wilson and B. Castro-Dominguez, *Crystal Growth and Design*, 2020, **20**, 1451–1457.

[48] C. A. Bonino, K. Efimenko, S. I. Jeong, M. D. Krebs, E. Alsberg and S. A. Khan, *Small*, 2012, **8**, 1928–1936.

[49] L. M. Padrela, B. Castro-Dominguez, A. Ziaee, B. Long, K. M. Ryan, G. Walker and E. J. O'Reilly, *CrystEngComm*, 2019, **21**, 2845–2848.

[50] N. Notman, in *Chemistry world, article 3009223*, 2018.

[51] M. Leonardi, M. Villacampa and J. C. Menéndez, *Chemical Science*, 2018, **9**, 2042–2064.

[52] R. Hilfiker, F. Blatter and M. Raumer, in *Polymorphism: in the Pharmaceutical Industry*, 2006, ch. 1, pp. 1–15.

[53] R. Davey and J. Garside, in *From Molecules to Crystallizers*, Oxford University Press, United States of America, 2000, ch. 6, pp. 44–51.

[54] C. A. Lipinski, F. Lombardo, B. W. Dominy and P. J. Feeney, *Advanced Drug Delivery Reviews*, 2001, **46**, 3–26.

[55] L. R. Agnew, D. L. Cruickshank, T. McGlone and C. C. Wilson, *Chemical Communications*, 2016, **52**, 7368–7371.

[56] S. R. Chemburkar, J. Bauer, K. Deming, H. Spiwek, K. Patel, J. Morris, R. Henry, S. Spanton, W. Dziki, W. Porter, J. Quick, P. Bauer, J. Donaubauer, B. A. Narayanan, M. Soldani, D. Riley and K. McFarland, *Organic Process Research and Development*, 2000, **4**, 413–417.

[57] J. Bauer, S. Spanton, R. Henry, J. Quick, W. Dziki, W. Porter and J. Morris, *Pharmaceutical Research*, 2001, **18**, 859–866.

[58] S. Lohani and J. Grant, in *Polymorphism in the Pharmaceutical Industry*, ed. R. Hilfiker, Wiley-VCH, 2006, ch. 2, pp. 21–40.

[59] H. G. Brittain, in *Polymorphism in Pharmaceutical Solids*, Informa Healthcare, 2nd edn., 2009, ch. 1, pp. 1–23.

[60] S. Kalepu and V. Nekkanti, *Acta Pharmaceutica Sinica B*, 2015, **5**, 442–453.

[61] T. Threlfall, *Organic Process Research and Development*, 2003, **7**, 1017–1027.

[62] H. Lorenz, in *Crystallization: Basic Concepts and Industrial Applications*, Wiley -VCH, 2013, ch. 3, pp. 36–72.

[63] A. Burrows, J. Holman, A. Parsons, G. Pilling and G. Price, in *Chemistry3*, Oxford University Press, 2nd edn., 2009, ch. 7, pp. 302–307.

[64] N. K. Duggirala, M. L. Perry, O. Almarsson and M. J. Zaworotko, *Chemical Communications*, 2016, **52**, 640–655.

[65] N. Qiao, M. Li, W. Schlindwein, N. Malek, A. Davies and G. Trappitt, *International Journal of Pharmaceutics*, 2011, **419**, 1–11.

[66] C. B. Aakeröy, S. Forbes and J. Desper, *Journal of the American Chemical Society*, 2009, **131**, 17048–17049.

[67] P. Yang, C. Qin, S. Du, L. Jia, Y. Qin, J. Gong and S. Wu, *Crystals*, 2019, **9**, 367.

[68] G. R. Desiraju, *Journal of the American Chemical Society*, 2013, **135**, 9952–9967.

[69] G. R. Desiraju, *Journal of Applied Crystallography*, 1991, **24**, 265.

[70] G. R. Desiraju, *Chemical Communications*, 1997, **16**, 1475–1482.

[71] J. R. G. Sander, D.-K. Bučar, R. F. Henry, B. N. Giangiorgi, G. G. Z. Zhang and L. R. MacGillivray, *CrystEngComm*, 2013, **15**, 4816–4822.

[72] C. Aakeröy and N. Schultheiss, in *Making Crystals by Design: Methods, Techniques and Applications*, ed. D. Braga and F. Grepioni, 2006, ch. 2.5, pp. 209–240.

[73] J. Bernstein and R. Davis, in *Implications of Molecular and Materials Structure for New Technologies*, ed. J. Howard, A. Frank and G. Shields, Springer, 1999, pp. 275–276.

[74] C. B. Aakeröy and K. R. Seddon, *Chemical Society Reviews*, 1993, 397–407.

[75] E. Arunan, G. R. Desiraju, R. A. Klein, J. Sadlej, S. Scheiner, I. Alkorta, D. C. Clary, R. H. Crabtree, J. J. Dannenber, P. Hobza, H. G. Kjaergaard, A. C. Legon, B. Mennucci and D. J. Nesbitt, *Pure and Applied Chemistry*, 2011, **83**, 1637–1641.

[76] G. A. Jeffrey, *Introduction to Hydrogen Bonding*, Oxford University Press, New York, 1997.

[77] G. R. Desiraju, *Crystal Growth and Design*, 2011, **11**, 896–898.

[78] R. Thakuria, N. K. Nath and B. K. Saha, *Crystal Growth and Design*, 2019, **19**, 523–528.

[79] V. Sivasakthi, A. Anbarasu and S. Ramaiah, *Cell Biochemistry and Biophysics*, 2013, **67**, 853–863.

[80] R. P. Matthews, T. Welton and P. A. Hunt, *Physical Chemistry Chemical Physics*, 2014, **16**, 3238–3253.

[81] E. Hadjittofis, S. Das, G. Zhang and J. Heng, in *Developing Solid Oral Dosage Forms*, Academic Press, 2nd edn., 2017, ch. 8, pp. 225–252.

[82] G. Cavallo, P. Metrangolo, R. Milani, T. Pilati, A. Priimagi, G. Resnati and G. Terraneo, *Chemical Reviews*, 2016, **116**, 2478–2601.

[83] S. Lawton, G. Steele, P. Shering, L. Zhao, I. Laird and X. W. Ni, *Organic Process Research and Development*, 2009, **13**, 1357–1363.

[84] H. Tung, E. L. Paul and M. Midler, in *Crystallisation of Organic Compounds*, Wiley, 2009, ch. 6, pp. 117–136.

[85] D. Wieckhusen, in *Crystallization: Basic Concepts and Industrial Applications*, Wiley -VCH, 2013, ch. 10, pp. 187–202.

[86] A. Florence, in *Modern Pharmaceutics Volume 1: Basic Principles and Systems*, ed. A. Florence and J. Siepmann, CRC Press, 2010, ch. 8, pp. 253–310.

[87] U. Bock, T. Kottke, C. Gindorf and E. Haltner, *System*, 1999, **129**, 1–7.

[88] W. Beckmann and D. Wieckhusen, in *Crystallization: Basic Concepts and Industrial Applications*, Wiley -VCH, 2013, ch. 14, pp. 275–285.

[89] M. Shamsipur, S. M. Pourmortazavi, A. A. M. Beigi, R. Heydari and M. Khatibi, *AAPS PharmSciTech*, 2013, **14**, 287–293.

[90] A. Arigo, N. Jawahar, K. Nikhitha and S. Jubie, *Journal of Pharmaceutical Sciences and Research*, 2019, **11**, 6–10.

[91] A. Newman and G. Zografi, *Journal of Pharmaceutical Sciences*, 2014, **103**, 2595–2604.

[92] S. R. Byrn, R. R. Pfeiffer, G. Stephenson, D. J. Grant and W. B. Gleason, *Chemistry of Materials*, 1994, **6**, 1148–1158.

[93] R. C. Copley, S. A. Barnett, P. G. Karamertzanis, K. D. Harris, B. M. Kariuki, M. Xu, E. A. Nickels, R. W. Lancaster and S. L. Price, *Crystal Growth and Design*, 2008, **8**, 3474–3481.

[94] J. Moncol, *Disorders: problems or new information in chemical crystallography*, `http://www.xray.cz/xray/csca/kol2014/abst/moncol.htm`.

[95] D. Chopra and T. N. Row, *Crystal Growth and Design*, 2008, **8**, 848–853.

[96] M. Neuburger, *Ph.D. thesis*, University of Basel Switzerland, 2012.

[97] S. R. Elliot, *Crystal Researh and Technology*, 1984, **20**, 1238.

[98] Nondestructive Testing resource centres, *Linear Defects - Dislocations*, `https://www.nde-ed.org/EducationResources/CommunityCollege/Materials/Structure/linear_defects.htm`.

[99] R. L. Smith, M. Vickers, M. Rosillo-Lopez and C. G. Salzmann, *Crystal Growth and Design*, 2019, **19**, 2131–2138.

[100] T. L. Malkin, B. J. Murray, C. G. Salzmann, V. Molinero, S. J. Pickering and T. F. Whale, *Physical Chemistry Chemical Physics*, 2015, **17**, 60–76.

[101] B. J. Murray, C. G. Salzmann, A. J. Heymsfield, S. Dobbie, R. R. Neely and C. J. Cox, *Bulletin of the American Meteorological Society*, 2015, **96**, 1519–1531.

[102] A. D. Bond, R. Boese and G. R. Desiraju, *Angewandte Chemie - International Edition*, 2007, **46**, 618–622.

[103] P. M. Blackett and G. Buckton, *Pharmaceutical Research*, 1995, **12**, 1689–1693.

[104] L. Mackin, R. Zanon, J. M. Park, K. Foster, H. Opalenik and M. Demonte, *International journal of pharmaceutics*, 2002, **231**, 227–236.

[105] S. Sheokand, S. R. Modi and A. K. Bansal, *Journal of Pharmaceutical Sciences*, 2014, **103**, 3364–3376.

[106] P. Begat, P. M. Young, S. Edge, J. Kaerger and R. Price, *Journal of Pharmaceutical Sciences*, 2003, **92**, 611–620.

[107] R. Price and P. M. Young, *Micron*, 2005, **36**, 519–524.

[108] M. Eddleston and W. Jones, in *Disordered Pharmaceutical Materials*, ed. M. Descamps, Wiley-VCH, 2016, ch. 4, pp. 103–134.

[109] V. Mote, Y. Purushotham and B. Dole, *Journal of Theoretical and Applied Physics*, 2012, 6:6.

[110] P. Muhammed Shafi and A. Chandra Bose, *AIP Advances*, 2015, **5**, 57137.

[111] F. G. Riddell and M. Rogerson, *Journal of the Chemical Society, Perkin Transactions 2*, 1996, 493–504.

[112] P. M. J. Szell, S. P. Brown, L. P. Hughes, H. Blade and S. O. Nilsson Lill, *Chemical Communications*, 2020, **56**, 14039–14042.

[113] A. Hedoux, in *Disordered Pharmaceutical Materials*, Wiley-VCH, 2016, ch. 12, pp. 361–392.

[114] P. Müller, *IUCrJ*, 2021, **8**, 150–151.

[115] W. Clegg, in *Crystal Structure Determination*, Oxford University Press, United States, 2003, ch. 1, pp. 1–26.

[116] W. Clegg and A. Bond, in *X-ray Structure Analysis*, BCA/CCG Intensive Teaching School, Durham, 17th edn., 2019, ch. 4, pp. 1–18.

[117] M. Ermrich and D. Opper, in *Analyst, XRD for the*, PAN alytical, 2nd edn., 2013, ch. 3, pp. 10–27.

[118] W. Clegg, A. Blake, R. Gould and P. Main, in *Crystal Structure Analysis Principles and Practice*, ed. W. Clegg, Oxford Science Publications, 2001, ch. 3, pp. 24–38.

[119] C. Hammond, in *The Basics of Crystallography and Diffraction*, Oxford Science Publications, 1997, ch. 2, pp. 32–44.

[120] H. J. Shepherd, in *X-ray Structure Analysis*, BCA/CCG Intensive Teaching School, Durham, 17th edn., 2019, ch. 6, pp. 1–28.

[121] C. Hammond, in *The Basics of Crystallography and Diffraction*, Oxford Science Publications, 1997, ch. 6, pp. 92–97.

[122] H. J. Shepherd, in *X-ray Structure Analysis*, BCA/CCG Intensive Teaching School, Durham, 17th edn., 2019, ch. 7, pp. 1–26.

[123] W. Clegg, in *Crystal Structure Determination*, Oxford University Press, United States, 2003, ch. 2, pp. 27–37.

[124] W. Clegg, A. Blake, R. Gould and P. Main, in *Crystal Structure Analysis Principles and Practice*, Oxford Science Publications, 2001, ch. 4, pp. 42–48.

[125] W. Clegg, A. Blake, R. Gould and P. Main, in *Crystal Structure Analysis Principles and Practice*, Oxford Science Publications, 2001, ch. 1, pp. 1–9.

[126] L. Palatinus, in *X-ray Structure Analysis*, BCA/CCG Intensive Teaching School, Durham, 17th edn., 2019, ch. 12, pp. 1–20.

[127] S. Parsons, in *X-ray Structure Analysis*, BCA/CCG Intensive Teaching School, Durham, 17th edn., 2019, ch. 10, pp. 1–22.

[128] D. Sayre, *Acta Crystallographica*, 1952, **5**, 843.

[129] W. Clegg, A. Blake, R. Gould and P. Main, in *Crystal Structure Analysis Principles and Practice*, Oxford Science Publications, 2001, ch. 9, pp. 102–114.

[130] R. Cooper, in *X-ray Structure Analysis*, BCA/CCG Intensive Teaching School, Durham, 17th edn., 2019, ch. 17, pp. 1–29.

[131] W. Clegg, A. Blake, R. Gould and P. Main, in *Crystal Structure Analysis Principles and Practice*, Oxford Science Publications, 2001, ch. 12, pp. 135–145.

[132] W. Clegg, in *Crystal Structure Determination*, Oxford University Press, United States, 2003, ch. 4, pp. 75–77.

[133] C. Hammond, in *The Basics of Crystallography and Diffraction*, Oxford Science Publications, 1997, ch. 10, pp. 171–181.

[134] D. Q. Craig, in *Polymorphism: in the Pharmaceutical Industry*, Wiley -VCH, 2006, ch. 3, pp. 43–59.

[135] D. C. Joy, *Ultramicroscopy*, 1991, **37**, 216–233.

[136] Diamond Light Source, *How It Works? Circular Dichroism*, 2017, `https://www.diamond.ac.uk/Home/News/LatestFeatures/Issue-8/06-11-17.html`.

[137] H.-G. Kuball, T. Höfer and S. Kiesewalter, in *Encyclopedia of Spectroscopy and Spectrometry*, ed. J. C. Lindon, G. E. Tranter, D. W. B. T. E. o. S. Koppenaal and S. T. Edition), Academic Press, Oxford, 3rd edn., 2017, pp. 217–231.

[138] A. Rodger, in *A. Rodger*, ed. G. C. K. Roberts, Springer Berlin Heidelberg, Berlin, Heidelberg, 2013, pp. 316–317.

[139] J. Keeler, *Understanding NMR Spectroscopy*, 2004, `doi.org/10.17863/CAM.1291`.

[140] G. P. Johari, *Journal of Chemical Physics*, 2016, **145**, 164502.

[141] Q. Jiang and M. D. Ward, *Chemical Society Reviews*, 2014, **43**, 2066–2079.

[142] CrysAlisPro, *version 1.171.38.43, Rigaku Oxford Diffraction, Oxford, UK*.

[143] G. Sheldrick, *Acta Crystallographica*, 2008, **A64**, 112–122.

[144] G. Sheldrick, *Acta Crystallographica*, 2015, **C71**, 3–8.

[145] O. V. Dolomanov, L. J. Bourhis, R. J. Gildea, J. A. K. Howard and H. Puschmann, *Journal of Applied Crystallography*, 2009, **42**, 339–341.

[146] F. C. Macrae, I. Sovago, S. J. Cottrell, P. T. Galek, P. McCabe, E. Pidcock, M. Platings, G. P. Shields, J. S. Stevens, M. Towler and P. A. Wood, *Journal of Applied Crystallography*, 2020, **53**, 226–235.

[147] S. Nelson, *Interference Phenomena, Compensation, and Optic Sign*, 2014, `www.tulane.edu/~sanelson/eens211/interference_of_light.htm`.

[148] A. Nanakoudis, *What is SEM? Scanning electron microscope technology explained, ThermoFisher Scientific*, 2019, `https://blog.phenom-world.com/what-is-sem`.

[149] L. Perge, J. Gröls, D. F. Segura, A. Al-Ani, M. Wilkinson and B. Castro-Dominguez, *Journal of Pharmaceutical Sciences*, 2020, **109**, 3027–3034.

[150] A. J. Al-Ani, P. Sugden, C. C. Wilson and B. Castro-Dominguez, *Crystal Growth and Design*, 2021, **21**, 3310–3315.

[151] T. P. Singh, T. N. Bhat and V. M, *Current Science*, 1973, **42**, 384.

[152] M. Haisa, S. Kashino and H. Maeda, *Acta Crystallographica Section B Structural Crystallography and Crystal Chemistry*, 1974, **30**, 2510–2512.

[153] M. A. Perrin, M. A. Neumann, H. Elmaleh and L. Zaske, *Chemical Communications*, 2009, **22**, 3181–3183.

[154] M. L. Peterson, S. L. Morissette, C. McNulty, A. Goldsweig, P. Shaw, M. LeQuesne and J. Monagle, *Journal of the American Chemical Society*, 2002, **124**, 10958–10959.

[155] F. Kesisoglou and Y. Wu, *The AAPS journal*, 2008, **10**, 516–525.

[156] L. K. Hansen, G. L. Perlovich and A. Bauer-Brandl, *Acta Crystallographica Section E*, 2006, **62**, 3627–3628.

[157] L. McGregor, D. A. Rychkov, P. L. Coster, S. Day, V. A. Drebushchak, A. F. Achkasov, G. S. Nichol, C. R. Pulham and E. V. Boldyreva, *CrystEngComm*, 2015, **17**, 6183–6192.

[158] L. H. Thomas, C. Wales, L. Zhao and C. C. Wilson, *Crystal Growth and Design*, 2011, **11**, 1450–1452.

[159] L. R. Agnew, T. McGlone, H. P. Wheatcroft, A. Robertson, A. R. Parsons and C. C. Wilson, *Crystal Growth and Design*, 2017, **17**, 2418–2427.

[160] Y. Liu, B. Gabriele, R. J. Davey and A. Cruz-Cabeza, *Journal of the American Chemical Society*, 2020, **142**, 6682–6689.

[161] K. Chadwick, A. Myerson and B. Trout, *CrystEngComm*, 2011, **13**, 6625–6627.

[162] B. A. Hendriksen, D. J. Grant, P. Meenan and D. A. Green, *Journal of Crystal Growth*, 1998, **183**, 629–640.

[163] C. Thompson, M. C. Davies, C. J. Roberts, S. J. Tendler and M. J. Wilkinson, *International Journal of Pharmaceutics*, 2004, **280**, 137–150.

[164] A. Saleemi, I. I. Onyemelukwe and Z. Nagy, *Frontiers of Chemical Science and Engineering*, 2013, **7**, 79–87.

[165] L. H. Thomas, G. A. Craig, C. A. Morrison, A. M. Reilly and C. C. Wilson, *Crystal Growth and Design*, 2011, **11**, 2045–2049.

[166] H. L. Lee, H. Y. Lin and T. Lee, *Organic Process Research and Development*, 2014, **18**, 539–545.

[167] C. Sudha and K. Srinivasan, *CrystEngComm*, 2013, **15**, 1914–1921.

[168] C. Sudha, R. Nandhini and K. Srinivasan, *Crystal Growth and Design*, 2014, **14**, 705–715.

[169] G. T. Rengarajan, D. Enke, M. Steinhart and M. Beiner, *Physical Chemistry Chemical Physics*, 2011, **13**, 21367–21374.

[170] J. S. Capes and R. E. Cameron, *Crystal Growth and Design*, 2007, **7**, 108–112.

[171] I. Wang, M. Lee, D. Seo, H. Lee, Y. Choi, W. Kim, C. Kim, M. Jeong and G. J. Choi, *AAPS PharmSciTech*, 2011, **12**, 764–770.

[172] S. Gaisford, A. B. M. Buanz and N. Jethwa, *Journal of Pharmaceutical and Biomedical Analysis*, 2010, **53**, 366–370.

[173] S. C. Barthe, M. A. Grover and R. W. Rousseau, *Crystal Growth and Design*, 2008, **8**, 3316–3322.

[174] J. Sibik, M. J. Sargent, M. Franklin and J. A. Zeitler, *Molecular Pharmaceutics*, 2014, **11**, 1326–1334.

[175] W. Beckmann, *Organic Process Research & Development*, 2000, **4**, 372–383.

[176] V. Colombo, L. L. Presti and A. Gavezzotti, *CrystEngComm*, 2017, **19**, 2413–2423.

[177] K. Kachrimanis, D. E. Braun and U. J. Griesser, *Journal of Pharmaceutical and Biomedical Analysis*, 2007, **43**, 407–412.

[178] P. Beale, J and T. Grainger, C, *Crystal Structure Communications*, 1972, **67**, 71–74.

[179] P. J. M. Leger and G. M. Gadret, *Acta Crystallographica*, 1978, **B34**, 1203–1208.

[180] J. A. Bis, P. D. Boyle, S. A. R. Carino, D. H. Igo and L. M. Katrincic, *Crystal Growth and Design*, 2014, **14**, 775–782.

[181] W. Liu, Q. Chen and L. Yu, *Acta Crystallographica. Section E, Crystallographic Communications*, 2017, **73**, 1333–1335.

[182] K. J. Paluch, L. Tajber, C. J. Elcoate, O. I. Corrigan, S. E. Lawrence and A. M. Healy, *Journal of Pharmaceutical Sciences*, 2011, **100**, 3268–3283.

[183] S. Aitipamula, A. B. H. Wong, P. S. Chow and R. B. H. Tan, *RSC Advances*, 2016, **6**, 34110–34119.

[184] W. Liu and L. Yu, *IUCrData*, 2017, **2**, x171189.

[185] J. A. Kaduk, K. Zhong, T. N. Blanton and S. Gates, *Powder Diffraction*, 2015, **30**, 158–162.

[186] J. Moreno and R. Peinado, in *Enological Chemistry*, ed. J. Moreno and R. B. T. E. C. Peinado, Academic Press, San Diego, 2012, ch. 8, pp. 109–120.

[187] M. O'Neil, *The Merck Index - An Encyclopedia of Chemicals, Drugs, and Biologicals*, 13th edn., 2001, p. 42.

[188] D. Lide and G. Milne, *Handbook of Data on Organic Compounds*, CRC Press, Inc., 2nd edn., 1994, vol. 1, p. 1793.

[189] I. Rozas, I. Alkorta and J. Elguero, *Journal of Physical Chemistry. A*, 1998, **102**, 9925–9932.

[190] G. Glockler, *The Journal of Physical Chemistry*, 1958, **62**, 1049–1052.

[191] L. J. Barbour, *Chemical Communications*, 2006, 1163–1168.

[192] S. P. Delaney, D. H. Pan, M. Galella, S. X. Yin and T. M. Korter, *Crystal Growth and Design*, 2012, **12**, 5017–5024.

[193] M. A. Palacio, S. Cuffini, R. Badini, A. Karlsson and S. M. Palacios, *Journal of Pharmaceutical and Biomedical Analysis*, 2007, **43**, 1531–1534.

[194] S. Xie, S. K. Poornachary, P. S. Chow and R. B. Tan, *Crystal Growth and Design*, 2010, **10**, 3363–3371.

[195] R. L. Harlow, *Journal of research of the National Institute of Standards and Technology*, 1996, **101**, 327–339.

[196] P. R. Ramel, R. Campos and A. G. Marangoni, *Crystal Growth and Design*, 2018, **18**, 1002–1011.

[197] A. Klapwijk, in *Disorder and additive control of solid form and morphology in continuous crystallisation.*, PhD Thesis, University of Bath, 2017, ch. 8, pp. 264–265.

[198] V. M. Nield, D. A. Keen and R. L. McGreevy, *Acta Crystallographica Section A*, 1995, **51**, 763–771.

[199] T. R. Welberry and D. J. Goossens, *IUCrJ*, 2014, **1**, 550–562.

[200] T. R. Welberry, *Diffuse X-ray Scattering and Models of Disorder. Monographs on Crystallography*, Oxford University Press, 2004.

[201] R. L. J. McGreevy, *Journal of Physics: Condensed Matter*, 2001, **13**, R87.

[202] C. P. Wong and H. Morita, in *Comprehensive Natural Products III*, ed. H. Liu and T. P. Begley, Elsevier, 2020, ch. 1.08.2.7, p. 259.

[203] S. C. Wallwork and H. M. Powell, *Acta Crystallographica*, 1957, **10**, 48–52.

[204] D. E. Braun, D. A. Tocher, S. L. Price and U. J. Griesser, *The Journal of Physical Chemistry B*, 2012, **116**, 3961–3972.

[205] T. R. Welberry, in *Diffuse x-ray scattering and models of disorder*, The Institute of Physics, 1985, ch. 1, pp. 1545–1556.

Chapter 9

Appendix

1 Research outputs

1.1 Publications

The following manuscripts have been published, or have been submitted for publication, from related work carried out during this doctoral programme:

A. J. Al-Ani, P.M.J Szell, Z. Rehman, H. Blade, H. P. Wheatcroft, L. P Hughes, S. P. Brown, C. C. Wilson, Combining X-ray and NMR Crystallography to Explore the Crystallographic Disorder in Salbutamol Oxalate, *Cryst. Growth Des.*, 2021 (submitted).

A. J. Al-Ani, P. Sugden, C. C Wilson, and B. Castro-Dominguez, Elusive Seed Formation via Electrical Confinement: Control of a Novel Cocrystal in Cooling Crystallization, *Cryst. Growth Des.*, 2021, 6, 3310–3315.

A. J. Al-Ani, C. Herdes, C. C. Wilson, and B. Castro-Dominguez, Engineering a New Access Route to Metastable Polymorphs with Electrical Confinement, *Cryst. Growth Des.*, 2020, 20, 1451-1457.

L. Perge, J. Grols, D. F. Segura, A. J. Al-Ani, M. Wilkinson, B. Castro-Dominguez, Concurrent Antisolvent Electrospraying: A Novel Continuous Crystallization Technique, *J. Pharm. Sci*, 2020, 109, 3027-3034.

1.2 Conferences

The following work has been presented at conferences as poster presentations:

Engineering Defects and Disorder for Enhanced Pharmaceutical Properties. Is there an order to disorder? RSC Solid State Chemistry Group: Early Careers Meeting, 09/2020.

Engineering a New Access Route to Metastable Polymorphs with Electrical Confinement for Enhanced Pharmaceutical Properties, British Crystallographic Association: Spring Meeting 2019, UK United Kingdom, 04/2019. - Awarded the RSC CrystEngComm Poster Prize.

1.3 Collaborations

Secondment at AstraZeneca, Macclesfield with the Right Particle Team, 05/2021-08/2021.

Involvement in a Knowledge Transfer Partnership between the University of Warwick and AstraZeneca, 11/2020-08/2021.

Visiting researcher at the Research Complex at Harwell, Rutherford Appleton Laboratory Didcot. 11/2018–11/2019

1.4 Crystal structures deposited into the CSD

The following crystal structures have been deposited into the CSD by the author during this doctoral program:

Paracetamol - metacetamol co-crystal, deposition number: 2058497.

Salbutamol hemi-oxalate, deposition numbers: 2106949-2106960

2 Appendix for chapter 4

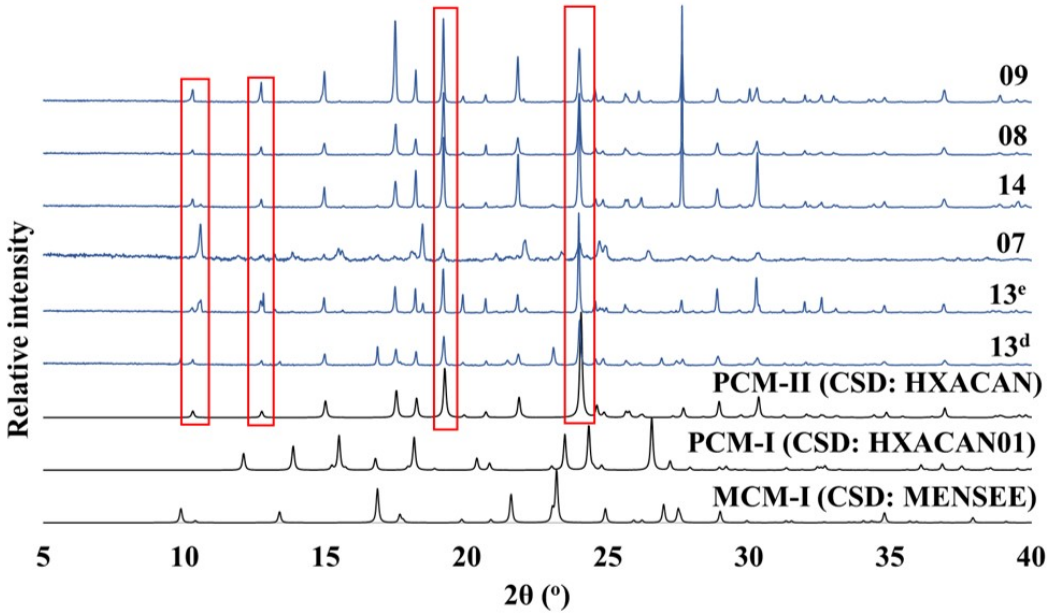

Figure 9-1: The PXRD patterns from experiments that correspond to PCM-II, Bragg reflections that belong to PCM-II are highlighted in red.

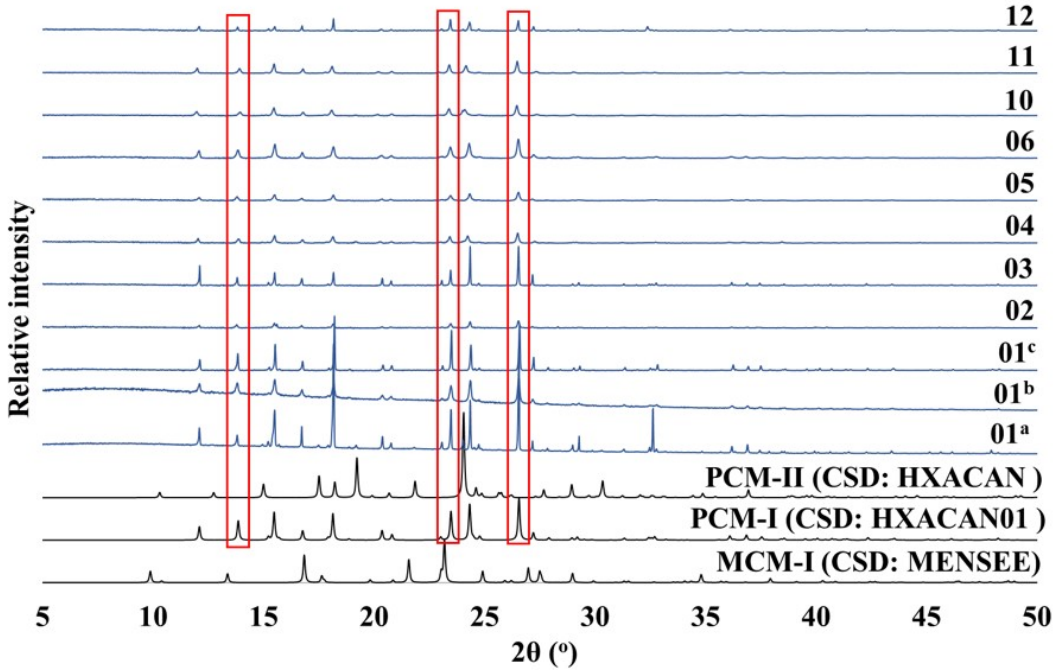

Figure 9-2: The PXRD patterns from experiments that correspond to PCM-I, Bragg reflections that belong to PCM-I are highlighted in red.

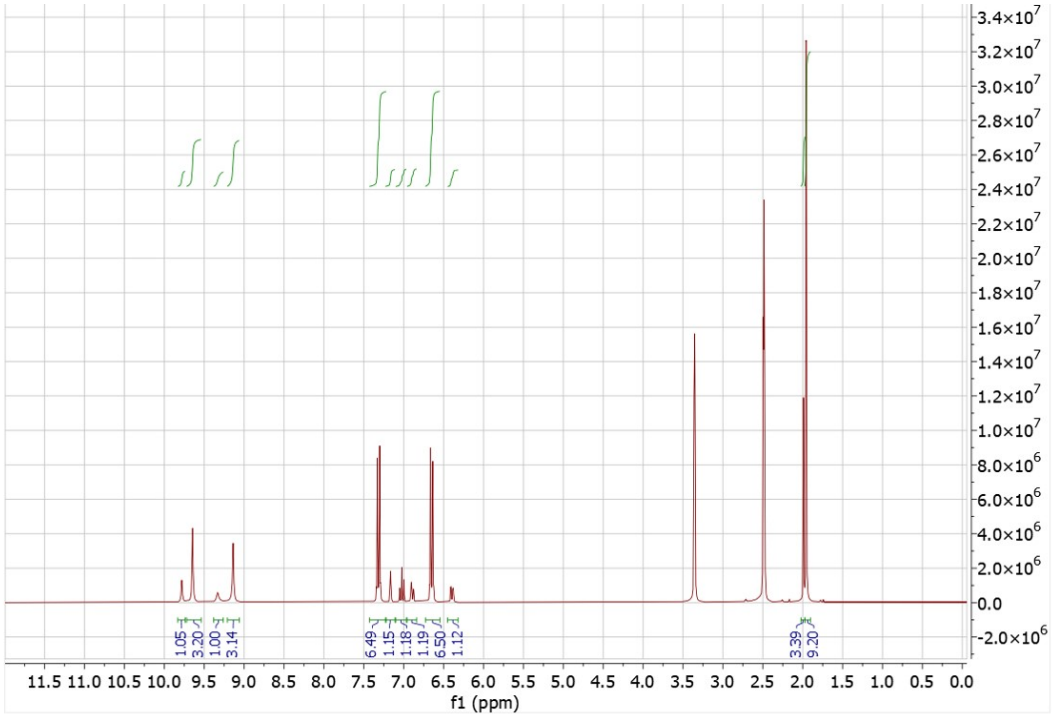

Figure 9-3: The ^{1}H NMR spectrum of electrosprayed PCM-II in DMSO (d6), showing the values obtained from peak integration.

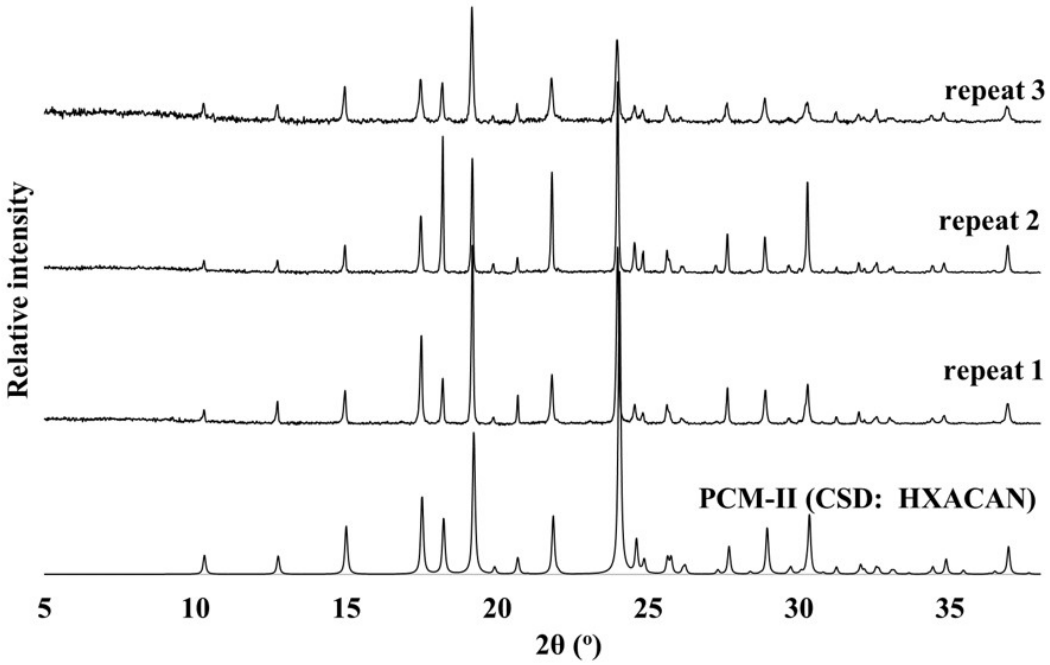

Figure 9-4: The PXRD pattern of PCM-II obtained from three experimental repeats under electrospraying.

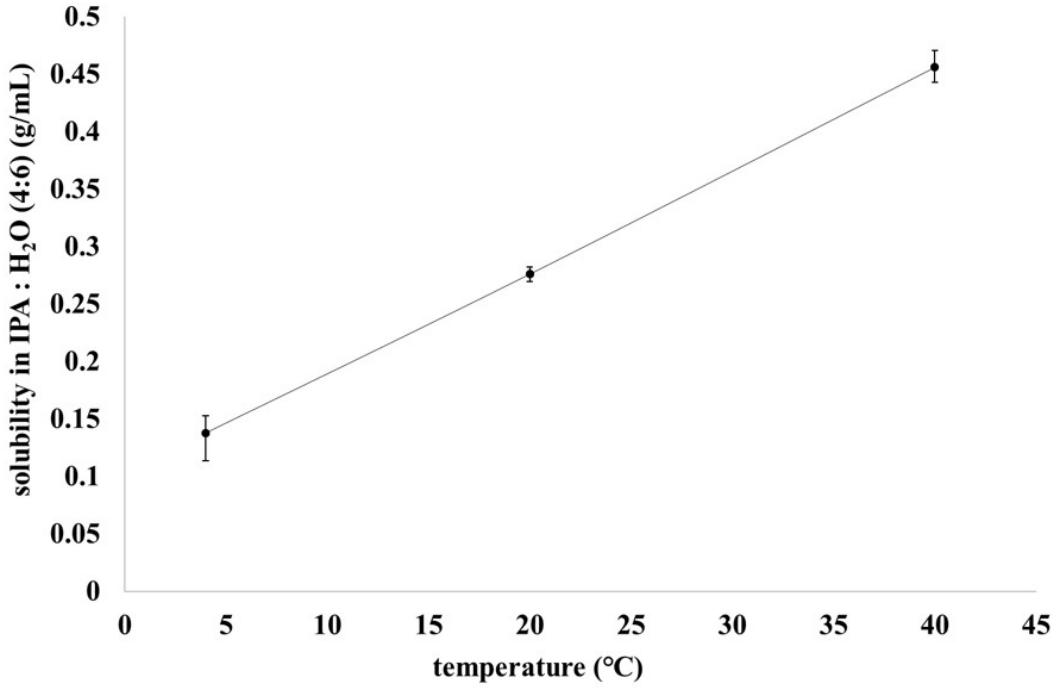

Figure 9-5: The solubility curve for PCM and MCM (1:1) in IPA and water (4:6), calculated by gravimetric methods.

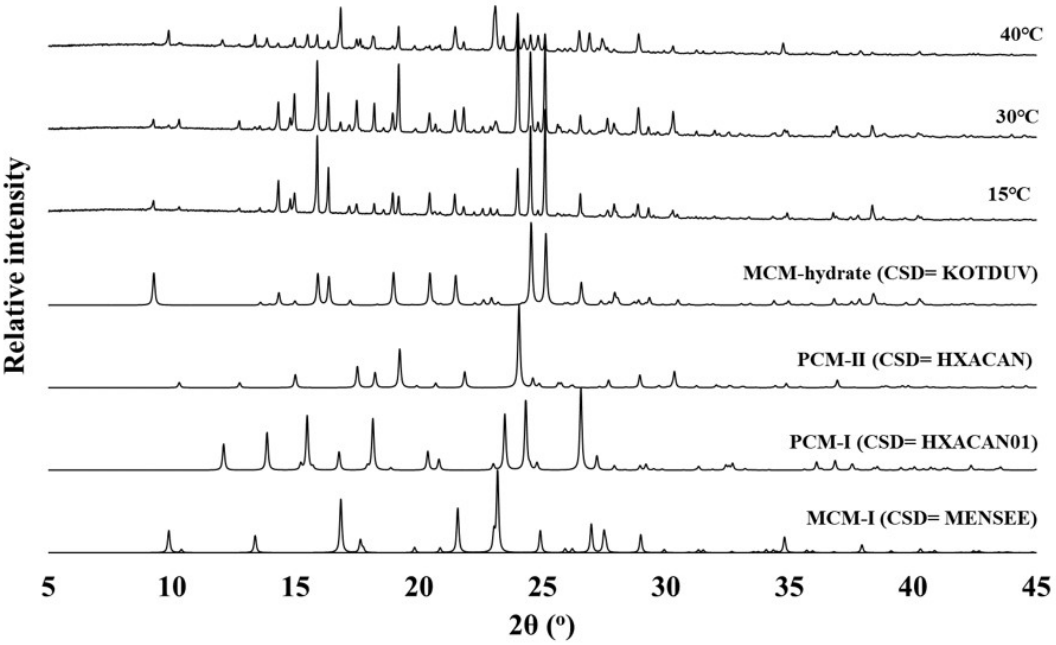

Figure 9-6: The PXRD patterns obtained for the filtered product from MSZW measurements at 15, 30 and 40°C. A combination of PCM-I, PCM-II, MCM-I and MCM mono-hydrate was observed.

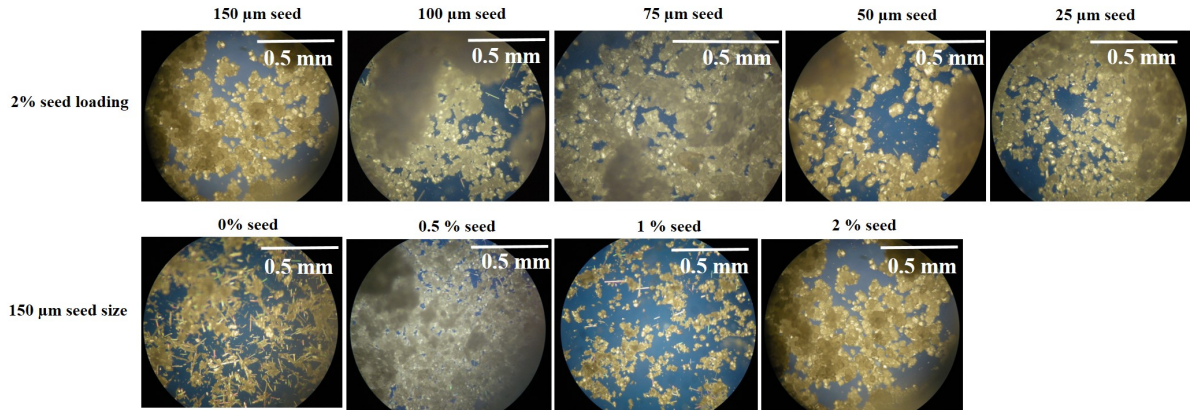

Figure 9-7: Images of the PCM-MCM co-crystal formed under different seed loading's and sizes.

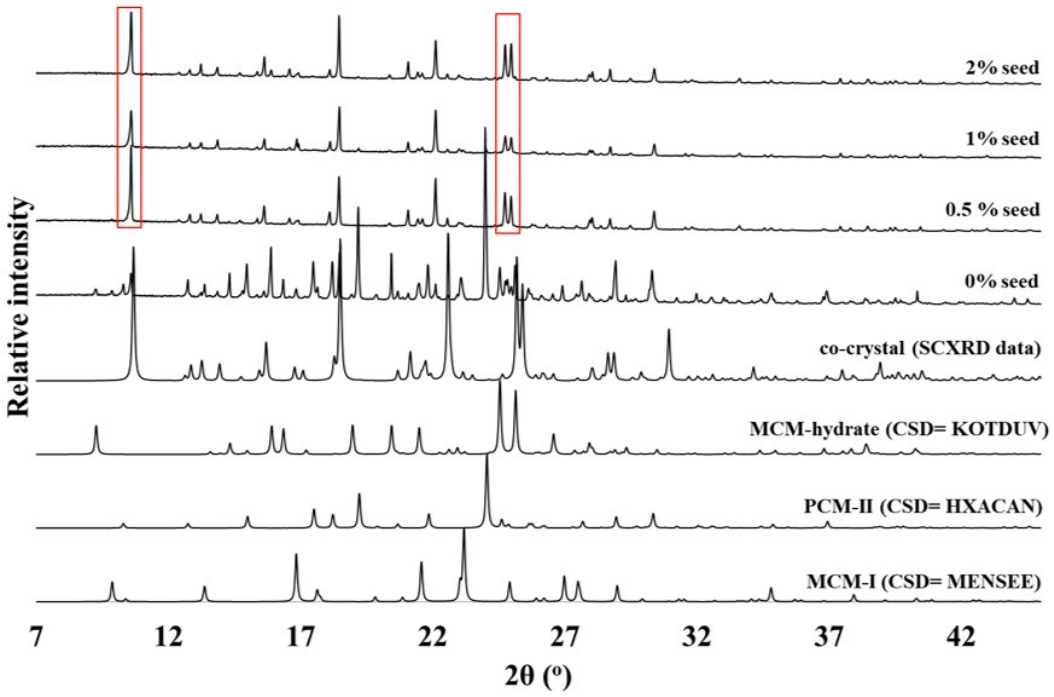

Figure 9-8: PXRD characterisation of experiments that used PCM-MCM co-crystal seeds from electrospraying. The PXRD patterns from different crystal seed loading percentages are displayed. The red box highlights Bragg reflections from the co-crystal.

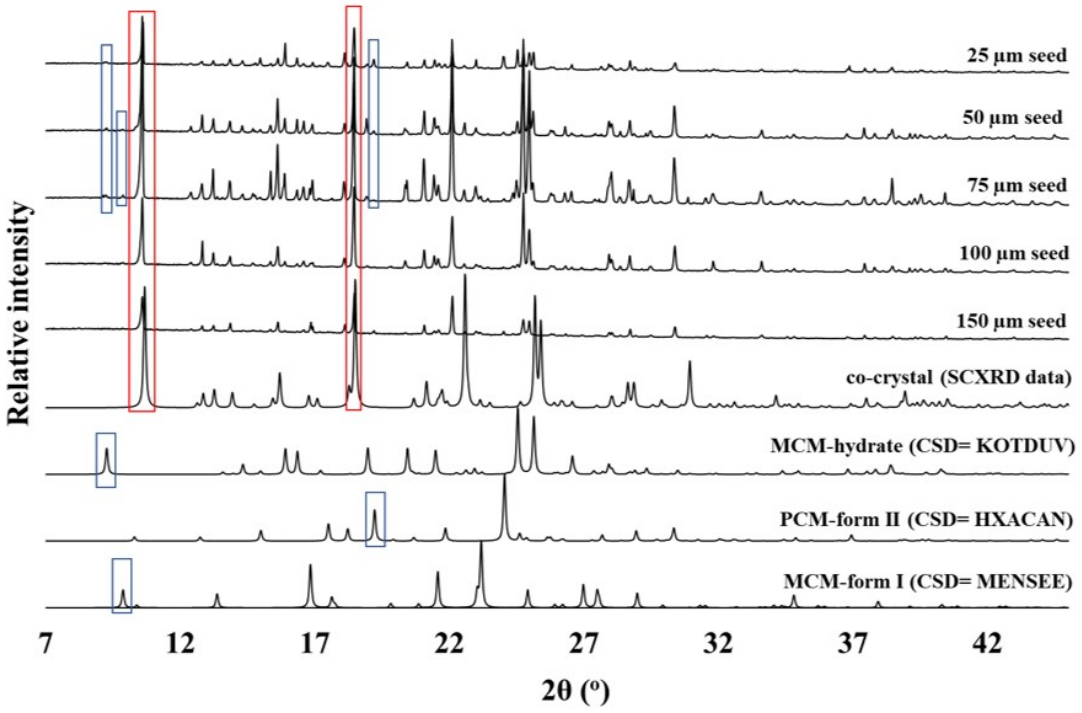

Figure 9-9: PXRD characterisation of experiments that used PCM-MCM co-crystal seeds from electrospraying. The PXRD patterns from different crystal sizes are displayed. The red box highlights Bragg reflections from the co-crystal and the blue box highlight impurities in the bulk material.

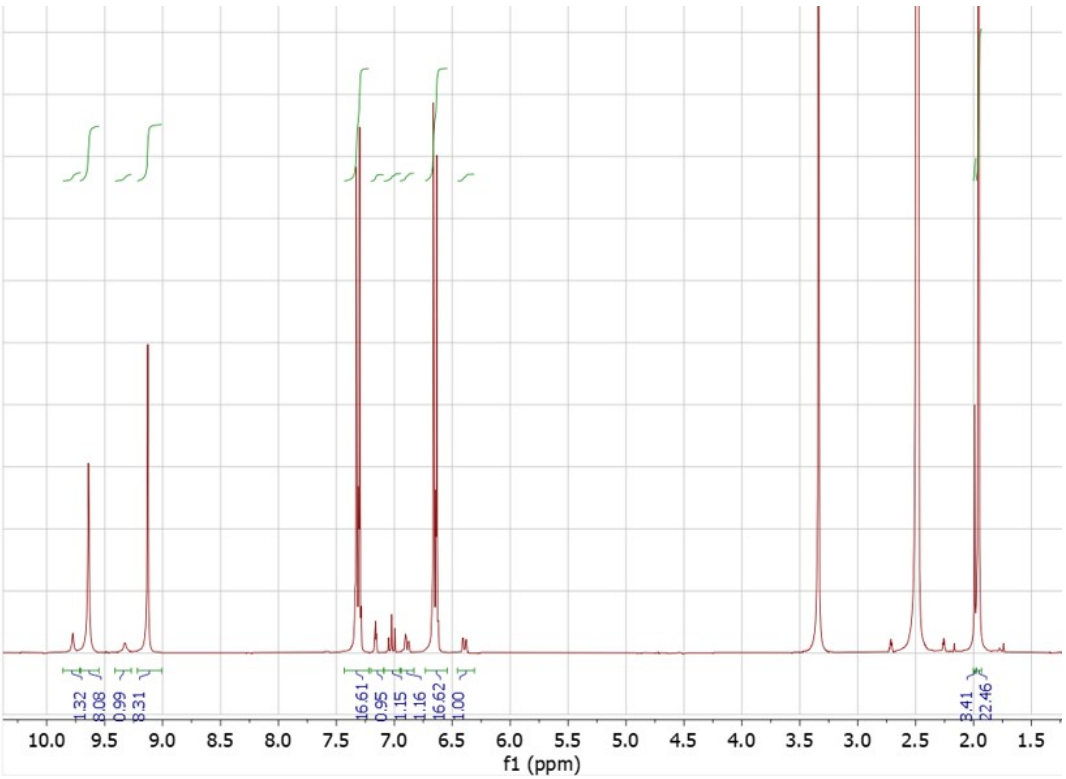

Figure 9-10: The ^{1}H NMR spectroscopy spectra gained from electrospraying a 10:90 ratio of MCM and PCM. Peak integration shows a 1:8 ratio of components.

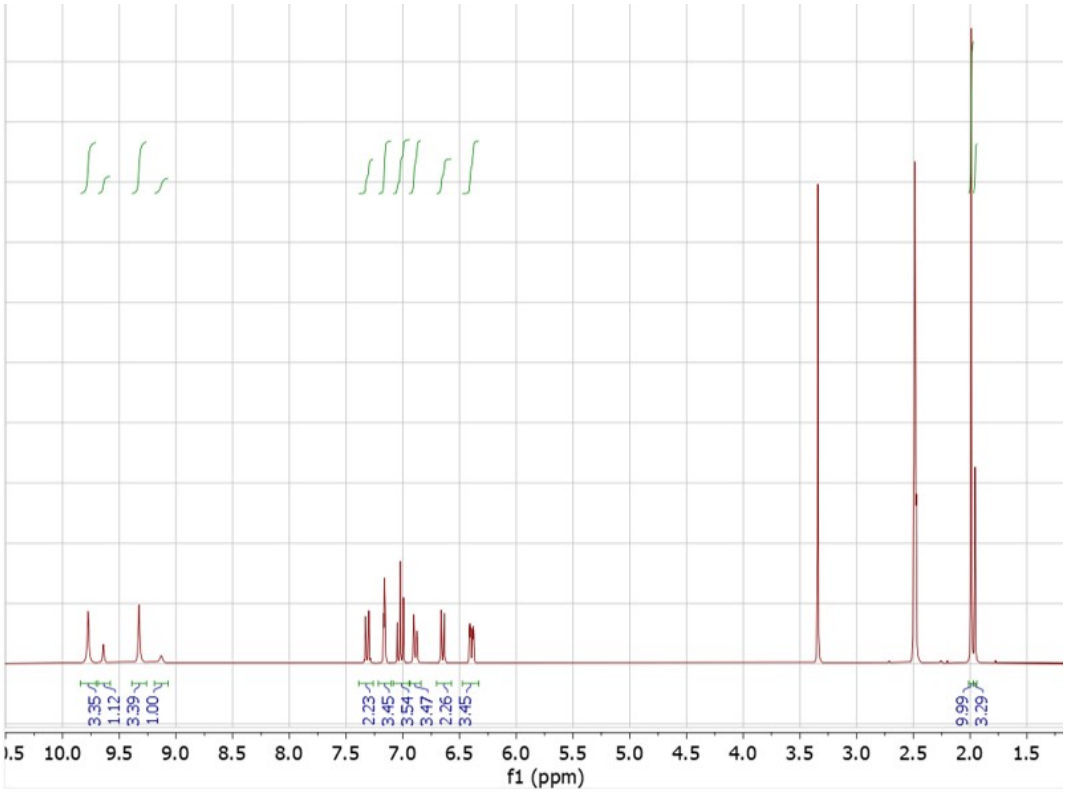

Figure 9-11: The ^{1}H NMR spectroscopy spectra gained from electrospraying a 75:25 ratio of MCM and PCM. Peak integration shows a 3:1 ratio of components.

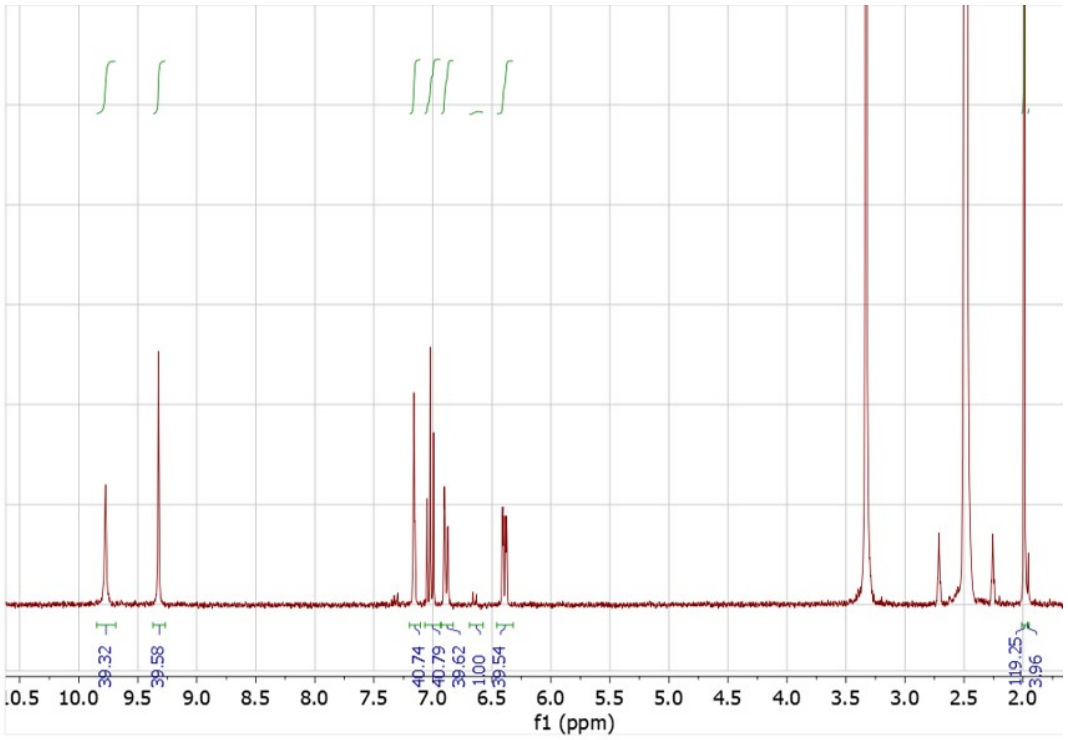

Figure 9-12: The ^{1}H NMR spectroscopy spectra gained from electrospraying a 90:10 ratio of MCM and PCM. Peak integration shows a 40:1 ratio of components.

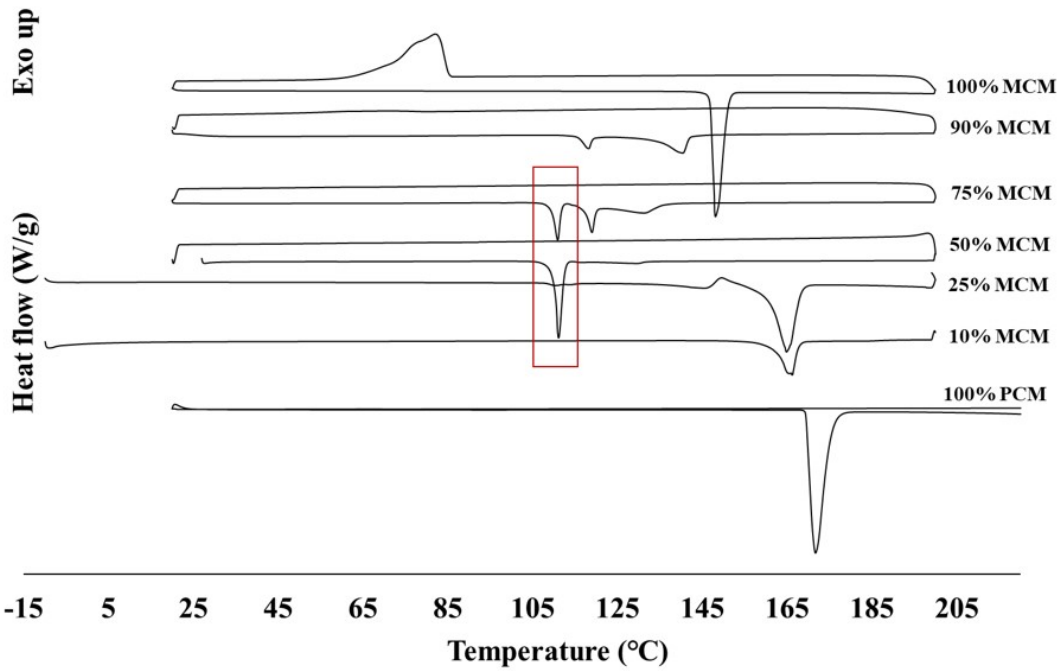

Figure 9-13: The DSC traces from experiments that studied different ratios of electrosprayed PCM and MCM. The red box highlights melting point endotherms of the co-crystal. No T_g are observed that would confirm the presence of an amorphous material.

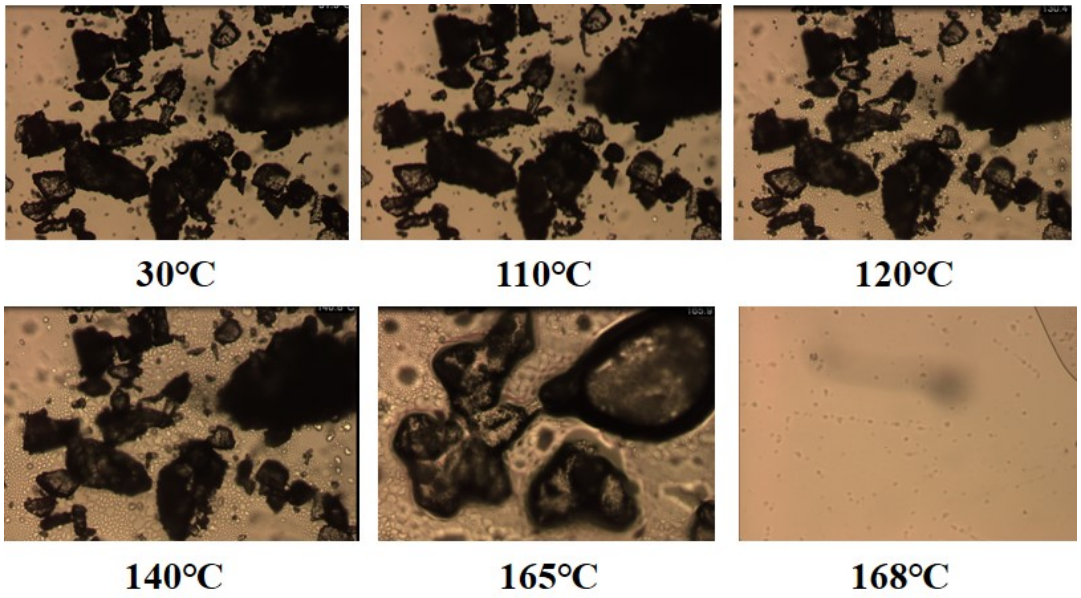

Figure 9-14: HSM images of experiment 19 in table 4.5, viewed under a temperature range of 30 to 170^{o}C.

co-crystal- electrosprayed

BET summary

Slope =	380.543 1/g
Intercept =	1.711e+02 1/g
Correlation coefficient, r =	0.996648
C constant=	3.225
Surface Area =	6.313 m²/g

co-crystal- seeded-cooling

BET summary

Slope =	1058.127 1/g
Intercept =	3.655e+02 1/g
Correlation coefficient, r =	0.986954
C constant=	3.895
Surface Area =	2.446 m²/g

Figure 9-15: A summary of results gained from BET; a method used to measure the surface area of material gained from electrospraying and cooling crystallisation.

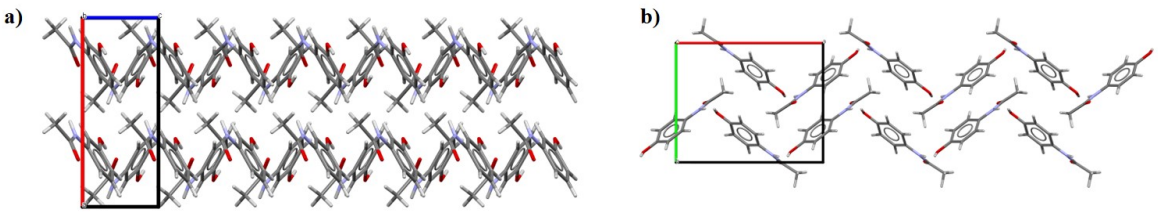

Figure 9-16: The packing arrangement observed in a) MCM-I (CSD= MENSEE), viewed along the b axis and b) PCM-I (CSD= HXACAN01) viewed along the c axis.

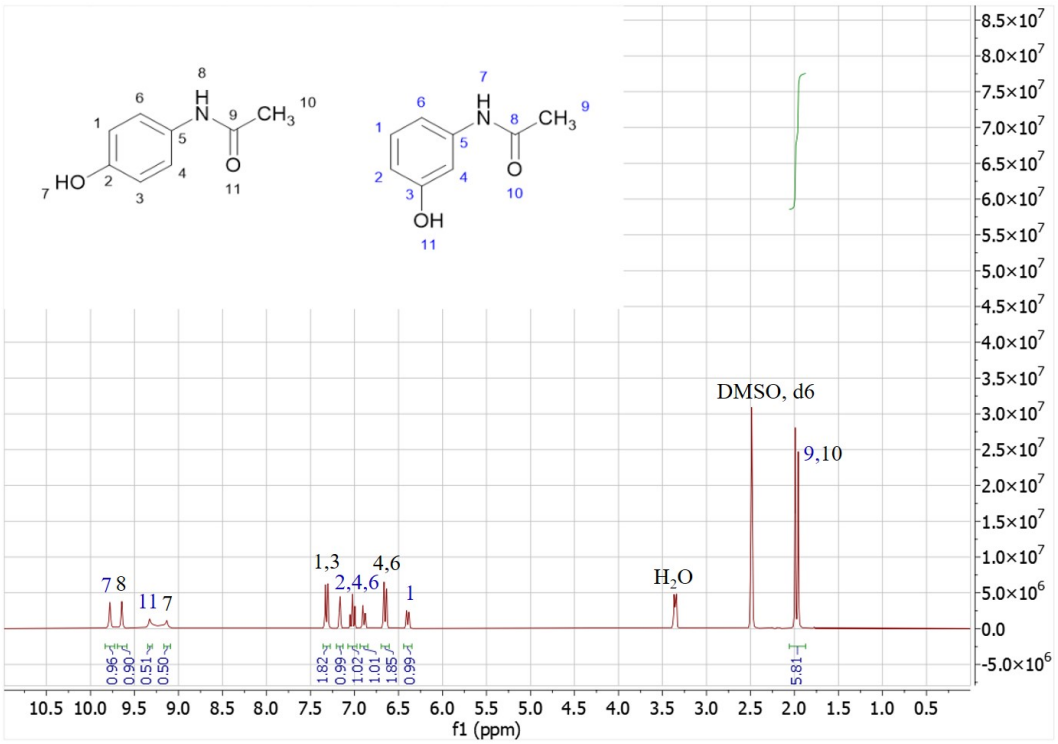

Figure 9-17: The ^{1}H NMR spectroscopy spectrum of the PCM-MCM co-crystal in DMSO (d6).

3 Appendix for chapter 5

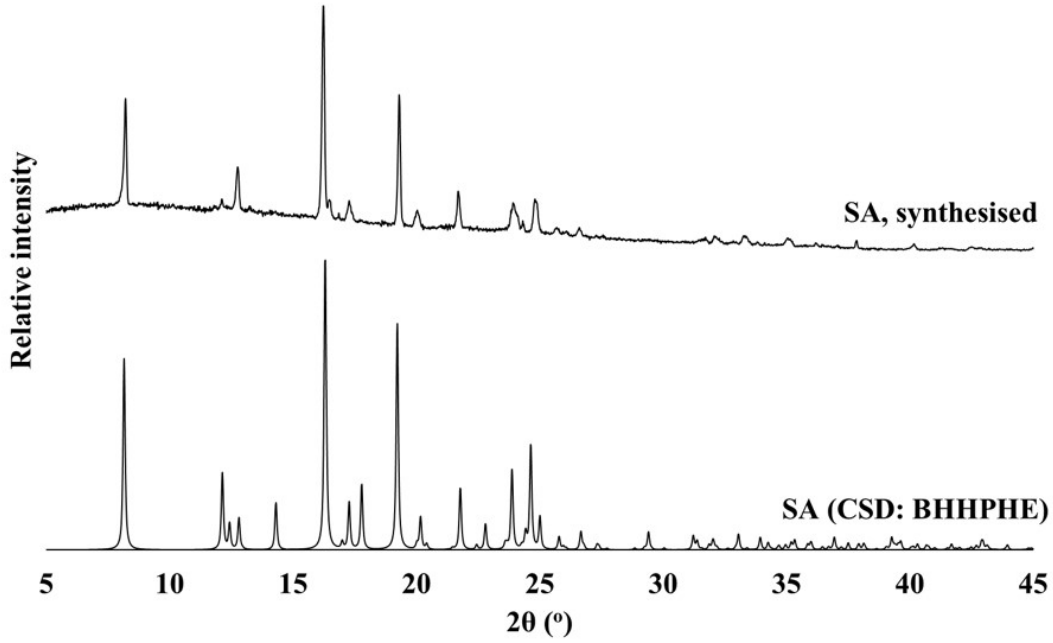

Figure 9-18: The PXRD trace obtained for salbutamol.

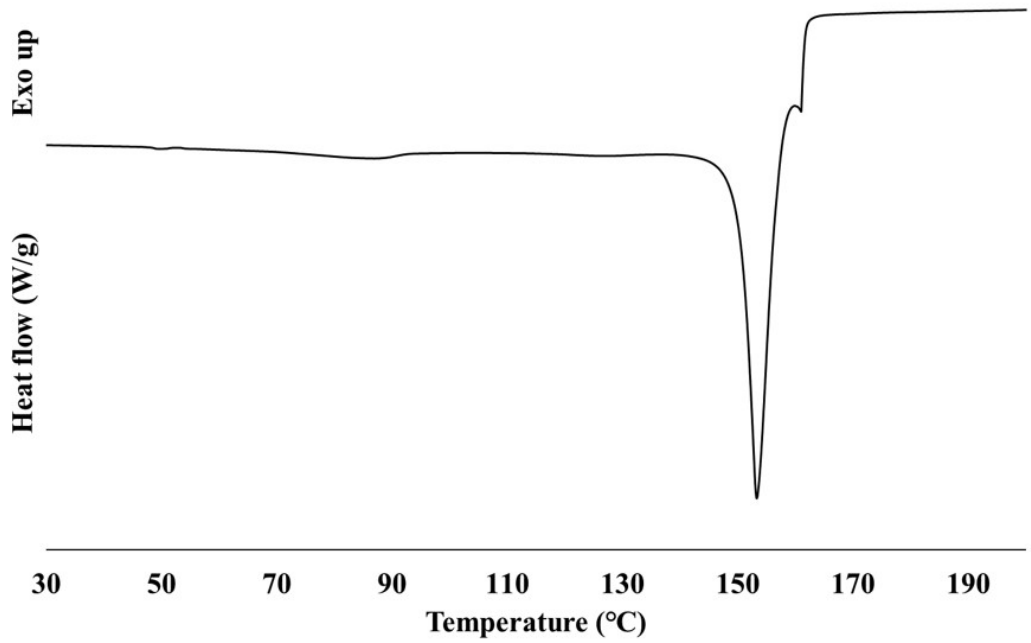

Figure 9-19: The DSC trace (onset= 141 ^{o}C, literature = 147-149^{o}C) obtained for salbutamol.

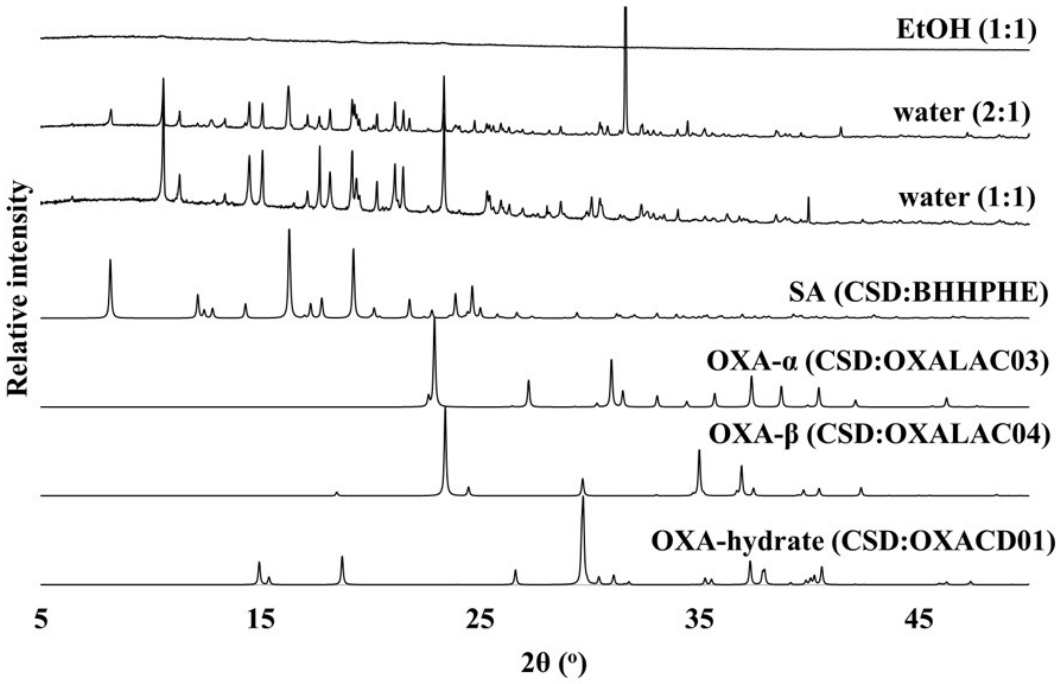

Figure 9-20: The PXRD traces obtained from evaporative crystallisation screening methods with SA and OX in water and EtOH

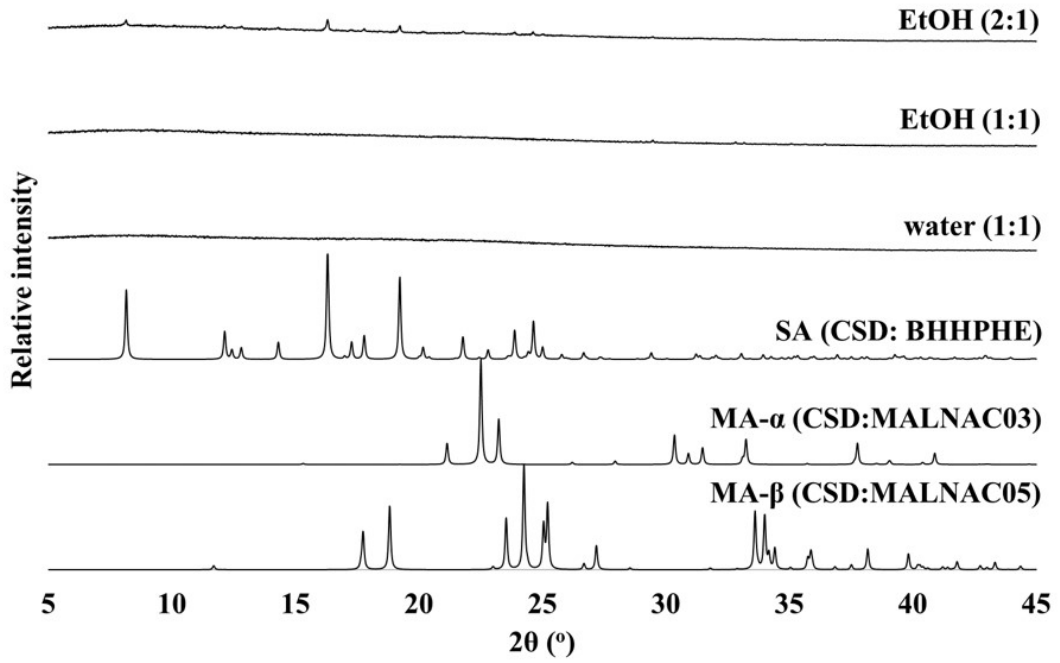

Figure 9-21: The PXRD traces obtained from evaporative crystallisation screening methods with SA and MA in water and EtOH

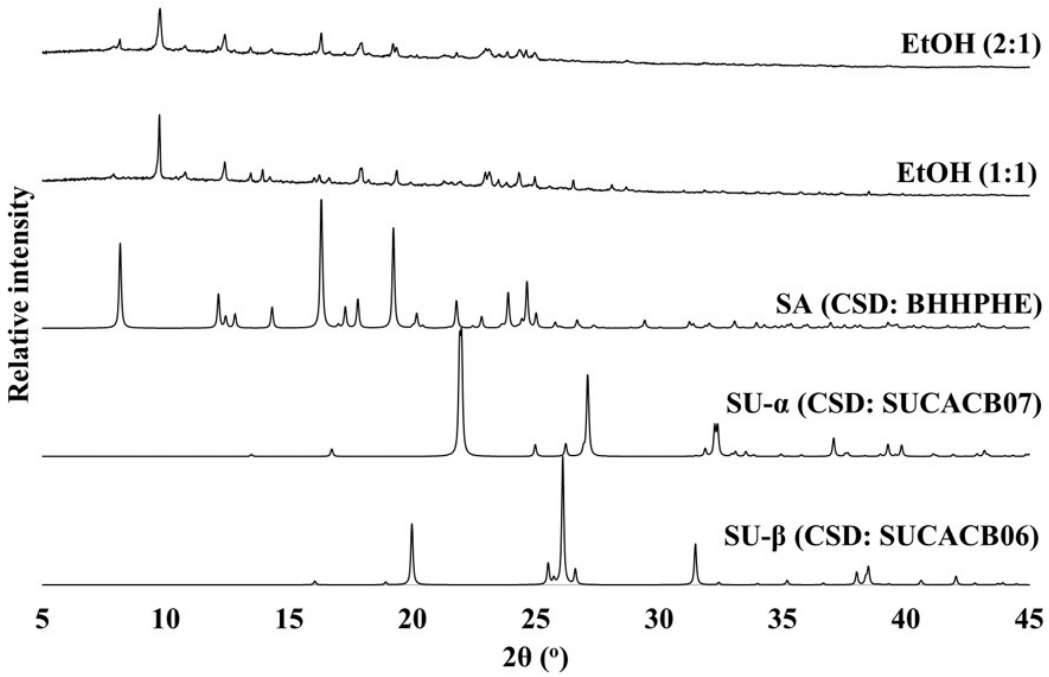

Figure 9-22: The PXRD traces obtained from evaporative crystallisation screening methods with SA and SU in water and EtOH

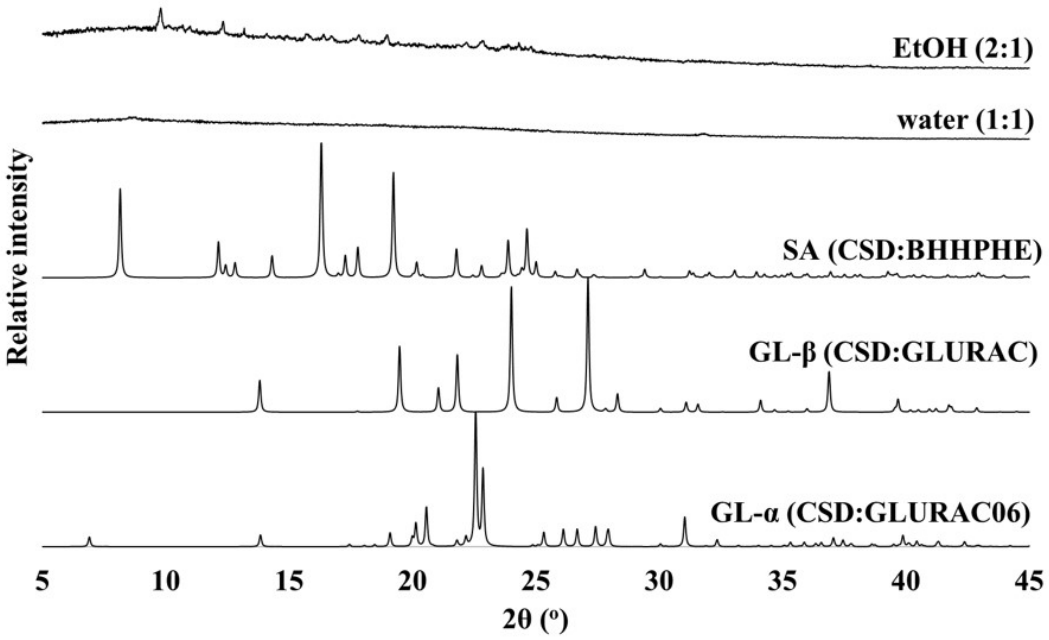

Figure 9-23: The PXRD traces obtained from evaporative crystallisation screening methods with SA and GL in water and EtOH

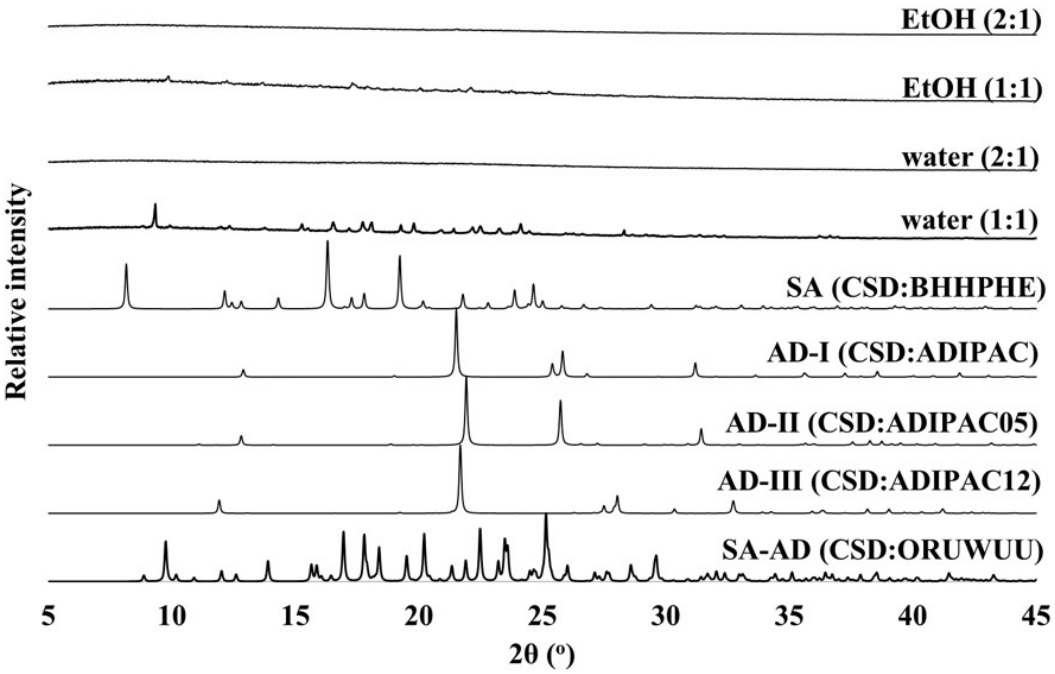

Figure 9-24: The PXRD traces obtained from evaporative crystallisation screening methods with SA and AD in water and EtOH

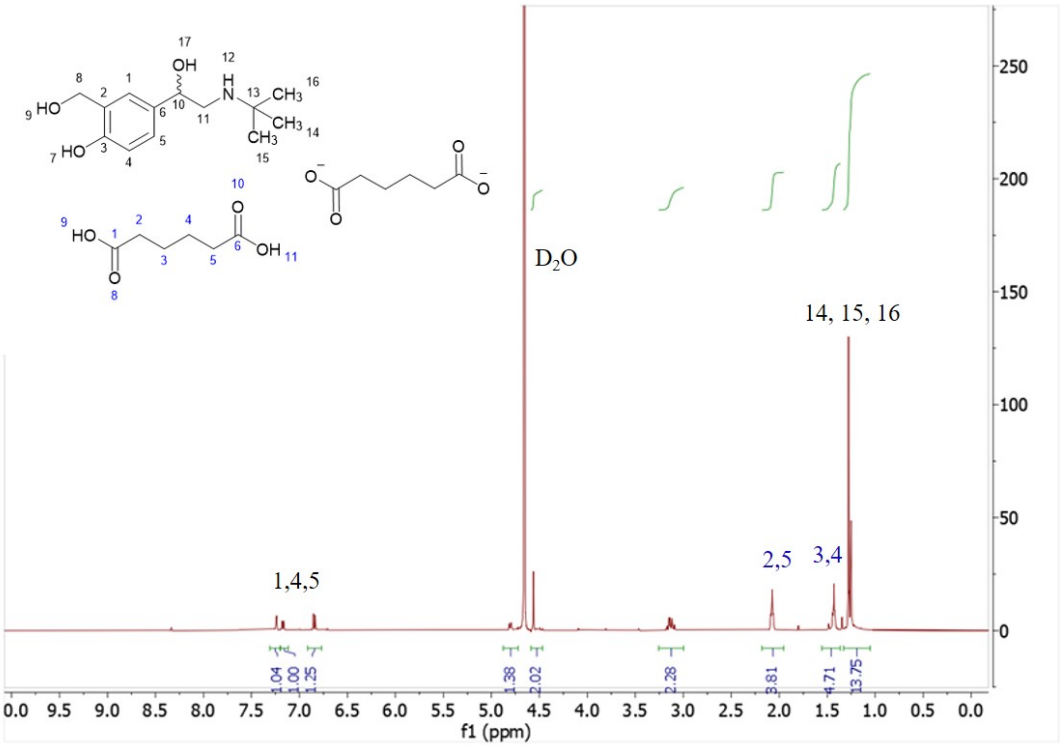

Figure 9-25: The ^{1}H NMR spectroscopy spectrum of the amorphous material obtained under evaporative co-crystallisation of SA and AD (2:1).

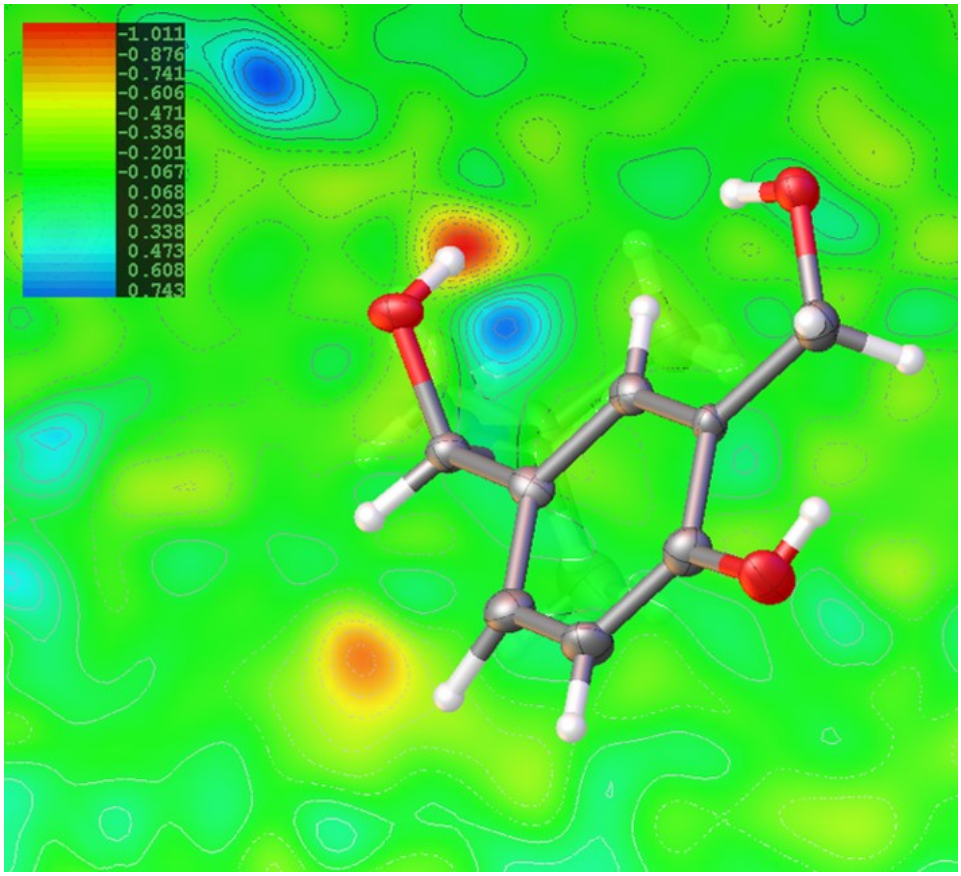

Figure 9-26: A weak cluster of electron density located in the expected region of the *C-OH minor occupancy position, shown in the electron density map of SA.

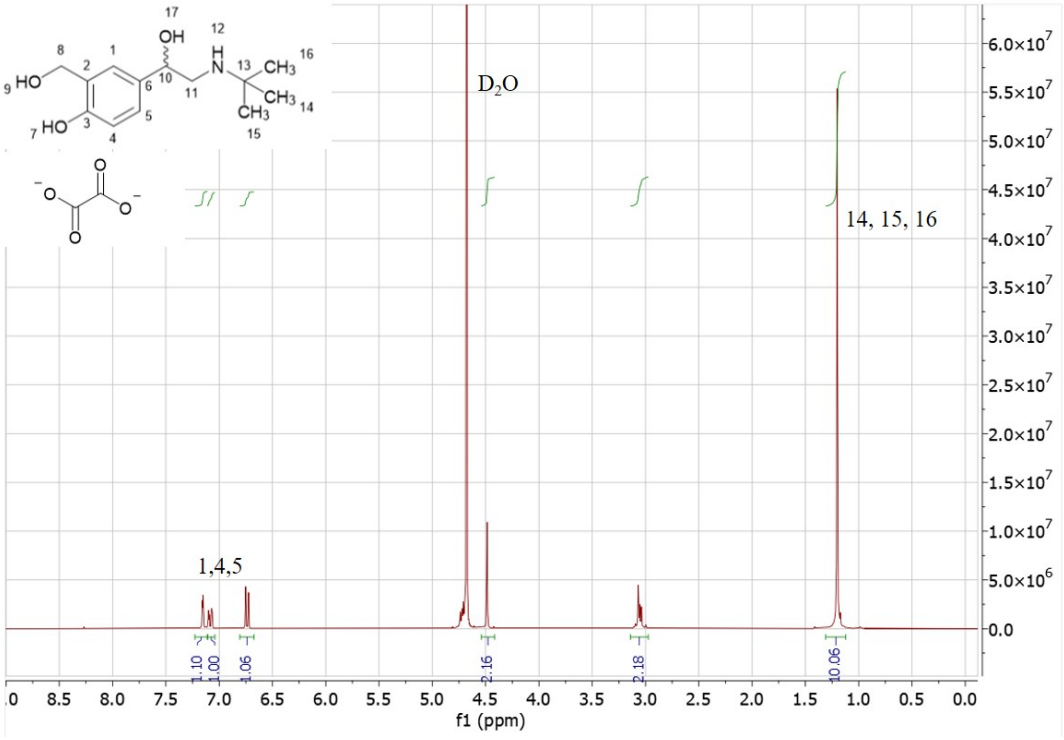

Figure 9-27: The ^{1}H NMR spectrum of SA-OX in D_2O.

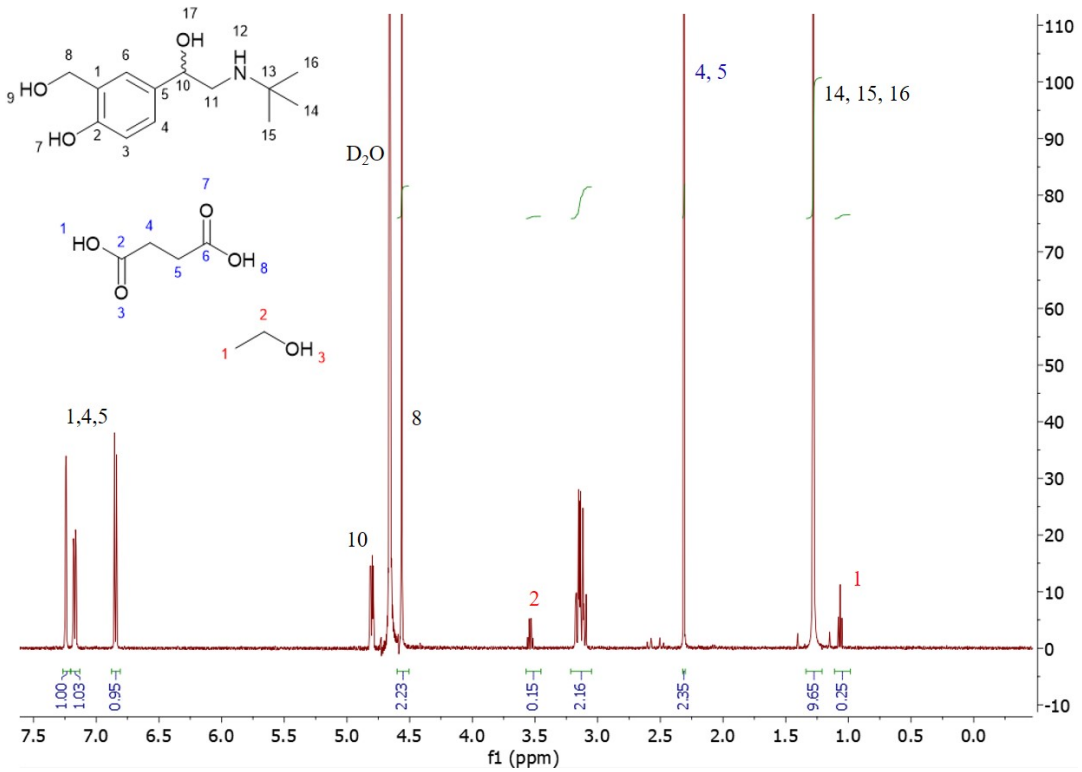

Figure 9-28: The ^{1}H NMR spectrum of SA-SU in D_2O.

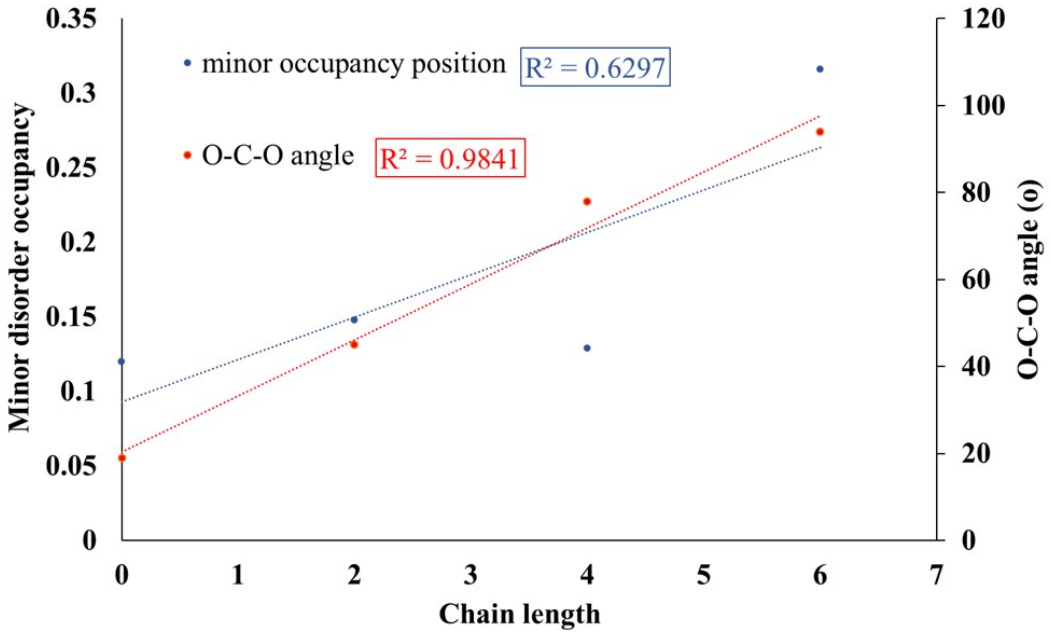

Figure 9-29: Co-former chain length as a function of minor occupancy position and angle.

4 Appendix for chapter 6

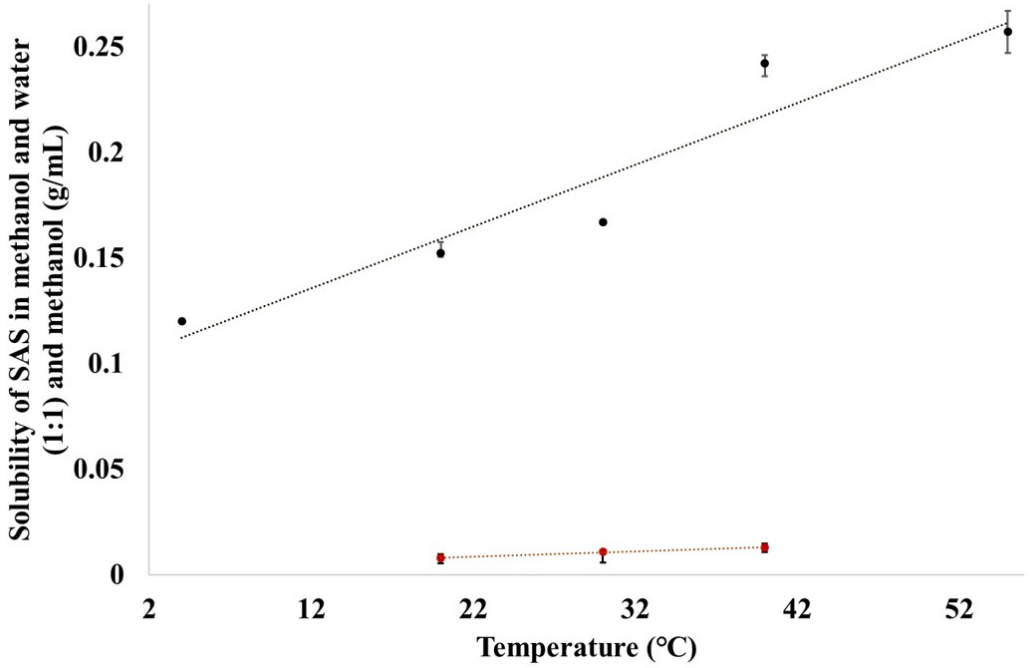

Figure 9-30: The measured solubility curve of SAS in MeOH and water 1:1 (black) and MeOH (red) using gravimetric methods.

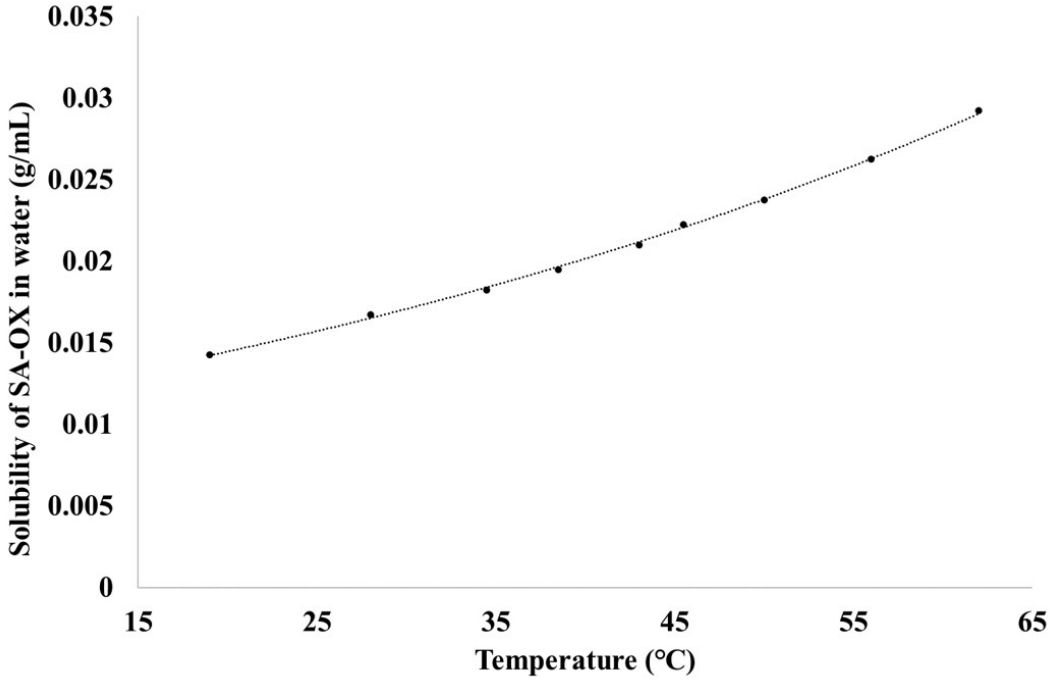

Figure 9-31: The measured solubility curve of SA-OX in water using observational methods. Repeat measurements gave a maximum error in the plotted temperature of +/ 1^oC.

material	molecular weight (g/mol)	mass (g)	moles	volume (dm^3)	concentration (mol/dm^3)	path length (cm)	absorbance	molar extinction coefficient ($L\ mol^{-1}cm^{-1}$)
SA	239.311	0.011	4.6383E-05	0.1	0.000463832	1	0.7826	1687.25
SA-OX	329.34	0.012	3.4918E-05	0.1	0.000349183	1	0.661682	1894.94
R-SA-HCl	275.77	0.008	2.8284E-05	0.05	0.000565689	1	0.938469	1658.98

Figure 9-32: The molar extinction coefficient calculation of each material analysed by CD. Chirascan Circular Dichroism Spectrometer was used to obtain the absorbance maxima from a solution of known concentration.

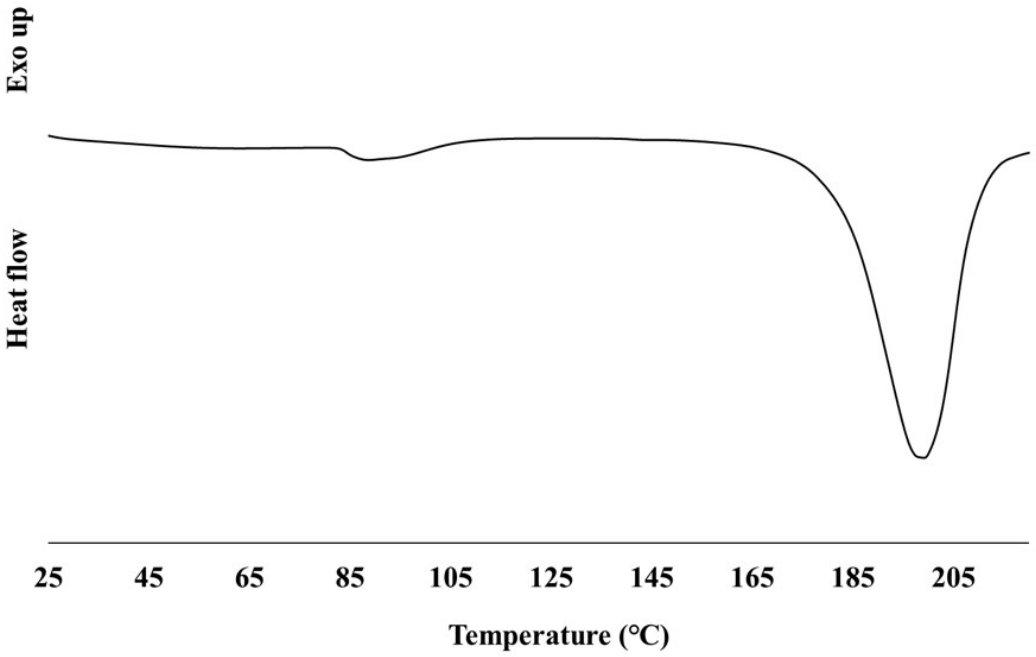

Figure 9-33: The DSC trace of an unidentified solvated form of SAS, crsyatllised under vapour diffusion with MeOH and hx.

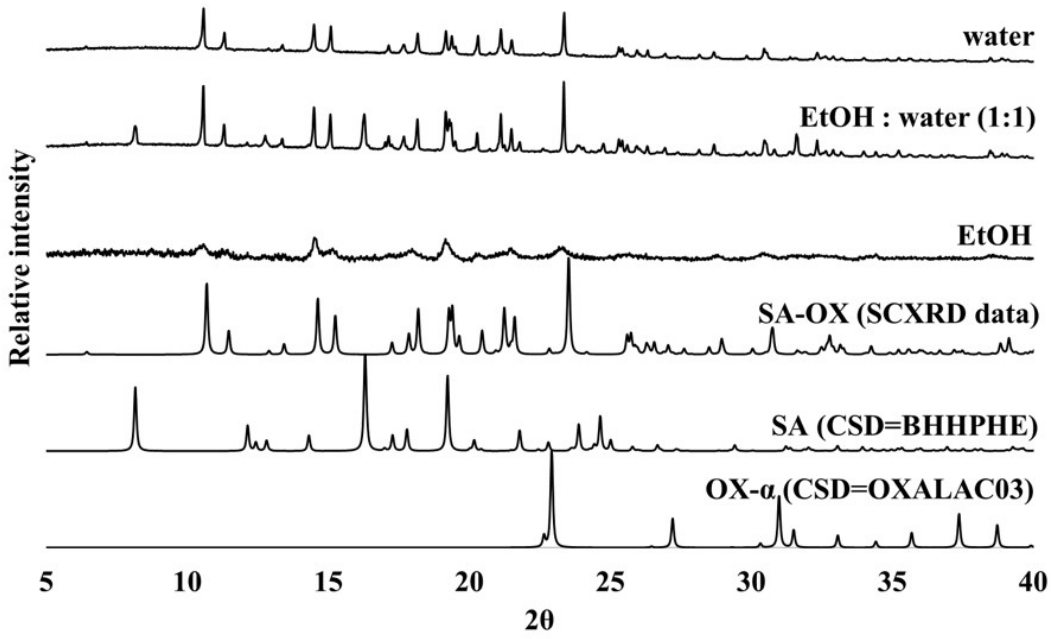

Figure 9-34: The PXRD traces obtained under evaporative crystallisation for good quality single crystals of SA-OX.

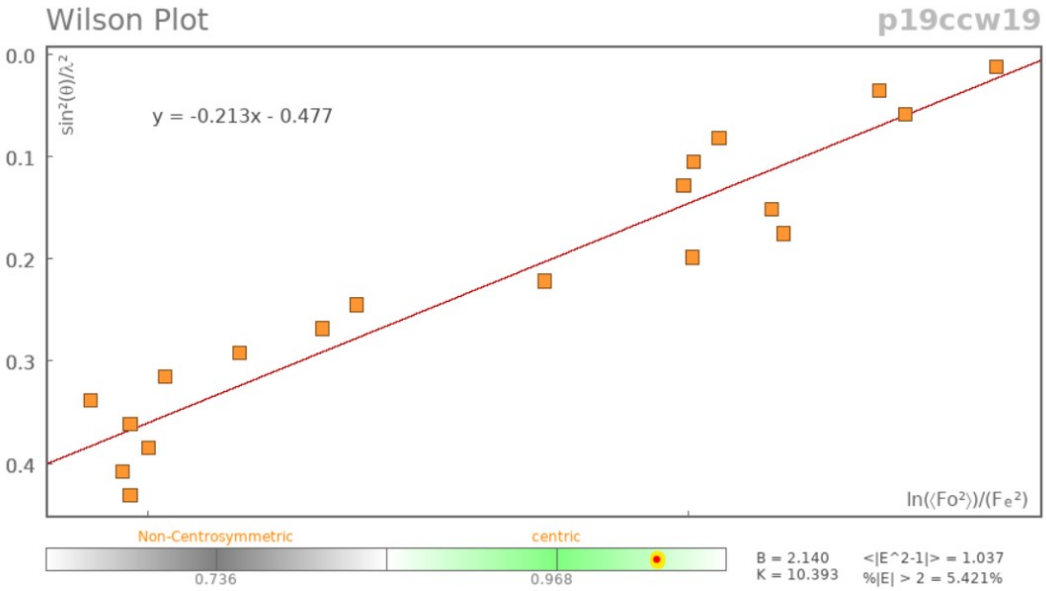

Figure 9-35: Reflection statistics of crystallographic data collected for SAS, showing a Wilson Plot.

5 Appendix for chapter 7

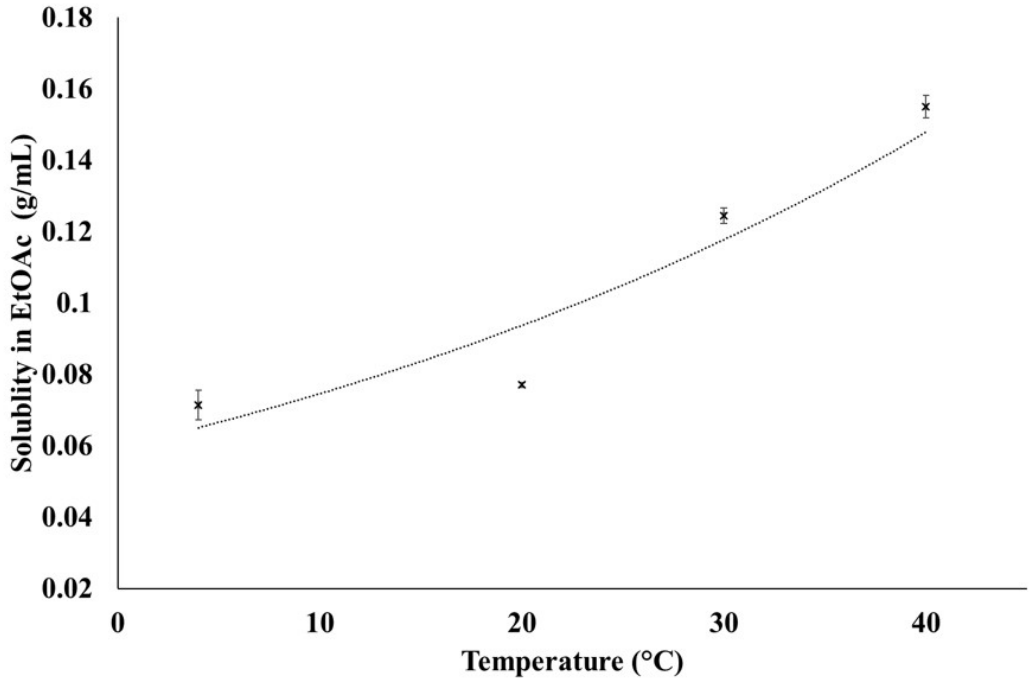

Figure 9-36: The measured solubility curve of PhG dihydrate in EtOAc, using gravimetric methods.